

**COST-EFFECTIVE CATALYST
DERIVED FROM NATURAL ZEOLITES THROUGH
BALL MILLING AND RECRYSTALLIZATION METHOD
FOR HYDROCARBON CONVERSION**

BY

TEGUH KURNIAWAN

A Dissertation Presented to the
DEANSHIP OF GRADUATE STUDIES

KING FAHD UNIVERSITY OF PETROLEUM & MINERALS

DHAHRAN, SAUDI ARABIA

In Partial Fulfillment of the
Requirements for the Degree of

DOCTOR OF PHILOSOPHY

In

CHEMICAL ENGINEERING

December 2017

KING FAHD UNIVERSITY OF PETROLEUM & MINERALS

DHAHRAN- 31261, SAUDI ARABIA

DEANSHIP OF GRADUATE STUDIES

This thesis, written by **TEGUH KURNIAWAN** under the direction of his thesis advisor and approved by his thesis committee, has been presented and accepted by the Dean of Graduate Studies, in partial fulfillment of the requirements for the degree of **DOCTOR OF PHILOSOPHY IN CHEMICAL ENGINEERING**.



Dr. Mohammed S. Ba-Shammakh
Department Chairman



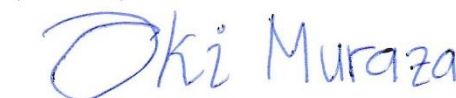
Prof. Salam A. Zummo
Dean of Graduate Studies



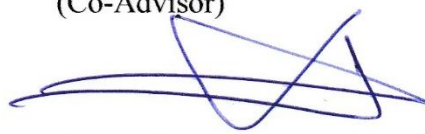
7/1/13
Date



Prof. Adnan M. Al-Amer
(Advisor)



Dr. Oki Muraza
(Co-Advisor)



Dr. Zain H. Yamani
(Member)



Dr. M. Mozahar Hossain
(Member)



Dr. Shaikh Abdur Razzak
(Member)

© Teguh Kurniawan

2017

To our beloved son

Muhammad Raya

May 10, 2017 – December 5, 2017

(Pink Tetralogy of Fallot)

ACKNOWLEDGMENTS

I am very grateful to my supervisor Prof. Adnan M. Al-Amer for his support and guidance. I highly thank my co-advisor Dr. Oki Muraza, who supported the research through ARAMCO project # 6600011900 and King Abdulaziz City for Science & Technology (KACST) project # 13-NAN1702-04 as part of the National Science, Technology and Innovation Plan. I also thank Dr. Zain H. Yamani as my committee member and Director of Center of Research Excellence in Nanotechnology (CENT), who supported me with the research facility at CENT. I sincerely thank Dr. Mohammed Mozahar Hossain and Dr. Shaikh Abdur Razzak as my committee members for correction and constructive discussions.

I am highly thankful to Dr. Abbas S. Hakeem for his kind assistance and fruitful discussions. I am very grateful to Prof. Nishiyama of Osaka University, Dr. Koji Miyake and Dr. Yuichiro Hirota for the research collaboration in catalysts testing for dimethyl ether to olefins. I would also thank Dr. Toshiyuki Yokoi and Mr. Toshiki Nishitoba of Tokyo Institute of Technology for catalysts characterization by using Aluminum Magic Angle Spinning Nuclear Magnetic Resonance (^{27}Al MAS NMR).

I acknowledge Dr. Nasiruzzaman Shaikh M. as CENT Laboratory Manager for the access to various research equipment. I also thank Dr. Oki's research group: Mr. Idris Akolade Bakare, Mr. Mohammed Sanhoob, Mr. Mohammed Hassan Ahmed, Mr. Annas Karrar Jamil, Mr. Rasheed, and Dr. Ganiyu Saheed Adewale for discussions and comments. I would like to thank CENT laboratory team Mr. Muhammad Qamaruddin, Mr. Muhammad

Ibrar, Mr. Mahmoud Abdelnaby, and Mr. Ibrahim Zarin for their technical assistance on the laboratory devices. I would like to thank the Indonesian Student Union (PPMI) for the support during the study.

I would like to express my gratitude to Chemical Engineering (CHE) Department KFUPM. My sincere thanks to Dr. Mohammed S. Ba-Shammakh, head of Chemical Engineering Department KFUPM, for his support to my Ph.D. studies. I also thank Dr. Nayef M. Al-Saifi and Dr. Mamdouh Al-Harthi as graduate coordinator for their kind supports during my PhD. studies. I also thank to Mr. Syed Amanullah and Mr. Abdelaziz Elgzoly as CHE laboratory engineer for their technical assistance during the research.

Finally, I would like to thank CENT KFUPM for sponsoring my Ph.D. studies through the Lecturer-B scheme, the University of Sultan Ageng Tirtayasa (UNTIRTA), and Ministry of Research, Technology and Higher Education Indonesia for the financial assistance.

TABLE OF CONTENTS

ACKNOWLEDGMENTS.....	V
TABLE OF CONTENTS.....	VII
LIST OF TABLES.....	XI
LIST OF FIGURES.....	XIII
LIST OF ABBREVIATIONS.....	XVII
ABSTRACT.....	XIX
ملخص الرسالة.....	XXI
CHAPTER 1 INTRODUCTION.....	1
1.1 Background.....	1
1.2 Problem Statement.....	5
1.3 Objectives	7
1.4 Outline of Thesis	7
CHAPTER 2 LITERATURE REVIEW: APPLICATION OF NATURAL ZEOLITES IN CATALYSIS	10
2.1 Summary.....	10
2.2 Introduction.....	10
2.3 Natural Zeolites Overview.....	12
2.3.1 Properties of Natural Zeolites	12
2.3.2 Commercial Applications of Natural Zeolites	15
2.3.3 Why Is Application of Natural zeolites in Catalysis Limited?.....	19
2.4 How to Improve the Purity of Natural Zeolites?	20
2.4.1 Physical Approach	21
2.4.2 Chemical Approach	23

2.5	Potential Application of Natural Zeolites in Catalysis	25
2.5.1	Natural Mordenite	26
2.5.2	Natural Clinoptilolite	29
2.5.3	Natural Chabazite	34
2.6	Strategy to Design Catalysts from Natural Zeolites	36
2.7	Concluding Remarks.....	39

CHAPTER 3 HIGH-QUALITY MORDENITE DERIVED FROM LOW-GRADE NATURAL ZEOLITES THROUGH HYDROTHERMAL RECRYSTALLIZATION..... 42

3.1	Summary.....	42
3.2	Introduction.....	42
3.3	Experimental.....	45
3.3.1	Materials	45
3.3.2	Ion-Exchange Procedure	46
3.3.3	Recrystallization	46
3.3.4	Synthetic Mordenite Preparation	46
3.3.5	Characterization	47
3.3.6	Catalysts Testing.....	48
3.4	Results and Discussion	48
3.4.1	Ion-Exchange Procedure	49
3.4.2	Recrystallization of Natural Zeolites.....	56
3.4.3	Comparison of Recrystallized Natural Mordenite and Synthetic Mordenite	65
3.4.4	Mechanism of Natural Mordenite Recrystallization	70
3.5	Concluding Remarks.....	72

CHAPTER 4 HIGH-ENERGY BALL MILLING ATTRITOR AND HYDROTHERMAL RECRYSTALLIZATION TO PREPARE MORDENITE NANOPARTICLES: THE EFFECT OF THE RELATIVE WEIGHT OF THE BALLS AND WATER..... 73

4.1	Summary.....	73
4.2	Introduction.....	74
4.3	Experimental.....	77
4.3.1	Material Characterization	77
4.3.2	High-Energy Ball Milling (HEBM) Attritor	78
4.4	Results and Discussion	80
4.4.1	Particles Size Analysis.....	80

4.4.2	Crystallinity Study.....	91
4.4.3	Textural Properties According to Nitrogen Physisorption.....	93
4.4.4	Taguchi Analysis	97
4.4.5	Hydrothermal Recrystallization.....	100
4.5	Concluding Remarks.....	102
 CHAPTER 5 MECHANOCHEMICAL ROUTE AND RECRYSTALLIZATION STRATEGY TO FABRICATE MORDENITE NANOPARTICLES FROM NATURAL ZEOLITES..... 103		
5.1	Summary.....	103
5.2	Introduction.....	104
5.3	Experimental.....	106
5.3.1	Material Characterization	106
5.3.2	Ball-Milling.....	107
5.3.3	Recrystallization	107
5.4	Results and Discussion	107
5.4.1	Ball Milling Effect on the Crystallinity of Natural Zeolites.....	109
5.4.2	Effect of Silica and NaOH Concentration on Mordenite Recrystallization	110
5.4.3	Effect of Hydrothermal Time on Mordenite Recrystallization	113
5.4.4	Effect of the Ratio of the Mass Sample to Solution on Mordenite Recrystallization	114
5.4.5	High Purity MOR of the Recrystallized Sample	115
5.4.6	FTIR Study of the Mordenite Samples.....	118
5.4.7	Particle Size Study	119
5.4.8	Textural Properties Study.....	121
5.4.9	Milling-Recrystallization Mechanism	125
5.5	Concluding Remarks.....	126
 CHAPTER 6 CONVERSION OF DIMETHYL ETHER TO OLEFINS OVER NANOSIZED MORDENITE FABRICATED BY COMBINED HIGH-ENERGY BALL MILLING WITH RECRYSTALLIZATION 127		
6.1	Summary.....	127
6.2	Introduction.....	128
6.3	Experimental.....	130
6.3.1	Material Characterization	130
6.3.2	High-Energy Ball Milling	131
6.3.3	Recrystallization	132
6.3.4	Conversion of Dimethyl Ether to Olefins.....	132

6.4 Results and Discussion	133
6.4.1 Natural Zeolites	133
6.4.2 High-Energy Ball Milling	136
6.4.3 Recrystallization	142
6.4.4 Qualitative Kinetics Dimethyl Ether to Olefins	146
6.4.5 Economic Evaluation of High-Energy Ball Milling and Recrystallization Process	152
6.5 Concluding Remarks.....	154
 CHAPTER 7 SELECTIVE ISOMERIZATION N-BUTANE OVER NANOPARTICLES MOR FROM NATURAL ZEOLITES FABRICATED VIA SEQUENTIAL BALL MILLING-RECRYSTALLIZATION-DEALUMINATION ROUTE.....	 155
7.1 Summary.....	155
7.2 Introduction.....	156
7.3 Experimental.....	159
7.3.1 Material Characterization	160
7.3.2 Nanosized MOR Preparation	161
7.3.3 Recrystallization	162
7.3.4 Acid Dealumination	162
7.3.5 Catalysts Evaluation	163
7.4 Results and Discussion	163
7.4.1 Characterizations of the Samples.....	163
7.4.2 Particle size effect on n-butane isomerization.....	174
7.4.3 Dealumination of Nanoparticles Recrystallized MOR	179
7.5 Concluding Remarks.....	185
 CHAPTER 8 CONCLUSIONS AND RECOMMENDATIONS.....	 186
8.1 General Conclusions.....	186
8.2 Recommendations	189
 REFERENCES.....	 190
 VITAE.....	 202
 LIST OF PUBLICATIONS.....	 203

LIST OF TABLES

Table 2.1: Research on the application of natural mordenite for catalytic reactions.....	26
Table 2.2: Research on the application of natural clinoptilolite for catalytic reactions. ..	30
Table 2.3: Research on the application of natural chabazite for catalytic reactions.	34
Table 3.1: Textural properties and Si/Al of the as-received sample and protonated MOR by using NH_4NO_3 (H-P-N) and HCl (H-P-H) solutions.	51
Table 3.2: The number of acid sites of protonated MOR by using NH_4NO_3 (H-P-N) and HCl (H-P-H) solutions.	54
Table 3.3: Textural properties and silicon to aluminum ratio of samples.	60
Table 3.4: Brønsted and Lewis acid sites of the parent & recrystallized samples.....	63
Table 3.5: Textural properties of recrystallized natural mordenite and synthetic mordenite.	67
Table 3.6: Brønsted and Lewis acid sites of recrystallized natural mordenite and synthetic mordenite.	68
Table 4.1: The Taguchi L9 design of the experiment.....	79
Table 4.2: Mean of particle size by DLS -SEM images and crystallite size	88
Table 4.3: Particle size distribution by volume.	90
Table 4.4: Textural properties of the as-received and milled natural zeolites.	95
Table 5.1: XRF analysis of the as-received of low-rank natural mordenite.	109
Table 5.2: The effect of silica and OH^- molar ratio in the mordenite recrystallization ..	112
Table 5.3: Crystallinity study based on the XRD analysis and Si to Al ratio.....	116
Table 5.4: Comparison of mean particle size by XRD, SEM and TEM.....	120
Table 5.5: Textural properties of the parent, milled, and selected recrystallized milled MOR	123
Table 5.6: Textural properties of the parent and the recrystallized parent	124
Table 6.1: Highlight of zeolite 1D performance on olefinic target from dimethyl ether (DME)/methanol feed.	129
Table 6.2: XRF analysis of natural zeolite as-received	134
Table 6.3: Milling time effects on crystallinity.	137
Table 6.4: Physicochemical properties of the parent and treated natural zeolite.....	138
Table 6.5: Mesoporous volume of parent and treated natural zeolites.	140
Table 6.6: DME conversion, selectivity, and yield of products over parent and treated samples at TOS 10 and 60 min.	150
Table 6.7: Milling operational cost calculation.	153
Table 6.8: Recrystallization cost calculation.	153
Table 7.1: Textural properties and silicon/aluminum ratio of the parent and treated samples.....	167
Table 7.2: Acid sites of the samples by NH_3 -TPD	169
Table 7.3: Brønsted and Lewis acidity of the samples	172

Table 7.4: Conversion of n-butane transformation and products distribution over the mordenite catalysts at TOS = 10 min and 200 min (in the bracket).	176
--	-----

LIST OF FIGURES

Figure 1.1: Author at a mining area of natural zeolites in Java, Indonesia.....	1
Figure 1.2: (a) XRD pattern and (b) electron probe microanalyzer (EPMA) image of natural clinoptilolite (Cpt-HEU) with impurities; i.e., CM-K = potassium-rich phyllosilicate, Kfs = alkali feldspar, Plg = plagioclase (albite), Qz = quartz.[6]	2
Figure 1.3: Illustration of nanoparticles ZSM-5 preparation through ball milling and post-milling recrystallization [13].....	4
Figure 2.1: Primary building unit (TO ₄).	12
Figure 2.2: Secondary building unit.....	13
Figure 2.3: Examples of zeolite frameworks.	13
Figure 2.4: Illustration of sodalite framework as it builds from the basic units.	13
Figure 2.5 (a) Brønsted acid sites dan (b) Lewis acid sites in the zeolite structure.....	15
Figure 2.6: Application of natural clinoptilolite in wastewater treatment plant at Tahoe-Truckee USA [38].	16
Figure 2.7: Castel dell'Ovo, Naples, Italy (Photograph by Richard Nevell distributed under the Creative Commons Attribution-Share Alike 2.0 Generic) [41].....	17
Figure 2.8: Gravity-magnetic separation to improve natural zeolite purity. Adapted from ref. [52].....	22
Figure 2.9: Modification of natural zeolites for catalyst application.....	38
Figure 3.1: XRD patterns of (a) the as-received natural zeolites, (b) synthetic Na-MOR.	49
Figure 3.2: XRD patterns of protonated MOR by using solutions of (a) NH ₄ NO ₃ and (b) HCl.....	50
Figure 3.3: Nitrogen isotherms of the as-received sample (As-Received) and protonated MOR by using NH ₄ NO ₃ (H-P-N) and HCl (H-P-H) solutions.....	51
Figure 3.4: SEM images of protonated MOR by using (a) NH ₄ NO ₃ and (b) HCl solutions.	52
Figure 3.5: NH ₃ -TPD curves of protonated MOR by using (a) NH ₄ NO ₃ and (b) HCl solutions.	53
Figure 3.6: Butane conversion and products selectivity over H-P-N and H-P-H.....	55
Figure 3.7: XRD patterns of the as-received sample (P) and Na-MOR recrystallized samples. Offset by 1500, 3000, 4500, and 6000 for R2, R14, R26, MOR-S respectively.	57
Figure 3.8: ²⁷ Al NMR spectra of the as-received sample (P) and recrystallized MOR (R2).	58
Figure 3.9: SEM images of the protonated parent and recrystallized samples after 2-26 h hydrothermal treatment.	59

Figure 3.10: Nitrogen isotherms of the parent (H-P-H) and recrystallized H-MOR.	60
Figure 3.11: Mesopore in the recrystallized after ion-exchange with HCl over the recrystallized MOR samples.	61
Figure 3.12: Ammonia-TPD of the protonated parent (H-P) and recrystallized samples.	63
Figure 3.13: Butane conversion and products selectivity over the parent and the recrystallized natural mordenite.	65
Figure 3.14: Isobutane yield over different time of hydrothermal recrystallization.	65
Figure 3.15: Nitrogen isotherms of recrystallized natural mordenite and synthetic mordenite.	66
Figure 3.16: SEM images of (a) recrystallized natural mordenite and (b) synthetic mordenite.	67
Figure 3.17: Ammonia-TPD of recrystallized natural mordenite and synthetic mordenite.	68
Figure 3.18: Comparison of activity and products selectivity of n-butane isomerization over (a) recrystallized natural mordenite and (b) synthetic mordenite.	69
Figure 3.19: Comparison of isobutane yield over recrystallized natural mordenite and synthetic mordenite.	70
Figure 3.20: Mechanism of natural zeolites recrystallization.	71
Figure 4.1: Effects of the relative weights of the balls and water on the particle size distribution by volume.	81
Figure 4.2: Effects of the relative weights of the balls and water on the particle size distribution by number.	84
Figure 4.3: FE-SEM images of (a) the parent and the milled samples (b) B10-W4, (c) B10-W5, (d) B10-W6, (e) B20-W4, (f) B20-W5), (g) B20-W6, (h) B30-W4, (i) B30-W5 and (j) B30-W6.	86
Figure 4.4: Particle sizes distribution based on the SEM images (a) B10-W4, (b) B10- W5, (c) B10-W6, (d) B20-W4, (e) B20-W5), (f) B20-W6, (g) B30-W4, (h) B30-W5, and (i) B30-W6.	87
Figure 4.5: High-energy ball milling attritor set up and the mechanism by which it reduces particle size.	91
Figure 4.6: (a) XRD patterns and (b) relative crystallinity.	92
Figure 4.7: Nitrogen-isotherms of the milled samples and parent.	94
Figure 4.8: Mesopore size distribution of the milled samples.	96
Figure 4.9: TEM images of the parent and the milled sample (B30-W5).	97
Figure 4.10: Mean S/N ratios of the ball-to-powder weight ratio and water-to-powder weight ratio (a) crystallinity, (b) particle size, (c) mesopore volume, and (d) external surface area.	98
Figure 4.11: Taguchi delta plot of of the effect ball-to-powder weight ratio and water-to-powder weight ratio on crystallinity, particle size, mesopore volume, and external surface area.	99

Figure 4.12: Effect of hydrothermal recrystallization on the crystallinity of MOR.	101
Figure 4.13: Effect of hydrothermal recrystallization on the particle size of MOR.	101
Figure 5.1: XRD pattern of the as-received natural zeolites from Klaten, Indonesia....	108
Figure 5.2: ^{27}Al NMR of the parent and milled samples.	110
Figure 5.3: The effect of different concentrations of silica on the crystalline phase of the recrystallized MOR (x SiO_2 : 12 NaOH : 780 H_2O).	111
Figure 5.4: The different NaOH concentrations effect on the crystallinity of the recrystallized MOR (18 SiO_2 : y NaOH : 780 H_2O).	112
Figure 5.5: The effect of hydrothermal time (2 to 48 h) on the crystalline phase of the recrystallized MOR (18 SiO_2 /12NaOH/780 H_2O).	113
Figure 5.6: Effect of different weight percentages of the milled to solution (W = 1, 2 and 5 g) on the crystallinity of the recrystallized MOR (18 SiO_2 /12NaOH/780 H_2O).	114
Figure 5.7: Comparison of XRD patterns of the parent, milled nanomordenite and selected recrystallized (18 SiO_2 /12 NaOH/780 H_2O) MOR at 2 h hydrothermal period.	116
Figure 5.8: TEM images in high magnification of (a) the parent, (b) milled, and (c) recrystallized.	117
Figure 5.9: Comparison XRD patterns of the parent and recrystallized parent.	118
Figure 5.10: FTIR spectra of the parent natural zeolites and modified samples.	119
Figure 5.11: SEM images of (a) the parent, (b) milled, and (c) recrystallized mordenite nanoparticles.	120
Figure 5.12: Particle size distribution based on SEM images of (a) the parent, (b) milled, and (c) recrystallized sample.	120
Figure 5.13: Intercrystalline mesopores captured on the TEM images of the milled and recrystallized mordenite.	121
Figure 5.14: N_2 isotherm of parent and mechanochemical treated sample (18 SiO_2 /12 NaOH/780 H_2O) at T = 170 °C for 2 h.	122
Figure 5.15: Pore size distribution calculated by the DFT method.	123
Figure 5.16: N_2 isotherm of the parent and recrystallized parent (18 SiO_2 :12NaOH:780 H_2O) at T = 170 °C for 2 h).	124
Figure 5.17: Illustration of the ball milling and recrystallization transformation of microsized natural zeolites into nanosized MOR with high purity and crystallinity.	125
Figure 6.1: XRD patterns of the parent and modified natural MOR zeolites.	133
Figure 6.2: TEM of (a) The parent, (b) milled-6h, (c) milled-8h, (d) milled-10h samples.	135
Figure 6.3: Nitrogen adsorption-desorption isotherms of the parent natural MOR zeolite.	136
Figure 6.4: Nitrogen adsorption isotherms of the parent and treated natural zeolites. ...	139

Figure 6.5: Mesopore size distribution of samples by NLDFT method.	141
Figure 6.6: NH ₃ TPD of parent and treated natural MOR zeolites.	142
Figure 6.7: XRD patterns revealed the disappearance of nonmordenite phases on recrystallized samples.	143
Figure 6.8: SEM images of the parent (a), milled-8h (d) and R-milled-8h (g). TEM images of the parent (b and c), milled-8h (e and f), and R-milled-8h (h and i).	144
Figure 6.9: DME conversion over parent and treated natural MOR zeolites at T= 350 °C, P= 1 bar, and W/F=0.85 h.	147
Figure 6.10: Products selectivity over parent and treated natural zeolites at TOS = 10 min.	148
Figure 6.11: Products selectivity over parent and treated natural zeolites at TOS = 60 min.	151
Figure 7.1: Flowchart of the experiment.	160
Figure 7.2: XRD patterns of H-MOR parent and modified H-MOR samples.	164
Figure 7.3: ²⁷ Al NMR spectra of H-MOR samples	165
Figure 7.4: Nitrogen isotherms of H-MOR samples.	166
Figure 7.5: Cumulative pore volume versus pore size of the parent and treated samples by the DFT method.	168
Figure 7.6: Acidity of H-MOR samples by ammonia-TPD.	169
Figure 7.7: FTIR spectra of H-MOR samples.	171
Figure 7.8: SEM images of (a) H-P, (b)H-M, (c) H-R, (d) H-R-8, and (e) H-R-24.	173
Figure 7.9: Particle size distribution of H-MOR samples.	174
Figure 7.10: Isomerization of n-butane over (a) H-P, (b) H-M, and (c) H-R at T = 350 °C, C ₄ H ₁₀ = 2 mL/min, N ₂ = 20 mL/min.	175
Figure 7.11: Isomerization n-butane over (a) H-R, Brønsted and Lewis acidity of the samples (b) H-R-8 and (c)H-R-24, at T = 350 °C, C ₄ H ₁₀ = 2 ml/min, N ₂ = 20 ml/min.	180
Figure 7.12: The spent catalysts of (a) the micro-sized parent and nanoparticles of (b) the milled, (c) recrystallized, (d) recrystallized-dealuminated 8 h, and (e) recrystallized-dealuminated 24 h.	182
Figure 7.13: Comparison between acid dealuminated 8 h of (a) the parent and (b) nano-MOR in n-butane isomerization at T= 420 °C.	183
Figure 7.14: Catalytic performance over nano-MOR (H-R-24) for n-butane isomerization at different temperature (a) T= 350 °C and (b) T= 420 °C..	184
Figure 7.15: Thermodynamic conversion of n-butane isomerization between 200 to 420 °C.	184

LIST OF ABBREVIATIONS

BAS	:	Brønsted acid sites
BET	:	Brunauer–Emmett–Teller
CEC	:	Cation exchange capacity
CHA	:	Chabazite
DLS	:	Dynamic light scattering
GC	:	Gas chromatography
FE-SEM	:	Field emission scanning electron microscope
FID	:	Flame ionization detector
FTIR	:	Fourier transforms infrared spectroscopy
HEBM	:	High-energy ball milling
HEU	:	Heulandite
LAS	:	Lewis acid sites
MAS NMR	:	Magic angle spinning nuclear magnetic resonance
MOR	:	Mordenite
OSDA	:	Organic solvent directing agent
PBU	:	Primary building unit

SAS	:	Strong acid sites
SBU	:	Secondary building unit
TEM	:	Transmission electron microscope
TPD	:	Temperature programmed desorption
WAS	:	Weak acid sites
XRD	:	X-ray diffraction
XRF	:	X-ray fluorescence

ABSTRACT

Full Name : Teguh Kurniawan
Thesis Title : Cost-effective Catalyst Derived from Natural Zeolites through Ball Milling and Recrystallization Method for Hydrocarbon Conversion
Major Field : Chemical Engineering
Date of Degree : December 2017

Natural zeolites are plentiful and inexpensive natural minerals, which have had wide applications in agriculture, aquaculture, soil adjustment, building materials, water purification, and wastewater treatment. However, the utilization of natural zeolites for catalysis purposes is limited due to low crystallinity and poor textural properties. In the present work, we investigate methods to synthesize catalysts from low-cost natural zeolites through facile methods, i.e. sequential milling-recrystallization, and sequential milling-recrystallization-dealumination. These catalysts were used in dimethyl ether to olefins conversion and n-butane isomerization.

We fabricated hierarchical mordenite nanoparticles from the low-cost natural mordenite through high-energy ball milling followed by hydrothermal recrystallization method. The as-received natural zeolites showed mordenite with impurity phases and low total surface area (ca. 133 m²/g) as indicated by X-ray diffraction study and nitrogen physisorption analysis, respectively. The as-received natural zeolites were milled by high-energy ball milling attritor to obtain nanoparticles within the size of 20-160 nm, which were confirmed by dynamic light scattering, field emission scanning electron microscopy, and transmission electron microscopy technique. The X-ray diffraction study revealed that crystallinity of the milled zeolites had decreased significantly. The crystallinity of mordenite nanoparticles was recovered after recrystallization of the milled sample in the hydrothermal basic silicate solution. The nitrogen physisorption study showed that the textural properties of recrystallized mordenite nanoparticles were improved with total surface area was ca. 240 m²/g and external surface area was ca. 150 m²/g, a 6-fold increase from the parent. The hierarchical pore system was observed in the recrystallized mordenite as the mesopore volume increased to 0.36 mL/g from only 0.04 mL/g in the as-received natural zeolites.

A high conversion of dimethyl ether was obtained over the recrystallized mordenite (99.7%) and milled natural mordenite (54.1%) as compared to the parent (1.2%). Moreover, the milling only and the sequential milling-recrystallization processes improved selectivity toward olefins and prolonged catalyst lifetime. The reduced particles size combined with the hierarchical porosity and acidity effectively enhanced catalysts activity and selectivity to olefins. The samples were further tested for n-butane isomerization. The isobutane selectivity over nanoparticles mordenite fabricated by the sequential milling-recrystallization increased to 28% as compared to 11% on the parent mordenite. Moreover, the recrystallized mordenite nanoparticles showed better catalyst stability as compared to the microparticles parent sample. Finally, dealumination procedures were applied to the

recrystallized mordenite nanoparticles. The total surface area of dealuminated nanoparticle sample increased to ca. 354 m²/g. The nanoparticles mordenite obtained by the sequential milling-recrystallization-dealumination exhibited the highest selectivity of ca. 58% to isobutane and less deactivation rate in the n-butane isomerization.

ملخص الرسالة

الاسم الكامل: تيقو كيرنوان

عنوان الرسالة: تحويل الهيدروكربونات عن طريق محفزات منخفضة التكلفة مشتقة من الزيوليت الطبيعي من خلال الطحن بالكرات و إعادة البلورة

التخصص: الهندسة الكيميائية

تاريخ الدرجة العلمية: ديسمبر 2017

المواد الزيوليتية الطبيعية هي مواد طبيعية وفيرة ورخيصة ولها تطبيقات واسعة في مجال الزراعة، تربية الأحياء المائية، تعديل التربة، مواد البناء، تنقية المياه، ومعالجة مياه الصرف الصحي. ولكن بسبب انخفاض التبلور والخصائص النسيجية المتردية لهذه المواد، فإن استخدام هذه المواد الزيوليتية الطبيعية كعوامل حفازة مازال محدودا. في هذا العمل البحثي، نقوم بالتحقيق في طرق تحضير المحفزات لتحضير مواد محفزة من المواد الزيوليتية الطبيعية منخفضة التكلفة بالأساليب البسيطة، أي طحن بالكرات و يليه إعادة التبلور و طحن بالكرات و يليه إعادة البلورة و إزالة الألمنيوم . و قد تم استخدام هذه المحفزات في تفاعل تحويل ثنائي ميثيل الأثير إلى الأوليفينات وكذلك تفاعل مأكبة البيوتان.

قمنا بتحضير مادة الموردينايت ذات البلورات النانوية وذات المسامات الهرمية من زيولايت طبيعي و منخفض التكلفة وذلك من خلال الطحن بالكرات-عالية الطاقة- تليها بلورة مائية حرارية. أظهرت دراسة الأشعة السينية وامتصاص النيتروجين أن المادة الطبيعية قبل التعديل تحتوي على تركيبة الموردينايت (mordenite) مع وجود بعض الشوائب، وقد كانت كثافة مساحة الأسطح تقريبا 133 م²/جم. و تم طحن الزيوليت الطبيعي بواسطة كرات عالية الطاقة وذلك للحصول على بلورات نانوية، يتراوح حجمها ما بين 20 إلى 160 نانومتر، حيث تم التأكد من حجمها عن طريق التحليل (DLS) و (FE-SEM) و (TEM). لكن كشفت دراسة حيود الأشعة السينية (XRD) أن درجة تبلور الزيوليت المطحون قد انخفض بشكل ملحوظ بعد الطحن. فتم استعادة تبلور البلورات النانوية للموردينايت عن طريق عملية إعادة البلورة للعينة المطحونة وذلك بالتسخين في وجود محلول السيليكا القاعدي. وأظهرت دراسة امتصاص النيتروجين أن الخصائص التكوينية للبلورات النانوية للموردينايت المعاد تكوينه قد تحسنت، حيث تحسنت كثافة مساحة الأسطح الكلية إلى 240 م²/جم و كثافة مساحة السطح الخارجي إلى 150 م²/جم، أي أنها أصبحت ستة أضعاف الزيولايت قبل المعالجة. كما لوحظ وجود المسام الهرمي على الموردينايت المعاد بلورته حيث ارتفع حجم المسامات المتوسطة بين البلورات إلى 0.36 ملتر / جم من أصل 0.04 ملتر / جم فقط في الزيوليت الطبيعي.

تم الحصول على نسبة تحويل عالية لثنائي ميثيل الإيثر عند اختبار الموردينايت المعاد بلورته بنسبة (99.7%)، بينما الموردينايت المطحون حوّل بنسبة مجرد (54.1%) بالمقارنة مع الموردينايت غير المعالج الذي حوّل بنسبة (1.2%). علاوة على ذلك، فإن عمليات الطحن فقط وعمليات الطحن مع إعادة البلورة قد حسنت الانتقائية تجاه الأوليفينات وطولت فترة فاعلية عمل المادة المحفزة. وقد أدى حجم البلورات الصغير إلى جانب المسامية الهرمية والحموضة إلى زيادة فعالية نشاط المادة الحفازة و كذلك

الانتقائية للأولييفينات. كذلك تم اختبار العينات لتفاعل تماكب البيوتان، حيث زادت الانتقائية للأيزوبيوتان عند البلورات النانوية التي تم طحنها ومن ثم إعادة بلورتها إلى 28٪ مقارنة بمجرد 11٪ للموردنايت غير المعالج. علاوة على ذلك، الموردنايت ذات حجم النانو والمعاد بلورته كان أفضل استقرارا بالمقارنة مع العينة الأم. أخيرا، تم إجراء عملية نزع الألمنيوم (dealumination) على البلورات النانوية المعاد بلورتها للموردنايت، حيث ارتفعت مساحة المادة بعد عملية نزع الألمنيوم إلى 354 م²/جم. وامتاز الموردنايت ذو الحجم النانوي والذي تم الحصول عليه عن طريق الطحن بالكرات يليه إعادة التبلور ونزع الألمنيوم انتقائية أعلى للأيزوبيوتان بنسبة (58%) مع معدل اخمد أقل في تماكب البيوتان.

CHAPTER 1

INTRODUCTION

1.1 Background

Zeolites are aluminosilicates crystalline compounds with highly ordered microporous structure filled by cations (Na^+ , K^+ , Ca^{2+}). The cations are required to compensate extra charge due to the replacement of tetravalent silicon with trivalent aluminum. Brønsted acid sites arise as the cations change to H^+ , which act as active sites in catalytic reactions. Zeolite catalysts are synthesized in the laboratory under controlled temperature, composition, and hydrothermal time. Yet, one can also find zeolites in nature. In fact, the first discovery of zeolites was with natural zeolites from Sweden and Iceland by Cronstedt in 1756.



Figure 1.1: Author at a mining area of natural zeolites in Java, Indonesia.

Natural zeolites are abundantly available throughout the world [1]. The natural zeolites are typically mined by a conventional open pit mining (Figure 1.1). The large deposit and

easiness of mining lead to a low price of natural zeolites (0.04 – 0.25 USD/kg) as compared to the synthetic one (10–20 USD/kg) [2, 3]. However, natural zeolites are mostly found in several crystalline phases and accompanied by non-reacted volcanic glass, feldspar, quartz, calcite, montmorillonite, calcium sulfate dihydrate, and cristobalite [4]. An example of this is natural clinoptilolite with accessories potassium-rich phyllosilicate, alkali feldspar, plagioclase, and quartz as presented in the XRD spectrum and electron probe microanalyzer, Figure 1.2. Furthermore, natural zeolites can vary in composition and crystalline phases even in the same sediment location due to the mineralogical dissimilarity of mother volcanic tuff and different mechanism of zeolites formation [5]. The presence of impurities and heterogeneity in the composition of natural zeolites are the main causes of limited utilization in industrial application, particularly for catalysis purposes [1].

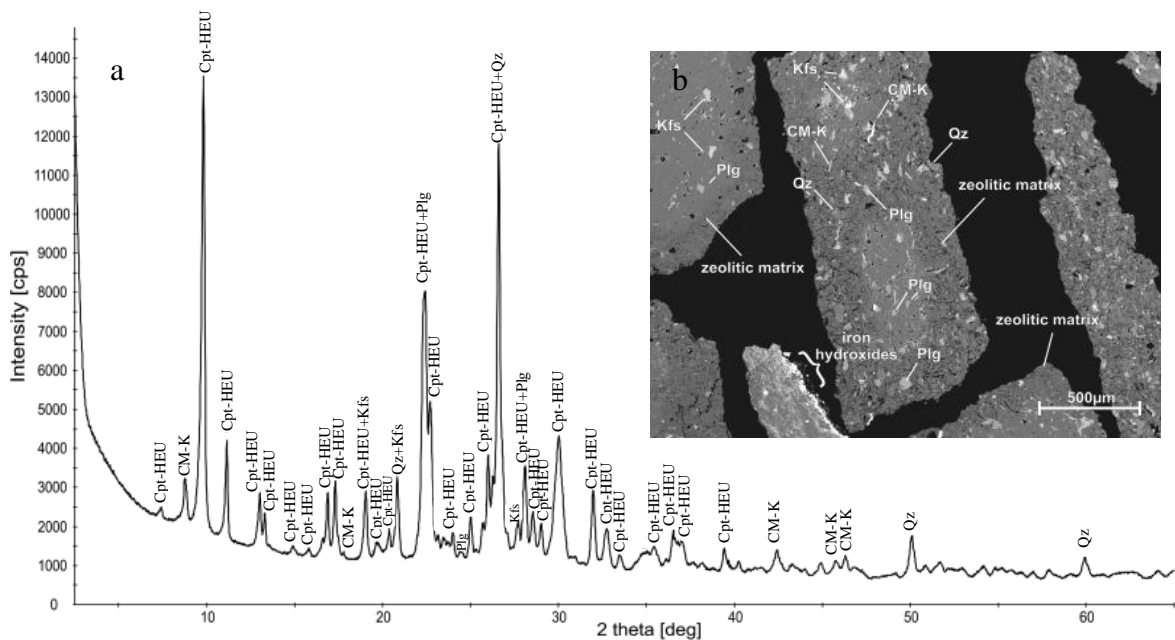


Figure 1.2: (a) XRD pattern and (b) electron probe microanalyzer (EPMA) image of natural clinoptilolite (Cpt-HEU) with impurities; i.e., CM-K = potassium-rich phyllosilicate, Kfs = alkali feldspar, Plg = plagioclase (albite), Qz = quartz.[6]

Researchers made several attempts to upgrade natural zeolite for broader industrial exploitation. Natural clinoptilolite-mordenite with accessories like feldspar, smectite, vermiculite, and quartz has been successfully converted to a high cation exchange capacity (CEC) zeolite Na-P through hydrothermal recrystallization by using sodium hydroxide solution; however, the non-zeolite impurity phases were difficult to transform into a zeolite phase [7]. Fusion of NaOH powder through natural clinoptilolite which contains quartz and feldspar as traces, followed by hydrothermal recrystallization effectively dissolved the clinoptilolite and impurity phases to be converted into a high CEC zeolite such as Na-P, Na-X, hydroxysodalite [8] and zeolite Na-Y [9]. Watanabe et al. [10] reported that natural mordenite and clinoptilolite with impurities quartz, feldspar, silicate was transformed to zeolite philipsite by extending the alkali hydrothermal treatment for seven days.

Top-down methods by ball milling to improve textural properties of natural zeolites were also reported in the literature [11] [12]. The nanosized zeolite was targeted to increase external surface area and overcome diffusion limitation. Sequential dry and wet milling method was investigated in order to effectively achieve nanosized particle and minimize crystallinity reduction [11]. The wet ball milling of zeolite HY was reported to provide a higher crystallinity as compared with dry ball milling method [12]. However, a decrease of zeolite phase crystallinity was inescapable after the ball milling step, both the dry and wet milling methods. Moreover, the wide particle size distribution was observed in the milled samples within the range of nanosize to microsize.

In the past few years, Wakihara and co-workers [13, 14] developed a top-down method combined with hydrothermal recrystallization to obtain nanosized of ZSM-5, zeolite A, and zeolite X with high crystallinity. The parent ZSM-5 with particle size in micron size

was milled into nanoparticle size. The demolished crystalline ZSM-5 structure was recovered back into high crystalline ZSM-5 after hydrothermal recrystallization step (Figure 1.3). Similarly, Yang et al. [15] have been successfully fabricated nanoparticles of SAPO-34 through ball milling-recrystallization method with improvement in its physicochemical properties resulted in a high methanol conversion to olefins and high catalysts stability.

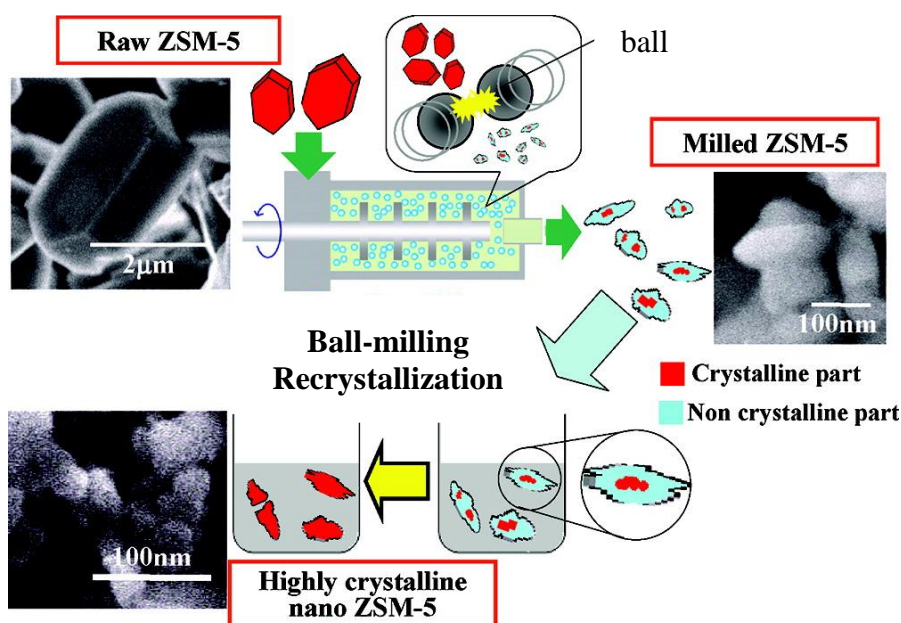


Figure 1.3: Illustration of nanoparticles ZSM-5 preparation through ball milling and post-milling recrystallization [13].

The combination of top-down and hydrothermal recrystallization is a potential method to fabricate nanoparticles from natural zeolites. However, up to date, there is no publication on fabrication nanoparticles from natural zeolites by sequential milling-recrystallization. The investigation of the effect of ball milling and recrystallization on natural zeolites phase

impurities is also interesting. The literature reported only for the synthetic zeolites, which is generally high in phase purity. Furthermore, an improvement in physicochemical properties of natural zeolites (i.e., high crystallinity, large surface area, high micropore volume, and large mesopore volume after the milling-recrystallization) could lead to better catalysis performance of the zeolites.

1.2 Problem Statement

Since the late 1980s, hydrothermal recrystallization method has been investigated to improve the purity of natural chabazite by transforming the impurities erionite and clinoptilolite into the major phase chabazite [16-18]. To date, there has been no investigation on recrystallization of the impurity phases of natural mordenite into high-crystalline mordenite phase. Mordenite is important for two reasons. Firstly, mordenite is widely utilized as commercial industrial catalysts, i.e., in hydroisomerization and alkylation. Secondly, mordenite is among the largest deposit of natural zeolites in the world [1]. The natural mordenite is frequently found with impurity phases such as clinoptilolite, quartz, and amorphous phase. Hence, it will be very interesting to investigate recrystallization of low-crystalline natural mordenite into high-crystalline mordenite.

Recently, ball milling was applied to obtain nanoparticle zeolites followed by hydrothermal recrystallization to recover the crystallinity of the nanoparticles [14, 19, 20]. However, the technique was only applied to synthetic zeolites, which have usually high purity phases. Applying the technique on natural zeolites with impurity phases will be beneficial to exploit the full potential of the ball milling-recrystallization technique to fabricate nanosized zeolites. Nanosized synthetic zeolites can be prepared either through a bottom-up or a top-down approach; however, a bottom-up strategy is not possible to be applied to

the natural zeolites. Hence, a top-down strategy, like ball milling, could be an appropriate way of preparing nanoparticles from natural zeolites.

The combination of ball milling and recrystallization has the potential for preparing a more homogeneous size of nanoparticles zeolites with high crystallinity. The size of nanoparticles zeolites is critically determined in the first step, viz. ball-milling. The fabrication of a high crystallinity nanoparticles mordenite through ball milling method frequently results in a wide particle size distribution. In the sequential ball milling-recrystallization approach, the nanoparticle size with narrow particle size distribution can be achieved by sacrificing the crystallinity and then recovering it by recrystallization. Hence, the investigation of the critical parameters in ball milling step is the first important aspect to be studied.

Aluminum content in natural zeolites is typically high which lead to fast deactivation rate and non-selective products in catalytic hydrocarbon conversion [21, 22]. In addition to the high aluminum content, metal impurities are usually observed in the natural zeolites. Acid dealumination could be applied to reduce the aluminum content and the metal impurities in the natural zeolites. Partial aluminum removal from the framework could also improve the textural properties of natural zeolites.

In summary, if we could systematically obtain the evidence derived from experiment that the ball milling, recrystallization, and dealumination techniques improve the quality of natural mordenite for catalytic hydrocarbon conversions, it would contribute immensely to enhance esoteric knowledge in upgrading the natural mordenite.

1.3 Objectives

The general objective of this thesis is to investigate methods to synthesize cost-effective catalysts from low-quality natural mordenite by recrystallization, ball milling, ball milling-recrystallization, and sequential ball milling-recrystallization-dealumination.

The specific objectives are:

- 1 Investigate the recrystallization of parent natural mordenite by hydrothermal method.
- 2 Evaluate the effects of high-energy ball milling on natural mordenite properties.
- 3 Study the recrystallization of the milled natural mordenite by hydrothermal method.
- 4 Investigate the effects of dealumination on the structural properties of nanoparticles of recrystallized mordenite.
- 5 Evaluate the catalysts for hydrocarbon conversion, viz. dimethyl ether to olefins and n-butane isomerization in a fixed bed reactor.

1.4 Outline of Thesis

This thesis comprises of 8 chapters, which can be grouped into 4 parts. The first two chapters provide an introduction and the research state-of-the-art. **Chapters 3-5** present methods to fabricate high quality mordenite nanoparticles from natural zeolites. **Chapters 6-7** discuss the performance of nanoparticles mordenite for specific catalytic hydrocarbon conversions. The last part is conclusions and recommendations.

The literature review of natural zeolites is discussed in **Chapter 2**. The overview of natural zeolites is discussed. This covers properties and commercial applications of natural

zeolites. Afterward, a discussion on the application of natural zeolites as catalysts is presented. Several types of natural zeolites have the potency to be used as catalysts are discussed thoroughly. Strategy to design catalysts from natural zeolites such as top-down method, recrystallization, and dealumination are presented.

Chapter 3 covers the hydrothermal recrystallization of low-crystalline natural mordenite with amorphous phase, clinoptilolite, and quartz as impurities. It is discovered that hydrothermal recrystallization by using sodium silicate solution is effective to obtain high crystallinity of natural mordenite. The effect of hydrothermal recrystallization time on crystallinity is also discussed thoroughly. The comparison of recrystallized mordenite and synthetic mordenite is presented.

Chapter 4 demonstrates the fabrication of nanoparticles mordenite by high-energy ball milling attritor and hydrothermal recrystallization. In particular, the chapter focuses on the effects of the relative weight of balls and water to the particle size in the milling step. The Taguchi analysis shows that the relative weight of balls gives the most significant effects on the parameter studies. The recrystallization recovers the crystallinity of mordenite; however, quartz still appears as a competing phase.

Chapter 5 assesses the parameters on recrystallization hydrothermal step in the sequential ball milling-recrystallization method. The target is to obtain mordenite nanoparticles with high crystallinity and low impurity phase. Parameters such as recrystallization time, the ratio of the milled sample weight to the solution, silica, and OH^- concentration were varied to study the effect on the crystallinity of the recrystallized mordenite sample.

Chapter 6-7 describes the application of nanoparticles mordenite for catalytic reactions. Conversion of dimethyl ether to olefins over nanoparticles mordenite is discussed in **Chapter 6**. The mordenite nanoparticles prepared by milling and sequential milling-recrystallization show a higher dimethyl ether conversion and better stability as compared to the parent natural zeolites. **Chapter 7** illustrates selective n-butane isomerization over nanoparticles of samples obtained by the sequential milling-recrystallization and the sequential milling-recrystallization-dealumination. The better selectivity of these samples is evidenced in the isomerization of n-butane as compared to the parent natural zeolites. The mordenite nanoparticles prepared by the sequential milling-recrystallization-dealumination show higher isobutane selectivity as compared to the non-dealuminated milled-recrystallized mordenite.

Conclusions on the findings and contributions of this thesis are presented in **Chapter 8**.

An outlook with some recommendations for future investigation is also described.

CHAPTER 2

LITERATURE REVIEW: APPLICATION OF NATURAL ZEOLITES IN CATALYSIS

2.1 Summary

Natural zeolites are well-known for applications in water purification and wastewater treatment, soil adjustment, aquaculture, and building materials. However, the utilization of the natural zeolites in catalysis field is very limited as compared to the synthetic zeolites due to the lack of purity and inconsistency in composition. The physical and chemical approaches to decrease impurities in natural zeolites are discussed thoroughly. Various types of potential natural zeolites from large to small pore, i.e., mordenite, clinoptilolite, and chabazite in several catalytic reactions are discussed with an explanation in the modifications of natural zeolites to improve physical and chemical properties of the catalysts. Natural zeolites utilization strategy for catalyst application is also proposed. In the future, the role of natural zeolites in catalysis field would be important particularly in abatement pollution through catalytic reactions, catalytic cracking of non-conventional oils, and biomass transformation to fuel and chemicals.

2.2 Introduction

Natural zeolites are aluminosilicates hydrated crystalline compounds with micropore structure filled by water and cations mostly alkaline (Na^+ , K^+) and alkaline earth (Ca^{2+}) metals which have a high ion exchange capacity, shape selectivity, and sorption properties. The more formal definition of natural zeolite was formulated by International Mineralogical Association as follows [23].

A zeolite mineral is a crystalline substance with a structure characterized by a framework of linked tetrahedra, each consisting of four O atoms surrounding a cation. This framework contains open cavities in the form of channels and cages. These are usually occupied by H₂O molecules and extra-framework cations that are commonly exchangeable. The channels are large enough to allow the passage of guest species. In the hydrated phases, dehydration occurs at temperatures mostly below about 400 °C and is largely reversible. The framework may be interrupted by (OH, F) groups; these occupy a tetrahedron apex that is not shared with adjacent tetrahedral.

The sedimentary tuffs of natural zeolites are found in large quantity throughout the world. The conventional open pit mining technique is used to mine natural zeolites which makes the exploitation cost low. Hence, natural zeolites are far cheaper than synthetic zeolites. Natural mordenite and clinoptilolite have shown its superiority as compared to synthetic zeolites in acid and heat resistance [24]. The latest report shows that 93 mineral species belong to 44 different framework types (plus 3 undefined) is found in nature categorized as zeolite according to the above definition [25].

Commercial application of natural zeolites is widely applied in water and wastewater treatment, soil amendment, aquaculture, cement, and gas purification [1, 4, 24, 26]. The utilization of natural zeolites for bulky gas separation is not effective; however, the gas purification to remove traces is more effective as reported elsewhere [24]. Natural zeolites are rarely as used for catalysis purposes as its synthetic counterpart because of the inconsistency of composition and the presence of competing phases [27]. Only natural erionite has been used as a catalyst in the selectoforming process developed by Mobil Oil Corporation to boost the octane number of gasoline [28].

In the following sections, characteristics of natural zeolites and utilization of natural zeolites in commercial sectors are briefly discussed including application in industrial catalytic reactions. Afterward, research activity on natural zeolites utilization in catalysis field is presented. Finally, strategies to improve and utilize natural zeolites for catalytic reaction purposes are proposed.

2.3 Natural Zeolites Overview

2.3.1 Properties of Natural Zeolites

Zeolite is built from the basic elements of silicon (Si) and aluminum (Al) which bond to four oxygen atoms forming a TO_4 tetrahedral structure called the primary building unit (PBU) (Figure 2.1). The letter T represents atom Si or Al. The PBU links with other PBUs to form secondary building units (SBU) (Figure 2.2). According to the International Zeolite Association (IZA), there are 23 SBU[29]. The SBU combines with other SBU to form a zeolite framework (Figure 2.3). The IZA has published 234 zeolite frameworks [30]. Clinoptilolite (HEU), mordenite (MOR), and chabazite (CHA) are found abundantly in nature [5]. Total world production of natural zeolites in 2008 was 2.8 million metric ton per year with more than 60% mined in China [31].

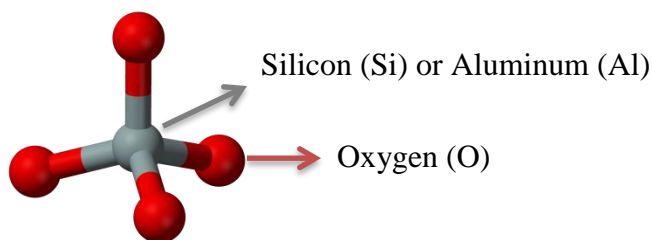


Figure 2.1: Primary building unit (TO_4).

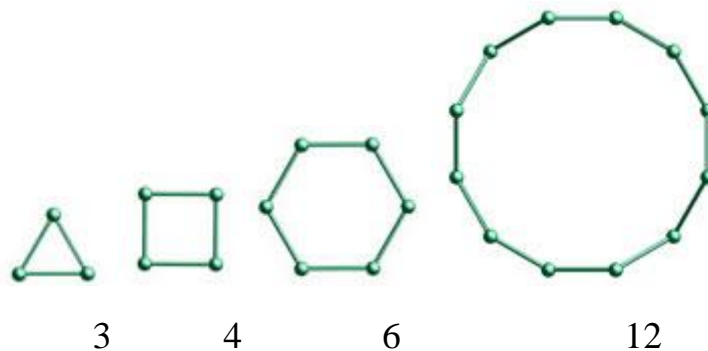


Figure 2.2: Secondary building unit.

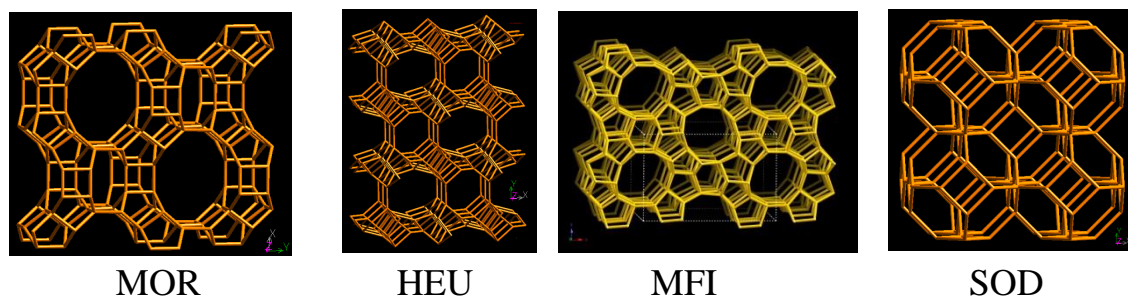


Figure 2.3: Examples of zeolite frameworks.

Illustration of the formation sodalite type zeolite framework (SOD) is presented in Figure 2.4 to give a clear picture of how the zeolite framework is formed.

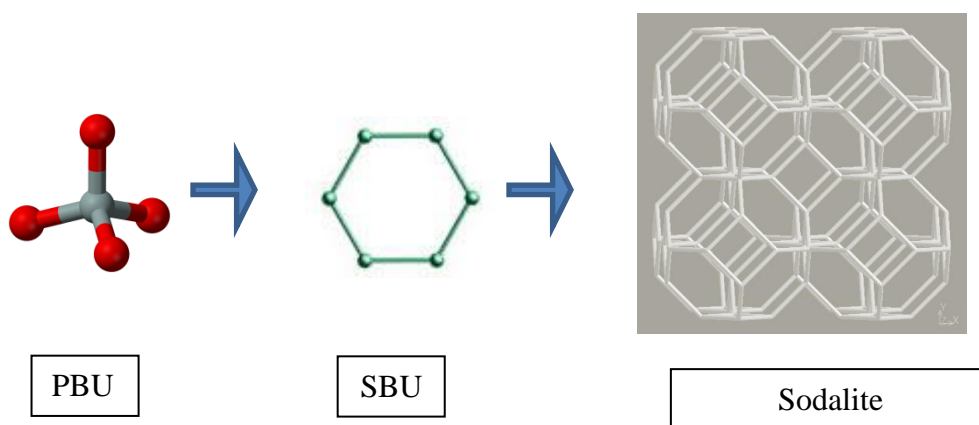


Figure 2.4. Illustration of sodalite framework as it builds from the basic units.

The important properties of natural zeolites are a high capacity of hydration and dehydration, large void space and low density after water evacuation, strong framework structure, high cation exchange properties, uniform pore sizes, adsorption properties, unique electrical properties, acid and basic properties [32]. Zeolites are able to selectively remove molecules when the size and shape of the molecule does not fit into the pores. This unique ability is called shape selectivity property. Therefore, zeolites are widely used in the molecular separation based on the different sizes and shapes of molecules. The selectivity of products in the catalytic reaction is also affected by the shape selectivity property of catalyst zeolites.

Cations are weakly attached in the extraframework of zeolite structure. Therefore, the cations can be exchanged relatively easy with a strong solution of another cation. The cation exchange capacities (CEC) of natural zeolites is high in aluminum-rich zeolites due to the more extraframework cations needed to balance the charge [33]. The CEC of natural zeolites is between 200 and 400 milliequivalent/100 g which is larger than bentonite clay and other inorganic cation exchangers [32, 33]. There are several factors governing the ion-exchange behavior of natural zeolite; i.e., framework type, charge density of the anionic framework, ion size and shape, ionic charge, and concentration of solution [34]. The capability of natural zeolites to exchange cations is important in water and wastewater treatment.

Surface acidity of zeolites, acid and basic sites, is closely related to the catalytic properties. The acid property is more important than basic property due to the wide application of the zeolite acid property in commercial catalytic reactions. There are two types of acid sites i.e., Brønsted acid sites (BAS) and Lewis acid sites (LAS). The acid sites are formed due

to extra negative charge when the Si^{4+} is replaced by Al^{3+} that has to be balanced by cations such as alkali metals, alkaline earth metals, and hydroxyl protons [35]. The hydroxyl proton leads to the Brønsted acid sites (Figure 2.5a). On the other hand, the alkali and alkaline earth lead to the weak LAS which also could be formed by dehydration process [36] (Figure 2.5b). The catalyst activity and selectivity are dictated mainly by the surface acidity and pore size of the zeolite.

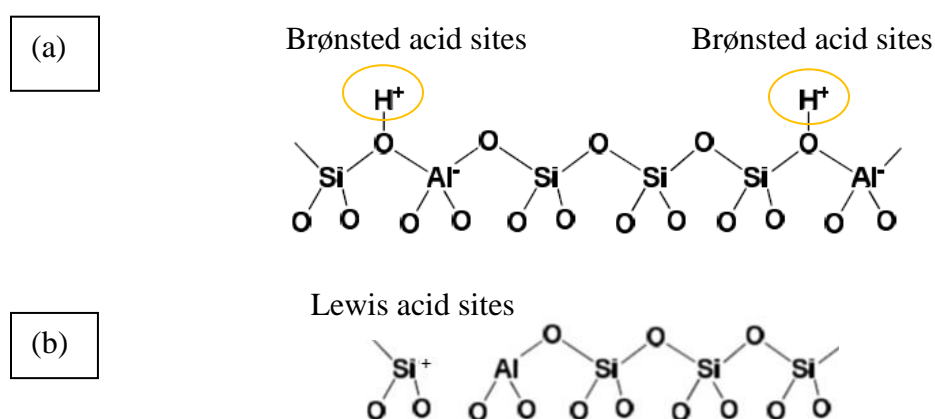


Figure 2.5 (a) Brønsted acid sites dan (b) Lewis acid sites in the zeolite structure.

2.3.2 Commercial Applications of Natural Zeolites

Natural zeolites are used in wide commercial application fields such as for domestic usage, agriculture, aquaculture, and industry. The price of natural zeolites is low 0.04 – 0.25 USD/kg for bulk applications and 1.5–3.5 USD/kg for industrial adsorbents applications as compared to synthetic zeolites (ZSM-5 or ferrierite zeolites) within the range of 10 – 20 USD/kg [2, 3]. Natural zeolites are used in domestic applications, for pet litter, odor removal, and drying agent. Farmers use natural zeolites in agriculture field for feed additive of poultry, odor (ammonia) and moisture control of livestock farm, and soil amendment. Asian fish farmers use natural zeolites in freshwater aquaculture for fish farming and fish

transportation to control ammonium in water. Natural zeolites are used in the industry for water and wastewater treatment, radioactive removal, pozzolana cement, and filler on paper.

The most successful commercial application of natural zeolites in the industry is for wastewater treatment in removing ammonium [4, 34, 37]. The ammonium source is mainly from municipal sewage (laundry, urine, and bathroom), fertilizer factory wastewater and agriculture runoff [34, 37]. The ion-exchange and molecular sieve properties play a vital role in the high selectivity of ammonium removal from wastewater effluent. Some of wastewater treatment plants are established using natural clinoptilolite to reduce the NH_4^+ content in California (27000 m³/d) (Figure 2.6) and Virginia, USA (245000 m³/d) [38, 39].



Figure 2.6: Application of natural clinoptilolite in wastewater treatment plant at Tahoe-Truckee USA [38].

Natural zeolites were utilized in the past as a building material. In the 12th century, there were some castles built from philipsite and chabazite, which are typical of natural zeolites abundant in Italy. Castel dell'Ovo is one example for such castles (Figure 2.7) [40]. Mayan Pyramid at Monte Alban, Mexico was also built of natural zeolites. People in the past used the natural zeolites for their buildings because the natural zeolites tuff are a lightweight stone and easy to carve [1]. In addition, the micropore channels adsorbed and desorbed water controls the microclimate of the building. In the present time, natural zeolites are still used in construction as can be seen in Tokaj, Hungary. The natural zeolites are also used as pozzolana cement which can save energy in cement processing up to 40% and reduce CO₂ emissions [27].



Figure 2.7: Castel dell'Ovo, Naples, Italy (Photograph by Richard Nevell distributed under the Creative Commons Attribution-Share Alike 2.0 Generic) [41].

Some review papers regarding the application of natural zeolites in agriculture have been published [40, 42, 43]. The Japanese farmers have been using natural zeolites in agriculture to regulate the moisture content, remove the odor of animal wastes, and neutralize the acidic volcanic soils [40]. Additions of amounts of clinoptilolite in poultry feed increases the weight and health of the poultry and reduce the odor feces. The utilization of zeolites for NH_4^+ removal in high salinity water was not effective since the competitions with other cations reduce the ammonium removal [26].

The application of natural zeolites in water purification, waste treatment, aquaculture, nuclear radioactive waste are based on ion exchange properties and molecular sieving. On the other hand, the application of natural zeolites in gas purification and separation is based on the shape selective properties. Natural chabazite from Bowie, Arizona is commercially used for removing chloric acid from hydrogen streams, water from chlorine gas streams, and carbon dioxide from flue gas emissions [33]. Oxygen can be separated from nitrogen in the air by using natural mordenite in pressure swing adsorption units. Bulky separation of gases is not effective over natural zeolites; however, the gas purification duty to remove traces is effective over natural zeolites such as N_2O removal from air [24].

There is no commercial application of natural zeolites for industrial catalyst except natural erionite in selectoforming process developed by Mobil Oil Corporation for removal of low octane normal alkanes by selective hydrocracking on erionite containing about one-tenth percent platinum [29]. The erionite has small pore channels (6-membered ring) with aperture window $3.6 \times 5.1 \text{ \AA}$. This excludes the branched paraffin and large molecule aromatics from the hydroconversion reaction [1, 44, 45]. Natural Ni-erionite configured with a noble metal in the series reactor has been utilized as a commercial catalyst to convert

the linear paraffins (C5 to C9) into C1 to C3 in the feed containing isoparaffins and aromatics. Mobil Oil corporation mined the natural erionite from 1965 to 1970 for catalysts used in oil refining and natural gas purification [46]. The selectoforming process which used erionite was replaced by the more sophisticated ZSM-5 catalyst by introducing a new process called M-Forming which is able to increase more octane number by producing branched paraffin [28]. The erionite is suspected as a carcinogenic substance where the erionite fibers can become stuck in various organs in the body increasing risks of mesothelioma cancer [47, 48]. Therefore, natural erionite has only little attraction in catalytic and other applications.

2.3.3 Why Is Application of Natural zeolites in Catalysis Limited?

Natural zeolites are frequently found in several zeolite phases and impurities such as unreacted volcanic glass, K-feldspar, montmorillonite, quartz, calcite, gypsum, cristobalite, and tridymite [33]. For example, natural zeolites from Klaten, Indonesia, consist of mordenite as major phase and clinoptilolite and quartz as the accessories phases [21]. Natural chabazite from Bowie, USA has phase impurities clinoptilolite and erionite [16]. The natural zeolites from Sivas-Yavu, Turkey consists of clinoptilolite (ca. 30%), mordenite (ca. 40%), quartz (ca. 10%), feldspar (ca. 10%) and clay (ca. 5%) [49]. The phase zeolite impurities reduces the catalyst activity and/or selectivity of desired products in the stringent catalytic reaction. The deficiency of purity such as the phase impurities, metals impurities, and inconsistency of composition are the main reasons why natural zeolites are rarely used as catalysts [1].

Cations impurities are varied in natural zeolites depending on the site location. Natural zeolites contain many cations in the micropore channels such as Na^+ , K^+ , Ca^{2+} , Mg^{2+} , Fe^{3+} ,

Mn^{2+} , etc. These cations are easily exchanged through the simple ion-exchange procedure. However, the problem arises if metals occur in oxide form which is difficult to remove. Metals impurities generally exist along with the natural zeolites. Metals impurities content will be disadvantageous for some catalytic reactions despite it possibly give benefits for other catalytic reactions. Iron impurities in natural chabazite are probably caused the metal complexation that benefit in enhancing the removal of vanadium and nickel in catalytic cracking of oilsands [16].

The composition of natural zeolites depends on the mining location [50, 51]. The natural zeolites composition may also vary even in the same deposit sediment location. The variation in composition is not acceptable in industry application particularly for a strict qualification such as catalysis and adsorptions. Hence, it is necessary to control the crystallinity and composition phase of natural zeolites to improve the physical and chemical properties.

2.4 How to Improve the Purity of Natural Zeolites?

Natural zeolites impurities can be effectively reduced through physical method i.e., gravitational-magnetic concentration and air blower separation. The purity can be increased by chemical methods i.e., hydrothermal interconversion and recrystallization. These methods can significantly improve the crystallinity and composition consistency of natural zeolites. However, it is still difficult to achieve 100% purity of natural zeolites with reasonable economic processing cost.

2.4.1 Physical Approach

Natural zeolites purity can be enhanced through physical methods such as crushing and grinding, gravity separation, magnetic concentration, and air blower classification [51-53]. The density of natural zeolites is different with the constituent impurities density. For instance, montmorillonite and quartz have a higher density as compared to the natural clinoptilolite. The difference in the density and hardness can be exploited to improve the purity of natural zeolite. Ibrahim and Inglethorpe [51] have successfully upgraded the low-rank natural zeolites from Aritayn Formation in Jordan (47% zeolites, 11% calcite, 42% pyroclasts) into high purity natural zeolites (89% zeolites) at 37% recovery through sequential comminution-gravity-magnetic beneficiation methods. They also studied the effect of pre-concentration method, autogenous and compression comminution on the beneficiation effectiveness. It was revealed that autogenous milling was effective to separate target zeolite minerals from the gangue impurities and improved the efficiency of successive magnetic concentration. On the other hand, compression comminution was not effective to release gangue constituents. Furthermore, the ground powder fed to magnetic separation was not effective as well. Similarly, Yusupov et al. [52] studied physical beneficiation method of natural zeolite from Shivyrtuisk deposit in Russia which is clinoptilolite dominant with impurities montmorillonite, quartz, feldspar, mica, and iron hydroxides (Figure 2.8). The separation process started by crushing, grinding, and sieving into two classes of powder size i.e., large class size (0.1-0.2 mm) and small class size (0.05 – 0.1 mm). The iron content was reduced by applying magnetic separation after gravity separation using table concentration. The natural clinoptilolite purity increased from 64% to 82% with yield 78% when classified from the large size of powder natural zeolite. The

small class size which apparently contains more impurities improved its purity from 44% to 88% at yield 50%. Combination of common technique of mineral processing, gravitational and magnetic separation decreased impurities significantly.

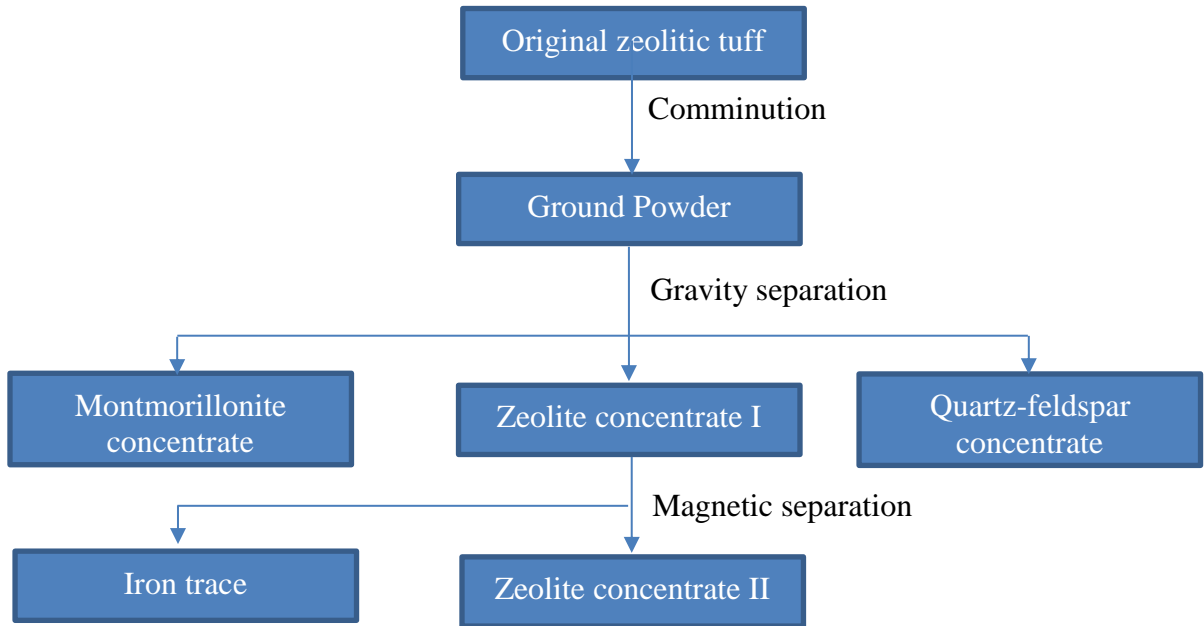


Figure 2.8: Gravity-magnetic separation to improve natural zeolite purity. Adapted from ref. [52].

An air blower classification method for natural zeolite purification was studied by Watanabe et al. [53]. The natural zeolites mined in Pohang, Korea consist of clinoptilolite and mordenite with feldspar and illite as accessories. The air classification was effective to decrease the impurities particularly feldspar due to the difference in density and hardness between zeolites and feldspar. However, the amounts of metals impurities were not affected by air classification technique. Air classification should be combined with the magnetic separation to remove iron impurity. The investigation results show that high purity natural zeolite can be effectively produced from low-grade natural zeolites by using

a simple physical approach which is widely applied in mineral processing technology, i.e. comminution, gravity, and magnetic separation.

2.4.2 Chemical Approach

It is well-known that a zeolite phase can be transformed into other zeolite phases by alkaline hydrothermal treatment [7, 54-58]. Interconversion of natural zeolites, consists of several zeolite phases transform into one pure zeolite phase, will lead to a better zeolite catalyst performance. Early attempts on interconversion of natural zeolites into other zeolite phases was reported by Robson and Rouge [59]. Their work showed that the natural clinoptilolite can be converted into zeolite-Y by alkaline hydrothermal treatment.

The effect of alkaline type on the hydrothermal interconversion of natural clinoptilolite to other zeolite frameworks was reported by de las Pozas et al. [60]. The natural clinoptilolite (85%) was obtained from Castillas, Cuba with impurities (15%) i.e., calcite, montmorillonite, quartz, and volcanic glass. The materials were initially ion exchanged five times with 3 M solution of NaCl or KCl at 100 °C. Subsequently, the ion-exchanged clinoptilolite samples were subjected to 7.5 M NaOH and 0.6 M NaCl solution with liquid to solid ratio 1 at 100 °C. It was proposed that the type of alkaline cation present in the sample strongly affected the hydrothermal interconversion of the natural clinoptilolite. The Na-clinoptilolite dissolves in alkaline solution into amorphous gel and recrystallized into metastable zeolite Y at 16 h and P-zeolite after 80 h. In contrast, K-clinoptilolite dissolution rate was slower in an alkaline solution which led to interconversion of K-clinoptilolite directly into zeolite P crystallizes from the gel after 65 h. It is important to note that the impurities still existed in the transformed zeolites.

Kang et al. [7] studied interconversion of natural clinoptilolite and mordenite into zeolite Na-P by hydrothermal in high alkaline solution; however, the impurities quartz and feldspar hardly transformed. The cation exchange capacity of the converted sample was 418 meq/100 g, which was higher than the parent with only 175 meq/100 g. The authors continued their work for transforming the impurities quartz and feldspar by sequential NaOH fusion and hydrothermal method [8]. The fusion with NaOH powder at 550 °C for 2 h prior to the hydrothermal reaction was effective to convert clinoptilolite and impurities (quartz and feldspar) to high cation exchange capacity zeolites such as zeolite Na-P, zeolite Na-X, and hydroxysodalite. Correspondingly, Wang and Lin [9] reported the interconversion of low-grade natural clinoptilolite into the high purity of zeolite Na-Y and Na-P which increased the cation exchange capacity of the natural zeolites by alkali fusion and hydrothermal method. Watanabe et al. [10] suggested that the transformation of the natural zeolites to phillipsite, hydroxyl-sodalite and analcime depended on the hydrothermal temperature and NaOH concentration.

Transformation of natural clinoptilolite into ZSM-5 was reported by Kartal and Onal [56] for alkylation of benzene with ethylene reaction. Prior to the hydrothermal treatment, the natural clinoptilolite was dealuminated by HCl to increase the silicon to aluminum ratio. Dealuminated clinoptilolite was hydrothermally treated in NaOH solution and tetrapropylammonium bromide (TPABr) at 180 °C for 110 h to obtain a high purity of ZSM-5. The TPABr is used as structure directing agent. However, the use organic structure directing agent TPABr is undesirable due to the high price and non-environmentally friendly chemical.

Selective transformation of impurities zeolite phase through hydrothermal chemical method is an effective method to improve the purity of natural zeolite. The impurities, erionite (3-5%) and clinoptilolite (5-10%), have been selectively transformed into chabazite-like phases by dissolving and recrystallizing the natural chabazite dominant phase in alkaline-alumina rich solution [16-18]. It was proposed that the mineral chabazite and other crystalline accessories dissolve into the highly alkaline, aluminum-rich solution and the Al-chabazite crystals growth from solution using the remaining chabazite crystals as a seeding template.

Recently, we published reports on recrystallization of amorphous phase formed in the milling process to fabricate nanoparticles mordenite into high crystalline mordenite phase by hydrothermal method using alkaline silicate solution in relatively a short time, i.e. 2 to 8 h [61, 62]. Hydrothermal treatment time, the ratio of the milled sample weight to the solution, silica and OH^- concentrations significantly affected the crystallinity of the recrystallized mordenite samples. It was suggested that the nano-mordenite acted as a seed to recover the crystallinity of milled amorphous phase. This method can possibly be applied for recrystallization of impurities amorphous silica phase of natural zeolites into high crystalline zeolite phase.

2.5 Potential Application of Natural Zeolites in Catalysis

Erionite is the only natural zeolite having applications in fuel processing as discussed in Section 2.3.2. Investigation of natural zeolites in catalytic applications is active especially for natural mordenite, clinoptilolite, chabazite, and erionite which are not only available in large deposits but also show promising results as a catalyst [49, 63, 64]. Large pore to small

pore natural zeolite i.e. mordenite (12-MR), clinoptilolite (10-MR), chabazite (8-MR) are discussed in the following sections.

2.5.1 Natural Mordenite

One of important commercial catalyst that occurs in nature is mordenite. The name of mordenite was coined by How (1864) after the place of mordenite was found at Morden, King's County, Nova Scotia, Canada. Mordenite has a 12-membered ring ($6.7 \times 7.0 \text{ \AA}$) and an 8-membered ring ($3.4 \times 4.8 \text{ \AA}$) [65]. The pore size allows some molecules to diffuse and discard the other molecules which is important in product selectivity of catalytic reactions. Synthetic mordenite has been applied as catalysts for hydroisomerization and alkylation in industrial scale [2]. Natural mordenite has potency for nitric oxide abatement, hydrocarbon conversion, and biomass transformation as can be seen in Table 2.1.

Table 2.1: Research on the application of natural mordenite for catalytic reactions.

Type of zeolite	Origin	Catalytic application	Modification	Ref.
Mordenite & clinoptilolite	Sivas-Yavu, Turkey	Selective catalytic reduction of nitric oxide with ammonia	Drying → Ion-exchange with NH_4NO_3 → Drying → solid state ion-exchange with Fe-salts	[49]
Mordenite	Palmarito, Cuba	Selective catalytic reduction of nitric oxide by ammonia	CuCl_2 ion-exchange.	[66, 67]

Mordenite	Izukulite, Japan	Selective catalytic reduction of nitric oxide by ammonia	H-MOR exchanged with vanadium ions and mixed with catalyst TiO ₂	[68]
Mordenite	Klaten, Indonesia	Dimethyl Ether to Olefins	Milling, Acid treatment, recrystallization, Ion-exchange with NH ₄ NO ₃ , and Calcination	[62, 69]
Mordenite	Klaten, Indonesia	Cracking of n- hexane	Acid treatment, Ion-exchange with NH ₄ NO ₃ , and Calcination	[21]
Mordenite- Clinoptilolite	Ukraine	Hydroisomerization of n-hexane	Acid treatment→ Ion-exchange with NH ₄ ⁺ → Calcination→ Pd impregnation	[70, 71]
Mordenite	Bayah, Indonesia	Cracking of n- hexane	Acid treatment, Ion-exchange with NH ₄ NO ₃ , and Calcination	[72]
Mordenite	Tokaj, Hungary	Xylene isomerization	Acid treatment, Ion-exchange with NH ₄ Cl followed by Silver ion- exchange	[73]
Mordenite	Pacitan, Indonesia	Palm oil transesterification to biodiesel	KOH Impregnation	[74]

Mordenite	Bayah, Indonesia	Wasted cooking oil transesterification to biodiesel	Desilication	[75]
Mordenite & Clinoptilolite	Bayah, Indonesia	Glycerol conversion to glycerol carbonate	Dealumination	[76]

The natural mordenite is not only has a low-price but also an excellent performance in the nitric oxide abatement. Ates et al. [49] studied that the iron impurities in the natural zeolites give advantageous than synthetic zeolite as iron is active in the nitric oxide degradation; however, more Fe loading was needed to perform higher conversions. Cu(II)-exchanged natural mordenite from Cuba is an efficient catalyst for the selective catalytic reduction (SCR) of nitric oxide (NO) by ammonia in an excess of oxygen exhibited 95% conversion at very low temperatures (177–327 °C), and do not create N₂O. Furthermore, natural mordenite is water tolerant and retains high NO conversion despite the attendance of 100 ppm of SO₂ [66]. Mashami et al. studied the performance of NO conversion over commercial V₂O₅/TiO₂ catalyst mixture and V-natural mordenite and catalyst TiO₂ [68]. The results showed that the V-natural MOR/TiO₂ showed better performance with 91% NO conversion than the commercial V₂O₅/TiO₂ with 52% conversion at temperature 300 °C.

Moderate acid dealumination (3 M HNO₃) for 6 h on the natural mordenite lead to higher dimethyl ether conversion 17% as compared to the parent 12% [69]. The dealuminated MOR was also showed a positive result in the hexane cracking [21]. The dealumination opens the access into the strong Bronsted acid sites in the natural mordenite. Kurniawan et al. [62] studied the nanoparticles derived from natural mordenite by ball milling-

recrystallization method. The DME conversion was improved over the nanoparticles milled MOR (54%) and nanoparticle recrystallized MOR (99%). Patrylax et al. investigated n-hexane hydroisomerization over modified natural mordenite-clinoptilolite after impregnated with palladium [70, 71]. Pd-natural mordenite performance was not inferior with n-hexane conversion 74% as compared to the synthetic mordenite n-hexane conversion 79% [70, 71]. The clinoptilolite phase as impurities was not affected the natural mordenite performance [71]. The number and type of acid site were important properties in the isomerization. The experiment showed that the natural mordenite impregnated with palladium could be used as the catalyst in hydroisomerization of linear alkane.

Biodiesel synthesis over modified natural mordenite was studied from palm oil by impregnation KOH on the mordenite [74]. The biodiesel yield was very high (95%) over the K₂O-MOR. In contrast, the desilicated mordenite without impregnation any metal base showed a poor catalyst activity as reported elsewhere [75]. Glycerol as a byproduct of biodiesel was studied to convert to glycerol carbonate over dealuminated zeolites [76]. Several parameters were investigated such as diameter catalyst, a catalyst to glycerol ratio sodium bicarbonate to glycerol ratio, and water to glycerol ratio. The optimum condition for the glycerol reaction with sodium bicarbonate was achieved at low glycerol/sodium bicarbonate ratio using less water as a solvent, small diameter particle size (0.46 mm) and temperature 100 °C.

2.5.2 Natural Clinoptilolite

Clinoptilolite is the most abundant natural zeolite in the world. The pore channels parallel to the c-axis are 10-membered ring (3.0 x 7.56 Å) and 8-membered ring (3.3 x 4.6 Å) which is bridged by 8-membered ring (2.6 x 4.7 Å) [29]. Despite a wide application in wastewater

treatment plant, natural clinoptilolite has no commercial application in catalysis field. However, there are some promising results reported on the utilization of clinoptilolite as a catalyst as listed in Table 2.2.

Table 2.2: Research on the application of natural clinoptilolite for catalytic reactions.

Type of zeolite	Origin	Catalytic applications	Modification	Ref.
Clinoptilolite	Youngil, Korea	Depolymerization of polyethylene	NH ₄ Cl ion-exchange → Calcination	[77]
Clinoptilolite & Heulandite	Žalec, Slovenia	Depolymerization of polyethylene	Acid treatment → NH ₄ NO ₃ ion-exchange → aluminum grafting	[78]
Clinoptilolite	Youngil, Korea	Degradation of polystyrene	NH ₄ Cl ion-exchange → Calcination	[79]
Natural zeolites	Harrat Ash-Shamah, Saudi Arabia	Degradation of polystyrene	No treatment	[80]
Clinoptilolite	Youngil, Korea	n-butene isomerization	Acid treatment → NH ₄ Cl ion-exchange → Calcination	[81, 82]
Clinoptilolite	Youngil, Korea	n-butene isomerization	Cobalt-cation-exchanged natural clinoptilolite zeolite (Co-HNZ)	[83]

Clinoptilolite	Thrace, Greece	Dehydrogenation of propane	NH ₄ Cl ion- exchange → calcination	[84]
Clinoptilolite	Western Anatolia, Turkey	Alkylation of benzene with ethylene reaction	Interconversion into ZSM-5	[56]
Clinoptilolite	Nevada, US	Alkylations and Knoevenagel condensation	Tandem dealumination- desilication	[3]
Natural Zeolite	Indonesia, Australia	Catalytic oxidation of phenolic	Co(NO ₃) ₂ ion- exchange → calcination	[85]
Clinoptilolite	Munro, Argentina	Pyrolysis of peanut shells	Calcination → NH ₄ Cl ion- exchange→ calcination	[63]
Clinoptilolite	Vranjska banja, Serbia	Pyrolysis of hardwood lignin.	NaCl ion- exchange→ MCl ₂ ion exchange (M= Ni, Cu, Zn) → Calcination	[86]
Clinoptilolite	Balikesir- Bigadic, Turkey	Pyrolysis of olive residue	Calcination	[87]
Natural Zeolite	Korea	Two-stage catalytic pyrolysis of lignin	In series use with H-ZSM5	[88]
Clinoptilolite	Kucin, Slovakia	α-pinene isomerization	Acid dealumination→ drying	[89]
Clinoptilolite	Balikesir, Turkey	α-pinene isomerization	Drying → Acid dealumination→ drying	[90]

Clinoptilolite	Balikesir, Turkey	α -pinene isomerization	Impregnated with HPW	[91]
----------------	----------------------	-----------------------------------	-------------------------	------

Application of natural clinoptilolite in the catalytic reaction can be classified into four groups, i.e., plastics depolymerization, hydrocarbon conversion, biomass pyrolysis, and organic reactions. Park et.al, studied depolymerization of polyethylene over H-natural clinoptilolite, H-ZSM-5, H-Y, and amorphous silica-alumina [77]. The natural clinoptilolite showed the highest liquid yield (65.1%) with research octane number (RON) 90.7%. Polyethylene was depolymerized over modified natural clinoptilolite with the main product liquid oil in the range of diesel fuel with less coke suitable for fuel additive in internal combustion [78]. In contrast, catalytic depolymerization over calcined natural mordenite and commercial H-USY showed product yield only slightly higher than thermal operation due to the fast deactivation rate [92]. Clinoptilolite from Youngil, Korea exhibited a good performance for polystyrene degradation with 99% selectivity to aromatic [93]. The authors also compared the natural clinoptilolite with the synthetic clinoptilolite which showed a comparable result. Rehan et al. [80] studied natural zeolites of Harrat Ash-Shamah, Saudi Arabia and commercial zeolite SDUSY for polystyrene degradation. The authors found that the natural zeolites produced fewer gases (12.8%) and higher liquid oil (54%) than synthetic zeolite (gas 22.6%; liquid oil 50%).

Hydrocarbon conversion over natural clinoptilolite was reported for n-butene isomerization, dehydrogenation of propane, and alkylation of benzene. The clinoptilolite from Metaxades was active for propane dehydrogenation. Propylene yield over Metaxades natural clinoptilolite comparable to the steamed Cr-modified ZSM-5 zeolite and significantly higher compared to the other natural clinoptilolite from Pentalofos and to the

steamed H-ZSM-5 zeolite [84]. High purity natural clinoptilolite (>97%) was treated by sequential acid-base treatment which created hierarchical pore system with large mesopore volume [3]. The hierarchical clinoptilolite and ZSM-5 were tested for toluene alkylation with benzyl alcohol which showed higher selectivity and yield to (methyl) benzyl benzene as compared to ZSM-5.

Biomass pyrolysis over natural clinoptilolite has reported in open literature exhibited promising results [63, 86-88]. Recently, Messina et al. [63] studied pyrolysis of peanut shells over alkaline clinoptilolite and H-protonated clinoptilolite. The H-form of clinoptilolite produced less water and more deoxygenated bio-oil than the alkaline form clinoptilolite. Less oxygen content in bio-oil improved its miscibility and stability with the conventional fuels. Putun et al. [87] reported that pyrolysis of olive residue over high purity clinoptilolite (95%) exhibited high yield of bio-oil as compared to the ZSM-5. Pyrolysis of lignin was studied by Lee et al. [88] using natural zeolites in the pyrolysis reactor and fed into the bed of H-ZSM-5 in the other reactor. The sequential reactors system decreased the coke deposition in the expensive HZSM-5 and improved the product oil quality due to increasing number of alkylphenols and pyrocatechols with a decrease in the amounts of guaiacols, eugenols, and heavy lignin pyrolyzates.

Isomerization of α -pinene over clinoptilolite was reported by many researchers [89-91]. Turpentine from a tree (*Pinus merkusii*) has a major content of α -pinene compounds. The catalysts used in the turpentine processing are phosphoric acid which is a homogeneous catalyst. The α -pinene isomers and its oxide are essential in the chemicals industry because they produce high-value products such as camphene, limonene, campholenic aldehyde (CPA) widely used in flavorings and perfumes in cleaning products, cosmetics, perfumes,

food additives, and pharmacy. As a heterogeneous catalyst, the separation of clinoptilolite from reactants and products would be easier than a homogeneous catalyst.

2.5.3 Natural Chabazite

Natural chabazite is a small pore zeolite with 8-membered ring and aperture window $3.8 \times 3.8 \text{ \AA}$ [29]. Over the last 10 years, natural chabazite from Bowie, USA has been investigated intensively for oilsands upgrading through catalytic reaction[16]. Current commercial method for extracting bitumen of oilsands is using a large amount of hot water, which produces high volume waste despite some is recycled. The hot water extraction method produces bitumen with highly viscous and has to further processing by mixing with expensive solvents or thermochemically upgraded in large capital-intensive facilities [94]. Reports in the potential of natural chabazite as catalysts for oilsands upgrading are presented in Table 2.3.

Table 2.3: Research on the application of natural chabazite for catalytic reactions.

Type of zeolite	Origin	Catalytic application	Modification	Ref.
Chabazite	Bowie, USA	Oilsands bitumen cracking	Digestion in alkaline silicate mixture → Partially ammonium exchange→ calcination	[16]
Chabazite Clinoptilolite	Bowie, USA Saint Clouds, USA	Oilsands bitumen cracking	Partially ammonium exchange→ calcination	[94]
Chabazite	Bowie, USA	Oilsands bitumen cracking	ammonium exchange→ calcination	[64]

Chabazite	Bowie, USA	Oilsands bitumen cracking	ammonium exchange→ calcination	[95]
Chabazite	Bowie, USA	Nitrogen removal from oil sand	Raw form (Ca-CHA) H-form	[96]
Chabazite	Bowie, USA	Ni and V removal from oil sand	Raw form (Ca-CHA) H-form CHA	[97]

Kuznicki et al. [16] pioneered research on the application of natural chabazite for oilsands cracking. The authors use high purity of natural chabazite which obtained by converting the phase impurities, clinoptilolite and erionite, into chabazite. The treated samples showed an excellent performance in catalytic cracking of oilsands as its reduce the oil products viscosity and decrease sulfur, nitrogen, nickel, and vanadium far higher as compared to the commercial zeolite-Y.

The products of cracked oilsands can be extracted by light alkane such as pentane and hexane which is selective in extracting more distillate oil and gas oil while retaining the residuum in the exhausted sand [94]. Junaid et al. [64] also suggested that higher acid strength and site density, combined with a platy shape morphology and a high fraction of mesopore and macropore surface area lead to the higher cracking ability of natural chabazite as compared to the more expensive zeolite-Y. Furthermore, less amount of water (3%) mixed with low dosing natural chabazite 1-5% of the oilsands showed an excellent residue conversion through catalytic cracking and high liquid yields at low severity conditions which showed the economic and environmentally process as compared to current bitumen extraction process [95].

Recent studies showed that chabazite not only catalyzes the cracking of bitumen oilsands but also remove nitrogen and heavy metals from bitumen effectively [96, 97]. The capability of natural chabazite to remove nitrogen from oilsands could also potentially applied to other petroleum feed such as heavy oil before the catalytic cracking to reduce catalyst poisoning, pretreatment for hydrotreating to reduce hydrogen consumption, and additive for cracking or hydrotreating catalyst [96]. The natural chabazite removed 67.5% of vanadium from oilsands through strong adsorbents for vanadium-containing complex aromatic structures [95, 97].

2.6 Strategy to Design Catalysts from Natural Zeolites

The most important aspect of a catalyst is the unique superior capability of a catalyst in performing one process among other catalysts which could possibly achieve by some modifications of certain materials. Natural zeolites usually contain some impurities even in high content zeolitic tuff, therefore application in non-selective reactions for environmental protection could give advantages of natural zeolites [98]. Modification of natural zeolites is important to improve catalysts performance. The following sections discuss various modifications and the effect on the physical and chemical properties of catalysts derived from natural zeolites such as particle size reduction, basic treatment, acid treatment, ion exchange and calcination. After modification, catalysts natural zeolites might be best to use in raw feed materials contain impurities such as combustion stream, oilsands, heavy oil, and biomass in pyrolysis reaction considering the metals impurities still occurred in the modified natural zeolites and the type of reaction does not need a strict catalyst requirement.

High phase purity is important for application zeolites in catalyst and adsorption. The Bowie natural chabazite is the best example of high-quality natural zeolites comparable with its synthetic counterparts. The natural chabazite from Bowie, USA is found in high purity phase, high surface area ($437 \text{ m}^2/\text{g}$), and large mesopore and macropore volume (0.146 mL/g) [64]. The high-quality natural zeolites might be applied as a catalyst with minimum treatment such as reducing particle size, ion-exchange, and calcination to activate the catalyst. However, the low to moderate phase purity of natural zeolites should be processed to improve the purity by methods discussed in Section 2.4.

Source type of feed reaction is an important consideration to employ the natural zeolites as a catalyst. For instance, flue gas of combustion products which may contain various impurity gases and water could be best use natural zeolites as catalysts for nitric oxide abatement as it has a comparable performance with the synthetic zeolites. The low-cost natural zeolites performed well for catalytic cracking of heavy oils and bitumen oilsands which contain impurities such as sulfur, nitrogen, vanadium, nickel [94, 96, 97, 99]. Natural zeolites frequently contain some metals impurities such as Fe, which possibly inhibited some reactions although it may become additive for other reactions such as removal of metals impurities in catalytic cracking of oilsands [16]. They can also act as a guard catalyst in the pretreatment section prior to the expensive commercial catalysts. The strategy to use low-cost natural zeolites as a guard catalyst can be applied in pyrolysis of biomass prior to treating the pyrolysis product in a separate reactor with the more expensive commercial catalyst [88].

Post-modification techniques can also be applied to the natural zeolites to improve the catalytic performance (Figure 2.9). Large mesopores volume is important for some

reactions which involve bulky molecules. The short diffusion path-length to achieve the acid sites within the micropore channels is offered by large mesopore size (2-50 nm). Mesopores channels introduced by desilication with sodium hydroxide was reported for aluminum-rich synthetic mordenite ($\text{Si}/\text{Al}=5.7 - 10$) [100]. The hierarchical class of mordenite showed a better catalytic performance of benzene alkylation with propene to produce cumene (isopropylbenzene) (6 times more active than its parent). The mesopore formation allowed the large molecules such as benzene and isopropylbenzene to diffuse more quickly into the acid sites due to its short diffusion path length.

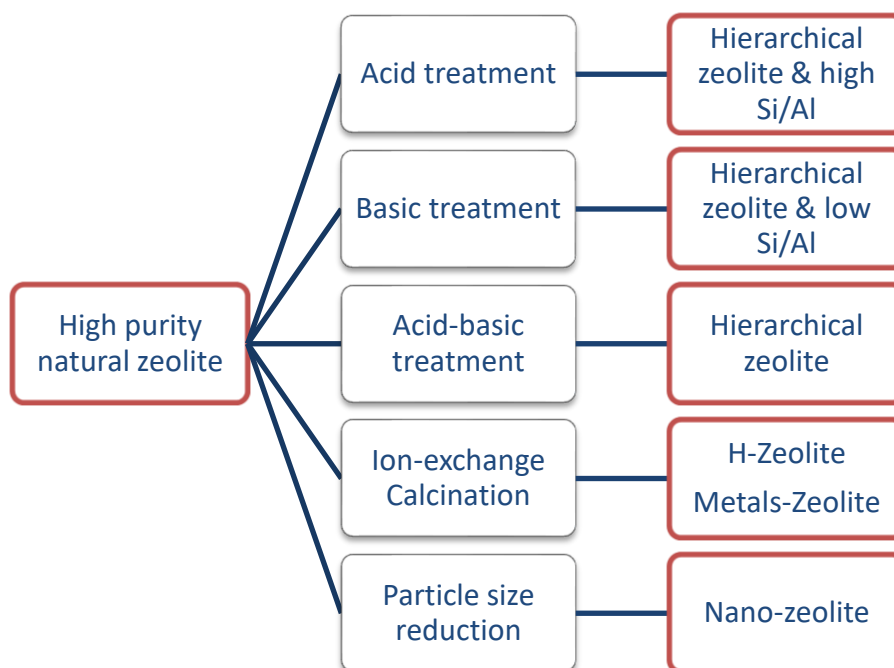


Figure 2.9: Modification of natural zeolites for catalyst application.

The Bronsted acid sites are generated by ion-exchange natural zeolites with ammonium nitrate followed by calcination to form protonated zeolites. Cracking of oilsands and heavy oil, and biomass pyrolysis depend on the hydrogen transfer supplied by the Bronsted acid

sites. Ion-exchange natural mordenite with copper improved the performance catalyst in selective catalytic reduction NO_x with NH₃ [66, 67].

Crystal sizes of zeolites play an important role in catalytic reactions. The smaller crystal size shorten diffusion of reactants and products. One could obtain a small crystal size of natural zeolite through top-down approach such as by ball milling method. High energy ball milling increased the activity of zeolites small pore (NaA, CaA) due to enhancement of the external surface area and opening the access to active sites [101]. Ball milling of K-Na-X zeolites improves the selectivity for base catalyzed reactions due to the decrease in the density of the strong Bronsted acid sites [102]. A systematic investigation was successfully conducted to study the effect of ball milling on physicochemical properties of various zeolites (synthetic mordenite, zeolite 13X, and zeolite 4A) [103]. It was suggested that ball milling affects in destruction of crystallinity of zeolite by breaking the external bond of Si-O-Si and Si-O-Al in their framework. Akcay et al. [12] investigated the effect of wet ball milling on the crystallinity of zeolite. The authors concluded that the wet ball milling led to less destruction of crystallinity as compared to the dry ball milling. Charkhi et al. [11] combined dry and wet milling in order to obtain nanoparticles of natural clinoptilolite.

2.7 Concluding Remarks

Natural zeolites have important application in water purification and waste treatment, agriculture, building materials, and gas purification. However, there was only one commercial application of natural zeolite in catalytic reactions which was natural erionite in the selectoforming process. The impurities, inconsistency composition of natural

zeolites and a limited number of industrial favorable frameworks are among the main factors of the rare application of natural zeolites as catalysts.

The purity of natural zeolites can be improved through either physical or chemical techniques. Common physical beneficiation methods in mineral processing are potentially applied to increase natural zeolites purity with a reasonable cost. Hydrothermal selective recrystallization method using alkaline-aluminum rich solution or alkaline-silicate solution showed a promising method to improve the phase purity of low-rank natural zeolites.

Natural mordenite, clinoptilolite, and chabazite are potentially developed as commercial industrial catalysts due to its unique catalytic properties and abundant deposit. Large pore natural mordenite has been proven effective for the isomerization linear alkane and selective catalytic reduction NO_x with NH_3 . Natural clinoptilolite exhibited promising results in catalytic pyrolysis of biomass into bio-oil. Natural chabazite was an active catalyst for catalytic cracking bitumen of oilsands and heavy oil, and removal metals impurities in the non-conventional oil.

Hierarchical natural zeolites could be formed as a superior class of natural zeolites as it shortens the diffusion path length for molecules to achieve the active sites. Nanoparticles of natural zeolite are also an important class which can improve the performance of catalysts by providing a large external surface area. Generally, the low-cost and huge supply of natural zeolites have advantages over expensive synthetic zeolites when dealing with raw materials with impurities which will be poisoned or quickly deactivated. Natural zeolites purification and post-modification could improve the quality of natural zeolites and might be comparable with synthetic zeolites in certain reactions. Therefore, further

investigations on improving the purity, interconversion zeolite, testing in new catalytic reactions are required to reveal more potency of the natural zeolites in catalysis field.

CHAPTER 3

HIGH-QUALITY MORDENITE DERIVED FROM LOW- GRADE NATURAL ZEOLITES THROUGH HYDROTHERMAL RECRYSTALLIZATION

3.1 Summary

The as-received natural zeolites showed a mordenite (MOR) dominant phase with impurity phases and low total surface area (ca. 133 m²/g) as indicated by the X-ray diffraction study and nitrogen physisorption analysis, respectively. High-quality mordenite, i.e., high crystallinity, large surface area (ca. 327 m²/g) was obtained through hydrothermal recrystallization of the low-grade natural mordenite followed by acid ion-exchange. The time of hydrothermal recrystallization affected the physical and chemical properties of the recrystallized natural mordenite. The morphology of the new mordenite crystals was examined by field emission scanning electron microscopy which was mainly observed as a needle shape. The n-butane isomerization in a fixed bed reactor was selected as a model reaction to evaluate the samples catalytic properties. The n-butane conversion boosted from 3.5 % in the parent natural MOR (H-P-H) to 25 % in the recrystallized natural MOR (H-R26-H). The yield of isobutane over the recrystallized natural MOR was 8 % which was far higher than the parent natural MOR with only 1 %. The recrystallized natural MOR also exhibited a comparable isobutane yield with the synthetic mordenite (ca. 7%).

3.2 Introduction

Zeolite literally means boiling stone. The term zeolite was coined by Cronstedt who found a stone that produced steam under blowing of hot air in 1756. The framework of the zeolite

was believed as stilbite for 250 years, despite there was no strong evidence. In 2007, Colella and Gualtieri reported that Cronsted's natural zeolite was composed of stellerite as the major phase and stilbite as the impurity phase [104]. Up to date, 44 natural zeolites framework have been identified as reported elsewhere [25]. There are a few of natural zeolites framework in the world that have been exploited such as clinoptilolite, mordenite, phillipsite, chabazite, and erionite as it is easily found in huge sedimentation deposits around the world. The most successful application of the natural zeolites is in wastewater treatment which exploits its ion-exchange properties [4, 5].

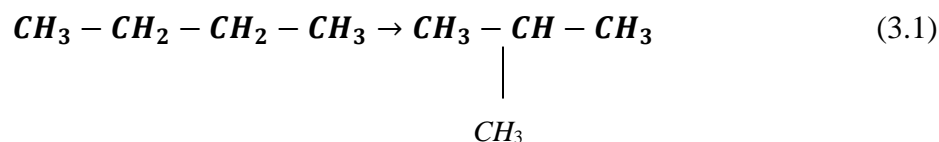
One of interesting natural zeolite framework is mordenite due to its unique pores architecture and the wide commercial application of its synthetic counterpart in catalysis field. The main large pore of mordenite is a 12-membered ring (MR) (0.67 x 0.70 nm) pore parallel with smaller pore an 8-MR (0.26 x 0.57 nm). Those channels are connected by an 8-MR (0.34 x 0.48 nm) which are also called the side pocket. Mordenite is also well-known for its strong acid sites among other zeolites. The strong acid sites primarily occur on the 8-MR side pocket [105]. However, the small pore 8-MRs are practically too small to be accessed for most molecules. Dealumination with moderate acid on the synthetic mordenite was reported effective to open the access to the strong Brønsted acid sites on the 8-MR side pocket and improve the performance of the catalyst in the n-hexane isomerization [106].

Natural zeolites normally exist in a mixture of several crystalline and amorphous phases [107]. The mordenite in nature occurred along with amorphous phase, quartz and other zeolite phases, i.e., clinoptilolite, heulandite [62, 74, 108]. Hydrothermal recrystallization technique applied to the amorphous milled crystals zeolite was investigated effectively to

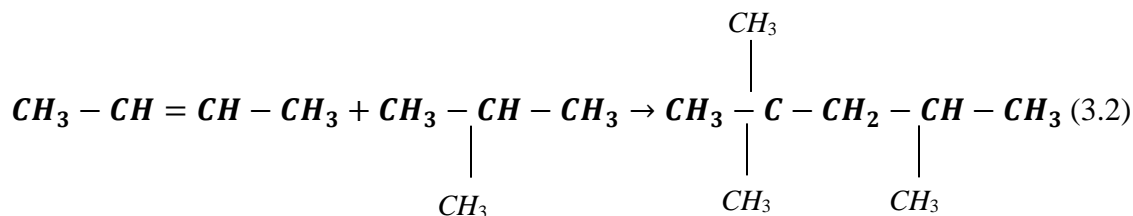
recover the zeolites crystalline phase [61, 109]. The natural mordenite needs to modify to meet the quality of synthetic mordenite which is well-recognized for commercial catalysts application such as alkylation, cracking, and isomerization. However, the literature regarding the improvement of natural zeolites through hydrothermal recrystallization technique is rarely reported.

Isomerization of n-butane has been attracting many researchers in the past decade in order to investigate the potential candidate catalysts to replace the non-environmentally friendly catalyst Pt/Cl-Al₂O₃. Recently, the price of n-butane has been decreasing because of increasing n-butane production from the fast growth exploitation of natural gas in shale and tight rock formation and low demand of n-butane in the market. Hence, an alternative chemical process is urged to convert low-price n-butane into more valuable chemical [110]. Alkylate or isooctane (2,2,4 trimethylpentane) is one of the more expensive chemicals which derived from n-butane. Alkylate is an important component to boost octane number which inhibits autoignition of gasoline in the engine. The process is started with n-butane isomerization to produce isobutane by using acid catalyst, i.e., Pt/Cl-Al₂O₃ and Pt/H-Zeolite (Equation 3.1). Then, the isobutane is reacted with 2-butene become alkylate by using sulfuric acid or hydrochloric acid as a catalyst (Equation 3.2).

Isomerization reaction:



Alkylation reaction:



The rise in environmental awareness is a signal to notify the heterogeneous eco-friendly catalyst such as natural mordenite for n-butane isomerization.

We investigated the hydrothermal recrystallization of low-rank natural zeolites to obtain cost-effective mordenite. In addition, the ion exchange procedure with different chemicals solution i.e. ammonium nitrate and hydrochloric acid were also examined. The catalyst samples were tested in a fixed bed reactor for n-butane isomerization.

3.3 Experimental

3.3.1 Materials

Natural zeolites tuff was obtained from Klaten, Central Java, Indonesia. The mining location is surrounded by three volcanoes which one of them remains active. The large size of greenish tuff was grounded and sieved to obtain smaller particle size from 0.1 to 0.3 mm. An H-protonated form of natural zeolites was prepared by two different methods which are discussed in Section 3.3.2. Modified natural mordenite samples were prepared by hydrothermal recrystallization method which is described in Section 3.3.3. Afterward, the H-protonated form of recrystallized natural zeolites samples was prepared by using HCl as described in Section 3.3.2 as follow.

3.3.2 Ion-Exchange Procedure

We studied two different chemical sources treatment to prepare H-protonated form, i.e., ammonium nitrate (NH_4NO_3) and hydrogen chloride (HCl). The sample was ion-exchanged with 2 M NH_4NO_3 for 30 min at 85 °C under microwave irradiation. The procedure was repeated to ensure complete removal of alkali metal and alkaline earth cations. The other sample was prepared with 1 M HCl by using the same microwave irradiation procedure. Solid particles were separated and dried overnight at 110 °C. Afterward, the dry powder samples were calcined in static air at 550 °C for 8 h. The H-protonated form samples were labeled as H-P-N and H-P-H for NH_4NO_3 ion-exchanged and HCl ion-exchanged, respectively.

3.3.3 Recrystallization

Sodium silicate solution ($18\text{SiO}_2/12\text{NaOH}/780\text{H}_2\text{O}$) was applied to recrystallize the natural zeolites at temperature 170 °C under autogenous pressure. The hydrothermal recrystallization time was varied by 2, 14, and 26 h. The samples were labeled as R2, R14, and R26, respectively. Afterward, samples were washed and centrifuged several times with deionized water. The sample dried overnight at 110 °C. The H-protonated form of recrystallized samples was prepared by using HCl as described in previous Section 3.3.2. The protonated samples were labeled as H-R2-H, H-R14-H, and H-R26-H.

3.3.4 Synthetic Mordenite Preparation

The synthetic mordenite sample was prepared by hydrothermal method with silicon/aluminum ratio of 15 according to the recipe, $30\text{SiO}_2/\text{Al}_2\text{O}_3/7\text{Na}_2\text{O}/780\text{H}_2\text{O}$, reported elsewhere [111]. Firstly, the sodium hydroxide pellets (Applichem) were dissolved in deionized water by stirring vigorously. The sodium aluminate was added to

the sodium hydroxide solution. After the homogeneous mixture solution, colloidal silica (40 wt.% in water, Sigma-Aldrich), was added to the solution and stirred for a half hour. The mixture solution was heated in an autoclave (Parr Inc.) at 170 °C for 48 h. The solution was decanted and the sample washed with deionized water several times by centrifugation. The sample of synthetic mordenite was dried in the oven at 110 °C for 12 h. The dried powder was ion exchanged with 2 M NH_4NO_3 and calcined. The sample was labeled as H-synthetic MOR.

3.3.5 Characterization

Natural zeolites phases were identified by using powder X-ray diffraction (XRD, Miniflex-Rigaku). The scanning rate was 3°/min from 2θ of 5° to 50° with a step size 0.03°. X-ray fluorescence (XRF) was carried out to determine elemental composition of the natural zeolites. Field-emission scanning electron microscopy (FE-SEM, LYRA 3 Dual Beam, Tescan) was used to study the morphology of samples. ^{27}Al Magic-Angle Spin Nuclear Magnetic Resonance (^{27}Al MAS-NMR) investigations were carried out to determine the aluminum is within the zeolites framework. Textural properties were assessed by nitrogen physisorption (ASAP 2020-Micromeritics). Prior to analyzing, the sample was degassed at temperature 350 °C for 6 hours under vacuum condition. Nitrogen physisorption was conducted at cryogenic temperature -196 °C. Ammonia-temperature program desorption (NH_3 -TPD, Micromeritics ChemiSoft TPx V1.02) analysis was performed to study the samples acidity. Pyridine-FTIR (Nicolet 6700 spectrometer) studies were carried out to determine Brønsted and Lewis acid sites. The spectra were taken at 150 °C and 300 °C. The amount of pyridine FTIR adsorbed was calculated by an equation published elsewhere [112].

3.3.6 Catalysts Testing

The samples were tested in a fixed bed reactor for n-butane isomerization. The reactor made of Inconel ID 5.16 mm was loaded with 0.2 g of H-protonated form samples. The temperature was increased from room temperature to 500 °C for 30 min and dwell for 30 min under a flow rate of 10 mL/min nitrogen. The temperature was reduced to 350 °C for 30 min followed by feeding 2 mL/min of n-butane (99.5%) and 10 mL/min nitrogen under atmospheric pressure. Products analyses were evaluated by using GC (Agilent 7890a) with two columns (Agilent HP-INNOWax PEG and Agilent J&W GC-GasPro) and flame ionization detectors (FID).

3.4 Results and Discussion

The crystalline phases of zeolites Klaten were observed by XRD in which three phases, i.e., mordenite, clinoptilolite, and quartz have been identified. Mordenite was confirmed as the major phase as compared with the other phases. The XRD pattern of natural mordenite was consistent with the XRD pattern of synthetic mordenite. However, the peaks intensity of natural mordenite were noticeably lower as compared to the synthetic mordenite, which indicated a low crystallinity of the natural mordenite and high content of amorphous phase (Figure 3.1).

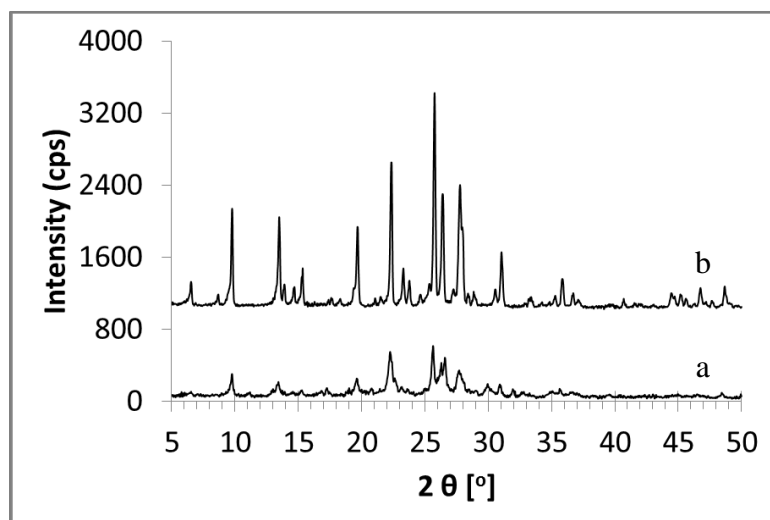


Figure 3.1: XRD patterns of (a) the as-received natural zeolites, (b) synthetic Na-MOR.

3.4.1 Ion-Exchange Procedure

The intensity of diffraction peaks of H-protonated samples slightly increased as compared with the as-received natural zeolites, which indicated higher mordenite crystallinity after ion-exchange and calcination. The acid treatment sample showed slightly lower XRD peak intensities than the ammonium nitrate ion-exchanged sample (Figure 3.2). It is important to note that the acid ion-exchange with mild concentration acid (1 M HCl) and short duration treatment retained the zeolite framework. Harsh acid concentration and longer period time treatment on the natural mordenite decreased the crystallinity as reported in our previous work [69].

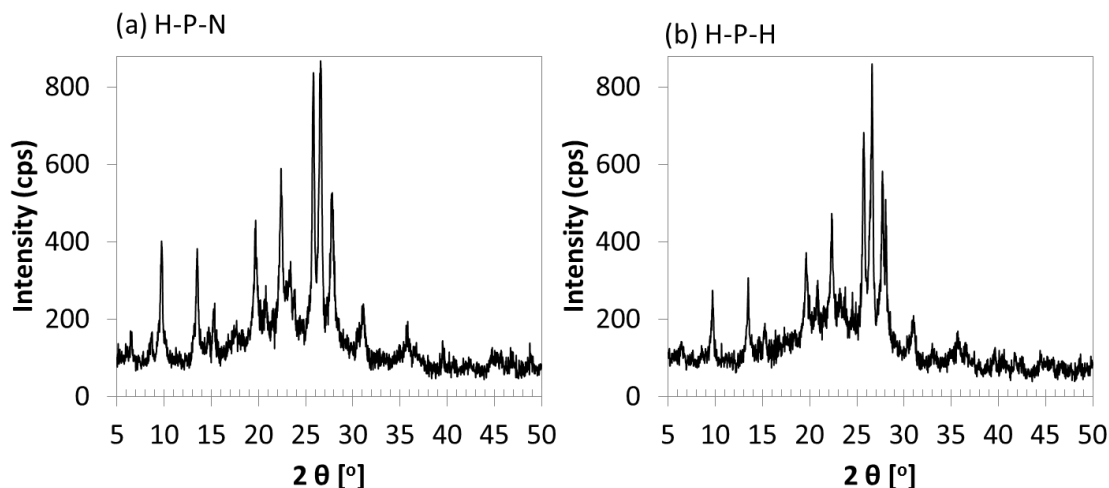


Figure 3.2: XRD patterns of protonated MOR by using solutions of (a) NH_4NO_3 and (b) HCl .

The textural properties of the ion-exchanged samples were significantly different with the as-received natural zeolite sample as shown in the nitrogen isotherms (Figure 3.3). The nitrogen uptake of the acid ion-exchanged was higher than the ammonium nitrate ion-exchanged. Micropore surface area increased from $110 \text{ m}^2/\text{g}$ in the as-received natural zeolites sample to $159 \text{ m}^2/\text{g}$ in the NH_4NO_3 ion-exchanged sample and $180 \text{ m}^2/\text{g}$ in the HCl ion-exchanged sample (Table 3.1). The replacement of potassium (K^+) and calcium (Ca^{2+}) cations in the as-received sample with H^+ in the ion-exchanged sample increased the surface area as the H^+ size much smaller as compared with the K^+ and Ca^{2+} . The surge of pore volume was observed in the HCl ion-exchanged sample with $0.13 \text{ cm}^3/\text{g}$ from $0.1 \text{ cm}^3/\text{g}$ in the as-received natural zeolites. This was mainly due to partial removal of aluminum within the framework of zeolites by the acid solution which created new micropore and mesopore channels [69, 113]. The ion-exchange procedure by using mild concentration of hydrochloric acid gave benefits, i.e., the H-protonated form generated along with an improvement of textural properties.

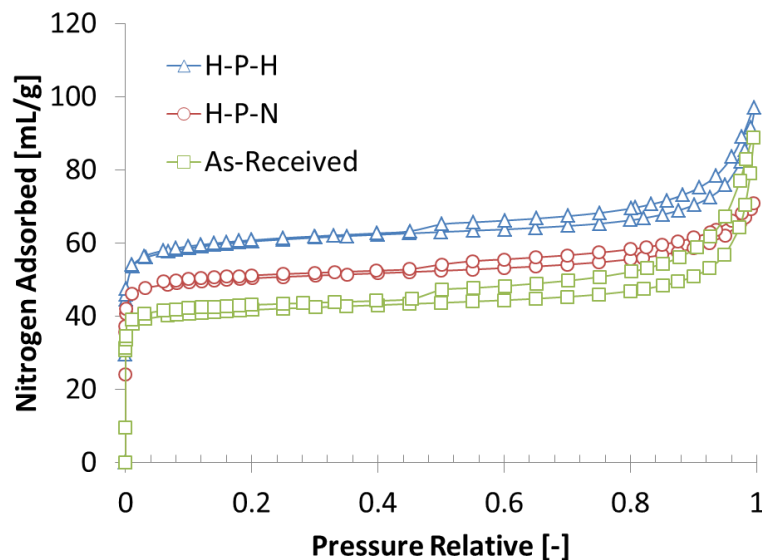


Figure 3.3: Nitrogen isotherms of the as-received sample (As-Received) and protonated MOR by using NH_4NO_3 (H-P-N) and HCl (H-P-H) solutions.

Table 3.1: Textural properties and Si/Al of the as-received sample and protonated MOR by using NH_4NO_3 (H-P-N) and HCl (H-P-H) solutions.

Sample	S_{BET} (m^2g^{-1})	S_{t} (m^2g^{-1})	S_{ext} (m^2g^{-1})	V_{total} (cm^3g^{-1})	V_{micro} (cm^3g^{-1})	V_{meso} (cm^3g^{-1})	Si/Al* (-)
As-Received	133	110	23	0.10	0.06	0.04	6.0
H-P-N	183	159	24	0.10	0.06	0.04	7.1
H-P-H	219	180	39	0.13	0.08	0.05	13.1

*XRF

The acid ion-exchanged sample (H-P-H) exhibited a rough surface texture as compared with the ammonium nitrate sample (H-P-N) which showed a smooth surface appearance (Figure 3.4). The acid treatment created secondary pore which marked on the rough surface SEM image as shown in Figure 3.4b. This fact was in agreement with the nitrogen

physisorption study which concluded that the mesopore volume of the H-P-H sample was higher than the H-P-N sample (Table 3.1). The hierarchical pore system, a combination of micropore and mesopore channels, shortened diffusion path length which greatly improved mordenite catalyst performance [114].

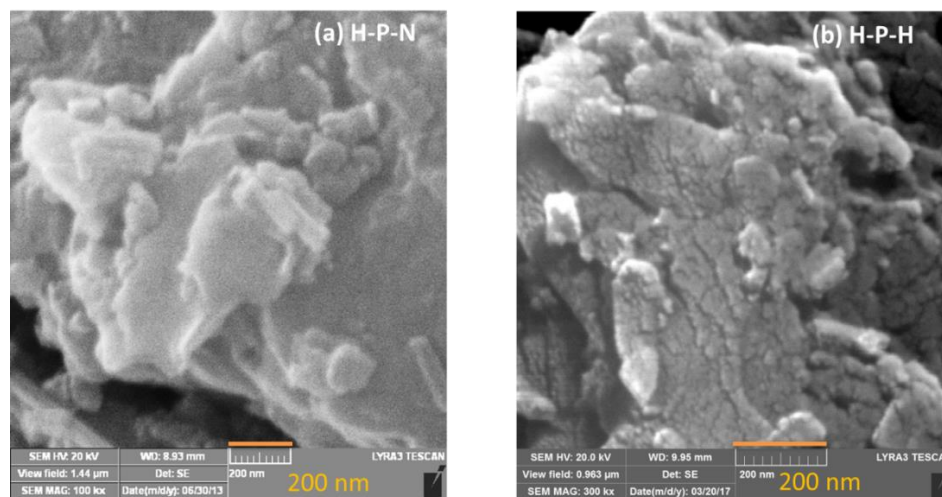


Figure 3.4: SEM images of protonated MOR by using (a) NH_4NO_3 and (b) HCl solutions.

The ion-exchange solution also affected sample acidity which studied by ammonia-TPD (Figure 3.5). The ammonium nitrate ion-exchanged sample (H-P-N) showed a higher total number of acid sites as compared with the acid ion-exchanged sample (H-P-H). The weak acid sites of the H-P-H was decrease significantly as compared to the H-P-N. However, there is a slight increase in the number of strong acid sites of the H-P-H. It is most likely as a result of dealumination process, which also occurred during the ion-exchange using hydrochloric acid solution. Partial removal of aluminum decreases the total acid sites of the natural zeolites.

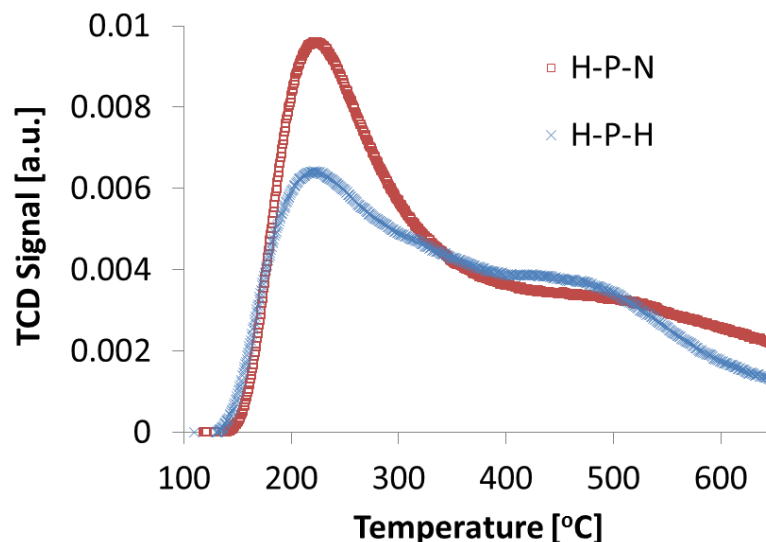


Figure 3.5: NH_3 -TPD curves of protonated MOR by using (a) NH_4NO_3 and (b) HCl solutions.

The acidity study by using pyridine-FTIR also showed a similar trend with the ammonia-TPD in the total number acid sites (Table 3.2). The number of Brønsted acid site (BAS) of the H-P-N sample was higher than the H-P-H sample. However, the number of Lewis acid sites (LAS) was slightly higher in the acid ion-exchanged sample as compared with the ammonia ion-exchanged sample. The high number of LAS of the H-P-H suggested that the extraframework aluminum (EFAL) formed during the acid ion-exchange procedure. On the other hand, the aluminum within zeolites framework preserved well after the ammonium nitrate ion-exchange which was shown by the high number of BAS and a close silicon/aluminum ratio with the parent.

Table 3.2: The number of acid sites of protonated MOR by using NH_4NO_3 (H-P-N) and HCl (H-P-H) solutions.

Sample	Brønsted acid sites (BAS) [$\mu\text{mol/g}$]*		Lewis acid sites (LAS) [$\mu\text{mol/g}$]*		BAS/LAS	
	150 °C	300 °C	150 °C	300 °C	150 °C	300 °C
H-P-N	62	40	24	16	2.6	2.5
H-P-H	42	26	28	15	1.5	1.7

*Pyridine-FTIR

H-protonated forms of mordenite were prepared by an ion-exchange method with two different chemical sources, i.e., hydrochloric acid (H-P-H) and ammonium nitrate (H-P-N). We tested the catalysts in the fixed bed reactor for n-butane isomerization. High selectivity to isobutane was exhibited over the H-P-H sample as a result of high silicon to aluminum ratio ($\text{Si/Al} = 13.1$) (Figure 6). The higher n-butane conversion with 10% was demonstrated over the H-P-N sample than the H-P-H sample with only 3.5% at time on stream (TOS) 10 min. However, the selectivity to isobutane over the H-P-N was very poor (ca. 14%). The high aluminum content in the H-P-N sample ($\text{Si/Al} = 7.1$) which also indicated by the high BAS density is the main reason of the high n-butane conversion and low isobutane selectivity.

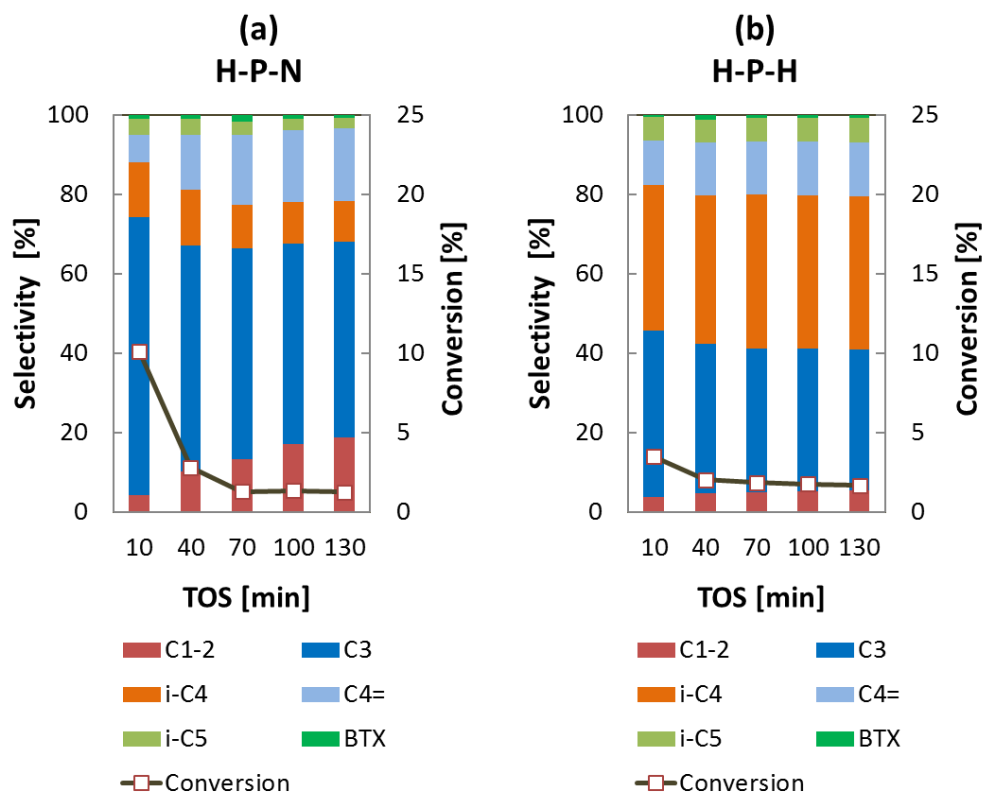
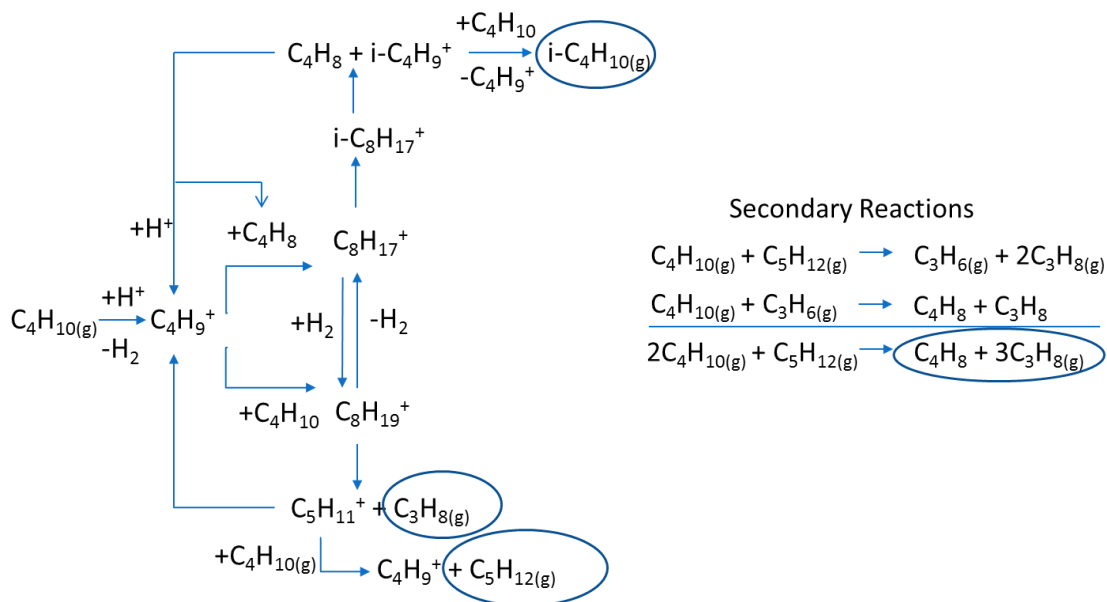
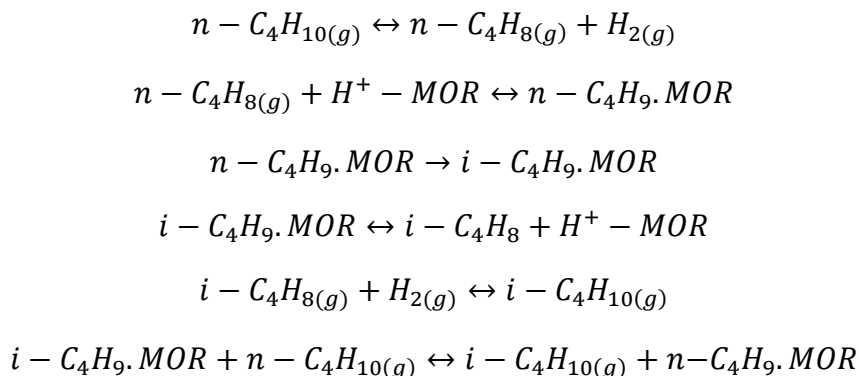


Figure 3.6: Butane conversion and products selectivity over H-P-N and H-P-H.



Route 1. Bimolecular pathway with successive secondary reactions for the n-butane isomerization. Adapted from ref.[115].

The high selectivity to propane over the H-P-N suggested that the n-butane transformation most likely followed the bimolecular pathway with disproportionation and successive secondary reaction in the micropore structure (Route 1).[115] On the other hand, the selectivity to isobutane was significantly high over the H-P-H sample (ca. 37%). It is not only due to the lower content of aluminum, less acid density, but also the opening new micropore channels during the ion-exchange with acid solution as suggested by the nitrogen physisorption study (Table 1). This enhanced the access of n-butane into the high strong acid sites in the side pocket of 8-MR channels. This finding was in agreement with literature reported that the acid treatment created the access to the new micropore channels in the side pocket.[113, 116]. Niwa et al. [105] studied that the acid sites in the 8-MR were stronger than the 12-MR. Hence, the high selectivity to isobutane over the H-P-H is most likely contributed through the monomolecular pathway on the strong acid sites (Route 2).



Route 2. Monomolecular pathway for the n-butane isomerization. Adapted from ref. [117].

3.4.2 Recrystallization of Natural Zeolites

The recrystallization of natural zeolites showed interesting results. The recrystallized samples exhibited higher crystallinity as compared with the as-received natural zeolites which indicated by the high peaks intensity of XRD patterns as seen in Figure 3.7. It seems

that the high crystallinity contributed by the new mordenite crystal growth during the hydrothermal process. As the time of hydrothermal increased, the XRD peaks intensity became higher which suggested a growth of new mordenite crystal along with the hydrothermal time. However, the competitor phase identified as quartz grew faster at longer hydrothermal time viz. 26 h. Hence, it is not suggested to recrystallize in a very long period of time.

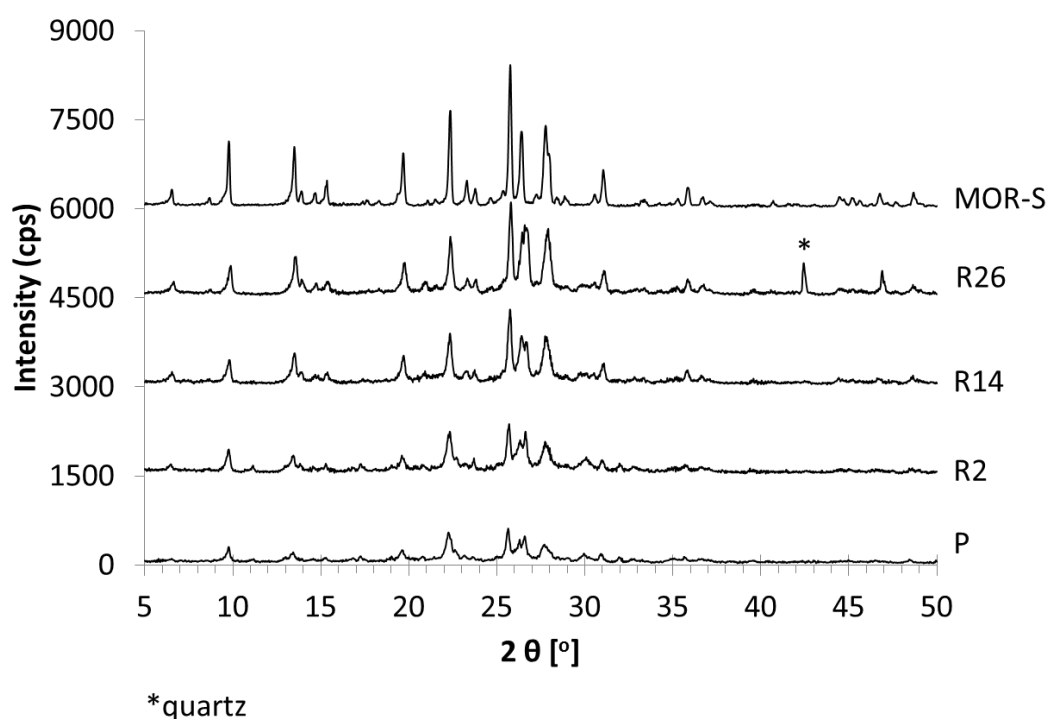


Figure 3.7: XRD patterns of the as-received sample (P) and Na-MOR recrystallized samples. Offset by 1500, 3000, 4500, and 6000 for R2, R14, R26, MOR-S respectively.

The ^{27}Al NMR analyses were performed to study the effect of recrystallization on the aluminum tetrahedral within the zeolites framework (Figure 3.8). The study revealed that the as-received natural zeolites have a small peak at 0 ppm which suggested the existence of extraframework aluminum (EFAL). The shoulder at main peak 60 ppm was also

detected in the parent sample. The EFAL peak and the shoulder disappeared after hydrothermal recrystallization. The ^{27}Al NMR results convinced that the aluminum within the structure of zeolite recrystallized sample is higher than the parent natural zeolites (P).

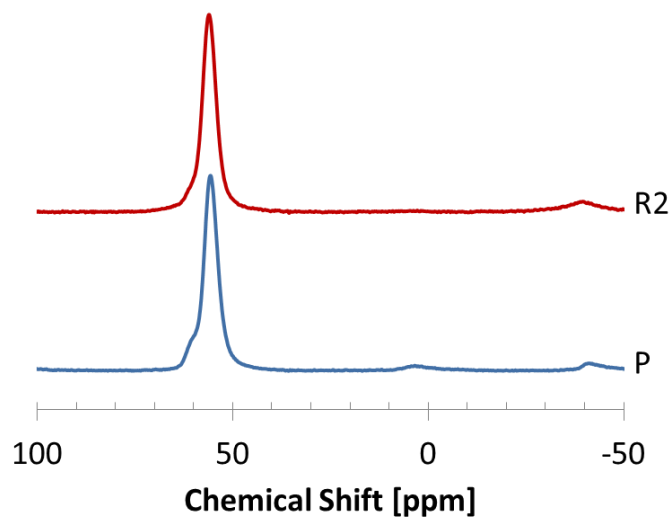


Figure 3.8: ^{27}Al NMR spectra of the as-received sample (P) and recrystallized MOR (R2).

The SEM images of the parent and recrystallized samples are presented in Figure 3.9. The typical shape of natural mordenite is needles [29]. The parent sample has only a few small size needles shape. The mordenite crystal growth was clearly seen as indicated by the more needles shape appearance after hydrothermal recrystallization for 2 h. The crystals size were even longer and increased in number after 14 h of recrystallization. At 26 h, the crystals became larger like a slab. The growth of crystal mordenite was in agreement with the XRD study that revealed the gradual increase in mordenite peak intensities along with the hydrothermal time.

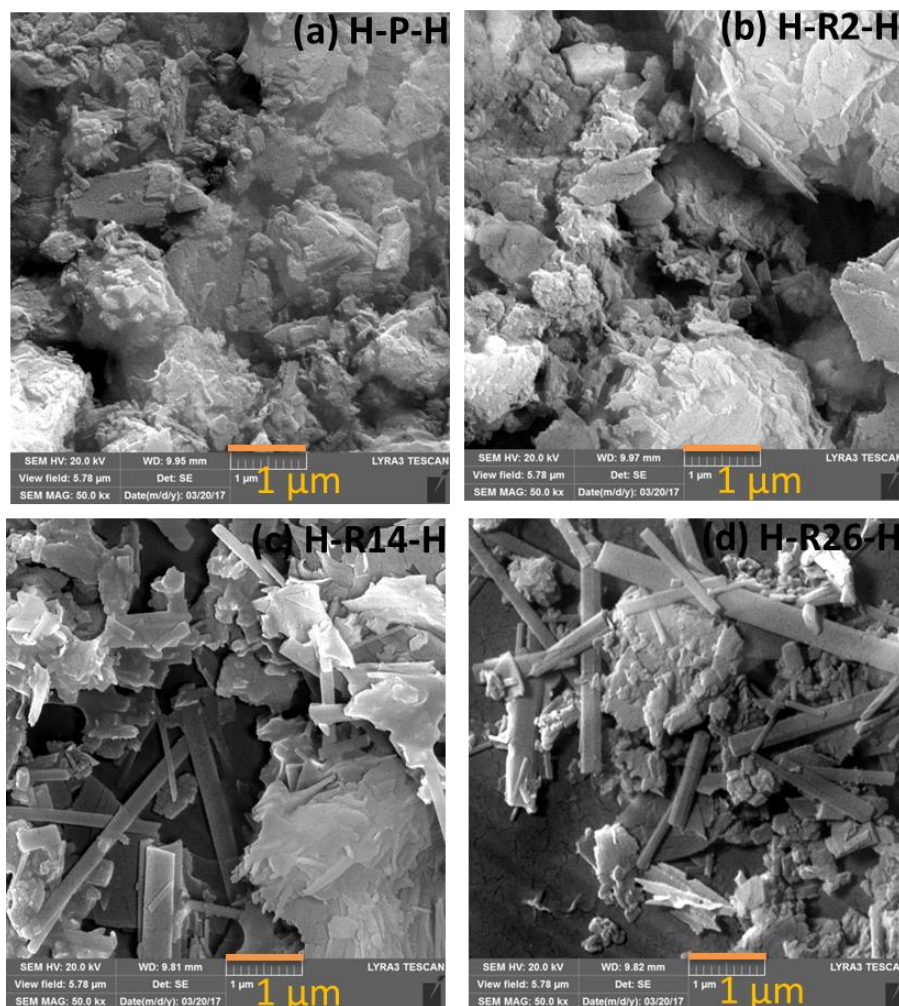


Figure 3.9: SEM images of the protonated parent and recrystallized samples after 2-26 h hydrothermal treatment.

The nitrogen physisorption isotherms are presented in Figure 3.10. The nitrogen uptake was increased with the time of hydrothermal recrystallization. It was arisen as a result of the formation of new mordenite crystal during the hydrothermal recrystallization. From the model calculation using the t-plot method, the micropore area increased significantly from 180 m²/g in the parent (H-P-H) to 285 m²/g after 26 h hydrothermal recrystallization (H-R26-H) (Table 3.3). The mesopore was observed in the SEM images of the acid treatment

recrystallized samples as shown by the arrows in Figure 3.11. This is in a good agreement with the nitrogen physisorption results which showed a higher mesopore volume at 2-14 h of recrystallized acid treated samples.

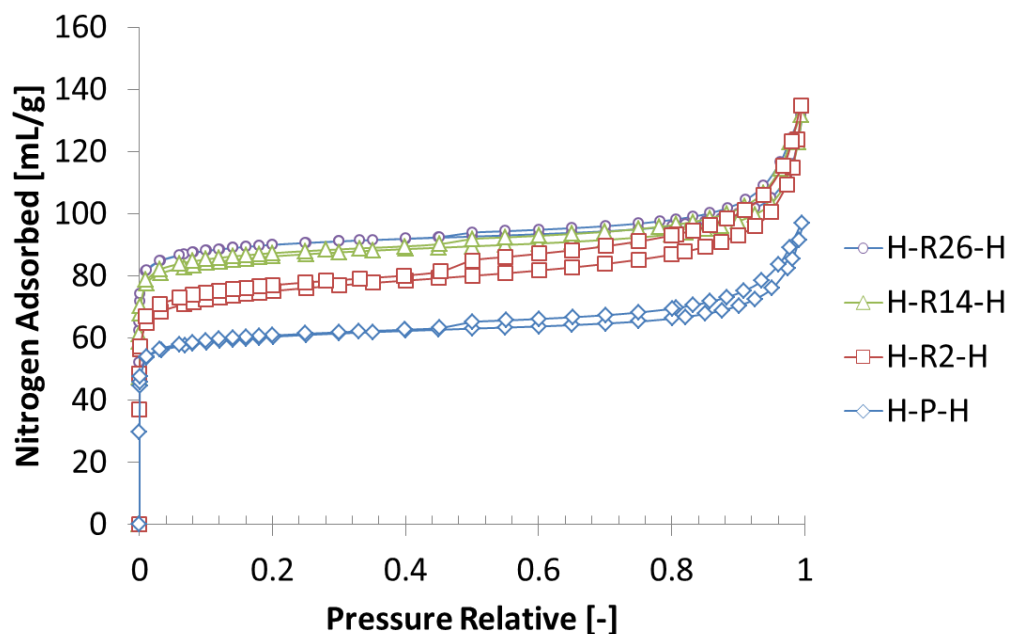


Figure 3.10: Nitrogen isotherms of the parent (H-P-H) and recrystallized H-MOR.

Table 3.3: Textural properties and silicon to aluminum ratio of samples.

Sample	S_{BET} (m^2g^{-1})	S_{t} (m^2g^{-1})	S_{ext} (m^2g^{-1})	V_{total} (cm^3g^{-1})	V_{micro} (cm^3g^{-1})	V_{meso} (cm^3g^{-1})	Si/Al* (-)
H-P-H	219	180	39	0.13	0.08	0.05	13.1
H-R2-H	272	212	60	0.17	0.09	0.08	15.5
H-R14-H	313	266	47	0.17	0.11	0.06	16.0
H-R26-H	327	285	42	0.17	0.12	0.05	16.6

*XRF

The mesopore was observed in the SEM images of the acid treatment recrystallized samples as shown by the arrows in Figure 3.11. This is in a good agreement with the nitrogen physisorption results which showed a higher mesopore volume at 2-14 h of recrystallized acid treated samples. However, the mesopore volume of the recrystallized acid treated sample at 26 h was in similar result with the parent (Figure 3.11b).

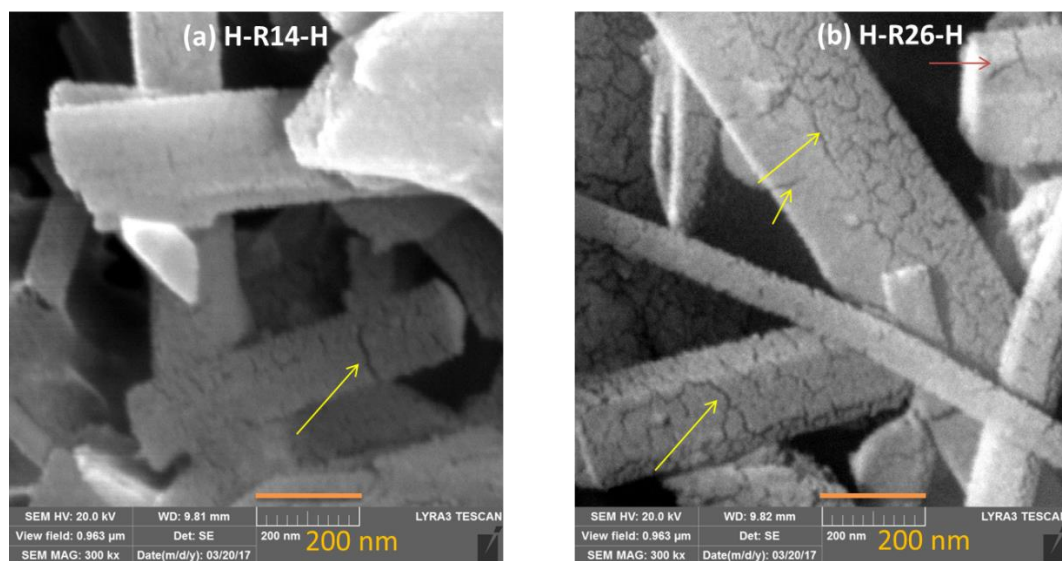


Figure 3.11: Mesopore in the recrystallized after ion-exchange with HCl over the recrystallized MOR samples.

The effect of hydrothermal recrystallization time to the acidity of the recrystallized samples is studied based on the NH_3 -TPD and pyridine-FTIR. The total acid sites increased by the recrystallization time as seen in the curve of ammonia-TPD results (Figure 3.12). It is worthwhile to mention here that the number of weak acid sites were increase significantly along with the recrystallization time. On the other hand, the number of strong acid sites reduced after the recrystallization step. Those facts suggested that the silicon/aluminum ratio of the samples were increase by the time of hydrothermal recrystallization. The XRF

study confirmed that the Si/Al ratio of the recrystallized samples were increase by the recrystallization time (Table 3.3). This was also in agreement with literature [118]. The authors showed that increasing of Si/Al ratio led to the increasing of weak acid sites and decreasing of the strong acid sites. The pyridine-FTIR was also performed in order to examine the Brønsted acid sites (BAS) and Lewis acid sites (LAS). The trend of higher number acid sites in the recrystallized samples as compared to the parent were also confirmed by the pyridine FTIR study. It is understandable that the number of acid sites increase as a result of the growth of new crystals mordenite phase replacing the amorphous phase in the as-received natural zeolites. The longer of recrystallization time leads to higher number both of Brønsted and Lewis acid sites (Table 3.4). The BAS was increase higher than the LAS, which was indicated by the increase of BAS/LAS ratio along with the recrystallization time. The BAS played a crucial part in the n-butane isomerization reaction. In fact, the strong BAS favored isobutane selectivity through the monomolecular mechanism. In contrast, the presence of LAS had a negative effect on the n-butane isomerization [119].

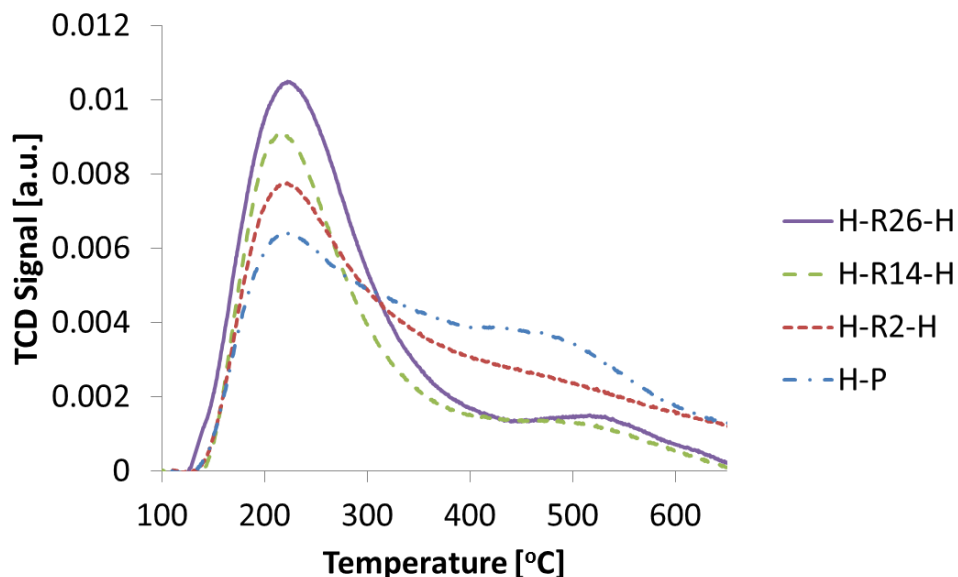


Figure 3.12: Ammonia-TPD of the protonated parent (H-P) and recrystallized samples.

Table 3.4: Brønsted and Lewis acid sites of the parent & recrystallized samples.

Sample	Brønsted acid sites (BAS) [$\mu\text{mol/g}$]*		Lewis acid sites (LAS) [$\mu\text{mol/g}$]*		BAS/LAS [-]	
	150 °C	300 °C	150 °C	300 °C	150 °C	300 °C
H-P-H	42	26	28	15	1.5	1.7
H-R2-H	63	35	34	21	1.9	1.7
H-R14-H	178	102	65	39	2.7	2.6
H-R26-H	190	135	58	32	3.3	4.2

*Pyridine-FTIR

The recrystallized and parent acid ion-exchanged samples were tested in the fixed bed reactor for n-butane isomerization. Conversion of n-butane increased along with the recrystallization time (Figure 3.13). The conversion of n-butane was very low ca. 4 % at a time on stream (TOS) 10 min in the H-P-H sample. However, the n-butane conversion increased significantly to 25% at TOS 10 min after 26 h of hydrothermal recrystallization

(H-R26-H). The high number of BAS in the H-R26-H sample governed the high conversion of n-butane.

The selectivity to isobutane was decreased from 37% in the H-P-H to 31%, 30%, and 28% in the H-R2-H, H-R14-H, and H-R26-H, respectively at relatively similar conversion (ca. 5%). The high number of weak acid sites in the recrystallized samples promoted transformation of n-butane through bimolecular pathway, which is less selective to isobutane product (Route 1). Owing to the highest weak acid sites density, the sample H-R26-H showed the lowest selectivity to isobutane among other samples. Improving the selectivity to isobutane might be achieved by shifting the bimolecular pathway to monomolecular pathway through reducing the number of weak acid sites and open the access to the strong acid sites in the side pocket. The strong acid sites in the side pocket of the 8-MR could be accessed by a longer period of acid treatment.

The isobutane yield was calculated by multiplying the n-butane conversion with the selectivity to isobutane. Despite the selectivity to isobutane in the recrystallized MOR were slightly lower than the parent, the n-butane conversion was significantly higher than the parent. As a result, the yield of isobutane showed remarkably higher in the recrystallized MOR samples with ca. 8% as compared with the parent with only ca. 1% (Figure 3.14). It can be deduced that the hydrothermal recrystallization was effective to improve the catalyst properties of the natural zeolites.

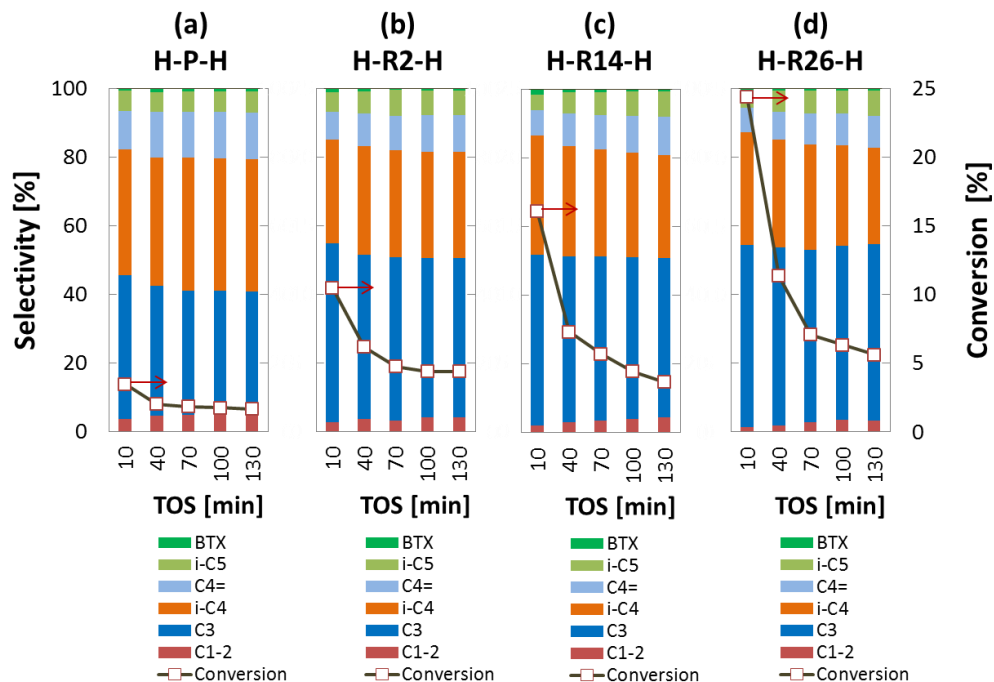


Figure 3.13: Butane conversion and products selectivity over the parent and the recrystallized natural mordenite.

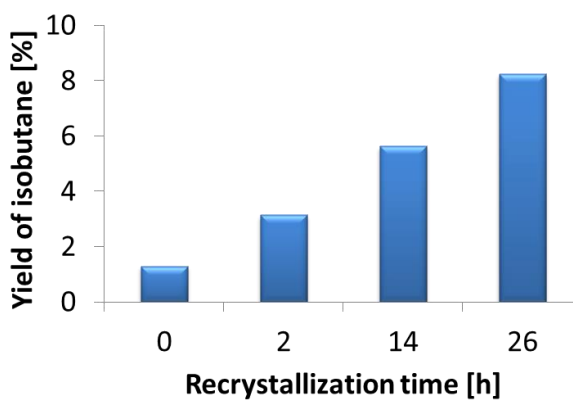


Figure 3.14: Isobutane yield over different time of hydrothermal recrystallization.

3.4.3 Comparison of Recrystallized Natural Mordenite and Synthetic Mordenite

The nitrogen isotherm of recrystallized natural mordenite displays different pattern as compared with the synthetic mordenite (Figure 3.15). Higher nitrogen uptake in the low-

pressure region as shown in the synthetic mordenite isotherm indicates a high micropore volume of synthetic mordenite than the recrystallized natural mordenite. The isotherm of synthetic mordenite had reached a plateau from relative pressure ca. 0.05 to 1 which indicated a very low external surface area. There was also no hysteresis observed in the isotherm of the synthetic mordenite which described a very low mesopore volume. In contrast, gradual increasing nitrogen uptake from lower relative pressure ca. 0.05 and a loop of hysteresis was detected at P/P_0 0.5 to 1 which indicated a high external surface area and large mesopore volume.

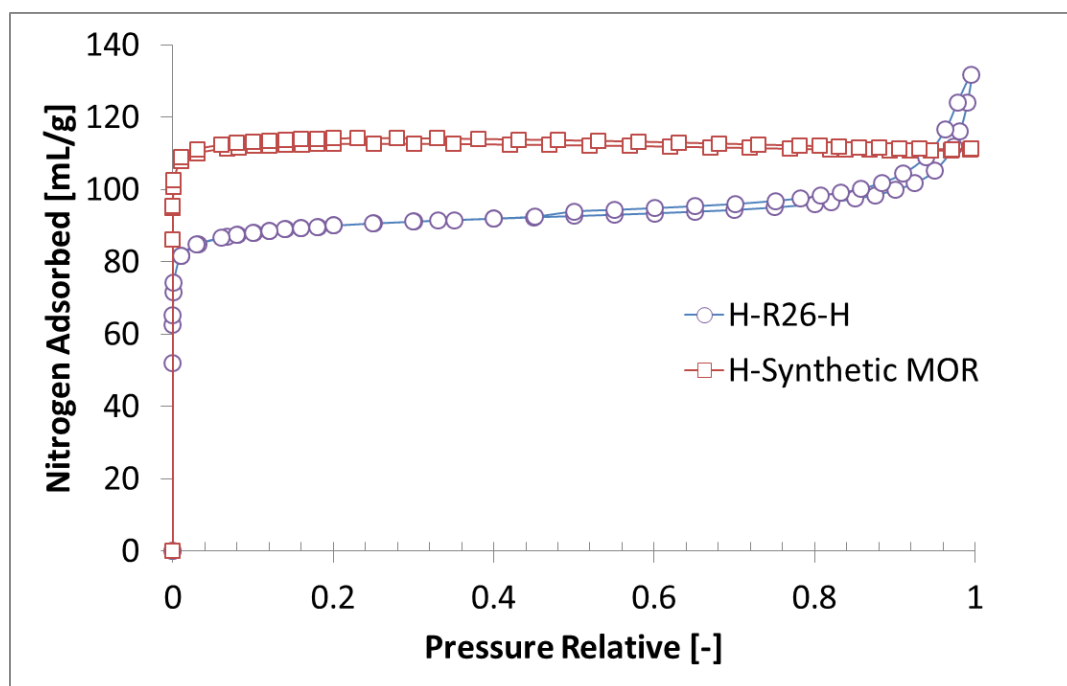


Figure 3.15: Nitrogen isotherms of recrystallized natural mordenite and synthetic mordenite.

Textural properties of the samples were calculated based on various model, i.e., Brunauer–Emmett–Teller (BET) for the total surface area, t-plot method for micropore area, volume and external surface area. It is clearly shown in Table 3.5 that the synthetic mordenite

mainly consisted of micropore. In contrast, the recrystallized natural mordenite has not only the micropore but also a significant amount of mesopore. The hierarchical pore architecture was inherent from the parent of natural zeolites which enriched by the new crystal needles shape in various size after the recrystallization.

Table 3.5: Textural properties of recrystallized natural mordenite and synthetic mordenite.

Sample	S_{BET} (m^2g^{-1})	S_{t} (m^2g^{-1})	S_{ext} (m^2g^{-1})	V_{total} (cm^3g^{-1})	V_{micro} (cm^3g^{-1})	V_{meso} (cm^3g^{-1})	Si/Al (-)
H-R26-H	327	285	42	0.170	0.120	0.050	16.6*
H-Synthetic MOR	420	406	14	0.170	0.168	0.002	8.8**

*XRF, **EDX

The particle size of the recrystallized natural mordenite was smaller ca. 1-5 μm as compared with the synthetic mordenite, ca. 5 – 20 μm (Figure 3.16). The morphology shape of the recrystallized was a mixture of needles and irregular shape. On the other hand, the synthetic mordenite was mainly a large hexagonal shape.

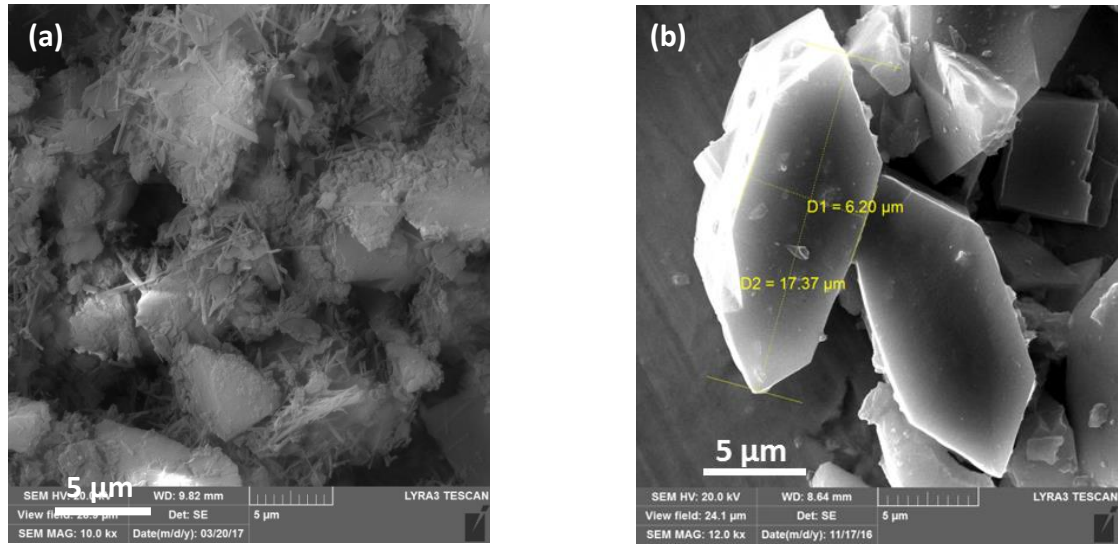


Figure 3.16: SEM images of (a) recrystallized natural mordenite and (b) synthetic mordenite.

The ammonia-TPD curves of synthetic and recrystallized natural mordenite are presented in Figure 3.17. It is clear that the total acid sites of synthetic mordenite was higher than the recrystallized natural mordenite. The number of Brønsted acid sites of the synthetic mordenite was higher than the recrystallized natural mordenite (Table 3.6). However, the Lewis acid sites of the synthetic mordenite was lower as compared with the recrystallized natural mordenite. The high crystallinity of synthetic mordenite and high micropore volume was correlated positively with the number of acid sites.

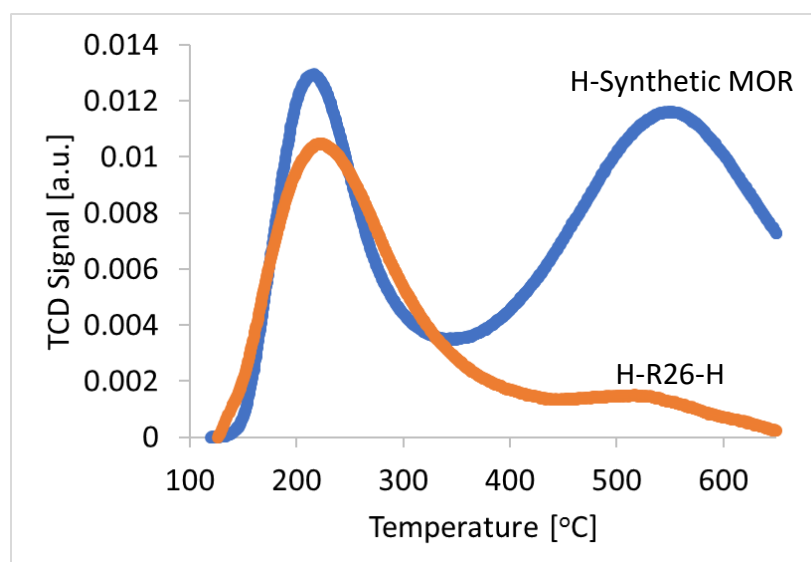


Figure 3.17: Ammonia-TPD of recrystallized natural mordenite and synthetic mordenite.

Table 3.6: Brønsted and Lewis acid sites of recrystallized natural mordenite and synthetic mordenite.

Sample	Brønsted acid sites (BAS) [μmol/g]*		Lewis acid sites (LAS) [μmol/g]*		BAS/LAS [-]	
	150 °C	300 °C	150 °C	300 °C	150 °C	300 °C
H-R26-H	190	135	58	32	3.3	4.2
H-Synthetic MOR	224	200	13	11	17.2	18.2

*Pyridine-FTIR

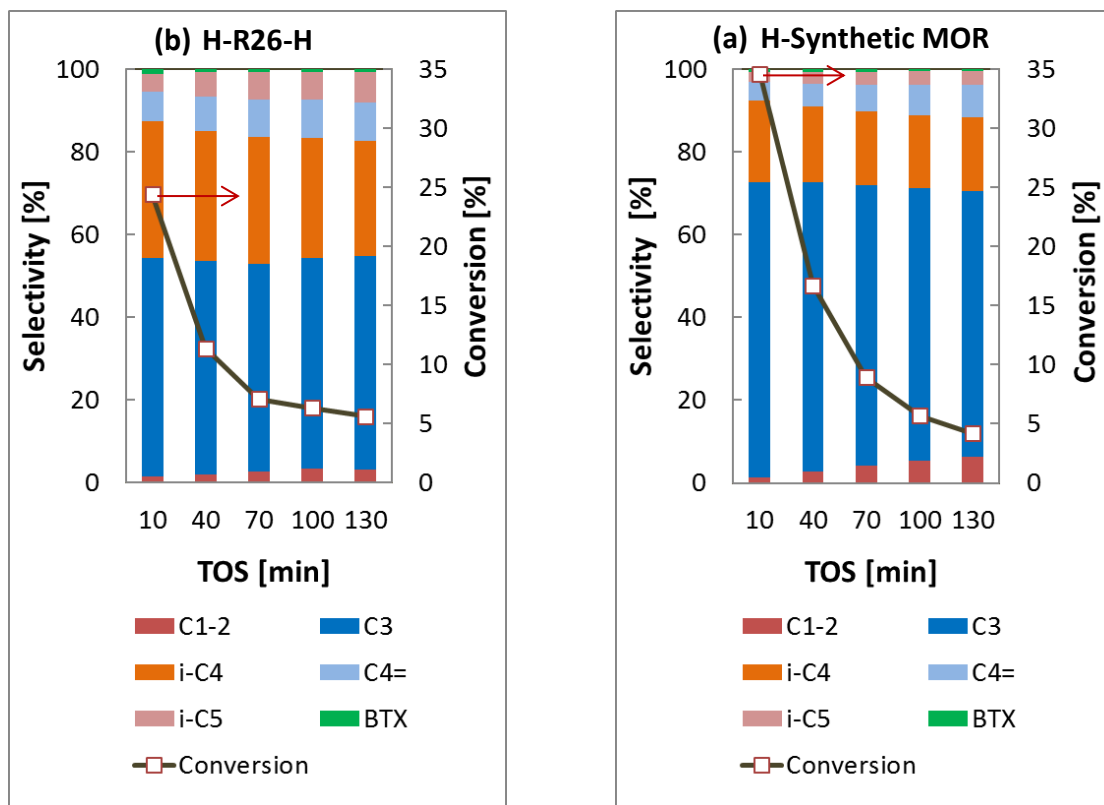


Figure 3.18: Comparison of activity and products selectivity of n-butane isomerization over (a) recrystallized natural mordenite and (b) synthetic mordenite.

The performance of recrystallized natural mordenite and synthetic mordenite for n-butane isomerization is compared in Figure 3.18. Conversion of n-butane over the synthetic mordenite was higher than the recrystallized natural mordenite during the initial 70 min of reaction. However, the activity of recrystallized mordenite was higher as compared with the synthetic mordenite after TOS 70 min reaction. The deactivation rate was higher on the synthetic mordenite due to high Brønsted acid sites density and high micropore volume but very low mesopore volume. Furthermore, the crystal size of 1-D synthetic mordenite was very large which favored the successive reactions to produce coke within the micropore channels. The coke condensation caused blocking on the micropore resulted in the fast deactivation rate [120]. The selectivity to isobutane over the recrystallized natural

mordenite (28-33%) was notable consistently higher than the synthetic mordenite (18-20%) over the time of reaction. The silicon to aluminum ratio of recrystallized natural mordenite, ca. 16.6, was higher than the synthetic mordenite, ca. 8.8 which favored selectivity to isobutane as reported in the open literature [115, 121]. The yield of isobutane on the recrystallized natural mordenite was higher than the synthetic mordenite (Figure 3.19). The combination of high silicon to aluminum ratio and high micropore and mesopore volume of the recrystallized natural mordenite gave a comparable catalyst performance with the synthetic mordenite.

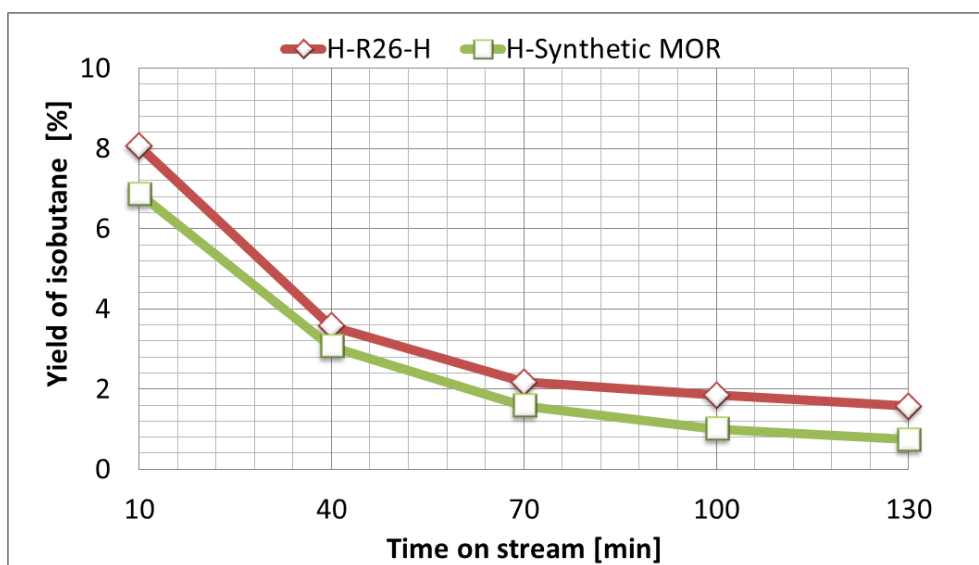


Figure 3.19: Comparison of isobutane yield over recrystallized natural mordenite and synthetic mordenite.

3.4.4 Mechanism of Natural Mordenite Recrystallization

The possible mechanism of low-grade natural mordenite recrystallization into high-quality mordenite is illustrated in Figure 3.20. The aluminum source originated from the natural zeolites which were rich in aluminum. Sodium hydroxide solution acted as mineralizer and controlled the high basicity which was suitable for the mordenite growth. Silica addition

into the aqueous NaOH was needed not only to prevent desilication of the parent mordenite but also to provide silicon for the formation of new mordenite crystals. The mordenite phase in the as-received natural zeolites acts as the seed to induce a new crystal growth of mordenite as shown by the shape of the needle in the illustration. The temperature 170 °C was selected for the optimum growth of mordenite phase. The amorphous phase which was high in the as-received sample was converted into the mordenite phase as indicated by the high peaks intensity of the XRD pattern. Finally, the mordenite phase in the recrystallized samples become far more dominant with high purity, better textural properties, and controlled silicon to aluminum ratio.

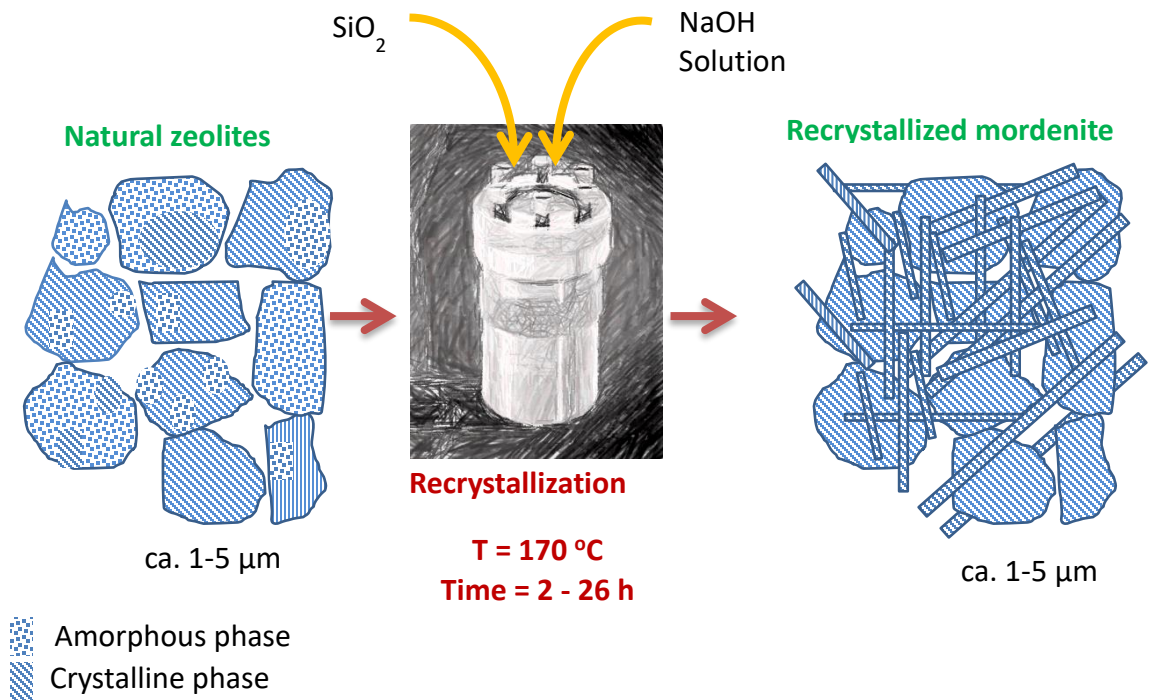


Figure 3.20: Mechanism of natural zeolites recrystallization.

3.5 Concluding Remarks

The low-grade natural zeolites with mordenite as dominant phase properties were improved by hydrothermal recrystallization technique. The recrystallized mordenite samples were exhibited superior textural properties, high crystallinity, and a high number of acid sites as compared with the parent natural zeolites. The H-protonated form of recrystallized natural mordenite via acid ion-exchange showed a better catalyst performance than the parent natural zeolites, particularly for n-butane isomerization application. The recrystallized mordenite catalytic performance was comparable with the synthetic mordenite. The simple recrystallization technique is potentially applied to improve properties of low-rank natural zeolites.

CHAPTER 4

HIGH-ENERGY BALL MILLING ATTRITOR AND HYDROTHERMAL RECRYSTALLIZATION TO PREPARE MORDENITE NANOPARTICLES: THE EFFECT OF THE RELATIVE WEIGHT OF THE BALLS AND WATER

4.1 Summary

An experiment with a Taguchi L9 orthogonal design was applied on a high-energy ball milling (HEBM) attritor to study the effects of the ball-to-powder weight ratio ($B = 10, 20$, and 30 wt./wt.) and water-to-powder weight ratio ($W = 4, 5$, and 6 wt./wt.) on the fabrication of nanoparticles from natural mordenite with the objective of minimizing the size of the particles and maximizing their crystallinity, external surface area and mesopore volume. The selected milled samples were subjected to a basic silicate solution to recover the mordenite crystalline phase. Characterizations of the samples were achieved by carrying out nitrogen physisorption, X-ray diffraction, dynamic light scattering, field emission scanning electron microscopy, and transmission electron microscopy investigations. The Taguchi analysis suggested that the ball-to-powder weight ratio was the most significant parameter to adjust for minimizing particle size and maximizing external surface, mesopore volume and crystallinity. The mean particle size by volume of the B30-W5 milled sample was 220 nm and the span $([d_{v0.9} - d_{v0.1}]/d_{v0.5})$ of this sample was 1.2 . The particle sizes ranged from 70 nm to 580 nm . About 10% of the sample by volume ($d_{v0.1}$) had particles sizes less than 100 nm and 50% of the

total number of particles ($d_{n0.5}$) were smaller than 100 nm. The crystalline nature of the mordenite nanoparticles was recovered by carrying out hydrothermal recrystallization.

4.2 Introduction

Zeolites are highly microporous crystalline minerals consisting of channels and voids filled by water and alkali or alkaline earth cations to balance the extra charge resulting from the substitution of Al^{3+} for Si^{4+} in the tetrahedral unit [2]. Zeolites have been synthesized in the laboratory and found in nature. The largest deposits of natural zeolites are found as volcanoclastic rocks, which are made from volcanic ash and magma [5]. Large deposits of natural zeolites in the western United States and other countries were discovered for the first time in 1959, and these discoveries led to the wide applications of zeolites in industrial, agricultural, environmental, and biological fields [33]. To date, 44 zeolite frameworks have been discovered in nature [25]. Clinoptilolite, mordenite, phillipsite, and chabazite are the most common zeolites and have been found as tuff deposits in vast quantities [5]. Mordenite is widely applied in the sorption and catalysis fields due to its high thermal and acid resistance. In fact, mordenite has been commercially applied as a catalyst for hydroisomerization, hydrocracking, alkylation and dewaxing [111, 122].

Over the past decade, fashioning zeolites into nanoparticles has been attracting considerable attention since this process shortens the diffusion path for substrates of the zeolite, increases the external surface area of the zeolite, makes the zeolite more stable and raises the catalytic activity and selectivity of the zeolite [62, 123]. Zeolite nanoparticles may be obtained either through a bottom-up approach with an appropriate selection of hydrothermal synthesis parameters or via a top-down approach by following a milling

procedure [124]. The use of mechanical milling to fabricate nanoparticles is interesting due to the low cost of this method and the ease of using this method to scale up production. Moreover, this method is carried out in the absence of any organic structure directing agent (OSDA), and hence poses relatively few problems for the environment.

Several types of milling techniques using different dispersion media and rotators have been developed. Two types of milling techniques are distinguished based on the dispersion medium used: wet milling uses a solvent to disperse the powder and dry milling functions without using a solvent. The wet milling method has some benefits over dry milling. For example, it eliminates the amorphization of zeolites, prevents the generation of dust and reduces the energy consumption [11, 12, 125, 126]. Two types of machines, with different rotator parts, have been developed for milling devices: the planetary ball mill and the ball milling attritor. Energy input into the planetary ball mill is used to rotate a heavy tank, while the ball milling attritor directly stirs the medium by using an agitator that is more energy-efficient than the planetary ball mill.

The problem with the top-down milling treatment approach is that the milled samples have a large particle size distribution. For example, low-energy ball milling (400-600 rpm) that combines the dry and wet milling techniques has been reported to result in a wide distribution of particle sizes, from less than 100 nm to 30 μm [11]. While another investigation of low-energy ball milling (600 rpm), one using the wet milling method, showed a reduced loss of crystallinity during the milling step, it nevertheless also showed a very large distribution of particle sizes, between 70 nm to 100 μm [12]. Due to the broad particle size distribution, a high-speed centrifugation step was introduced after a low-energy ball milling treatment (at 22 rpm) in order to separate the nanosized particles from

the micron-sized particles, and this process resulted in several grades of zeolite particle sizes [127].

The use of high-energy ball milling (HEBM), with speeds greater than 1000 rpm, to realize comminution has also been reported in the literature [14, 61, 102, 128]. KNaX zeolite particles resulting from HEBM were reported to show increased product selectivity of ethyl benzene and styrene during their catalysis of the alkylation of toluene with methanol [102], but unfortunately the particle size was not reported. An HEBM treatment applied on small-pore zeolites successfully improved the initial catalytic activity of the zeolite due to an increase in its accessible surface area [101]. An issue with HEBM, however, is the amorphization of the milled sample. HEBM has been shown to diminish the crystallinity of ZSM-5 and other zeolites [14, 19, 61]. But combining HEBM with the recrystallization method has successfully yielded nanosized ZSM-5 [19], and the hydrothermal recrystallization method has been reported to effectively recover the crystallinity of the milled samples [14, 61].

HEBM is also a common technique to combine metals into alloys and into intermetallic compounds of nanocrystals [129, 130]. However, there are few published studies of the effects of HEBM parameters on nanosized zeolite particles where the particles were prepared using HEBM together with recrystallization. In this study, we used the Taguchi L9 orthogonal design to obtain nanoparticles from natural mordenite by deploying an HEBM attritor followed by the recrystallization method. We specifically investigated the effect of the ratio of the weight of the ball to the weight of the powder, as well as of ratio of the weight of water to the weight of the powder, on various features of the mordenite nanoparticles.

4.3 Experimental

4.3.1 Material Characterization

The parent natural zeolite was obtained from Klaten, Indonesia. The zeolite phase was studied by using powder X-ray diffraction (XRD, Miniflex-Rigaku) with 2θ from 5° to 50° . The scanning rate and step sizes were $3^\circ/\text{min}$ and 0.03° , respectively. Mordenite was identified as a predominant phase of the natural zeolite as discussed in our previous report [69]. The morphology and particle sizes of the samples were examined by carrying out field-emission scanning electron microscopy (FE-SEM, LYRA 3 Dual Beam, Tescan) and transmission electron microscopy (TEM, JEOL-JEM-2100F) investigations. The particle size distributions were measured by using a dynamic light scattering (DLS) Zetatract (Microtract) with deionized (DI) water, pH 7, as a solvent. Nitrogen physisorption was carried out using an ASAP 2020 (Micromeritics). Prior to adsorption, the samples were heated up to 350°C and kept at this temperature for six hours. Subsequently, the samples were cooled to ambient temperature. Liquid nitrogen was used to maintain the temperature of the sample tube at 77 K during the nitrogen gas adsorption-desorption. The micropore volume, surface area and external surface area were estimated by using the t-plot method [131]. Total pore volume was computed at a relative pressure (P/P_0) of 0.98. Mesopore volume was obtained by subtracting the micropore volume from the total pore volume. Pore size distributions were estimated by using the nonlocal density functional theory (NLDFT)-Tarazona method [132].

4.3.2 High-Energy Ball Milling (HEBM) Attritor

To reduce the particle size, a high-energy ball milling attritor (Union Process HDDM-01) was used together with the wet milling method employing water as the dispersion medium. Prior to the milling, samples were ground and sieved to obtain powder particles with dimensions of 0.1-0.3 mm. A constant 50 g mass of natural zeolite was milled by controlling the agitator speed at 2000 rpm for 8 h. The ratio of the weight of the balls to the weight of the powder (B) and the ratio of the weight of the water used to the weight of the powder (W) were each varied as shown in Table 4.1. The ball was made of zirconia (ZrO_2) and had a diameter of 650 microns. The heat generated during the milling process was dissipated by circulating cold water, maintained at 13 °C, through the jacket of the milling tank.

4.3.3 Hydrothermal recrystallization

The selected milled samples were treated hydrothermally using an alkaline silicate solution (18 SiO_2 : 12 NaOH : 780 H_2O) according to our previous work [61]. A mass of 1 g of milled powder was mixed with the solution. After mixing for 15 minutes, the solution was heated at 170 °C for 6 h in an autoclave (Parr). The slurry was centrifuged and washed with deionized (DI) water several times until neutral pH was reached. Solid particles were separated and dried overnight at 110 °C.

4.3.4 Taguchi Method

The Taguchi method was used to analyze the effects of the B and W ratios (defined in section 4.3.2). Three levels for each of these two types of ratios resulted in the L9 design of the experiment (Table 4.1). B10-W4, for example, denotes a B ratio of 10 and W ratio of 4. Crystallinity, particle size, mesopore volume, and external surface area values were determined for the particles produced using the nine different combinations of B and W. The signal-to-noise (S/N) ratio was calculated based on “the larger the better” for crystallinity, mesopore volume, and external surface area, whereas it was calculated based on “the smaller the better” for particle size [133].

Table 4.1: The Taguchi L9 design of the experiment

Sample	Ball-to-powder weight Ratio	Water-to-powder weight ratio
B10-W4	10	4
B10-W5	10	5
B10-W6	10	6
B20-W4	20	4
B20-W5	20	5
B20-W6	20	6
B30-W4	30	4
B30-W5	30	5
B30-W6	30	6

4.4 Results and Discussion

4.4.1 Particles Size Analysis

The effects of the relative weights of the balls and water on the volume-based distribution of sizes of the zeolite particles we produced are presented in Figure 4.1. The results suggested that the HEBM attritor effectively reduced the average size of the parent zeolite particles, with the milled particles having nanometer to submicron dimensions. Nanoparticles were observed in all of the milled samples, but their sizes differed for the different ball-to-powder weight ratio (B) and water-to-powder weight ratio (W) values used. Smaller particles tended to be produced when larger B values were used (Figures 1a-c). Using a relatively greater total weight of balls led to a higher contact frequency between the powder and the balls and resulted in the greater particles comminution.

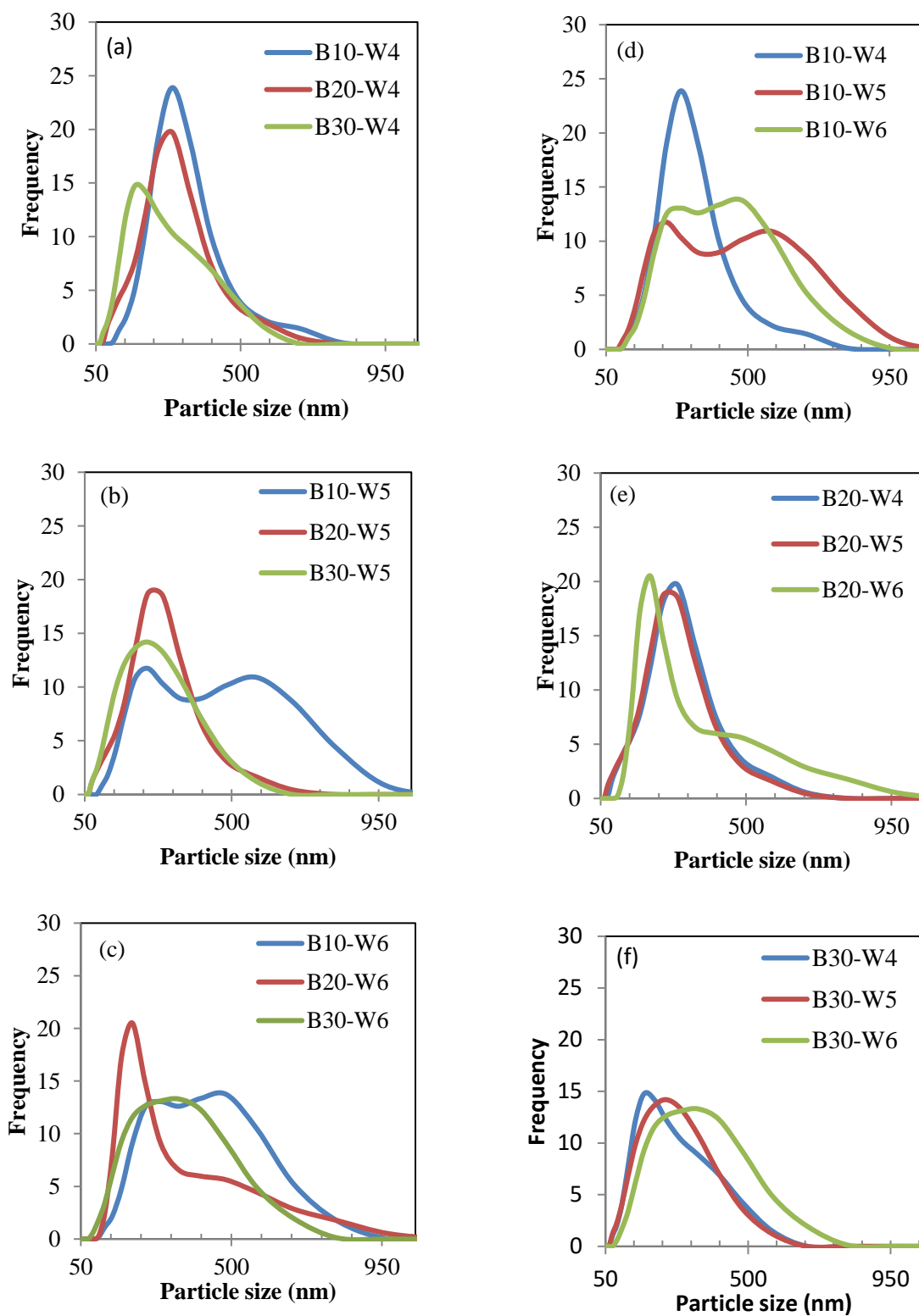


Figure 4.1: Effects of the relative weights of the balls and water on the particle size distribution by volume.

The effect of the relative amount of water used is presented in Figures 4.1d-f. Using less water led to a narrower particle size distribution (Figures 4.1d-f). The effect of the amount of water was more pronounced on the samples with a lower relative weight of balls. The distributions of the sizes of the B10-W5 and B10-W6 samples were found to be wider than that of B10-W4. The greater amount of water apparently dissolved the powder and increased the number of paths for the balls to have contact with the zeolite powder. As the result, the frequency of collisions between the balls likely decreased. A water-to-powder weight ratio (W) of 4, which was the lowest W tested, yielded the smallest particles and the narrowest size distribution.

The combination of a low relative total weight of balls and high relative weight of water, such as in the B10-W5 and B10-W6, resulted in a bimodal distribution, and in larger particles with a broader particle size distribution; whereas the combination of high relative total weight of balls and low relative weight of water led to smaller particles and a narrower size distribution. The smallest particle, less than 70 nm, was detected for the B30-W5 sample. The largest particle, at ca. 972 nm, was detected for the B10-W5 sample. The results showed that the concentrations of the ball and water components of the suspension controlled the comminution process.

The particle size distributions by number are shown in Figure 4.2. The particle size distribution by number obtained using DLS is important since it is comparable with the FE-SEM and TEM observations. In any collection of items, there tend to be more small particles than large particles. As shown in Figure 4.2 (and similar to the above-described results for particle size distribution by volume shown in Figure 4.1), use of the higher relative total weight of balls generally led to an especially greater number of small

particles: the DLS study revealed that 10 % of the particles (determined by number) had dimensions less than 100 nm in the B10 samples for the various water-to-powder weight ratios tested, whereas 50 % of the particles had dimensions less than 100 nm in the B20-W5, B30-W5, and B30-W4 samples. Note, however, that only 20 % and 10 % of the particles had dimensions less than 100 nm in the B30-W6 and B20-W6 samples, respectively, indicating that using more water appeared to have yielded larger particles.

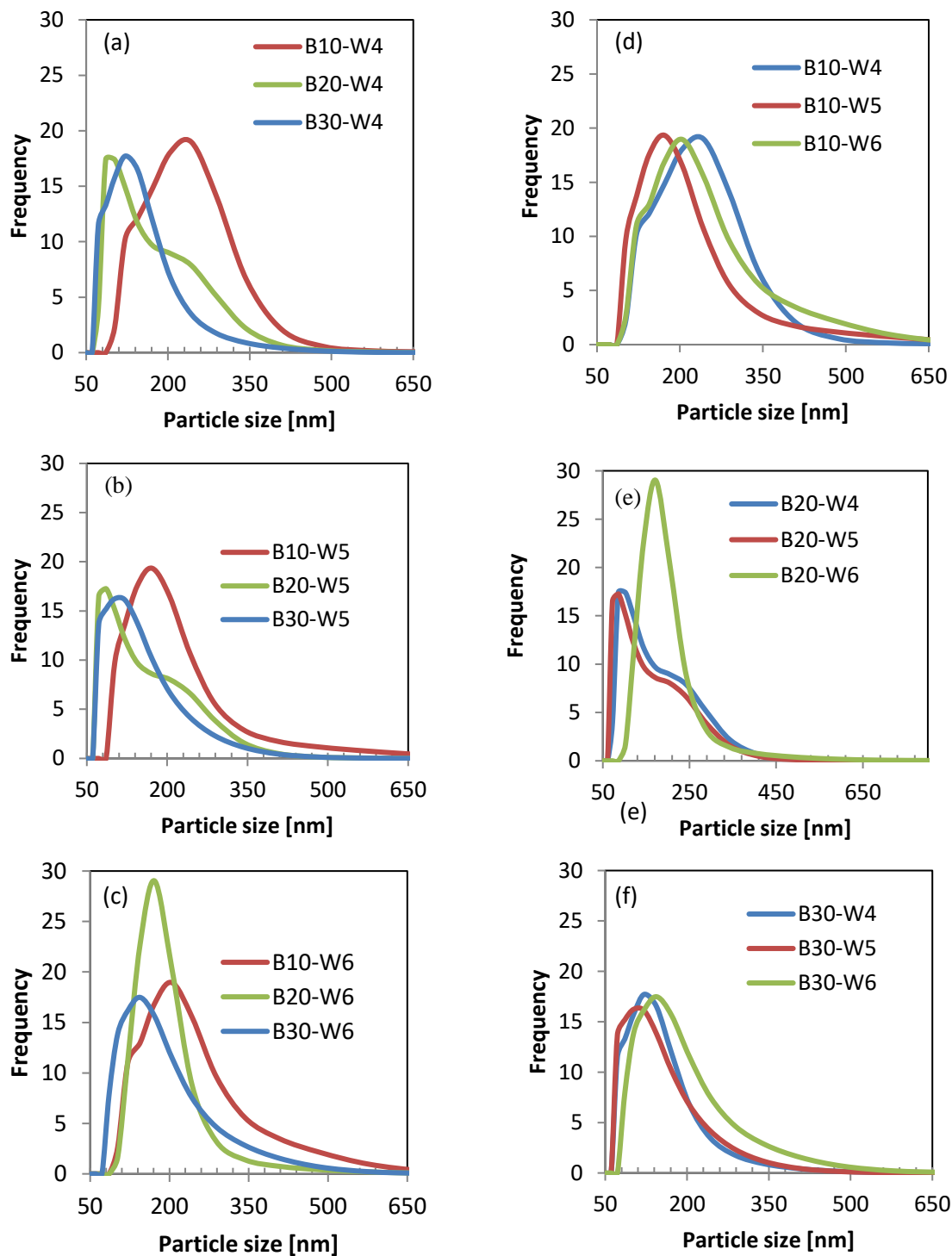


Figure 4.2: Effects of the relative weights of the balls and water on the particle size distribution by number.

We also evaluated the shapes and sizes of the milled and parent particles using SEM (Figure 4.3). The parent natural zeolite particles were observed to be large and have smooth external surfaces as shown in Figure 3a. The mordenite crystal shape was not clear, as the crystallites were very small (34 nm) and agglomerated to form larger particles. The particles resulting from milling (Figure 3b-j) showed more irregular shapes and were smaller than the parent particles. The milled particles also showed various sizes. Such irregularity in shape is in general important for providing intercrystalline mesoporosity. In the current work, the particles were observed to stack on each other and create voids; this formation was attributed to the shapes and tiny sizes of particles. It also can be seen clearly in the SEM figures that the particles produced using the lowest relative total weight of balls (i.e., the B10 samples) were bigger than the particles produced using the higher relative total weight of balls (i.e., the B20 and B30 samples), consistent with the results of the DLS study.

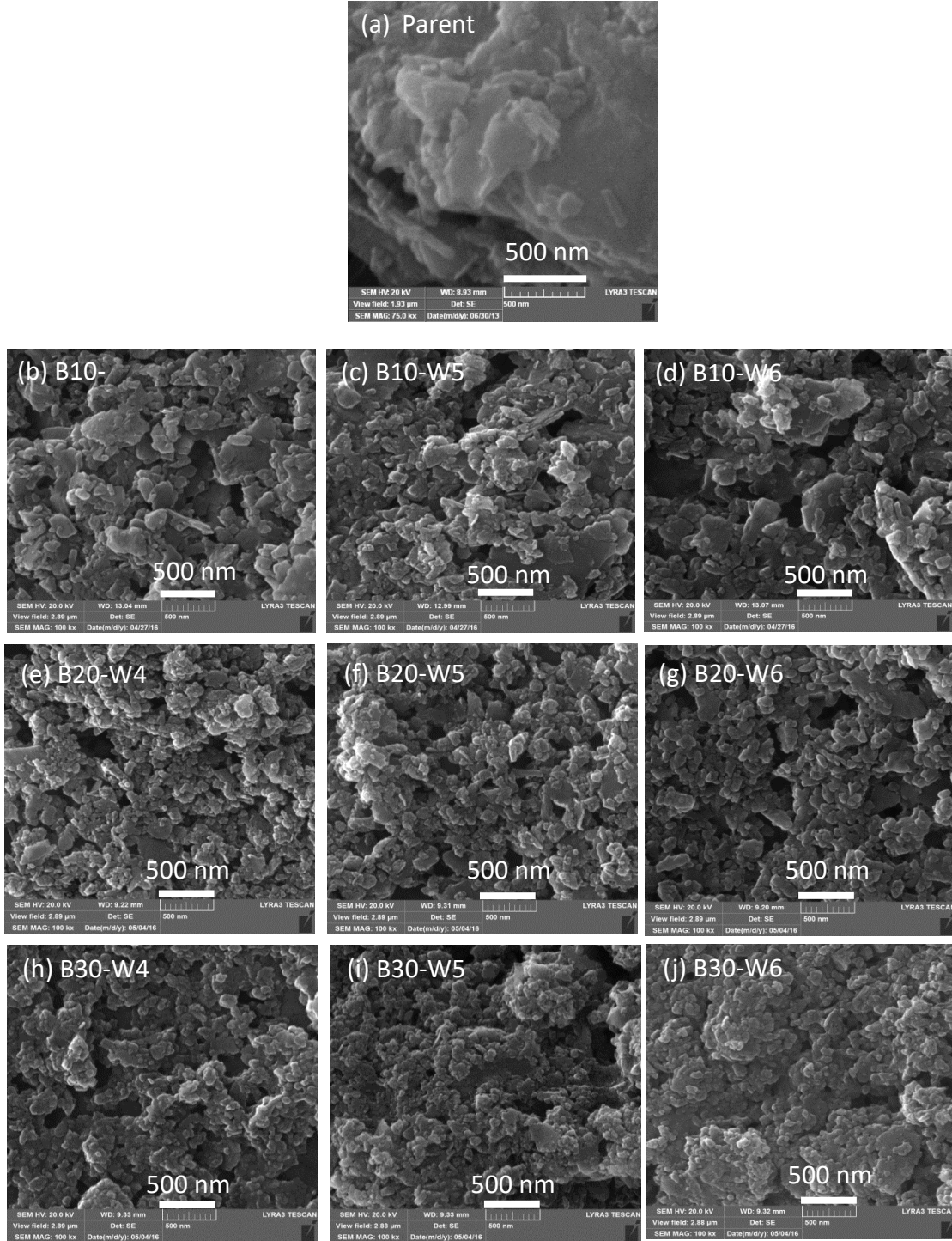


Figure 4.3: FE-SEM images of (a) the parent and the milled samples (b) B10-W4, (c) B10-W5, (d) B10-W6, (e) B20-W4, (f) B20-W5, (g) B20-W6, (h) B30-W4, (i) B30-W5 and (j) B30-W6.

Distributions of the sizes of the particles were also obtained from analyzing the SEM images in Figure 4.3, and the results were used to confirm the DLS technique. The sampling population consisted of 200 particles. The area of each particle was measured and converted into a diameter. Particle size distributions based on the SEM images are presented in Figure 4.4. Increasing the weight of the balls relative to the weight of the powder led to smaller particles. In contrast, changing the water-to-powder weight ratio did not significantly affect the particle size. In term of the qualitative comparison of the effects of the relative weight of balls and of water used, the size measurements using the SEM view field images were in agreement with the DLS results.

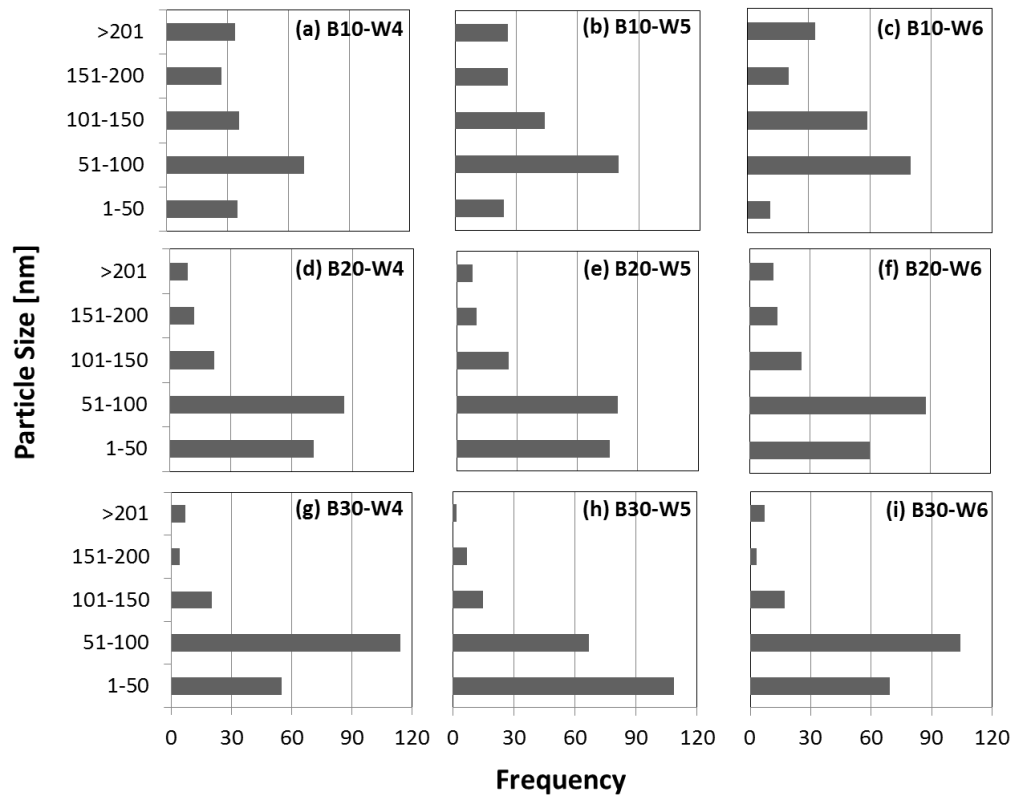


Figure 4.4: Particle sizes distribution based on the SEM images (a) B10-W4, (b) B10-W5, (c) B10-W6, (d) B20-W4, (e) B20-W5, (f) B20-W6, (g) B30-W4, (h) B30-W5, and (i) B30-W6.

A comparison of mean particle sizes determined from the SEM images and DLS data is presented in Table 4.2. The analysis of the DLS data resulted in larger calculated sizes for the particles than did the analysis of the SEM images. This difference may have been due to the agglomeration/aggregation of the nanosized particles. The light scattering technique measured the whole agglomerate or aggregate of particles instead of each individual particle. Strong interactions between submicron-sized particles promote agglomeration. The agglomerate of nanoparticles was noticed on the SEM images as shown in Figure 4.5. The agglomeration was also reported when using longer milling times: after a certain duration of milling, a continuation of the milling was indicated to result in larger rather than smaller particles due to the compacting of the fine powder [101].

Table 4.2: Mean of particle size by DLS -SEM images and crystallite size

Sample	Mean of Particle size $\pm \sigma$ Based on Volume DLS (nm)	Mean of Particle size $\pm \sigma$ Based on Number DLS (nm)	Mean of Particle size $\pm \sigma$ Based on Number SEM images (nm)	Crystallite size ** [nm]
Parent		100-300*		34
B10-W4	277 \pm 80	200 \pm 68	123 \pm 83	20
B10-W5	353 \pm 190	176 \pm 58	122 \pm 94	23
B10-W6	343 \pm 148	202 \pm 71	133 \pm 96	22
B20-W4	245 \pm 90	139 \pm 61	76 \pm 54	19
B20-W5	236 \pm 90	127 \pm 59	75 \pm 48	17
B20-W6	263 \pm 122	168 \pm 38	87 \pm 66	18
B30-W4	215 \pm 98	124 \pm 44	76 \pm 45	14
B30-W5	220 \pm 96	123 \pm 47	60 \pm 40	13
B30-W6	280 \pm 126	155 \pm 57	71 \pm 50	13

* In micron size using sieve mesh 100-300 micron

** Scherrer equation

The particle size distribution by volume is presented in Table 4.3. In order to study the effect of different milling conditions on particle size distribution quantitatively, the span of the particle size distribution was calculated using the equation

$$\text{Span} = \frac{d_{v0.9} - d_{v0.1}}{d_{v0.5}} \quad (4.1).$$

Here, 10, 50, and 90% (by volume) of particles have sizes less than $d_{v0.1}$, $d_{v0.5}$, and $d_{v0.9}$, respectively. A small span is a measure of a narrow particle size distribution. The particle size distributions of the various milled samples were found to be quite similar (Table 3). The two smallest mean particle sizes by volume were obtained for sample B30-W4, which showed a mean particle size of 215 nm and span of 1.3, and for B30-W5, which showed a mean particle size of 220 nm and span of 1.2. These span values were indicative of the narrow particle size distributions of our milled samples, and were smaller than the 2.4 span value reported for particles of natural zeolite produced using a planetary ball mill together with combining the dry and wet milling method [11] and the span value of 3 reported for particles of synthetic zeolite when using only the wet milling method for 8 h [12]. The results suggested HEBM to be effective at fabricating nanoparticles with a narrow distribution of sizes.

Table 4.3: Particle size distribution by volume.

Sample	D_{v0.1} (nm)	D_{v0.5} (nm)	D_{v0.9} (nm)	Mean by volume (nm)	Span
B10-W4	174	262	391	277	0.8
B10-W5	157	305	620	353	1.5
B10-W6	178	318	544	343	1.1
B20-W4	124	236	368	245	1.0
B20-W5	118	227	355	236	1.0
B20-W6	143	207	478	263	1.6
B30-W4	104	189	364	215	1.3
B30-W5	105	203	356	220	1.2
B30-W6	138	258	454	280	1.2

The mechanism by which the wet milling attritor operates is that the balls impact and shear the particles dispersed in the fluid [134]. Figure 4.5 shows a schematic of the milling attritor and its comminution of powder. The balls roll chaotically in various directions and exert shearing forces on the slurry. The liquid shearing and ball impact forces lead to reductions in the particle size and also create good dispersions [135]. The high kinetic energy of the stirrer transfers energy into the suspension and balls to create the impacting, rolling and sliding of the balls, and result in the grinding process.

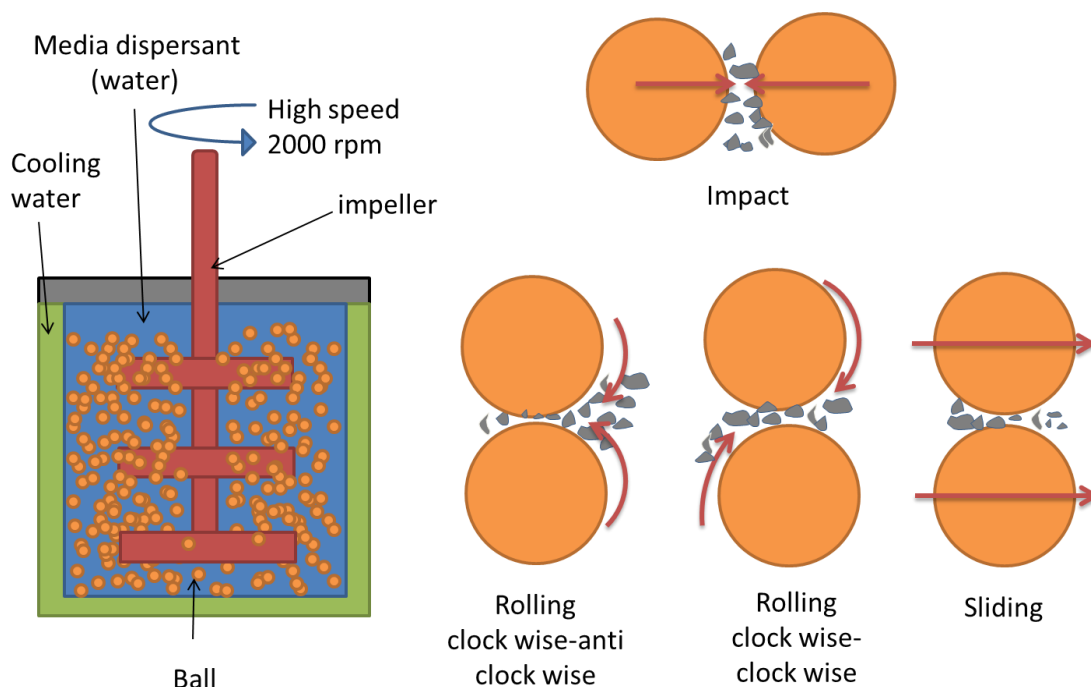


Figure 4.5: High-energy ball milling attritor set up and the mechanism by which it reduces particle size.

4.4.2 Crystallinity Study

XRD patterns revealed that the crystallinity levels of the milled samples were less than that of the parent zeolite (Figure 4.6). The peak intensities decreased gradually as the ball-to-powder weight ratio was increased. The water-to-powder weight ratio had less of an impact on the crystallinity of the milled samples. Amorphization of impurity phases such as quartz was faster than that of the major mordenite phase. Peaks at 2θ of 26.7° and 27.6° , corresponding to diffraction from quartz, were not observed in the XRD patterns of the milled samples. In contrast, peaks corresponding to the mordenite crystalline phase were observed in the XRD patterns of all of the milled samples. This result is in agreement with a previous report in which the grinding of natural mordenite for 6 h, even when using the dry ball milling method, yielded milled particles still showing the XRD peaks

corresponding to the mordenite phase [136]. In contrast, as reported elsewhere, the synthetic mordenite was completely transformed into the amorphous phase when using the dry method with planetary ball milling for 3 h [103]. It took a longer time to amorphize the natural zeolite, which was due to the presence of phase impurities in the natural zeolites [136].

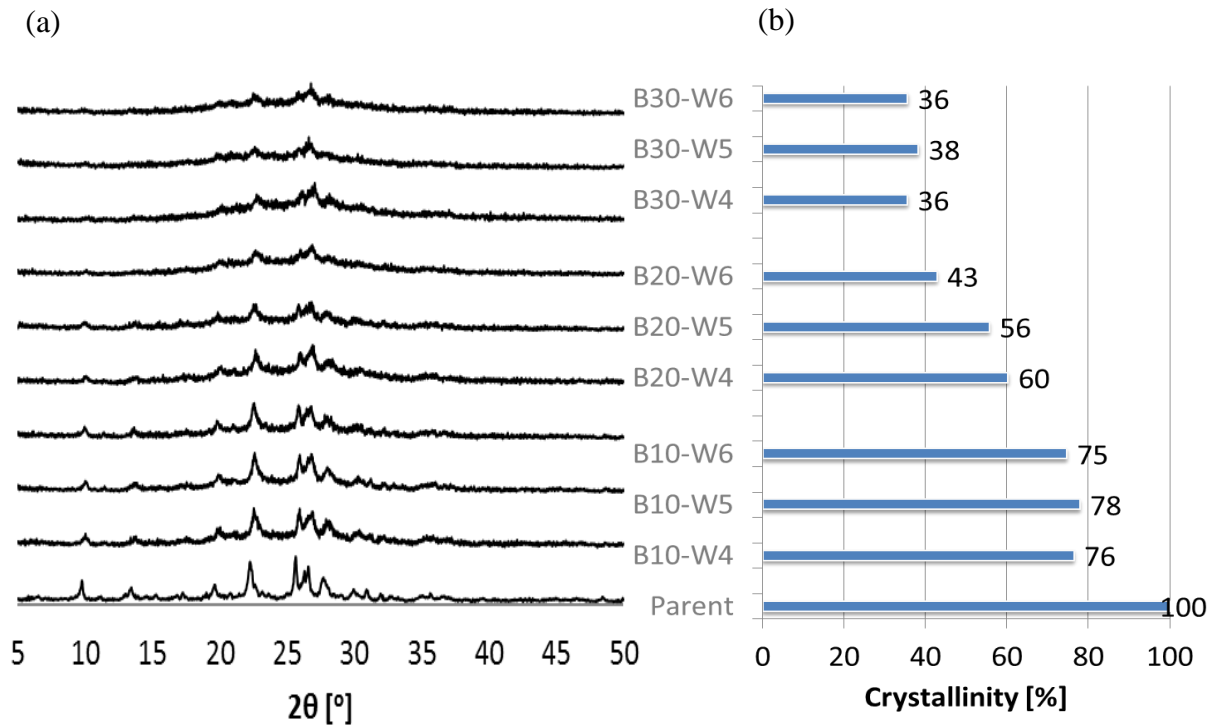


Figure 4.6: (a) XRD patterns and (b) relative crystallinity.

The crystallite size, which is an important parameter to study for the purpose of improving the milling procedure, can be calculated by applying the Scherrer equation [137]:

$$d = \frac{k\lambda}{\beta \cos\theta}$$

where d is the mean crystallite diameter, λ the X-ray wavelength, k is the Scherrer shape factor (0.9), $\beta_{1/2}$ is the full-width at half-maximum (FWHM) of the diffraction peak, and θ is the diffraction Bragg angle. The size of the parent crystal investigated was 34 nm, but the SEM and TEM images showed larger particles due to the agglomeration of tiny crystals. The crystallite size calculated using the Scherrer equation was found to decrease as the ball-to-powder weight ratio was increased, but was not significantly affected by the amount of water (Table 4.2). This trend was in agreement with the results of the DLS and SEM studies.

4.4.3 Textural Properties According to Nitrogen Physisorption

Milling was found to affect the textural properties of the particles, as discussed elsewhere [101]. The nitrogen isotherms of the milled samples and the parent zeolite are presented in Figure 4.7. Three aspects of the isotherms of the milled samples differed from those of the parent: the height of the curve in the low-pressure region, the gradient of the line in between the low- and high-pressure regions, and the height of the curve and the hysteresis shape in the high-pressure region. These isotherms suggested that the micropore volume, external surface area, and the mesopore volume were greatly affected by the HEBM attritor. The lower height of the curve in the low-pressure region of the milled samples was attributed to the micropore volumes of the milled samples being less than that of the parent. The greater slope of the line in between the low- and high-pressure regions of the milled samples corresponded to their greater external surface areas. The hysteresis in the isotherms of the milled samples was an indication of capillary condensation on the mesopore voids.

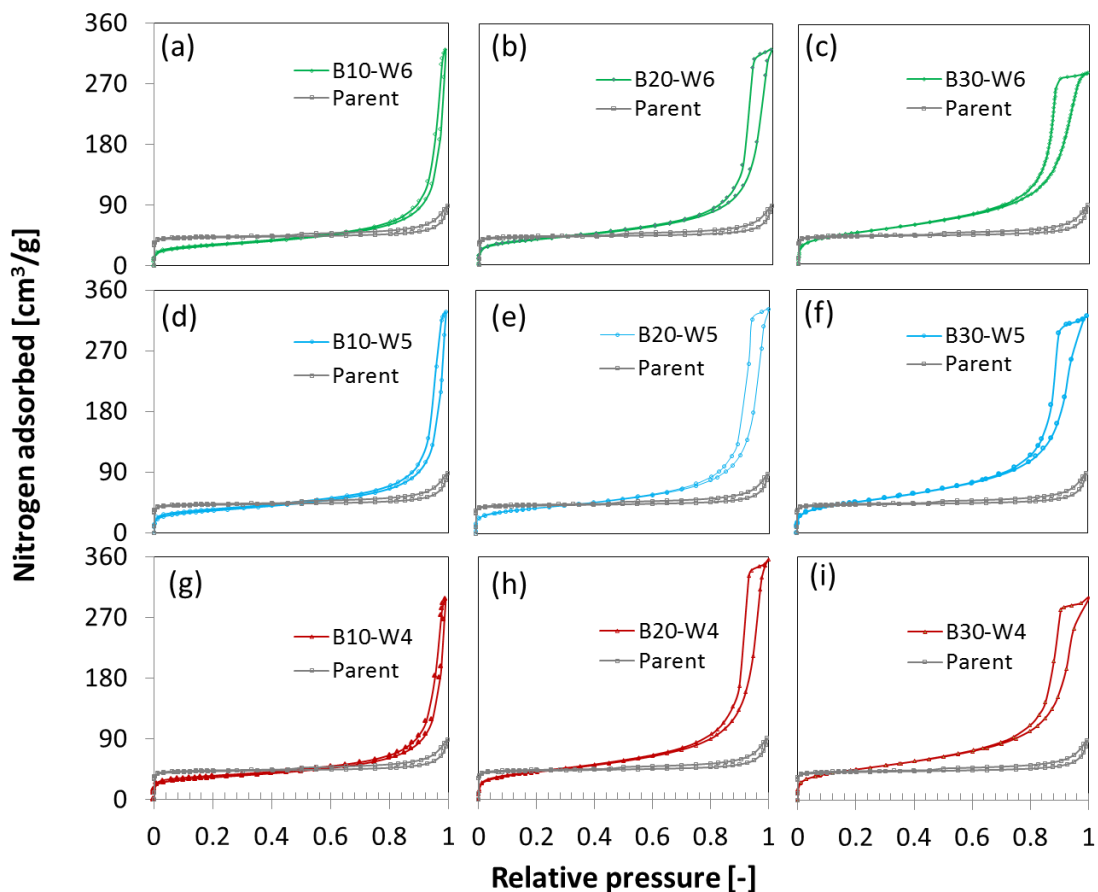


Figure 4.7: Nitrogen-isotherms of the milled samples and parent.

The B10 samples showed the smallest BET surface areas among the other milled samples and also lower than the parent (Table 4.5). The decreasing of the micropore area was higher than the increasing of external surface area hence the total BET surface area becomes lower compared with the parent. In contrast, the greater BET surface areas of the B20 and B30 samples than of the B10 samples were a result of the positive differences between the external surface areas of the B20 and B30 samples and those of the B10 samples being greater than the magnitude of the negative differences between micropore volumes of the B20 and B30 samples and those of the B10 samples. The high external surface areas of the

B20 and B30 samples were attributed to these samples having formed more nanosized particles.

Table 4.4: Textural properties of the as-received and milled natural zeolites.

Sample	S_{BET} (m^2g^{-1})	S_{t} (m^2g^{-1})	S_{ext} (m^2g^{-1})	V_{total} ($\text{cm}^3 \text{g}^{-1}$)	V_{micro} ($\text{cm}^3 \text{g}^{-1}$)	V_{meso} ($\text{cm}^3 \text{g}^{-1}$)
Parent	133	110	23	0.099	0.055	0.044
B10-W4	117	42	75	0.280	0.018	0.262
B10-W5	118	28	90	0.323	0.012	0.311
B10-W6	107	21	85	0.290	0.009	0.281
B20-W4	142	17	125	0.468	0.007	0.461
B20-W5	133	23	110	0.425	0.009	0.416
B20-W6	138	26	110	0.438	0.011	0.427
B30-W4	162	15	148	0.462	0.006	0.456
B30-W5	163	12	150	0.488	0.005	0.483
B30-W6	164	11	154	0.430	0.006	0.424

The mesopore size distributions are presented in Figure 4.8. The different samples only showed slight differences in the volumes of mesopores with widths between 2 nm and 12 nm. On the other hand, those samples with different ball-to-powder weight ratios showed large differences in the volumes of mesopores with widths between 12 nm and 42 nm. As the ball-to-powder weight ratio was increased, the mesopore volume increased (Figures 4.8a-c). The water-to-powder weight ratio had little effect on the mesopore volume (Figure 4.8d-f). Some of the mesopores formed after milling resulted from the formation of intercrystalline mesopores due to the particles having been reduced to the nanometer level.

The presence of intercrystalline mesopores in the milled B30-W5 sample was confirmed by TEM images of this sample (Figure 4.9). Intercrystalline mesopores are defined as the networks of voids in the space between nanosized crystals [138]. In the current work, nanosized particles with dimensions between 20 nm and 40 nm were observed to agglomerate, and to create intercrystalline mesopore voids (Figures 4.9b-c), with one such mesopore measured to span about 10 nm (Figure 4.9d), which was in agreement with the mesopore size distribution indicated by the NLDFT model.

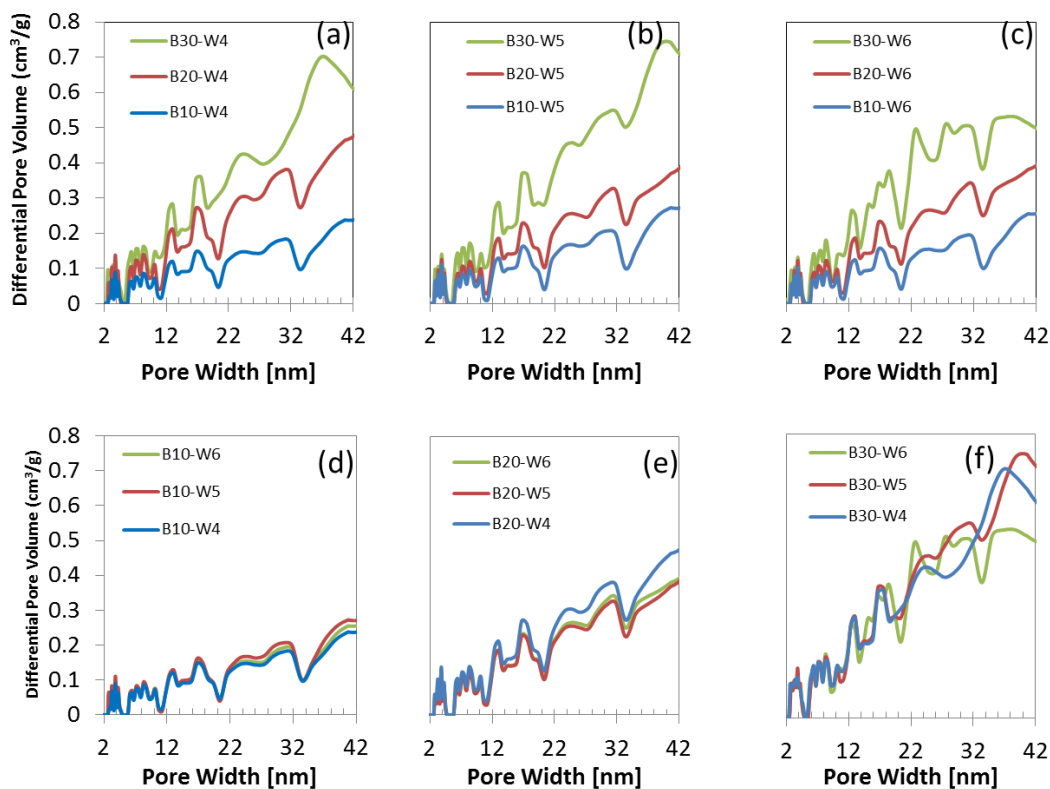


Figure 4.8: Mesopore size distribution of the milled samples.

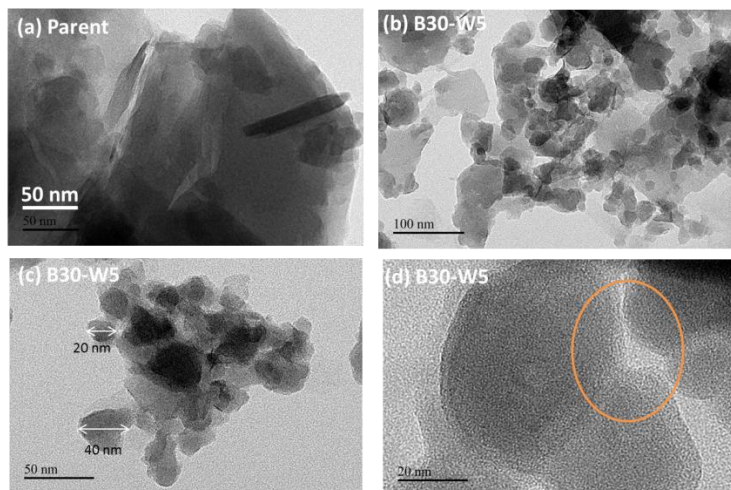


Figure 4.9: TEM images of the parent and the milled sample (B30-W5).

The high mesopore volume and external surface area levels of the HEBM-obtained zeolites were due to the use of the water as a dispersant medium. Mordenite has two types of channels: one consisting of large ($6.7 \times 7.0 \text{ \AA}$) 12-membered rings and the other consisting of small ($3.4 \times 4.8 \text{ \AA}$) 8-membered rings. A molecule of water is relatively small, with its longest dimension being about 2.8 \AA , and could thus easily enter the pores of mordenite. This process may have promoted a deterioration of the micropore channels. Intercrystalline mesopore with smaller volumes were created when a greater water-to-powder weight ratio was used in the milling process. This result may have been due to a reduction in the strength and number of interactions between the balls and the powder. Another possibility is that the amount of kinetic energy transferred from the propeller to the ball and powder was less when there was a greater relative amount of water.

4.4.4 Taguchi Analysis

The signal-to-noise (S/N) ratios of various measures (responses) of the milled zeolite samples are shown in Figure 4.10. The “larger the better” approach was used for the

calculation and interpretation of the S/N ratios of the crystallinity, mesopore volume and external surface area levels; here a greater S/N ratio corresponds to a higher value of the measure. On the other hand, the “smaller the better” technique was used for particle size; here, a greater S/N ratio corresponds to a smaller particle. The ball-to-powder weight ratio had a more significant effect on each of these four measures than did the water-to-powder weight ratio. The high effect of the ball-to-powder weight ratio was even more pronounced on the crystallinity and external surface area response, which each showed a linear relationship between the mean S/N ratio and the relative weight of the balls. The water-to-powder weight ratio showed little effect on the response, particularly for crystallinity, mesopore and external surface area.

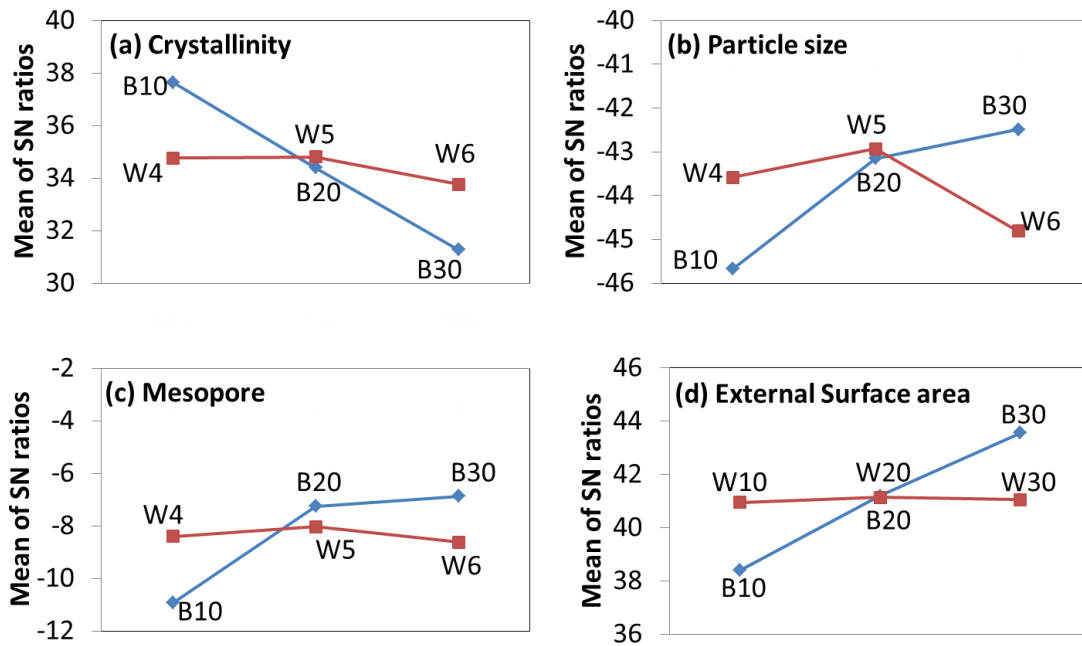


Figure 4.10: Mean S/N ratios of the ball-to-powder weight ratio and water-to-powder weight ratio (a) crystallinity, (b) particle size, (c) mesopore volume, and (d) external surface area.

The delta value is the difference between the maximum mean S/N ratio and the minimum mean S/N ratio for a given response (measure) [133]. A plot of delta values, which was constructed to indicate the significant effect of factors evaluated on the responses, is presented in Figure 4.11. This plot showed that the delta value of the ball-to-powder weight ratio was greater than that of the water-to-powder weight ratio for each of the four measures. The response parameters affected by ball-to-powder weight ratio from the largest to smallest were crystallinity > external surface area > mesopore volume > particle size. The response parameters affected by the water-to-powder weight ratio from the largest to smallest were particle size > crystallinity > mesopore volume > external surface area.

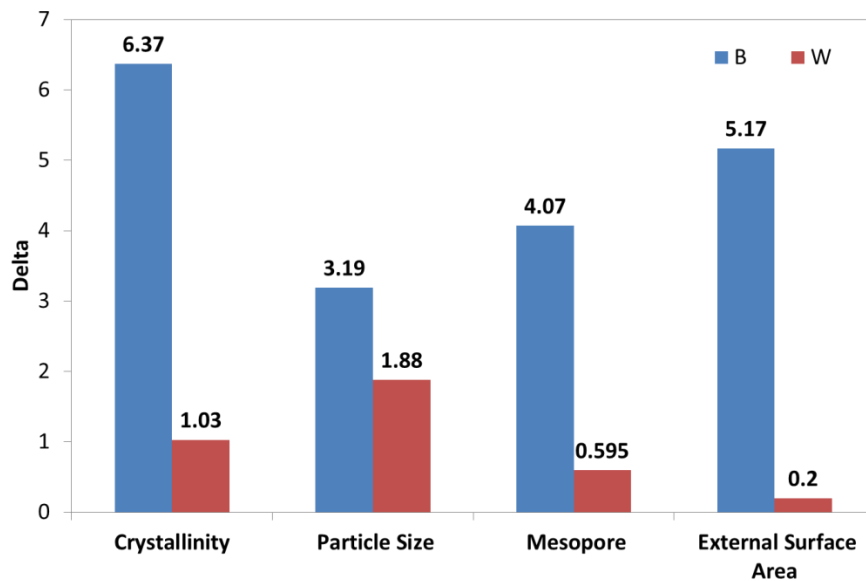


Figure 4.11: Taguchi delta plot of the effect ball-to-powder weight ratio and water-to-powder weight ratio on crystallinity, particle size, mesopore volume, and external surface area.

4.4.5 Hydrothermal Recrystallization

The crystallinity levels of the recrystallized samples were higher than those of the corresponding milled samples and of the parent, as indicated by their XRD patterns (Figure 4.12). In fact, the peak intensity of the XRD pattern of recrystallized B30-W5 (R-B30-W5) was double that of the parent XRD pattern and slightly greater than that of the R-B10-W4 XRD pattern. There appeared to be more quartz in R-B10-W4 than in R-B30-W5, as indicated by the intensities of the peaks at $2\theta = 21^\circ$ and 26.7° . The extents of amorphization of the zeolites and quartz were severe when a high ball-to-powder weight ratio was used, as indicated according to the XRD pattern of B30-W5. The recrystallization of the highly amorphous B30-W5 milled sample appeared to have favored the growth of the mordenite crystal instead of quartz when the recrystallization was carried out in a basic silicate solution at 170°C for 6 h. This preference was probably caused by the amorphous phase having been more reactive in the alkaline silicate solution during the hydrothermal mordenite recrystallization. The particle size of the recrystallized sample appeared to have depended on the particle size of the original sample. R-B30-W5 was found to consist of more smaller particles than was R-B10-W4 (Figure 4.13), with this result attributed to the smaller size of the particles of the corresponding milled sample (B30-W5) (Figure 3i). Selecting appropriate HEBM parameters is the first crucial step to control the particle size of mordenite. The recrystallized sample tended to consist of relatively more of the larger particles due to the growth of mordenite crystals. The non-amorphous MOR in the milled sample acted as a seed in the hydrothermal recrystallization [61]. It can be concluded that the HEBM provided the nanoparticle feedstock and reduced the impurities for the next step, which was the hydrothermal recrystallization.

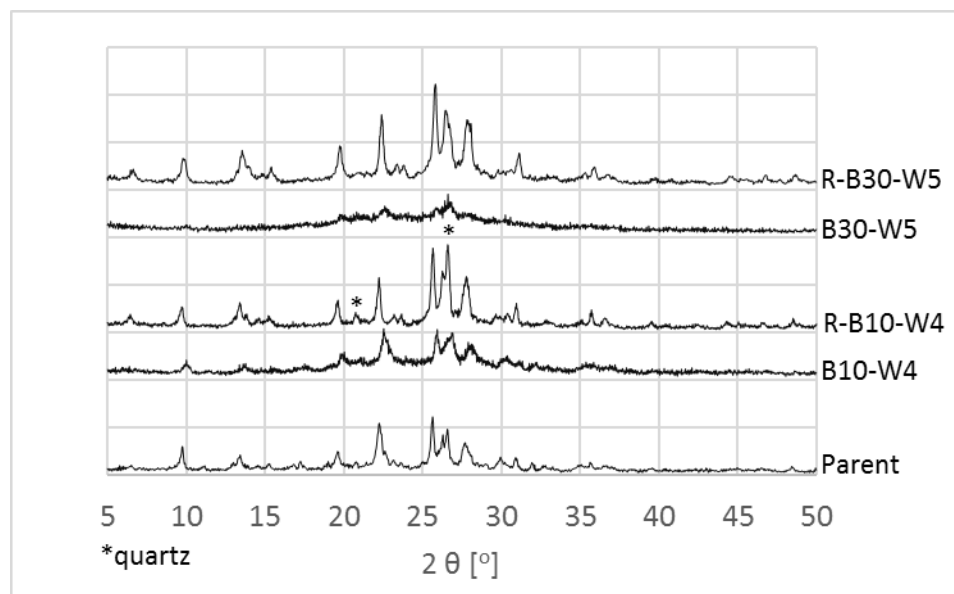


Figure 4.12: Effect of hydrothermal recrystallization on the crystallinity of MOR.

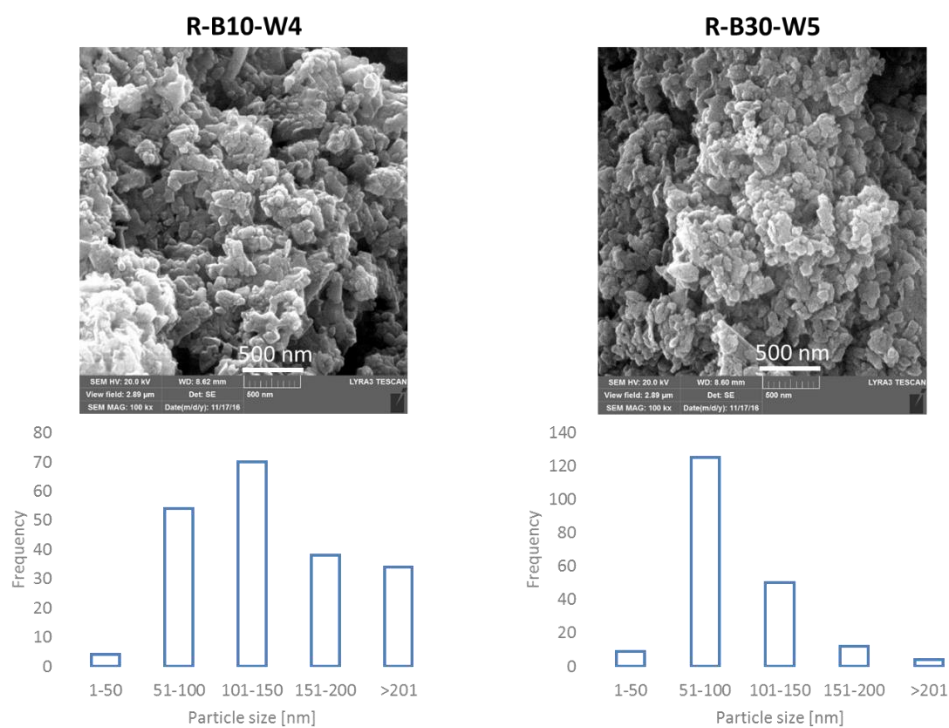


Figure 4.13: Effect of hydrothermal recrystallization on the particle size of MOR.

4.5 Concluding Remarks

A high-energy ball milling attritor was successfully used to fabricate nanosized to submicron-sized particles from natural mordenite with water used as a dispersant. The dimensions of the milled particles ranged from 70 nm to 580 nm with 10% of the sample volume ($d_{v0.1}$) having particles with dimensions less than 100 nm and the 50% of the sample number ($d_{n0.5}$) having particles with dimensions less than 100 nm. The mean particle size by volume for B30-W5 was 220 nm and the span was 1.2. The Taguchi analysis showed that the increasing ball-to-powder weight ratio resulted in a decrease in particle size and increase in external surface, mesopore volume, and crystallinity. Moreover, changing the ball-to-powder weight ratio had a greater effect on these measures than did changing the water-to-powder weight ratio. The hydrothermal recrystallization succeeded in recovering the crystallinity of mordenite nanoparticles.

CHAPTER 5

MECHANOCHEMICAL ROUTE AND RECRYSTALLIZATION STRATEGY TO FABRICATE MORDENITE NANOPARTICLES FROM NATURAL ZEOLITES

5.1 Summary

For the first time, we fabricated hierarchical mordenite nanoparticles from low-cost natural zeolites through high-energy ball milling followed by recrystallization strategy. The analysis of the as-received natural zeolites revealed that it is comprised of mordenite (MOR) as the main phase and clinoptilolite (HEU) as the impurities phase. The natural zeolites samples were milled by a high-energy ball milling attritor to obtain nano-zeolites within the size of 20-160 nm, which were confirmed by field emission scanning microscopy and transmission electron microscopy analysis. The X-ray diffraction study revealed that crystallinity of the milled nano-zeolite has decreased significantly. The high crystallinity of nanosized MOR with less phase HEU impurities was recovered after recrystallization of the milled sample in the hydrothermal basic silicate solution. The nitrogen physisorption study showed that the textural properties of recrystallized nano-mordenite were improved with enhancements in the external surface area at 6-fold of the parent. The hierarchical pore system was observed on the recrystallized MOR as the intercrystalline mesopore volume increased to 0.36 cm³/g from only 0.04 cm³/g in the as-received natural zeolites. Recrystallization time, the ratio of the milled sample weight to the solution, silica, and the silica OH⁻ concentration were varied to study the effect on the crystallinity of the recrystallized MOR sample. The developed technique has the potential

to be applied as an efficient method to prepare better natural mordenite properties for the industrial application.

5.2 Introduction

Low-grade natural zeolites are abundantly available inexpensively throughout the world. However, natural zeolites are mostly found in several crystalline phases accompanied by the nonreacted volcanic glass, K-feldspar, quartz, calcite, montmorillonite, calcium sulfate dihydrate, and cristobalite [33]. Natural zeolites even in the same sediment location can vary in composition and crystalline phases due to the mineralogical dissimilarity of the mother volcanic tuff and different mechanism of zeolites formation [5]. The presence of impurities and heterogeneity in composition of natural zeolites are the main issues of limited utilization in industrial application particularly for catalysis applications [1, 5].

Researchers made several attempts to upgrade natural zeolites for broader industrial exploitation. Natural clinoptilolite with accessories like feldspar, smectite, vermiculite, and quartz has been successfully converted to a high cation-exchanged capacity (CEC) zeolite Na-P through sodium hydroxide hydrothermal treatment; however, the impurities were difficult to be transformed [7]. Fusion of sodium hydroxide powder through natural clinoptilolite which contains quartz and feldspar as traces, followed by hydrothermal treatment, effectively dissolved the clinoptilolite and impurities to be transformed to high CEC zeolites such as Na-P, Na-X, hydroxysodalite [8], and zeolite Na-Y [9]. Natural mordenite and clinoptilolite with impurities quartz, feldspar, silicate were successfully converted to zeolite phillipsite by extending the alkali hydrothermal treatment for 7 days [10].

The nanosized zeolites have some advantageous such as high external surface area and low diffusion limitation. The hierarchical pore system will form in the nanosized zeolites as the voids created among the nanoparticles which are important to facilitate the fast molecules diffusion [139]. The top-down approach is the most appropriate way to obtain the nanosized zeolites from natural zeolites as the zeolites framework with large crystal size has already been synthesized in nature. Dry ball milling of natural zeolites effectively reduces the particle size; however, this causes the loss of zeolite crystallinity [103]. Wet ball milling conditions have been investigated in order to effectively achieve particle and minimize crystallinity destruction [11]. Wet ball milling of zeolite HY was reported to provide higher crystallinity compared with dry ball milling. However, the decreased of the zeolites crystallinity after the wet milling was inevitable [12]. Recently, the top-down method combined with recrystallization has been developed to attain nanosized zeolites with a highly crystalline zeolite by Wakihara et al. who prepared nanosized H-ZSM-5 [109], zeolite A [20], and zeolite X[140]. Another research study on the ball milling-recrystallization method has successfully attained nanoparticles of SAPO-34 with improved physicochemical properties for methanol to olefin application [15].

The ball-milling recrystallization method is potentially applicable for natural zeolite preparation in order to obtain nanoparticles zeolites. In this manuscript, we fabricated nanoparticles mordenite with a hierarchical pore system and high purity crystalline MOR from low-cost natural zeolites by a top-down approach using ball milling and a hydrothermal recrystallization technique.

5.3 Experimental

5.3.1 Material Characterization

The crystalline phase was identified by X-ray diffraction (XRD, Miniflex-Rigaku) using Cu K-alpha with angle 2θ from 5° to 50° . Scanning rate was $3^\circ/\text{min}$ with a step size 0.03° . Crystallinity degrees of milled and recrystallized mordenite were calculated by main peak relative intensities of crystalline mordenite for parent and treated zeolite as follows.

$$\text{crystallinity} = \frac{\text{Summation of the treated samples main peak areas at } 2\theta (5^\circ - 35^\circ)}{\text{Summation of the parent sample main peak areas at } 2\theta (5^\circ - 35^\circ)}$$

Morphology and particle sizes of samples were examined by field-emission scanning electron microscopy (FE-SEM, LYRA 3 Dual Beam, Tescan) and transmission electron microscopy (TEM, JEOL-JEM-2100F). Nitrogen physisorption was carried out in ASAP 2020 (Micromeritics). Prior to adsorption, the samples were heated up to 350°C and dwelled for 6 h. The liquid nitrogen was used to maintain the temperature of sample tube at 77 K during the nitrogen gas adsorption-desorption. The volume of micropore, surface area, and the external surface area were estimated by the t-plot method. Total pore volume was computed at relative pressure $(P/P_0) = 0.98$. Pore size distribution was estimated by the density functional theory (DFT) method. The Nicolet 6700 spectrometer was used for the Fourier transform infrared (FTIR) study. The samples were prepared by mixing the powder of samples with KBr to be pelletized. The parameters of resolution 8 cm^{-1} in the range wavenumbers of $400\text{--}4000\text{ cm}^{-1}$ and 100 scans were applied during the analysis.

5.3.2 Ball-Milling

The ball milling attritor (Union Process HDDM-01) was used to reduce the particle size by wet milling method using water as a dispersion medium. Prior to the milling, samples were grounded and sieved to obtain the powder between 100 to 300 μm in size. A total of 50 g of natural zeolites was milled in 250 mL distilled water by controlling the agitator speed at 3000 rpm for 8 h. The ball material was made of zirconia with fine individual ball size of 650 μm in diameter and a total weight of 1.5 kg. The heat generated from the milling process was removed by circulating cold water at 13 $^{\circ}\text{C}$ through the jacket of the milling tank.

5.3.3 Recrystallization

The milled sample was recrystallized by using sodium silicate solution with a ratio of $x \text{ SiO}_2 / y \text{ NaOH} / 780 \text{ H}_2\text{O}$. The fumed silica (Sigma-Aldrich) was varied with a molar ratio $x = 3, 9, 12$, and 18. The sodium hydroxide (Applichem) was studied over a molar ratio $y = 6, 12, 18$. The ratio between the milled natural zeolites and the gel solution was $z : 50$ (wt./wt.) with z was 1, 2, and 5. The mixture solution was heated at fixed temperature 170 $^{\circ}\text{C}$ for a different period of time 2, 8, 24, and 48 h using an autoclave (Parr Inc.). The solid was separated from the solution by centrifuge and washed several times with deionized water. Afterward, the wet solid was dried in the oven at 110 $^{\circ}\text{C}$ overnight.

5.4 Results and Discussion

Natural zeolites rarely exist in a pure crystalline phase. The crystalline phases of natural zeolites were observed by XRD in which three phases, i.e., mordenite (card no: 00-011-0155), clinoptilolite (card no: 01-079-1462), and quartz (card no: 01-077-3162) have been identified (Figure 5.1). Mordenite was confirmed as the major phase, which has often been

found as the main phase in many locations in Java, Indonesia [141, 142]. The Klaten zeolite occurs mainly in calcium-MOR followed by potassium-MOR form as shown on the XRF analysis result (Table 5.1). The silicon to aluminum ratio was low at ca. 6. There were also some metal impurities detected by XRF such as iron, phosphorus, and titanium. The XRF and XRD studies suggested that the natural zeolites have some metal impurities and are categorized as a nonsingle crystalline phase.

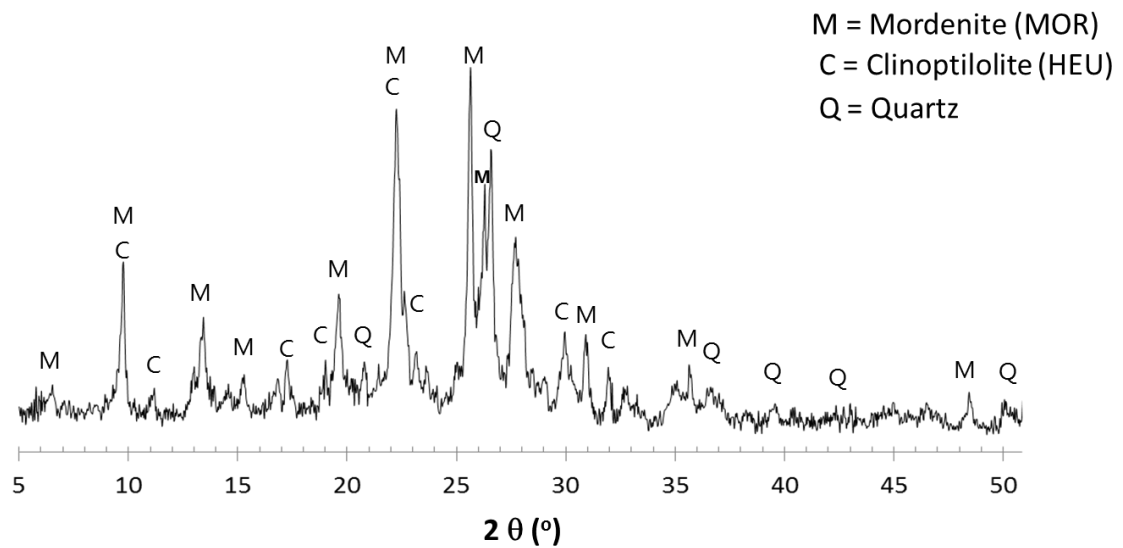


Figure 5.1: XRD pattern of the as-received natural zeolites from Klaten, Indonesia.

Table 5.1: XRF analysis of the as-received of low-rank natural mordenite.

Element	Parent (wt. %)
Al	3.5
Si	20.7
P	0.3
K	0.8
Ca	2.5
Ti	0.2
Fe	1.4
Si/Al	6

5.4.1 Ball Milling Effect on the Crystallinity of Natural Zeolites

The XRD study showed that the milling decreased the crystallinity of the natural zeolites significantly. The relative crystallinity of the milled zeolites was calculated to be ca. 65% of the parent crystallinity. Amorphization of the impurities phases like clinoptilolite and quartz were faster than the major phase mordenite. It can be seen in the XRD pattern of the milled samples that clinoptilolite and quartz no longer exist. On the other hand, the main phase MOR was still observed as indicated by the XRD peaks of 2θ 22.2° and 26.4°. The loss of crystallinity was due to the external breakage bonding Si-O-Si and Si-O-Al bonds as reported elsewhere [103]. Recently, a report suggested that from Raman analysis the ball milling resulted in the distorted crystal structure to form various T-O-T angle [143]. The ^{27}Al NMR analysis of the milled sample showed that the extraframework aluminum was not detected, however, the peak intensity was broader and lower as compared with the parent (Figure 5.2). The ^{27}Al NMR result confirmed that the ball milling distorted the aluminum tetrahedral structure in the framework.

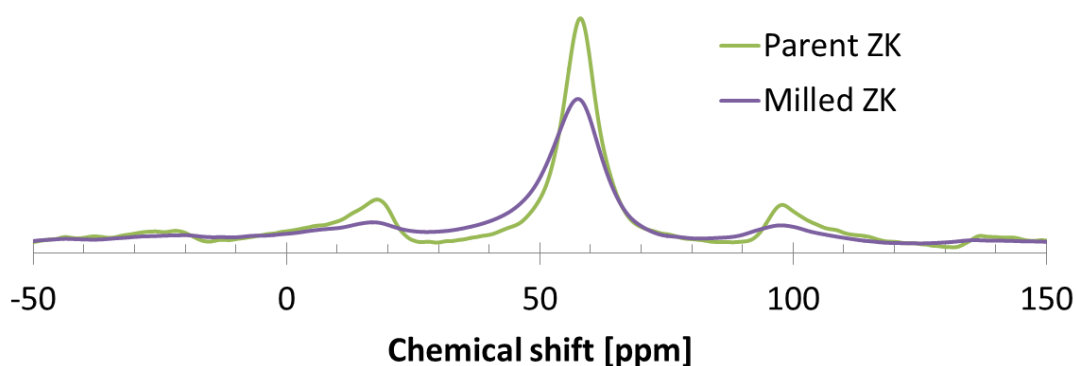


Figure 5.2: ^{27}Al NMR of the parent and milled samples.

5.4.2 Effect of Silica and NaOH Concentration on Mordenite

Recrystallization

Silica concentration effect on the crystallinity of samples is presented in Figure 5.3. The low concentration of silica (Si-3) yielded only 0.6 g of recrystallized sample from 1 g of the milled sample introduced into the basic silicate solution. The XRD peaks were attributed to the analcime and zeolite P phase. The MOR phase was not detected in the low silica concentration solution. It was probably the silica in the amorphous phase, and MOR crystalline parts were dissolved in the sodium low silicate concentration. The amorphous phase was easily dissolved in the solution followed by the MOR nanoparts seeds. Afterward, the components in the gel solution with a low silica to alumina ratio built a more favorable framework at the hydrothermal conditions applied, which was analcime and zeolite P. The MOR phase was favored to form as the silica ratio increased to 18. Sample weight of the recrystallized MOR obtained was 1.2 g, which indicated there was a growth of mordenite from the silica introduced to the solution.

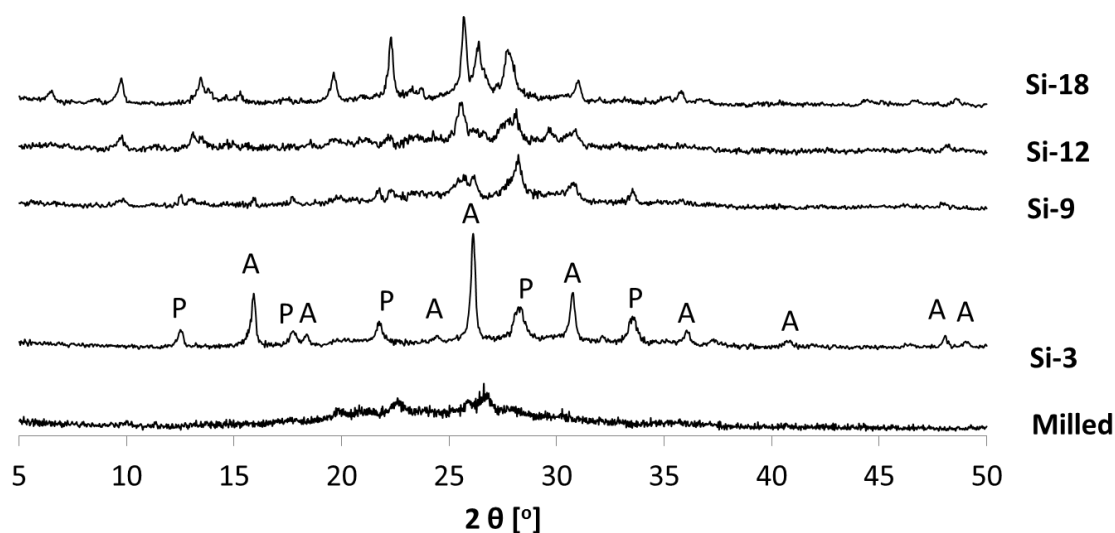


Figure 5.3: The effect of different concentrations of silica on the crystalline phase of the recrystallized MOR (x SiO₂ : 12 NaOH : 780 H₂O).

The OH⁻ has a role as a mineralizer to transport the silica. The higher concentration of OH⁻ the more solubility of silica in the solution. The high alkalinity (OH⁻ 18) resulted in the high dissolution of the milled MOR. As the result, the crystallinity of MOR phase was low at a high alkaline solution (OH⁻18) (Figure 5.4). In contrast, the moderate OH⁻ concentration favored the high crystallinity of the MOR phase. The function of the OH⁻ here is to maintained the silica on the saturation condition and hence prevent the further dissolution of silica in the milled sample.

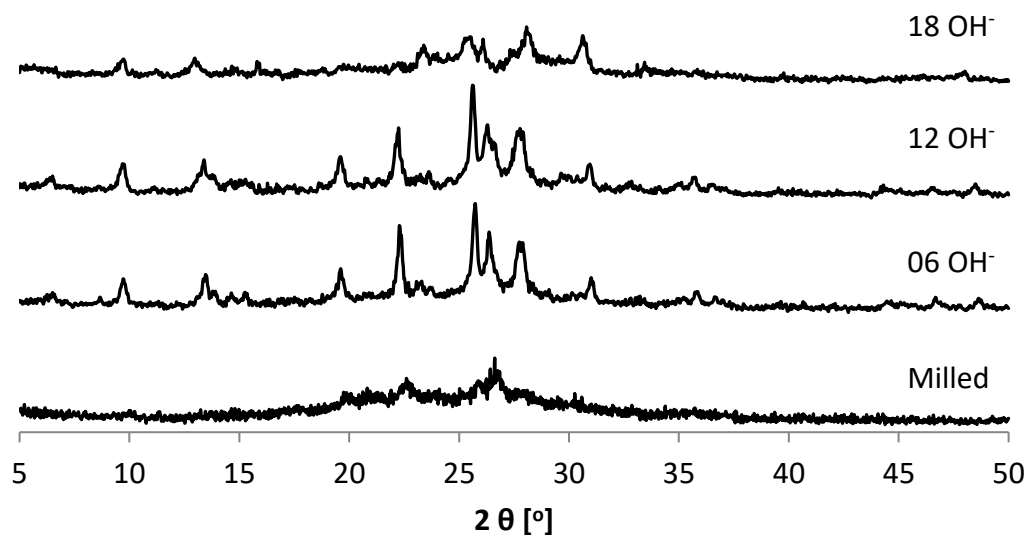


Figure 5.4: The different NaOH concentrations effect on the crystallinity of the recrystallized MOR (18 SiO₂ : y NaOH : 780 H₂O).

The effect of silica and OH⁻ were vital in the MOR phase recrystallization as presented in Table 5.2. The MOR phase was obtained within the range of OH⁻/SiO₂ from 0.3 to 1.3 with the high crystalline MOR attained over the range from 0.3 to 0.7. The highest OH⁻/SiO₂ at 4 resulted in the growth of analcime and the zeolite P. The lowest OH⁻/SiO₂ at 0.2 failed to obtain the crystalline phase.

Table 5.2: The effect of silica and OH⁻ molar ratio in the mordenite recrystallization

Sample no.	SiO ₂ (x)	NaOH (y)	OH ⁻ /SiO ₂	Phase	Crystallinity
1	3	12	4.0	Analcime + Zeolite-P	High
2	9	12	1.3	MOR	Low
3	12	12	1.0	MOR	Low
4	18	12	0.7	MOR	High
5	18	6	0.3	MOR	High
6	18	18	1.0	MOR	Low
7	24	4	0.2	Amorphous	Non-crystalline

5.4.3 Effect of Hydrothermal Time on Mordenite Recrystallization

The shortest time for recrystallization to pure mordenite was observed after only 2 h of hydrothermal treatment. We obtained the relatively short time of recrystallization as compared with the synthetic MOR, which required longer hydrothermal treatment ca. 48 h. The fast recrystallization time was due to the nanoparts acting as seeds and the dissolution materials growth on the surface of the seed. The pure mordenite phase was still obtained until 6 h of hydrothermal treatment. The impurity appeared as the time of hydrothermal treatment was prolonged to 24 and 48 h (Figure 5.5). The impurities phase on the XRD patterns was attributed to the quartz as indicated at 2θ 21° and 26.7° . From the literature, the longer time of hydrothermal treatment in the nanocrystal MOR synthesis resulted in the larger crystal size [144].

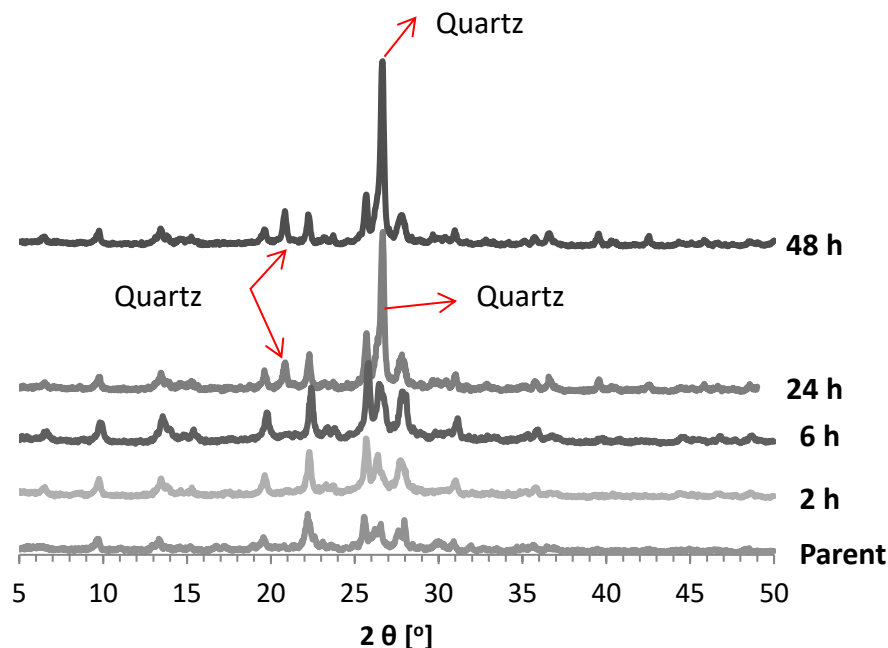


Figure 5.5: The effect of hydrothermal time (2 to 48 h) on the crystalline phase of the recrystallized MOR ($18\text{SiO}_2/12\text{NaOH}/780\text{ H}_2\text{O}$).

5.4.4 Effect of the Ratio of the Mass Sample to Solution on Mordenite Recrystallization

Effect of sample weight is presented in Figure 5.6. The high loading of sample weight (10%-wt) led to decrease in the crystallinity of the recrystallized sample as compared with the low percentage of sample weight (< 4%-wt). This is probably due to some of the amorphous dissolved in the solution during the hydrothermal treatment. Hence, as the more sample loading introduced to the solution the higher silica concentration in the solution that changes the optimum condition to recrystallize the MOR phase.

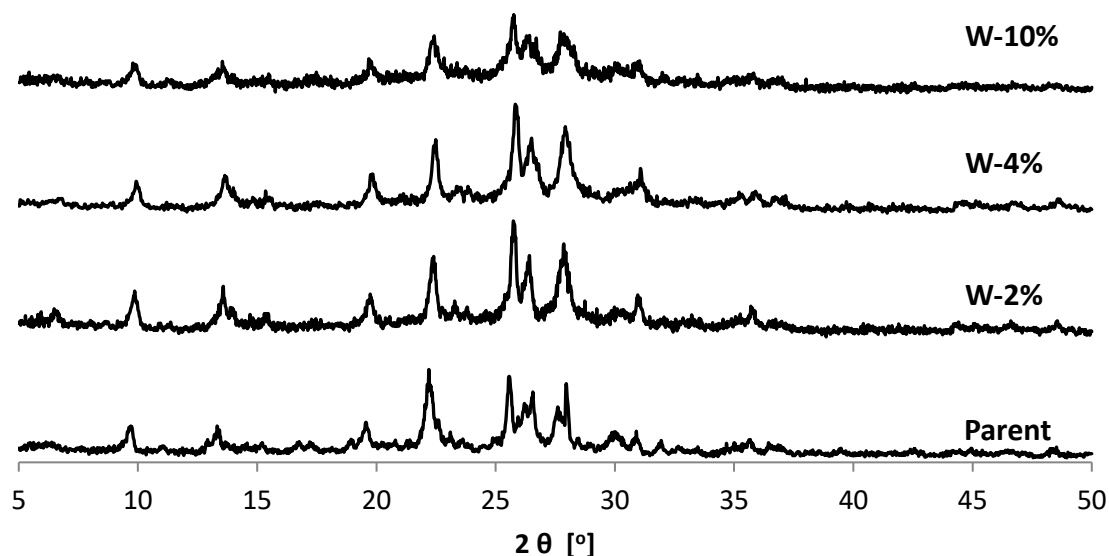
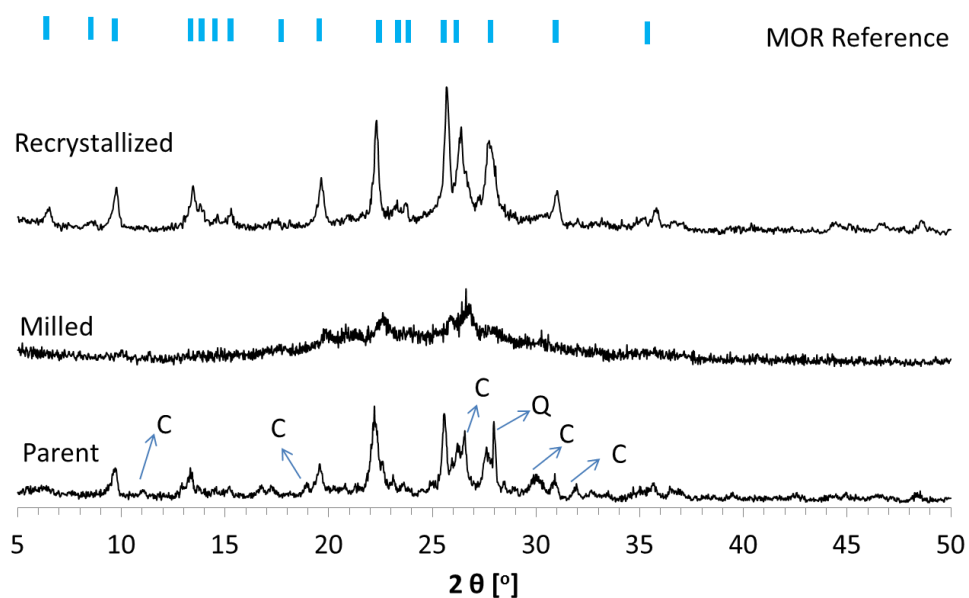


Figure 5.6: Effect of different weight percentages of the milled to solution (W = 1, 2 and 5 g) on the crystallinity of the recrystallized MOR ($18\text{SiO}_2/12\text{NaOH}/780\text{H}_2\text{O}$).

5.4.5 High Purity MOR of the Recrystallized Sample

The optimum condition for MOR recrystallization was at solution composition 18SiO₂/12NaOH/780H₂O for 2 h and sample weight 2%. Recrystallization resulted in a higher intensity of mordenite peaks, which represent higher crystallinity of the sample. Relative crystallinity of the recrystallized was 150% as compared with the parent (Table 5.3). Moreover, some peaks, which belong to clinoptilolite and quartz in the parent, disappeared after milling step such as the peaks on 2 θ : 11, 19, 26.5, 28, 30, and 32 deg. The solution composition, operation conditions, and time (2 h) were selective for mordenite crystal phase growth as the impurity phases such as; clinoptilolite and quartz, reduced, which resulted in high crystallinity and purity of the mordenite phase. The high magnification of the TEM image of the recrystallized sample showed a well-faceted particle (Figure 5.8). The TEM information was in agreement with the high crystalline MOR as shown by high intensity of the XRD pattern of the recrystallized sample (Figure 5.7).



Main phase = Mordenite, C = Clinoptilolite, Q = Quartz

Figure 5.7: Comparison of XRD patterns of the parent, milled nanomordenite and selected recrystallized (18 SiO₂/12 NaOH/780 H₂O) MOR at 2 h hydrothermal period.

Table 5.3: Crystallinity study based on the XRD analysis and Si to Al ratio

Sample	Relative MOR Crystallinity (%)	Main phases	Si/Al (XRF)
Parent	100	Mordenite, Clinoptilolite & Quartz	6
Milled	65	Mordenite	6
Recrystallized	150	Mordenite	9

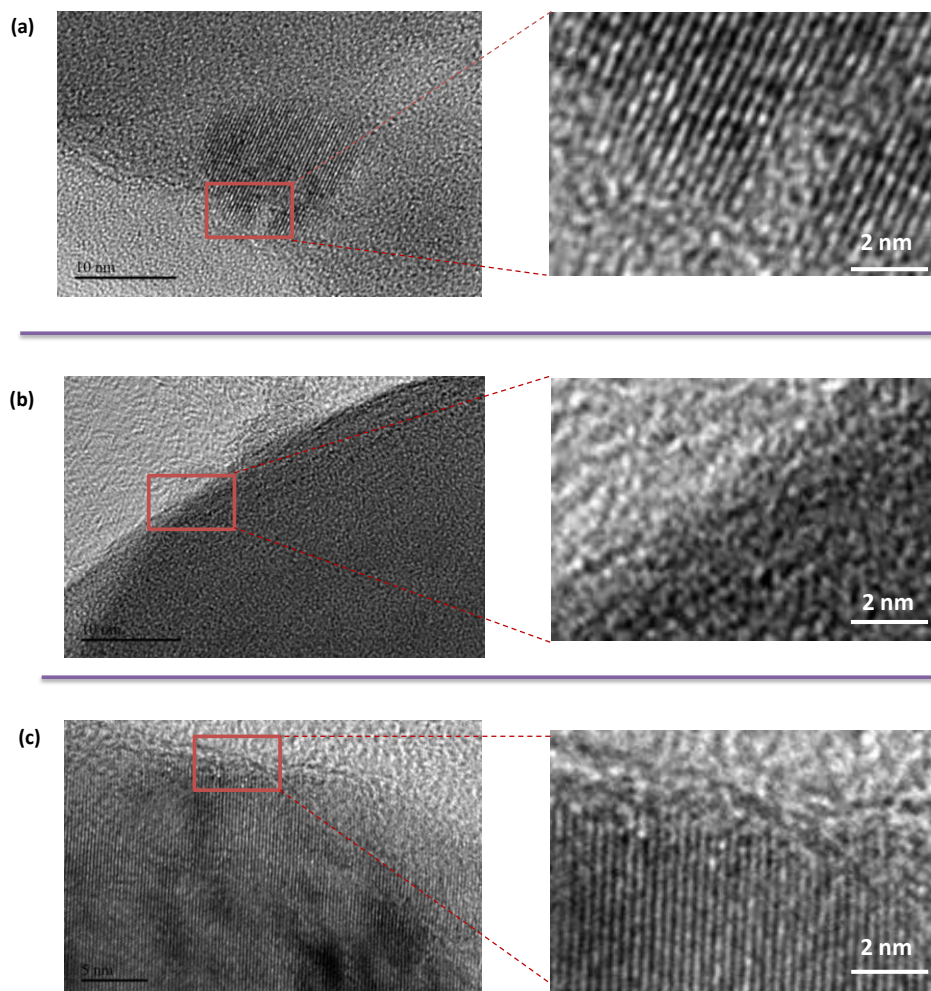


Figure 5.8: TEM images in high magnification of (a) the parent, (b) milled, and (c) recrystallized.

We applied the optimum condition to recrystallize the parent sample without the milling step in order to confirm the role of recrystallization on the phase purity of the sample. The crystallinity of the recrystallized parent was increased as it can be seen in Figure 5.9. In contrast, the impurities phase such as clinoptilolite and quartz were also reduced as it dissolves and changes to the MOR phase. However, the extent of diminishing of the impurities phase was much higher on the recrystallization of the milled one as compared with the parent recrystallization. We can conclude here that the recrystallization step was important not only to recover the crystallinity but also to reduce the impurities phase.

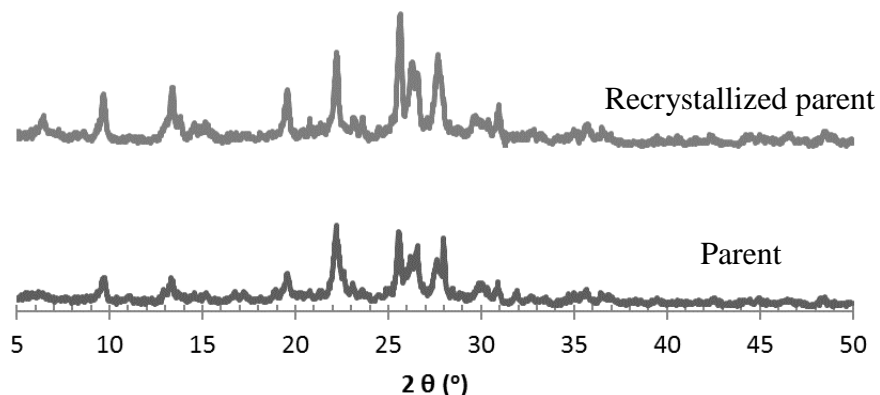


Figure 5.9: Comparison XRD patterns of the parent and recrystallized parent.

5.4.6 FTIR Study of the Mordenite Samples

The aluminosilicate framework of the parent, milled, and recrystallized zeolites was observed by the FTIR technique (Figure 5.10). Similar IR spectra of the parent and treated natural zeolites were observed. The vibrational bands at $780\text{--}820\text{ cm}^{-1}$ conform to the vibration of the Al-O fragment. The main vibrational bands at about $960\text{--}1250\text{ cm}^{-1}$ were assigned to the asymmetric stretch mode of SiO_4 and AlO_4 , while the bands at about $1560\text{--}1690\text{ cm}^{-1}$ were attributed to the vibration of HOH. The milling step reduces the intensity of vibrational bands at $960\text{--}1250\text{ cm}^{-1}$ significantly which indicated that the breakage of the external linkage. The low-intensity peak of zeolites after milling treatment was in agreement with another high-energy ball milling investigation reported elsewhere, which indicated that the loss of crystallinity was caused by the structural modifications on the molecular level [103].

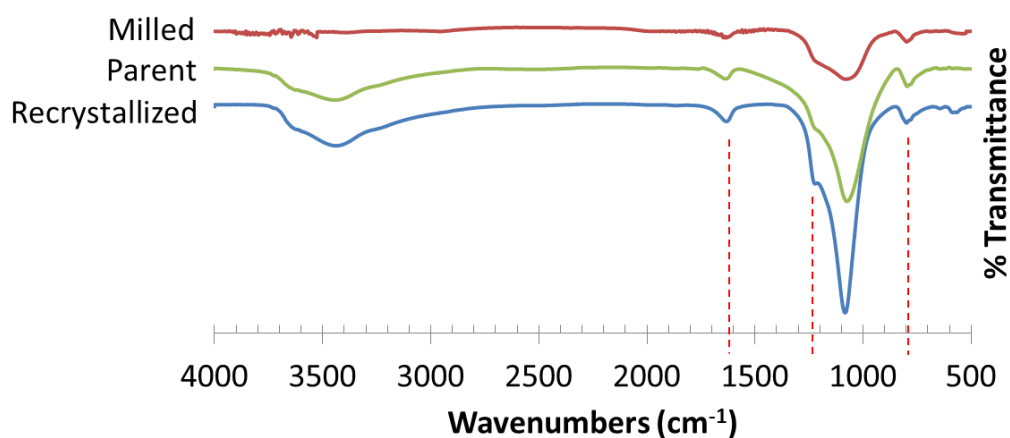


Figure 5.10: FTIR spectra of the parent natural zeolites and modified samples.

5.4.7 Particle Size Study

The particle size was measured based on the SEM images. Particle size distribution based on the SEM images is presented in Figure 5.11. FE-SEM micrographs of the parent have a smooth appearance and have large particles (in a range of 1 to 6 μm) sizes. After ball milling, the particle size reduced to the nanosized range which estimated from the SEM micrographs was in the range from 20 to 160 nm (Figure 5.12). The particle size appearing on the SEM and TEM study might be the aggregate of some zeolite crystals as the crystallite size that estimated from the Scherrer equation was smaller as compared with the one from SEM and TEM particles size image (Table 5.4). The particles size was slightly increased after the recrystallization process due to the crystal growth of MOR nanoseeds (Figure 5.11 and 5.12). It was observed from the XRF study that the silicon to aluminum (Si/Al) ratio of the milled sample was similar to the parent. The ball milling process has no effect on the composition of silicon and aluminum. However, the Si/Al ratio increased from 6 to 9 after recrystallization (Table 5.3). The XRF analysis showed

that the silicon content was increased from 20% to 33% after recrystallization, which means that mordenite growth was not only originated from the crushed parent crystalline, but also from the additional silicate solution.

Table 5.4: Comparison of mean particle size by XRD, SEM and TEM

Sample	XRD* (nm)	SEM (nm)	TEM (nm)
Parent	32 ± 17	2500 ± 1100	-
Milled	7 ± 4	90 ± 25	18 ± 4
Recrystallized	25 ± 13	95 ± 21	82 ± 55

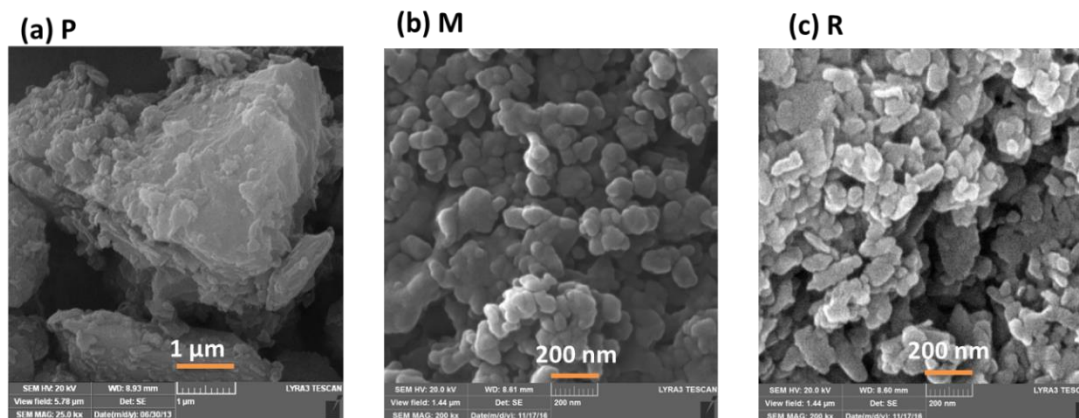


Figure 5.11: SEM images of (a) the parent, (b) milled, and (c) recrystallized mordenite nanoparticles.

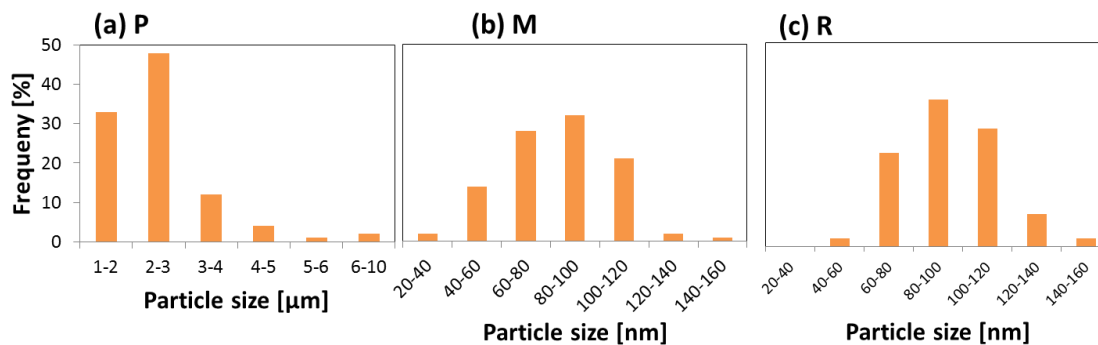


Figure 5.12: Particle size distribution based on SEM images of (a) the parent, (b) milled, and (c) recrystallized sample.

The voids were formed by the stacking of the nanoparticles created the hierarchical pore system as indicated by the SEM and TEM study (Figure 5.11 and 5.13). The intercrystalline mesopores are important to provide access to the acid sites on the surface of nanoparticles in the catalytic reaction. The mesopore volume was also confirmed through nitrogen physisorption analysis as discussed in the next section.

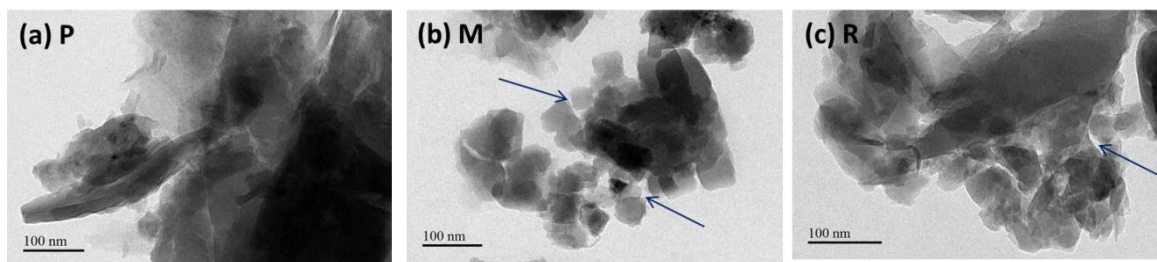


Figure 5.13: Intercrystalline mesopores captured on the TEM images of the milled and recrystallized mordenite.

5.4.8 Textural Properties Study

The isotherm adsorption-desorption of the parent, milled, and recrystallized zeolite appeared in isotherm type 1 (Figure 5.14). The surface area (S_{BET}) was increased from 133 m^2/g in the parent to 163 m^2/g in the milled sample. The high surface area of the milled sample was mainly due to the high external surface area, which improved from 23 m^2/g (the parent) to 150 m^2/g (the milled) (Table 5.5). The external surface area of the milled that increased nearly seven times of the parent indicated the small nanoparticles obtained which also was confirmed by the SEM and TEM observation that the milling reduced the particle sizes from large particle size into the nanosized zeolites. The mesopore volume of the milled sample was 0.48 m^2/g , which was far higher as compared with the parent sample ca. 0.04 m^2/g . The mesopore size distribution is presented in Figure 5.15. The random

stacking of nanoparticles milled mordenite creates voids called intercrystalline mesopores which feature a hierarchical pore system [139]. The way of nanoparticles stacking is important in catalytic reactions as if the nanoparticles stacking in such a way created no void, and it will lead to difficulty of the molecules to reach the surface area in the pore. The importance of hierarchical nanosized zeolite was reported elsewhere which increases the stability and product selectivity in the 1-butene isomerization [145] and dimethyl ether to olefins [146].

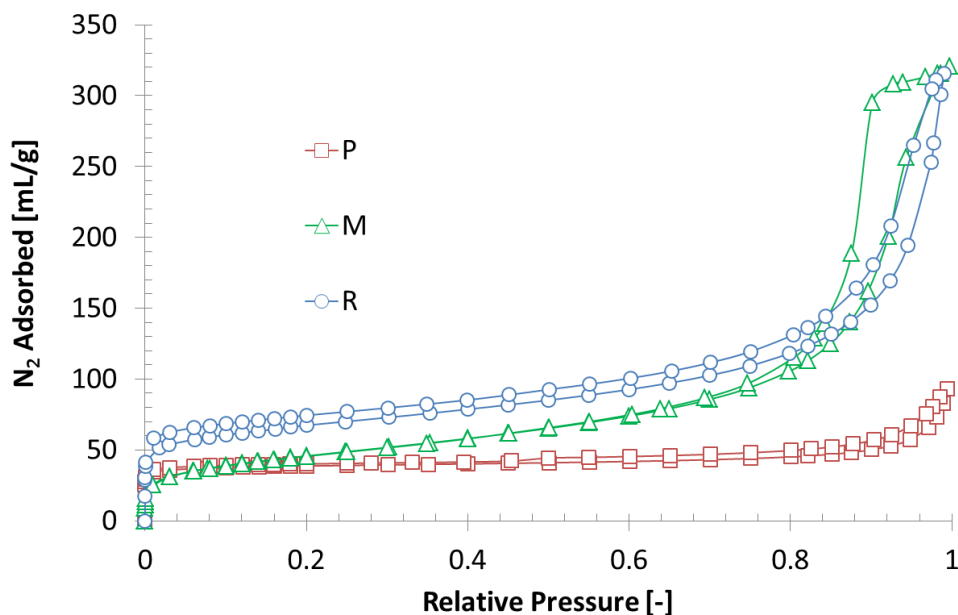


Figure 5.14: N₂ isotherm of parent and mechanochemical treated sample (18SiO₂/12 NaOH/780H₂O) at T = 170 °C for 2 h.

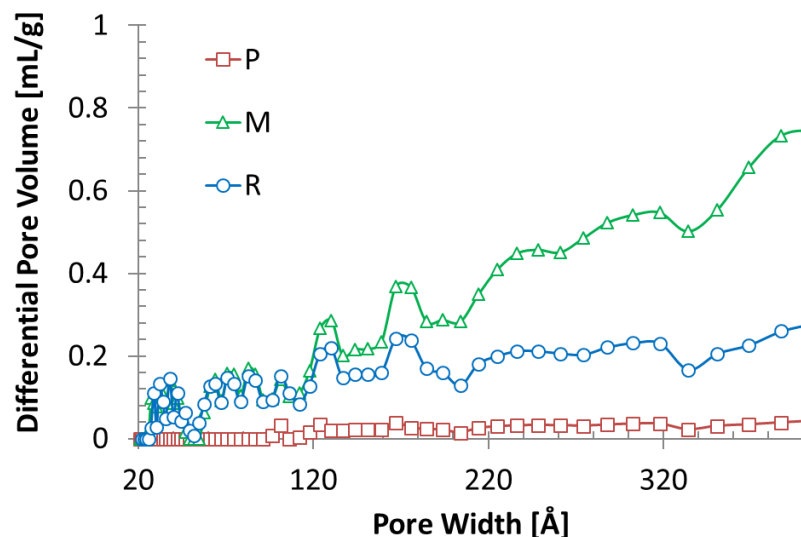


Figure 5.15: Pore size distribution calculated by the DFT method.

Table 5.5: Textural properties of the parent, milled, and selected recrystallized milled MOR

Sample	S_{BET} (m^2g^{-1})	S_{t} (m^2g^{-1})	S_{ext} (m^2g^{-1})	V_{total} (cm^3g^{-1})	V_{micro} (cm^3g^{-1})	V_{meso} (cm^3g^{-1})
Parent	133	110	23	0.10	0.06	0.04
Milled	163	12	150	0.49	0.01	0.48
Recrystallized	240	92	148	0.40	0.04	0.36

The ball milling step effectively fabricated the nanoparticles zeolites, however, the micropore structure was partially demolished. The micropore area was decreased significantly from 110 m^2/g to 12 m^2/g after the milling process. The recrystallization process successfully recovered the micropore structure of the MOR framework as the micropore surface area (S_{t}) increased from 12 m^2/g of the milled to 92 m^2/g of the recrystallized mordenite. The recrystallization treatment of the parent also increased the micropore significantly as can be seen from the isotherm (Figure 5.16). The micropore volume was increased from 0.05 cm^3/g to 0.08 cm^3/g . The mesopore volume of the

recrystallized parent remained similar as compared with the parent (Table 5.6). The formation of the mesopore by desilication did not occur due to the composition of basic silicate solution applied to prevent the dissolution of the silica in the framework of zeolites. The higher micropore volume of the recrystallized parent probably caused by the converting the impurities phases to MOR as indicated in the XRD patterns (Figure 5.16) and the growth of mordenite crystals. It is worth mentioning here that the weight of recrystallized parent was increased 25% from the initial parent sample, which suggested that the growth of crystals occurred under the hydrothermal recrystallization.

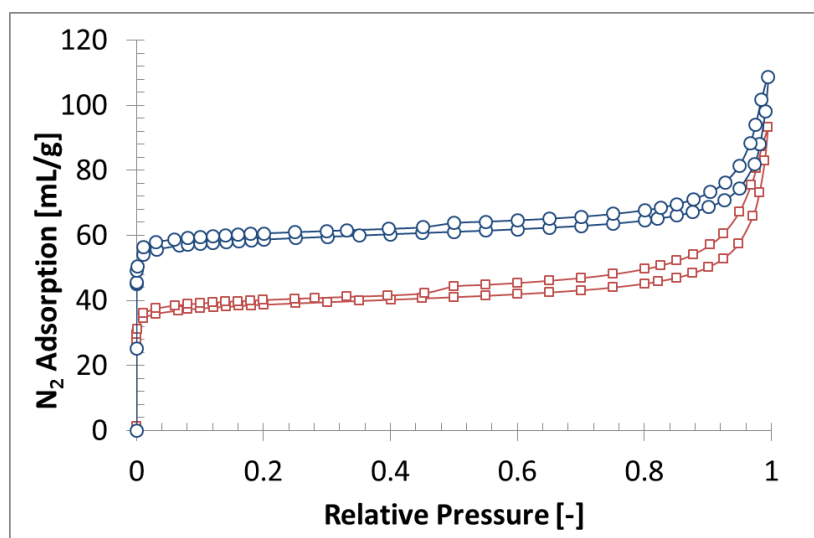


Figure 5.16: N₂ isotherm of the parent and recrystallized parent (18SiO₂:12NaOH:780H₂O) at T = 170 °C for 2 h).

Table 5.6: Textural properties of the parent and the recrystallized parent

Sample	S _{BET} (m ² /g)	S _t (m ² /g)	S _{ext} (m ² /g)	V _{total} (cm ³ /g)	V _{micro} (cm ³ /g)	V _{meso} (cm ³ /g)
Parent	133	110	23	0.10	0.06	0.04
Recrystallized parent	213	186	27	0.12	0.08	0.04

5.4.9 Milling-Recrystallization Mechanism

The possible mechanism of recrystallization to obtain a high-quality mordenite is illustrated in Figure 5.17. The ball milling played a significant role in demolishing crystalline phases to some extent and provided a very small crystal size as a seed for the recrystallization step surrounded by the noncrystalline phase. The noncrystalline phase rearranges itself to build the mordenite phase which was controlled by the solution composition, temperature, and time of recrystallization. In addition, the crystal growth of mordenite occurred as the mass of the recrystallized sample was significantly higher than the milled zeolites. As the proper hydrothermal conditions were applied on the recrystallization step, the high purity mordenite phase with high micropore volume and the large external surface area have been obtained instead of other impurities phases.

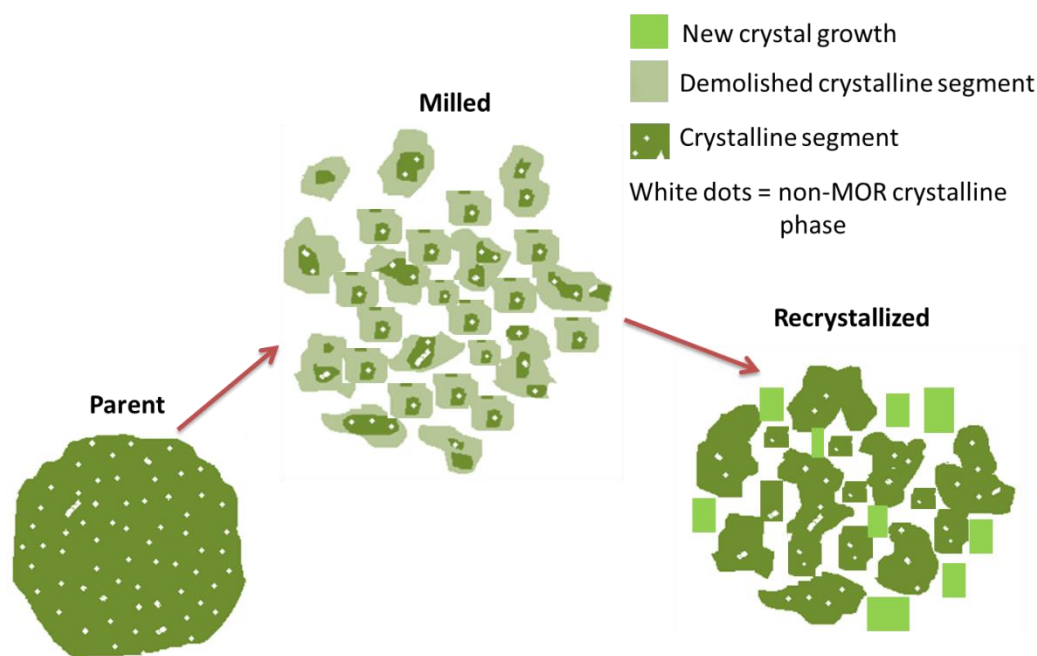


Figure 5.17: Illustration of the ball milling and recrystallization transformation of micro-sized natural zeolites into nano-sized MOR with high purity and crystallinity.

5.5 Concluding Remarks

The nanoparticles of MOR were obtained by high-energy ball milling. However, the milling caused the decrease of crystallinity. The high crystallinity and purity of nano-mordenite were recovered after recrystallization of the milled nano-zeolite in basic sodium silicate solution. In addition, the hierarchical pores system was also formed on the milled and recrystallized mordenite. The textural properties of recrystallized nano-mordenite were improved with enhancements in the external surface area, intercrystalline mesopore, and micropore volume. The fast recrystallization time (2 to 6 h) favored the mordenite phase. The silica and OH^- concentration determined significantly the framework of the recrystallized sample. The high ratio of sample mass to basic silicate solution reduced the crystallinity of recrystallized MOR.

CHAPTER 6

CONVERSION OF DIMETHYL ETHER TO OLEFINS OVER NANOSIZED MORDENITE FABRICATED BY COMBINED HIGH-ENERGY BALL MILLING WITH RECRYSTALLIZATION

6.1 Summary

Fabrication of cost-effective catalysts is one of the key strategies to monetize natural gas derivatives such as dimethyl ether to olefins. In this study, the particle size of natural mordenite (MOR) was reduced into micro and nanosize by high-energy ball milling with variation in milling time. Furthermore, the selected milled MOR was recrystallized by using silicate solution that favored the growth of mordenite phase to recover the demolished mordenite structure. The mesopore volume and external surface area were increased significantly after milling treatments and remained large even after recrystallization. A high conversion of dimethyl ether was obtained over the recrystallized MOR (99.7%) and milled natural MOR (54.1%) as compared to the parent (1.2%). Moreover, the milling only and the milling-recrystallization processes improved selectivity toward olefins and prolonged catalyst lifetime. The reduced particle size combined with the hierarchical porous and acidity effectively enhanced catalysts activity and selectivity to olefins.

6.2 Introduction

Natural zeolites are abundant and low-cost aluminosilicate hydrated crystalline compounds with a microporous structure filled by water and cations, mostly alkaline (Na, K) and alkaline earth (Ca), which have a high ion exchange capacity, shape selectivity, and sorption properties. Natural zeolites are potential catalytic materials since they have a high surface area and acid property [32] as also shown by the synthetic zeolites. However, the utilization of natural zeolites in industries has been limited due to impurities, non-single phase, heterogeneity in composition [1] and limited framework occurrences. In fact, to the best of our knowledge, there is only natural erionite that was used as commercial catalyst fabricated from natural zeolite in petroleum refining and petrochemicals. However, some investigations on modified natural zeolite for catalytic purposes have been reported elsewhere [61, 62, 122]. The common methods to modify the properties of natural zeolites are thermal treatment, dealumination, and ion exchange, which are adapted differently according to appropriate catalytic reactions [147].

One of the important frameworks zeolites used in industrial catalysts, which also occur in nature is mordenite (MOR). Synthetic mordenite has been applied as a commercial catalyst for hydroisomerization and alkylation in industrial scale [2]. There are two types of mordenite zeolite that are distinct on adsorption performance, namely, small-port and large-port. Natural mordenite is known as a small-port mordenite, which adsorbs molecules less than 4.2 Å. Meanwhile, the commercial synthetic mordenite as a large-port can adsorb larger molecules (more than 4.5 Å) [148], which is more advantageous for industrial applications. Transformation of the small-port into large-port mordenite can be accomplished through the dealumination method using mild acid treatment [149, 150].

Mordenite has a 12-membered ring (6.7 x 7.0 Å) parallel with an 8-membered ring (3.4 x 4.8 Å) [65]. However, the smallest pore size is not accessible; hence, practically the mordenite has a 1-dimension (1D) zeolite channel system. The common problem of a 1D zeolite pore system on hydrocarbon conversion is the fast deactivation due to mass-transfer limitation and coke deposition. A highlight of different 1D pore zeolites and their performance in dimethyl ether and methanol conversion is presented in Table 6.1.

Table 6.1: Highlight of zeolite 1D performance on olefinic target from dimethyl ether (DME)/methanol feed.

Zeolite	Feed	Conversion (%)	Olefins ^a selectivity	P/E ^b [-]	TOS ^c	T [°C]	WHSV [h ⁻¹]	Ref.
Dealuminated mordenite (3M-6h)	DME	16.9 (6.3)	33 (0)	0.7 (-)	5 (60)	350 (350)	1.18 (1.18)	[22]
Desilicated EU-1 (0.25 M)	DME	17 (3)	19 (0)	3.3 (-)	5 (60)	350 (350)	1.18 (1.18)	[151]
Desilicated-dealuminated EU-1	DME	48	36	2.1	5	350	1.18	[152]
Milled-alkaline-acid treated ZSM 22	CH ₃ OH	100 (90)	42 (18)	7.4 (8)	5 (500)	400 (400)	2 (2)	[25]

^a(ethylene + propylene). ^bratio propylene to ethylene

^cTime on stream. The numbers inside the bracket are data of different time on stream.

The mass-transfer properties are improved in the mesoporous system and nanosized zeolite [139]. A hierarchical system that contains a mesoporous channel is important for catalytic reaction because it enhances the diffusion of reactants and products and reduces coking.

Desilication of mordenite by alkaline treatment was applied to develop the mesoporosity, which improved the diffusion particularly for the 1D zeolite pore system [2]. Mesoporous mordenite has been successfully synthesized for pyrolysis biomass and cracking vacuum gasoil [153]. Another type of mesoporosity is intercrystalline mesopores, which is defined as the void networks in the intercrystalline space of nanosized crystals [139]. The nanosized particles can be obtained by a top-down strategy using ball milling, particularly applied for natural zeolites [11]. For instance, milled zeolite KNaX improved the selectivity to ethylbenzene and styrene in the alkylation of toluene with methanol due to the reduction of the Brønsted acid site density [102]. The application of high-energy ball milling for small pore zeolites (NaA and CaA) effectively gave access to the active sites, which led to an improvement in the catalyst activity [101]. Recently, selective deactivation of the external surface of ZSM-5 to reduce the acidity on external surface by ball milling was applied for a short time duration (3-30 min), which reduced the side reaction on the external surface of ZSM-5 in toluene alkylation [154].

A systematic research on natural zeolite and the controlled modification to obtain a hierarchical system for catalytic hydrocarbon conversion is rarely reported. In this work, we examined a method to fabricate cost-effective hierarchical catalysts from natural zeolites, which were applied in dimethyl ether to olefins reaction.

6.3 Experimental

6.3.1 Material Characterization

Natural zeolite tuff was obtained from Klaten, Indonesia. Characterization of the zeolite phase has been conducted using X-ray diffraction (XRD, Miniflex-Rigaku). Radiation of

Cu K α was used with a scanning rate 3°/min and a step size 0.02° from 2 θ angle 5° to 50°. The XRD pattern was compared with that of the mordenite reference in the international zeolite association (IZA) Atlas book [155]. The relative crystallinity of zeolite was calculated by comparing the areas of the main peaks of treated zeolites with those of the parent zeolites. N₂-physisorption (Micromeritics, ASAP 2020) was used to study the pore system in liquid nitrogen at -196 °C. Prior to adsorption analysis, samples were degassed at 350 °C for 10 h to remove adsorbed gas and water. X-ray fluorescence (XRF) was used for elemental analysis. The morphology of the zeolite was studied by field-emission scanning electron microscopy (FE-SEM, LYRA 3 Dual Beam, Tescan). Transmission electron microscopy (TEM, JEOL-JEM-2100F) was used to examine the morphology and particle sizes of zeolite samples. Ammonia temperature-programmed desorption (NH₃-TPD, Micromeritics, Chemisoft TPx V1.02) was used to quantify the acidity of the modified catalysts. Ammonia was desorbed by a 10 °C/min heating ramp from 120 °C to 750 °C.

6.3.2 High-Energy Ball Milling

High-energy ball milling attritor (Union Process HDDM-01) was used to reduce the particle size by wet milling method. A 50 g sample of natural zeolite (0.1-0.3 mm) was milled for 6 h (milled-6h), 8 h (milled-8h), and 10 h (milled-10h) in a 350 mL ethanol (99.5% Merck) as a dispersion medium. The ball material was zirconia (ZrO₂) with 0.65 mm diameter. The speed of agitator was 2000 rpm. The temperature was maintained at 13 °C by cooling water media. The optimum milled zeolite (with milling time of 8 h) was selected for further treatment by hydrothermal recrystallization.

6.3.3 Recrystallization

Milled natural zeolites (milled-8h) were treated hydrothermally at 170 °C for 2 h with an autoclave (Parr) using basic silicate solution (9 SiO₂ : 12 NaOH : 780 H₂O). The silica source was silica gel of Sigma-Aldrich. The ratio between milled natural zeolites and the silicate solution was 1 : 45 (wt.%). The slurry was centrifuged and washed with deionized (DI) water several times until the neutral pH was reached. Solid particles were separated and dried for 16 h at temperature of 25 °C (milled 8 h-Recrystallized).

6.3.4 Conversion of Dimethyl Ether to Olefins

The acid form of mordenite was prepared by ion exchange in a microwave followed with calcination. Ammonium nitrate (NH₄NO₃) solution was used to obtain NH₄-MOR. The suspension (1 g sample to 20 ml of 2 M NH₄NO₃) was heated from temperature 25 °C to 85 °C within 5 min and maintained for 10 min. Centrifugation at 3500 rpm for 2 min was conducted to separate the solid from the liquid phase. The ion exchange procedure was repeated to guarantee a high degree of ammonia protonated form. Subsequently, the wet samples were dried for 16 h at room temperature. The dried zeolite samples were calcined with rate 5 °C/min and maintained constant at 550 °C for 12 h in static air to obtain an acid form of zeolite.

Catalyst testing for dimethyl ether (DME) conversion over the parent, milled, and recrystallized natural zeolites was examined at 1 atm and 350 °C. The catalyst (0.050 g) was placed in a fixed-bed reactor made of quartz glass with an inside thickness of 4 mm (ID). The helium (gas carrier) and DME feed flow rates were 0.3167 and 0.0217 mmol/min. The catalyst weight to DME flow rate ratio (W/F) was controlled at 0.039 (kg.h)/mol. Reaction products were analyzed using online GC system with flame

ionization detectors (GC-FID, Shimadzu; GC-14B) and a J and W scientific column (Alumina PLOT).

6.4 Results and Discussion

6.4.1 Natural Zeolites

XRD patterns revealed that the as-received natural zeolite (parent) was identified as a mordenite dominant, which coexist with clinoptilolite and quartz (Figure 6.1). An analysis by XRF showed that the ratio of silicon to aluminum was very low ($\text{Si}/\text{Al}=6$), which indicates a rich aluminum content of mordenite (Table 6.2). The pores of the parent were filled by water and cations of potassium (K), alkaline earth (Ca) and other metal impurities (Fe, Ti). These pore occupancies may block the molecules to enter zeolitic pore system. Demetalation by acid treatment is a well-known treatment to remove the cations and the aluminum on the framework of zeolite, which resulted in a higher Si/Al ratio [156].

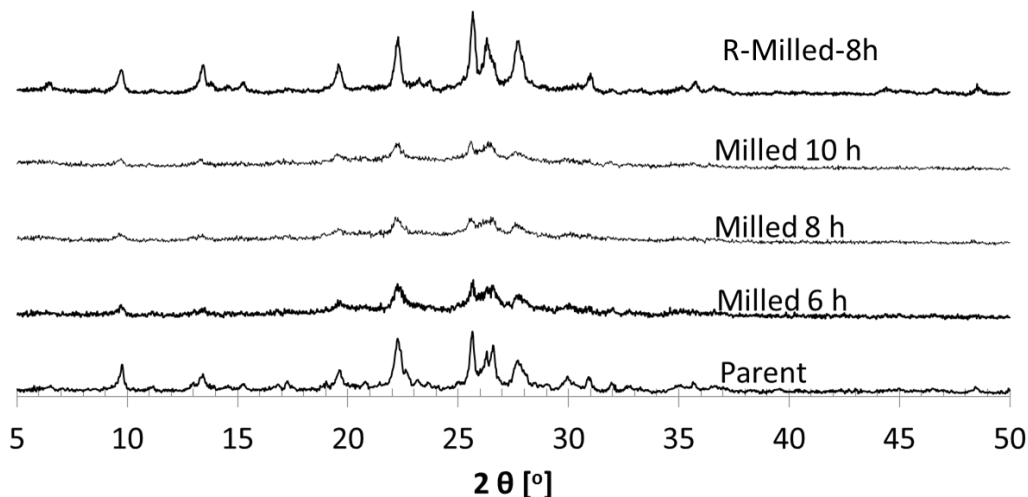


Figure 6.1: XRD patterns of the parent and modified natural MOR zeolites.

Table 6.2: XRF analysis of natural zeolite as-received

Oxide form	%
Al ₂ O ₃	6.61
SiO ₂	44.38
P ₂ O ₅	0.62
K ₂ O	0.99
CaO	3.44
TiO ₂	0.35
Fe ₂ O ₃	1.99

The morphology of the parent natural zeolites, as can be observed from the TEM images, were needles with 50-100 nm in width and more than 500 nm in length (Figure 6.2a). This mordenite morphology shape is in agreement with most of the reported morphologies of other natural mordenite found in different countries [157, 158]. This needle shape is one of the characteristics of the small-pore mordenite type which are easily blocked due to the structural defect [149]. Plate-shape morphology was also observed on the natural zeolites parent, which possibly attributed to the clinoptilolite phase as confirmed by the XRD pattern.

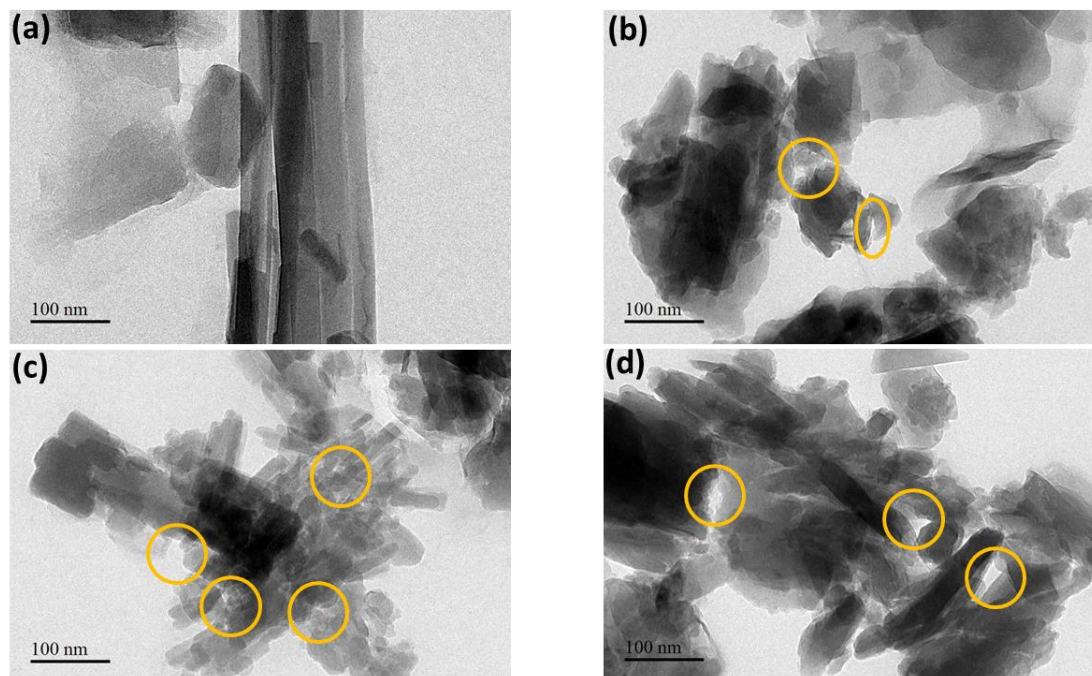


Figure 6.2: TEM of (a) The parent, (b) milled-6h, (c) milled-8h, (d) milled-10h samples.

The nitrogen adsorption-desorption curve shows a type I and IV isotherm (Figure 6.3). Adsorptive (nitrogen) started to fill on the micropores at very low relative pressure (6×10^{-6} [-]) and created a monolayer approximately at 1×10^{-4} in relative pressure which appeared as the rounded knee on the isotherm. The natural zeolite consists of relatively high microporous volume as compared to other natural mordenite from different continents such as Ukrainian mordenite [147] and Chilean mordenite [159]. The nitrogen isotherm of the parent natural zeolite within the P/P_0 range of 0.5-1 shows the hysteresis that is an indication of the capillary condensation in the mesopores and macropores of the parent mordenite.

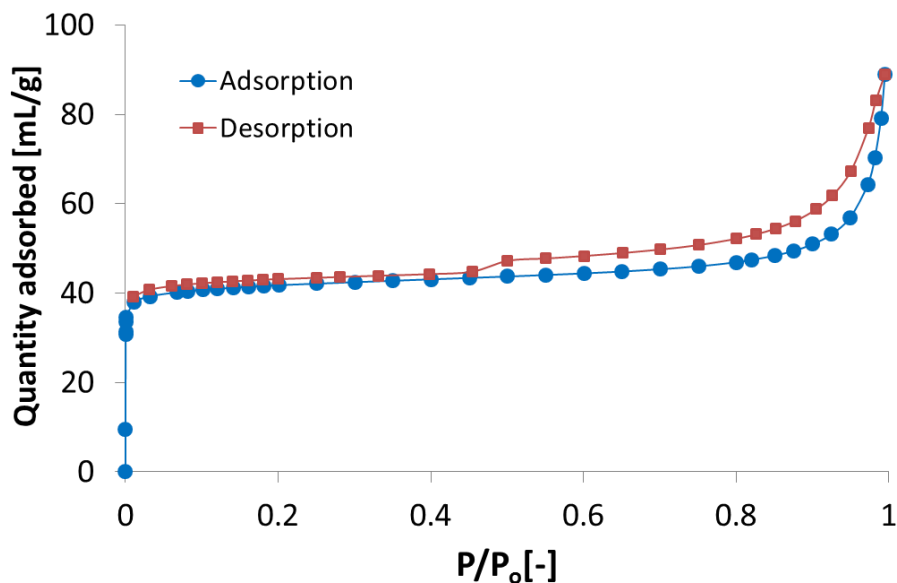


Figure 6.3: Nitrogen adsorption-desorption isotherms of the parent natural MOR zeolite.

6.4.2 High-Energy Ball Milling

Milling has reduced the crystallinity of all zeolite phases and led to amorphization of natural zeolites. The intensity of the peaks was reduced after milling 6 h, which clearly show at 2θ of 9.74° , 22.22° , 25.61° , 26.3° , and 27.6° (Figure 6.1). The crystallinity of milled-6h was decreased to 86% as compared with the one for the parent (Table 6.3). This attributed to the destruction of zeolite framework structure in which the external Si-O-Si and Si-O-Al bonds were damaged after milling [103]. The crystallinity of the MOR further decreased for 8 h milling time to 73% (Table 6.3).

Table 6.3: Milling time effects on crystallinity.

sample	crystallinity
parent	100%
milled-6h	86%
milled-8h	73%
milled-10h	75%
milled-8h-recrystallized	151%

However, further increase of milling time to 10 h has not much affected the crystallinity negatively anymore. This was possibly originated from the limitation the large size of the ball, which was unable to break down the tiny nanoparticles of the milled zeolites. Moreover, the wet milling method prevented the natural mordenite structure from collapsing completely into an amorphous phase. The result is in agreement with a publication of the wet milling method of zeolite HY, which reported that the particle size reduced significantly without much losing its crystallinity even for long-hour milling treatment [12].

The effect of milling time on the morphology of natural zeolite was studied using the TEM microscopy. The TEM images of parent zeolite showed compact and large crystals sizes (Figure 6.2a). The high-energy ball milling reduced the crystallite size drastically and

changed the shape of the long needle of mordenite crystals into a smaller crystal size and more irregular forms (Figure 6.2b, c, and d) with a large distribution range. These crystallites tend to agglomerate to form a larger particle size. The intercrystalline mesopores, which were created during the milling step are also observed on the micrographs as voids between the nanosized crystals.

Table 6.4: Physicochemical properties of the parent and treated natural zeolite.

Sample	$S_{\text{BET}}^{\text{a}}$	S_{t}^{b}	S_{ext}	V_{total}	$V_{\text{micro}}^{\text{b}}$	$\text{NH}_3 \text{ TPD}$
	$(\text{m}^2 \text{ g}^{-1})$	$(\text{m}^2 \text{ g}^{-1})$	$(\text{m}^2 \text{ g}^{-1})$	$(\text{cm}^3 \text{ g}^{-1})$	$(\text{cm}^3 \text{ g}^{-1})$	$(\text{cm}^3 \text{ g}^{-1})$
Parent	133	110	23	0.099	0.055	7.0
Milled 6 h	98	31	67	0.160	0.015	4.1
Milled 8 h	80	18	62	0.178	0.009	3.1
Milled 10 h	83	18	65	0.170	0.009	3.0
Milled 8 h- Recrystallized	233	165	68	0.220	0.082	10.6

^aTotal surface area was calculated using BET method within $P/P_0 = 0.01-0.3$

^bMicropore volume and surface area were estimated using the t-plot method.

From Figure 6.4, it can be seen that the milling process has changed the patterns of the nitrogen isotherms, which appear lower on the left side (lower relative pressure) and higher on the right side (higher relative pressure) as compared with the parent. The lower curve on the left side is attributed to a destruction of the microporous system, while the higher

curve on the right side is an indication of high mesopores and external surface area. The longer the milling time from 6 h to 8 h, the lower the left curve of N₂ isotherm, which indicates a lower nitrogen adsorption on the microporous system due to the collapse of some zeolite micropores (Figure 6.4). The isotherm slope of the mordenite also slightly increased after milling step. This can be attributed to the increase of the filled multilayers as the creation of intercrystalline mesopores on the milled zeolites.

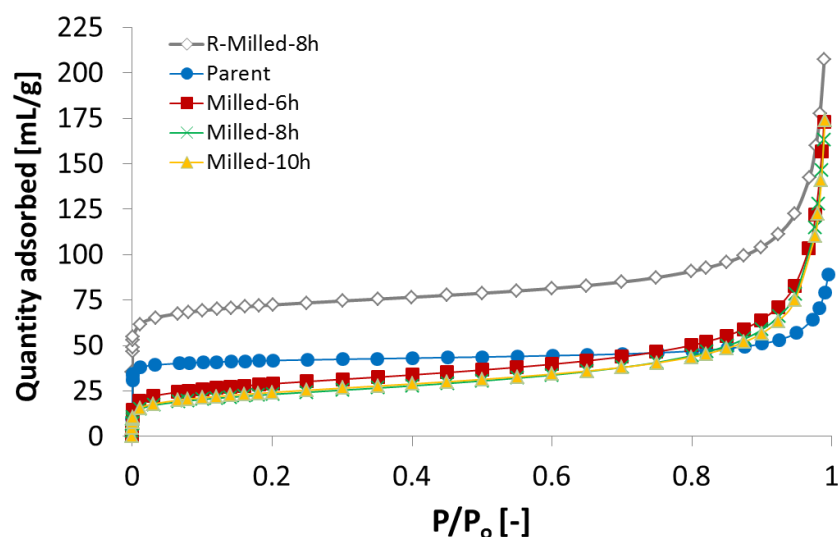


Figure 6.4: Nitrogen adsorption isotherms of the parent and treated natural zeolites.

The micropore volume was decreased drastically from 0.055 cm³g⁻¹ (for the parent) to 0.009 cm³g⁻¹ for the milled 8 h. In contrast, the external surface areas increased nearly threefold after the milling process (Table 6.4). Some of the nanosized particles contributed on the increment of the external surface areas. As the milling time longer, the mesopores volume also increased up to 230% (for milled 6h) and 284% (for milled 8h) (Table 6.5). However, it stopped to increase further at the milling time of 10 h, which has a slight decrease of mesopore volume as compared with the milled 8 h. The agglomeration

possibly occurred among the nanosized particles, which hence reduced its intercrystalline mesopore volume.

Table 6.5: Mesoporous volume of parent and treated natural zeolites.

sample	V_{meso}^* ($\text{cm}^3 \text{g}^{-1}$)	% change**
parent	0.044	0
milled-6h	0.145	230%
milled-8h	0.169	284%
milled-10h	0.161	266%
milled-8h-recrystallized	0.138	214%

* $V_{\text{meso}} = V_{\text{total}} - V_{\text{micro}}$

**% change = $(V_{\text{milled}} - V_{\text{parent}}) / V_{\text{parent}}$

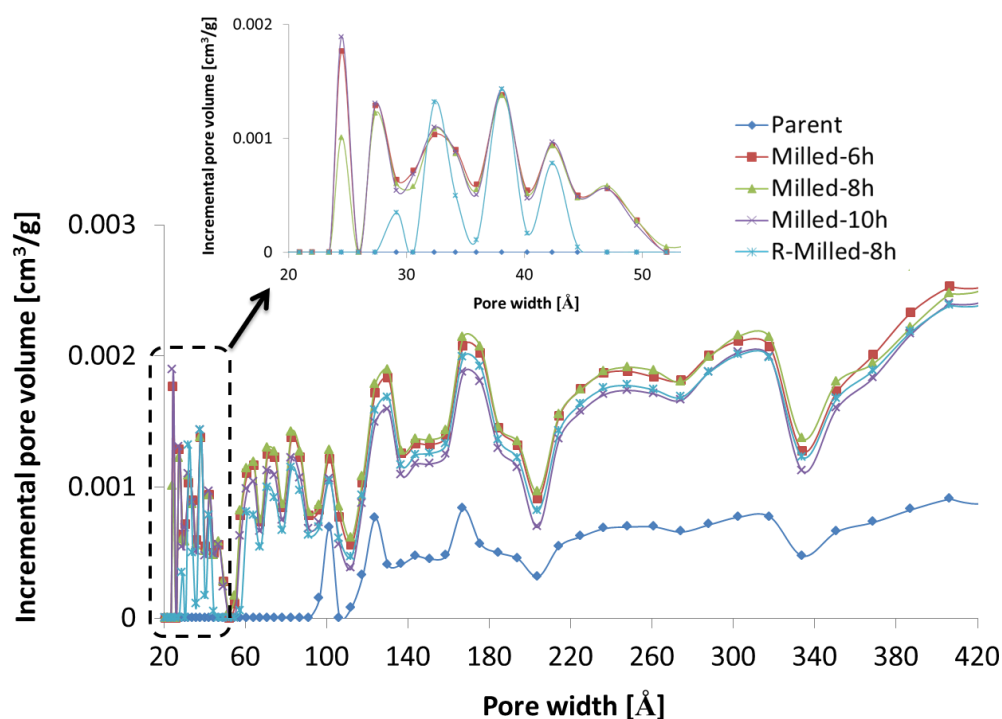


Figure 6.5: Mesopore size distribution of samples by NLDFT method.

The mesopore size distribution is presented in Figure 6.5, which is calculated by the NLDFT method. Overall, the patterns are almost similar for all samples, except the incremental pore volume of the parent which is the lowest among others and the different pattern within pore width 20-100 Å as compared with that of the milled and recrystallized samples. It is clear that the milling step greatly affected the pore size distribution of zeolite. As the particle size smaller, the intercrystalline mesopore increased on the milled zeolite. The mesopore size created on the milled zeolite started from 23 Å. The recrystallized zeolite shows different incremental pore volume patterns between 28 Å and 52 Å. It is possible that the decrease in mesopore volume of the recrystallized sample was caused by the slight growth of crystal size during the autoclave recrystallization treatment.

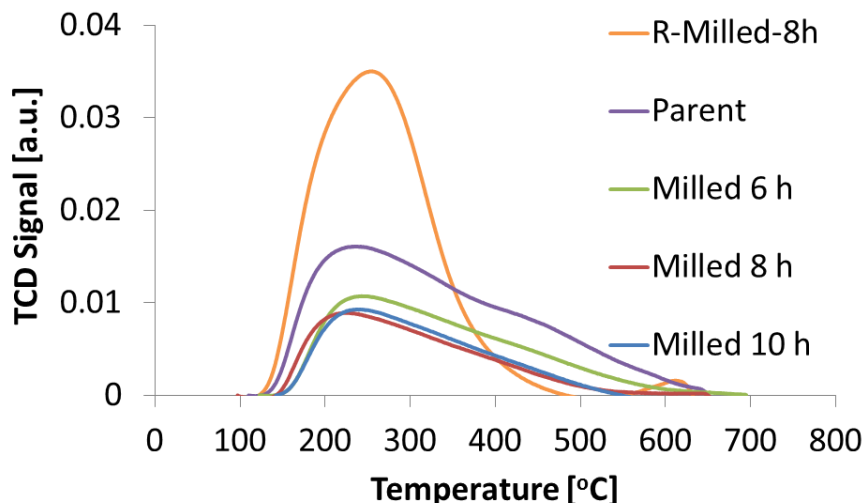


Figure 6.6: NH_3 TPD of parent and treated natural MOR zeolites.

The acidity of natural mordenite was affected through mechanical treatment. The acidity curves show that the acidity decreased after milling as the milling time increased up to 8 h (Figure 6.6). The total acid of natural zeolites was reduced from 7 to $4 \text{ cm}^3/\text{g}$ after 6 h of milling. The acidity further decreases to $3.1 \text{ cm}^3/\text{g}$ over the 8 h milled sample. This can be attributed to the collapse of the mordenite structure and the transformation of the crystalline phase into an amorphous phase during the milling process.

6.4.3 Recrystallization

The natural zeolite recovered its structure significantly after the recrystallization using silicate solution in a hydrothermal treatment into purer mordenite. A milling process followed by recrystallization using alkaline-silica solution favors the growth of mordenite and diminished other nonmordenite phases such as clinoptilolite and quartz. It is clearly shown on the clinoptilolite peaks at 2θ 17.06° , 19° , 22.5° , 29.8° , and 31.73° were no longer appear on the XRD patterns of the recrystallized zeolite (Figure 6.7). The quartz at 2θ

20.6° and 26.51° also disappeared after milling for 8 h and recrystallization. Hence, the recrystallized natural zeolite also resulted in purer MOR as compared with the case with the parent. The crystallinity of milled-recrystallized mordenite has raised one and a half fold as indicated at all of the mordenite peaks. The high crystallinity after ball milling-recrystallization of MFI and LTA framework was also reported by Wakihara and co-workers [19, 20].

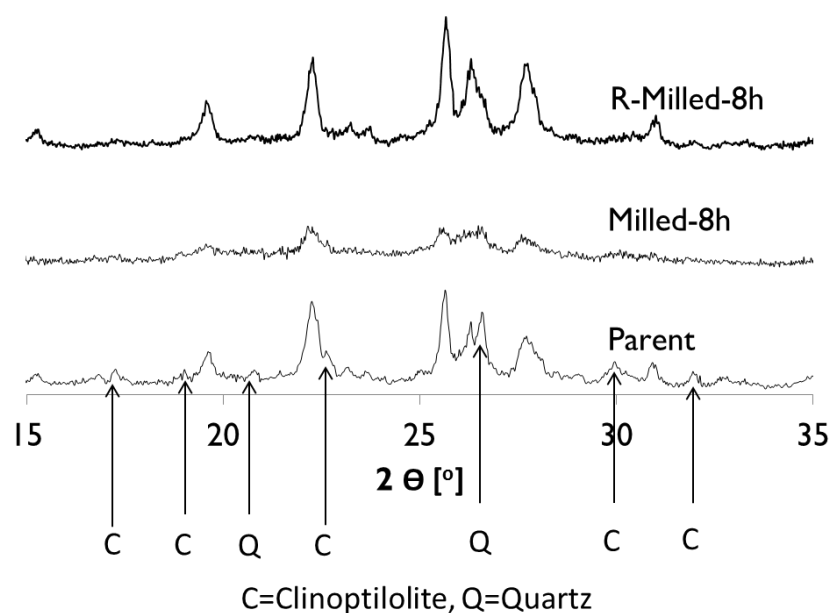


Figure 6.7: XRD patterns revealed the disappearance of nonmordenite phases on recrystallized samples.

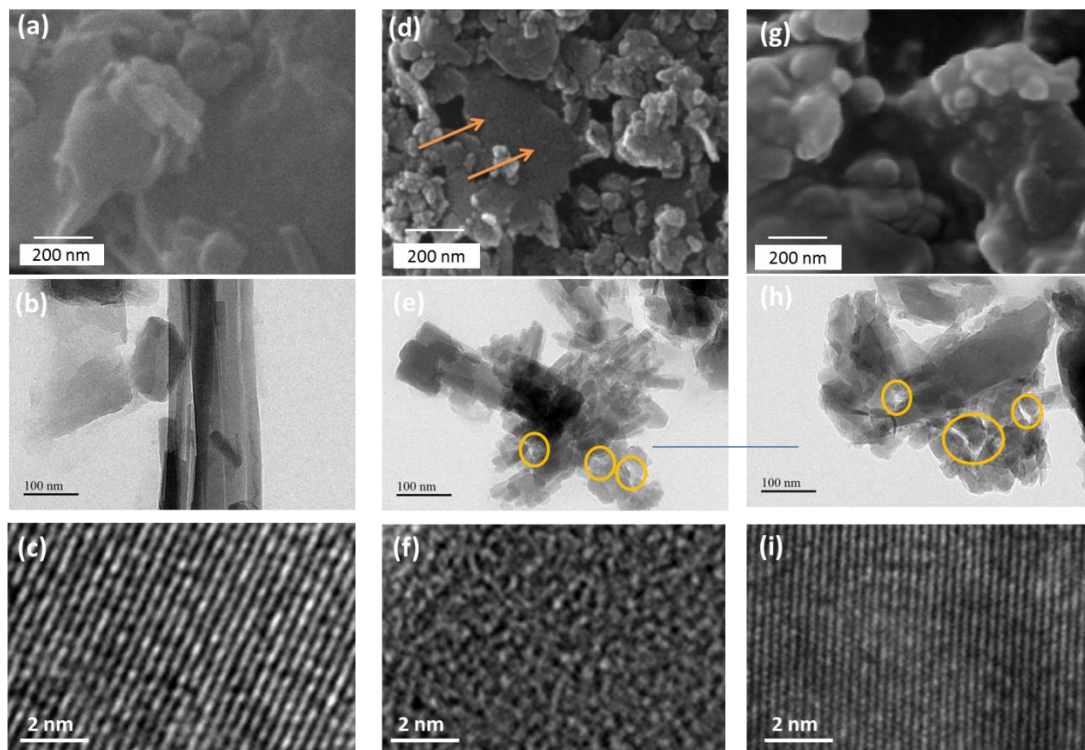


Figure 6.8: SEM images of the parent (a), milled-8h (d) and R-milled-8h (g). TEM images of the parent (b and c), milled-8h (e and f), and R-milled-8h(h and i).

The as-received parent sample was very large in particle size, as shown in the SEM and TEM images (Figures 6.8a, b). The high crystallinity of the parent zeolites is shown in the regular order of lattice fringe on the TEM micrograph (Figure 6.8c). The high-energy ball milling not only reduced the crystallite size (Figures 6.8d, e) but also destroy its crystallinity as shown by the disorder of the lattice fringe (Figure 6.8f). The recrystallization step has been applied to recover the crystallinity of the milled sample. After the recrystallization step, the TEM image of the recrystallized sample shows high crystallinity (Figure 6.8i), while retaining the nanosized crystals (Figure 6.8h). The amorphous phase on the nanosized milled zeolites has been recrystallized with the very tiny crystalline parts of the undestroyed zeolite that act as the seed. We noticed that the

weight of the recrystallized sample has increased to 1.2 g from the initial 1 g of the milled sample. Hence, the yield of zeolite in the recrystallization step was 44%. Here, the yield of zeolite was calculated as the weight ratio of the dried recrystallized sample to the sum of dry weights of silica gel and the milled zeolites. It is worth mentioning that the zeolite yield in the ball milling step was almost 100%. The mesopores were observed on the SEM image of the milled mordenite (Figure 6.8d) whereas it was not clearly seen on the recrystallized SEM image. The TEM images revealed clearly the intercrystalline mesopores as the results of stacking nanosized crystal on the milled and the recrystallized mordenite (Figure 6.8e, h). The way of nanosized crystal packing is important because the voids formed between the crystals provide access for the molecules to diffuse in and out the micropores channel.

The total BET surface area was increased dramatically as the microporous pore-system was recovered 1.5 times the parent micropore area. The increase of the micropore channel was probably due to the conversion of the amorphous phase and the impurities phase i.e. quartz and clinoptilolite to the MOR framework as shown in the XRD study (Figure 6.7). The recrystallized sample exhibited higher intensity and fewer impurity peaks than the parent. The volume of mesopores, which was created during the milling process, remained high as compared to the volume of the parent as well as the external surface (Tables 6.4 and 6.5). A slight decrease in mesopore volume of recrystallized mordenite as compared with that of the milled sample was probably due to the growth of the new mordenite phase (Figure 6.5). The number of acid sites also increased significantly as compared with the cases of the milled and parent samples (Figure 6.6). The total acid sites of recrystallized mordenite was $10.6 \text{ cm}^3/\text{g}$ whereas the parent was only $7.0 \text{ cm}^3/\text{g}$. The acid sites on the

MOR micropore channels of the recrystallized sample were the main contributor to increasing the total acid sites. The recrystallized sample presented a narrow distribution NH_3 -TPD curve which probably caused by the more homogeneous of mordenite phase.

6.4.4 Qualitative Kinetics Dimethyl Ether to Olefins

The DME conversions over the parent, milled and recrystallized zeolite were 1.2%, 54.1%, and 99.7%, respectively, as presented in Figure 6.9. It was noticed that the activity of parent natural zeolites was far lower than the milled and recrystallized zeolites. Typically, the molecular size of DME is within the range 4.3-5 Å [160]. Natural mordenite is known as a small-port mordenite with an effective aperture of about 4 Å, which much smaller than the effective aperture of the large-port mordenite (ca. 7 Å) [149, 157, 161]. It is needed to explain that the small-port mordenite has a similar size micropore channel with the large-port mordenite. However, the adsorption performance of large-port mordenite is higher than the small-port mordenite. The structural defects on the micropore channel systems of the small-port mordenite interrupt the continuity of the micropore channel, leading to poor adsorption performance [149, 150]. As described in Section 3.2, the morphology of the parent mordenite was observed as a long size fibrous crystal shape. The fibrous shape has fewer of the largest 12-membered ring channels than the plate-shaped large-port mordenite [157]. The small-port type, long size fibrous crystal shape, 1-D pore structure of the natural mordenite parent, and large molecular size of DME restricted the molecules of DME from diffusing into the micropores. Moreover, the impurities and extraframework aluminum might block the pores of the parent and limit the access to the acid sites in the micropores. These direct us to the reasons why the DME conversion of the parent natural zeolite was very low.

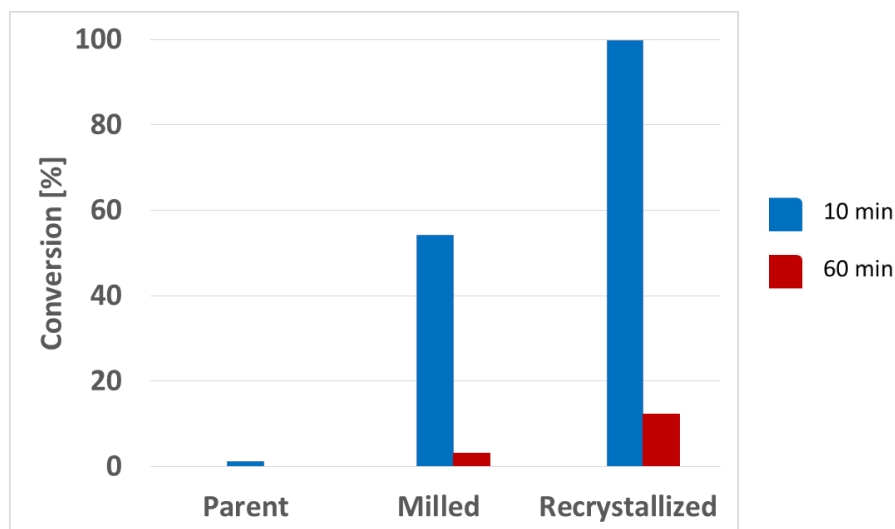


Figure 6.9: DME conversion over parent and treated natural MOR zeolites at T= 350 °C, P= 1 bar, and W/F=0.85 h.

The nanosized particles and presence of intercrystalline mesoporosity over the milled and the recrystallized mordenite enhance the accessibility of molecules to and from the active sites, which induces a higher DME conversion. The parent, small-port mordenite, might be re-formed into the large-port mordenite behavior after milling as the catalytic activity was 45 times much higher on the milled mordenite even though the acidity was reduced by more than a half. This fact suggested that the undestroyed acid sites on the micropore channel of the milled mordenite were effectively reached by the DME. In contrast with the parent that most of the acid sites were not utilized due to the small-port behavior that excluded molecules larger than 4.2 Å. The interesting catalytic activity presented over the recrystallized mordenite at TOS 10 min showed that almost all of DME converted into the products. This is probably due to the recovered microporous system of mordenite, which led to a higher acidity after recrystallization. The hydrothermal recrystallization treatment was conducted at 170 °C which favored the growth of the large-port mordenite. The first

large-port mordenite was synthesized by Sand [148] at a temperature less than 260 °C, whereas the small-port mordenite was synthesized under high temperature 275-300 °C. In addition, the intercrystalline mesoporous system and the number of small particle sizes that formed in the milling step remained high in the recrystallized mordenite which is highly important to provide access and to shorten the diffusion path to the active sites for the molecules.

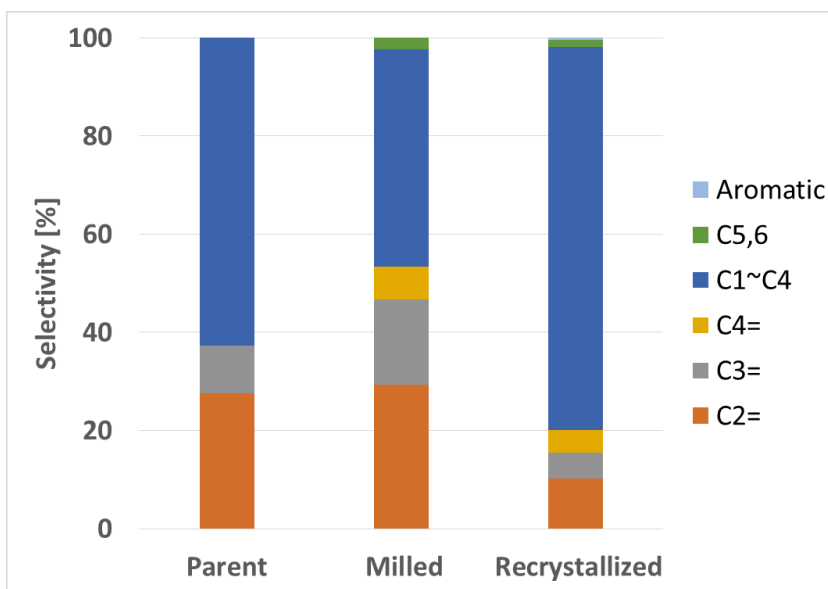


Figure 6.10: Products selectivity over parent and treated natural zeolites at TOS = 10 min.

Dimethyl ether over the parent natural mordenite was converted to light alkanes (methane, ethane, propane, butane) and olefins (ethylene, propylene, butylene). Besides the light alkane and olefin products, DME also transformed into traces of longer hydrocarbons (pentane, hexane) over the milled mordenite and additionally aromatic products over the recrystallized mordenite (Table 6.6). The selectivity to olefins over the milled-8h zeolite was the highest (53%) as compared with that for the parent (37%) and the recrystallized

MOR (20%) for 10 min reaction (Figure 6.10). Selectivity to olefins was highly related to the zeolite acidity as reported elsewhere [22, 162] that the lower concentration of acid sites favor high selectivity to light olefin products. In agreement with the reports, the reduced acidity after the milling process led to high selectivity to olefins while the recrystallized mordenite with a high density of acid sites showed the lowest selectivity to olefins as compared with that of the parent and the milled mordenite. The parent showed the moderate acidity to be between that of the recrystallized and the milled mordenite; hence the selectivity to olefins also in between the recrystallized and the milled mordenite. Another technique like dealumination over natural mordenite has also successfully decreased the acidity of mordenite, which contributed a better selectivity to olefins [22]. The silicon to aluminum ratio is very important in tuning the selectivity to light olefins and it was investigated that the high silica to alumina (280) provided the highest selectivity to olefins [162]. Hence, the dealumination technique, with either physical or chemical treatment will be beneficial in designing an olefin selective catalyst.

Table 6.6: DME conversion, selectivity, and yield of products over parent and treated samples at TOS 10 and 60 min.

sample	DME Conversion (%)	C ₂ ⁼ (%)	C ₃ ⁼ (%)	C ₄ ⁼ (%)	C ₁ ~C ₄ (%)	C _{5,6} (%)	aromatic (%)	olefin yield (%)
parent	1.2 (0)	27.6 (0)	9.7 (0)	0 (0)	62.7 (0)	0 (0)	0 (0)	0.4 (0)
milled-8h	54.1 (3.1)	29.2 (6.0)	17.4 (3.9)	6.7 (0)	44.4 (90.1)	2.3 (0)	0 (0)	29.0 (0.3)
milled-8h- recrystallized	99.7 (12.3)	10.2 (10.2)	5.2 (4.8)	4.7 (0)	78.0 (85.1)	1.4 (0)	0.40 (0)	20.1 (1.8)

The bracket values are data at TOS = 60 min.

The selectivity to olefins (ethylene, propylene, and butylene) over recrystallized MOR at TOS 10 min was the lowest, whereas the selectivity to paraffin (C1-C4) was the highest among other zeolite samples. The aromatics were also observed on the product stream of the recrystallized MOR. These facts suggest that the secondary reaction of the olefins through hydrogen transfer and cyclization caused the high selectivity to paraffin and aromatic, subsequently. The high acidity favors the hydride transfer which shifts the olefins selectivity to alkane selectivity. After 60 min of reaction, the selectivity to light olefins over the parent and the milled zeolite decreased significantly. On the contrary, the selectivity to light olefins over the recrystallized zeolite was relatively stable for the same reaction time and the highest as compared with the selectivity over the parent and the milled zeolite (Figure 6.11). This probably can be explained by the number of accessed

acid sites being still much higher as compared with numbers for the parent and the milled zeolite, especially due to the acid sites on the external surfaces because the acid sites located on the micropores were blocked due to coke deposition. The recrystallized zeolite has the highest acidity concentration as confirmed by the NH_3 -TPD result with the narrow curve distribution on the weak acidity. The external surfaces on the recrystallized mordenite most probably consist of the active acid sites. In contrast, the external surface area on the milled zeolite was inactive due to the demolished MOR framework after the milling step. It was confirmed by the lower activity of the milled MOR as compared with that of the recrystallized mordenite.

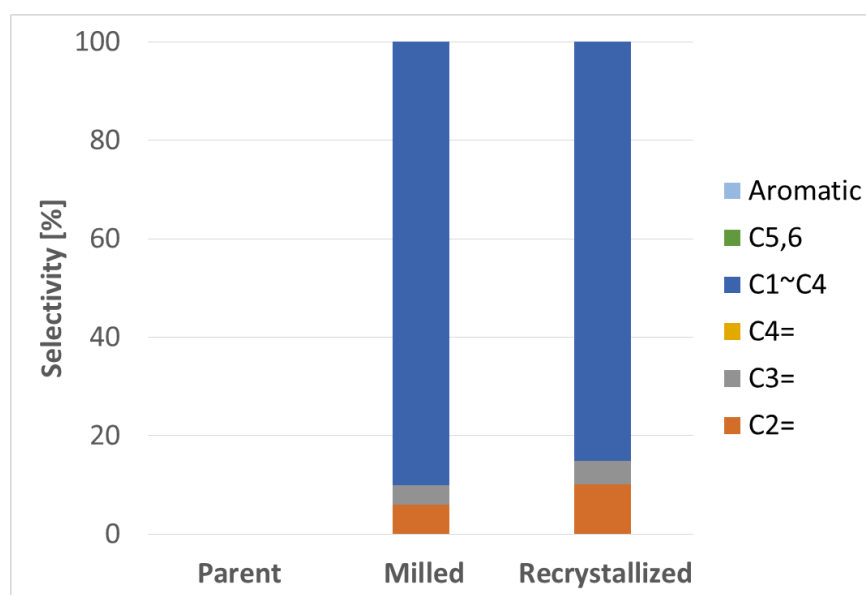


Figure 6.11: Products selectivity over parent and treated natural zeolites at TOS = 60 min.

As the reaction time increased, the coke deposition started to block the pore channels and covered the acid sites. There was no activity over the parent natural zeolites after 1 h reaction due to the coke deposition. The one-dimensional pore structure is rapidly

deactivated due to the fast coke deposition, which inhibited dimethyl ether from entering the micropore [163]. The catalyst lifetime increased over the milled zeolite and the recrystallized zeolite due to the mass transfer enhancement as a result of the smaller particle sizes and formation of hierarchical systems. This phenomenon also can be found in another report on methanol-to-hydrocarbon conversion over H-ZSM 22, which concluded that the increase in catalyst lifetime was favored by the reduction of the crystal size [25]. Similarly, the wet milling of another zeolite framework (H-ZSM-5) reduced the crystal size and the acidity, which were the main factors that improved the lifetime of catalyst in the oxidation of benzene to phenol [164].

6.4.5 Economic Evaluation of High-Energy Ball Milling and Recrystallization Process

The price of natural zeolite as received was only ca. \$ 0.3 per kg (USD) which was obtained from a company in Indonesia. From the literature survey, we find the synthetic zeolite price was \$ 247 /kg [165] for commercial scale in the industry. The laboratory grade of synthetic mordenite was more expensive such as \$ 558 [166] in sodium form and 720 \$ /kg [167] in the ammonium form. The ball milling is an efficient unit operation which is widely practiced in the industrial process. The recrystallization process was a very fast hydrothermal process with 2 h only as compared with the synthetic MOR with 48 h of hydrothermal treatment. Moreover, there is no need for OSDA (organic solvent directing agent) and alumina in the recrystallization process which will cut the chemical cost as compared with the synthetic mordenite preparation. In addition, the OSDA free of the recrystallization process is environmentally friendly. From our laboratory scale calculation (Table 6.7 and 6.8), the ball milling operation cost was ca. \$ 2.9 per kg and the

recrystallization step cost was ca. \$ 3.8 per kg. Hence, the recrystallized-milled mordenite derived from natural zeolites was ca. \$ 7.0 per kg which is still far cheaper than the laboratory grade synthetic one (ca. \$ 247 to 720/kg) and technical grade synthetic (ca. \$ 10 to 20/kg) [2].

Table 6.7: Milling operational cost calculation.

Sample (kg)	Power (kW)	Time (h)	Total power (kWh)	Power cost (USD/kWh)	Total power cost (USD)	Cost per kg sample (USD/kg)
0.2	0.6	8	4.8	0.12	0.576	2.9

Table 6.8: Recrystallization cost calculation.

Sample (kg)	Chemical	Mass required (kg)	Price (USD/kg)	Total (USD)	Cost per kg sample (USD/kg)
0.005	Silica gel	0.00347	5	0.01735	3.5
	NaOH	0.00154	1	0.00154	0.3

6.5 Concluding Remarks

Hierarchical natural mordenite has been synthesized from low-cost natural zeolites through a high-energy ball milling and a combined ball milling-recrystallization method. Crystallinity was decreased to a certain extent with the milling time. The recrystallization technique has recovered the zeolite microstructure while retaining the intercrystalline mesoporous and large external surface is formed in the milling step. High conversion of DME and selectivity to olefins was obtained over the milled MOR. The low acidity after milling step favors high selectivity to olefins. The nanosized crystals combined with the intercrystalline mesopores generated on the milling step effectively enhance the catalyst activity and selectivity to olefins. An improved catalyst lifetime has been achieved over the milled MOR zeolite and the recrystallized MOR zeolite. The recrystallized zeolite gave the highest conversion of DME and the most stable sample in this selected process. Both milling and milling-recrystallization routes are potential to synthesize a cost-effective catalyst from natural zeolites.

CHAPTER 7

SELECTIVE ISOMERIZATION N-BUTANE OVER NANOPARTICLES MOR FROM NATURAL ZEOLITES FABRICATED VIA SEQUENTIAL BALL MILLING- RECRYSTALLIZATION-DEALUMINATION ROUTE

7.1 Summary

A sequential fabrication step involving mechanochemistry, recrystallization and dealumination were developed to convert low-cost natural zeolites to mordenite (MOR). Natural zeolites are mostly found having poor textural properties and high aluminum content, which are not suitable for most industrial catalytic reactions. The parent natural mordenite (MOR) within the size of 1-10 μm were treated by the ball milling in order to obtain the nanosized mordenite with size in the range of 20-160 nm. The nitrogen physisorption study revealed that the external surface area and intercrystalline mesopore volume of the milled nanoparticles increased by 4 and 7-fold respectively. The recrystallization by hydrothermal treatment in basic silicate solution was applied to recover the MOR crystallinity at 170 $^{\circ}\text{C}$ for 6 h. Recrystallized MOR zeolite were further subjected to acid dealumination treatment for different time. The H-MOR samples were evaluated in a fixed bed reactor for n-butane isomerization to study the particle size effect. The isobutane selectivity over the recrystallized nanoparticle increased from 11% to 28% when the parent microparticle was substituted by the recrystallized nanoparticles. Moreover, the catalyst stability improved over the recrystallized nanoparticles. The dealuminated-

recrystallized nanoparticle exhibited the highest selectivity of ca. 58% to isobutane and less deactivation rate a result of low acid site density and small nanoparticle size.

7.2 Introduction

Natural zeolites are abundantly available around the world particularly as sedimentary deposits around volcanic regions. Open-pit mining operation, an easy mining technique, is being used to exploit the natural zeolites. As a result of these reasons, the cost of natural zeolites is far cheaper than that the synthetic zeolites. However, natural zeolites have several drawbacks, such as high impurities, poor textural properties, lower adsorption capacity, and inconsistency composition. Consequently, natural zeolites are mostly commercialized for applications with non-strict application and required in bulky scale. Natural zeolites are applied as an adsorbent water purification and wastewater treatment, as a fertilizer in agriculture, for ammonium removal in aquaculture, and as raw materials for construction [5]. There are several types of frameworks that are frequently occurring in nature as sedimentary rocks such as clinoptilolite (HEU), analcime (ANA), philipsite (PHI), chabazite (CHA), and mordenite (MOR) [1]. The synthetic counterpart of the MOR framework has a wide commercially use as industrial catalyst.

Mordenite zeolite comprises of two pore types, which are a 12-membered ring (MR) with a size $6.5 \times 7 \text{ \AA}$ and an 8-MR with a compressed size of $2.6 \times 5.7 \text{ \AA}$ along the c-axis. The 12-MR and 8-MR are bridged by 8-MR side pockets with a size of $3.4 \times 4.8 \text{ \AA}$ along the b-axis [65, 157]. However, those 8-MR are not accessible for most of the molecules; hence, MOR is often considered as a unidimensional pore. There are two types of MOR based on adsorption capacity, i.e., large-pore and small-pore. The large-pore is capable of adsorbing more molecules than the small-pore, which excludes the molecules more than 4.5 \AA [148].

The small-port MOR blocks large molecules as a result of the structural fault [149]. Recently, Simoncic and Amrbruster reported that both the small- and large-port MORs have similar defects; hence, the behavior of natural MOR acting as a small-port is still enigmatic [157]. The synthetic MOR is the large-port MOR, which is synthesized at a temperature less than 260 °C. On the other hand, the small-port MOR is produced at a higher temperature within 275 to 300 °C. The natural mordenite is commonly found as a small-port type. It is well-known that dealumination is an effective technique to convert the small-port to large-port mordenite [150, 168].

MOR is commercially used as industrial catalysts for toluene disproportionation, amination, C₂-C₃ transalkylation, naphtha isomerization, ethylbenzene isomerization, and n-butane isomerization [169]. Isomerization of n-butane to isobutane over Pt/chlorinated alumina is an important reaction in the industry, of which isobutane is converted alkylates [170]. The chemical is capable of improving the octane number of gasoline. Unfortunately, Pt/chlorinated alumina is a non-regenerable catalyst and sensitive to contaminants, such as sulfur and nitrogen [169]. One potential candidate to replace the Pt/chlorinated alumina catalyst is Pt/H-MOR. The MOR catalyst offers some advantages, i.e., tolerate to water and sulfur and easy regeneration.

Over the past decade, nanosized zeolites have been attracting researchers as a result of their superiority over conventional micro-sized crystals. Nanoparticle MOR has a large specific surface area, owing to its small crystal size. This gives several benefits, such as less mass transfer limitation, prolonging the catalyst lifetime, and high catalyst activity [171]. The nanoparticles also created intercrystalline mesopores, which are formed by the stacking of nanoparticles. Recently, Chu et al. [93] reported that the intercrystalline mesopores of

ferrierite zeolite increased the stability and product selectivity in 1-butene isomerization. The nanosized zeolite is prepared through bottom-up strategies by hydrothermal synthesis or a top-down approach by milling treatment [11, 111]. The top-down approach is a potential method to obtain nanoparticles from natural zeolites. However, the milling technique reduces the zeolite crystalline phase remarkably. The combination of milling with hydrothermal recrystallization has been reported successful in producing highly crystalline nanoparticle MOR [59, 60].

A high silicon/aluminum ratio (Si/Al) of MOR favored the isobutane selectivity and catalyst stability in the n-butane isomerization. On the other hand, aluminum-rich MOR favored selectivity to propane and less stability as cokes developed faster during the reaction [121, 172, 173]. A post-modification treatment that is commonly practiced to increase Si/Al is acid dealumination. Acid dealumination will also decrease the number of acid sites, particularly the Brønsted acid sites (BAS) and create micro- and mesopores in the MOR framework [22, 113, 174]. The micropore volume and the strong acid sites were responsible for the high activity in hexane isomerization [106]. The mesopore are important to shortening the molecule path length in the zeolite pores.

The n-butane isomerization mechanism has been studied by many researchers in which the mechanistic pathway is still arguable whether through monomolecular or bimolecular pathway [174-177]. Monomolecular pathway explains that the isobutane is formed through formation of primary carbenium ions as an intermediate, which required strong acid sites provided by a high silica to alumina ratio MOR [172]. However, the bimolecular pathway explains that the isobutane formed through dimerization→isomerization→cracking, which involved C₈ carbenium intermediate [175]. Recently, a study was conducted to investigate

the butene effect on the reaction mechanism, which showed that low butene concentration favored the monomolecular and high butene concentration favored the bimolecular pathway [177]. Through experiment by poisoning the Brønsted acid sites particularly on the external surfaces area and mesopores by using 1,1,1,3,3,3-hexamethyldisilazane revealed that the high external surface area and/or mesopore favored n-butane isomerization through the bimolecular pathway [174].

In this work, we investigated the effect of MOR nanoparticles in n-butane isomerization. The nanosized MOR samples were derived from low-cost natural zeolites through ball milling-recrystallization and ball milling-recrystallization-dealumination techniques. To the best of our knowledge, the systematic study of MOR nanoparticles for n-butane isomerization is rarely reported

7.3 Experimental

The natural zeolite samples were modified through various treatments such as high-energy ball milling, hydrothermal recrystallization, and acid dealumination. We also prepared synthetic mordenite via hydrothermal as a comparison with the natural zeolites. The flowchart of the experiment is presented in Figure 7.1. Here, the detailed explanation of the experiment is provided as below.

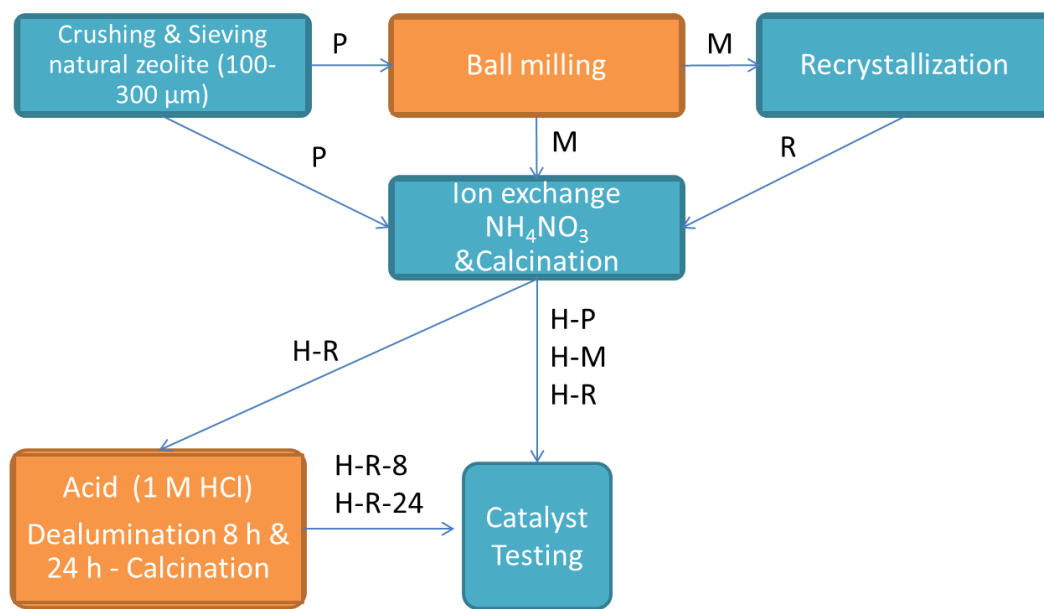


Figure 7.1: Flowchart of the experiment.

7.3.1 Material Characterization

The zeolite phase has been studied using powder X-ray diffraction (XRD, Miniflex-Rigaku) with an angle 2θ from 5° to 50° . The scanning rate was $3^\circ/\text{min}$ with a step size of 0.03° . The morphology and particle sizes of samples were examined by field-emission scanning electron microscopy (FE-SEM, LYRA 3 dual beam, Tescan). The aluminum structure was studied by the ^{27}Al magic angle spin nuclear magnetic resonance (^{27}Al MAS-NMR). Elemental composition was measured by X-ray fluorescence (XRF) (Bruker).

Physisorption adsorption-desorption was carried out in ASAP 2020 (Micromeritics). The samples were heated up to 350°C and maintained for 6 hours before nitrogen adsorption. Liquid nitrogen was used to maintain the temperature of the sample at -196°C during the nitrogen gas adsorption-desorption. Pore size distributions were estimated by density functional theory (DFT)-Tarazona method.

The acid strength was performed by ammonia-temperature programmed desorption (NH_3 -TPD, Micromeritics ChemiSoft TPx V1.02). The sample was heated to 600 °C, dwelled for degassing 30 min under flowing of 25 mL/min helium. Thereafter, the temperature was decreased to 120 °C. Ammonia was introduced to the sample for 30 min and then flushed by helium for 1 h. Subsequently, the temperature was raised at a rate 10 °C/min from 120 °C to 700 °C for ammonia desorption.

The Nicolet 6700 spectrometer was used for pyridine Fourier transform infrared spectroscopy (FTIR) study. The samples for normal FTIR were prepared by mixing the 10 mg of samples powder with 200 mg of KBr to be pelletized. The samples for the pyridine-FTIR study were prepared by pelletizing 20 mg of sample. The pellet was dried at 500 °C for 30 min. After cooling to 150 °C, pyridine was introduced into the sample for 15 min, followed by evacuating pyridine that physically adsorbed for 30 min. Spectra were taken at 150 °C, 250 °C, and 400 °C. The parameters with a resolution of 8 cm^{-1} in the range wavelength of 400–4000 cm^{-1} and 100 scans were applied during the analysis. The calculation of pyridine FTIR adsorbed followed an equation published elsewhere [112].

7.3.2 Nanosized MOR Preparation

A high-energy ball milling attritor (Union Process HDDM-01) was used to reduce the particle size using water as a dispersion medium. The natural zeolites were obtained from Klaten, Central Java, Indonesia. The particle size of the as-received natural zeolites was 4-5 mm. Prior to milling, the sample was crushed and sieved into a smaller size, 0.1-0.3 mm. A total of 50 g of natural zeolite was milled by controlling the agitator speed at 2000 rpm for 8 h. The ball material was made of zirconia (ZrO_2), with a fine ball size of 650 μm in diameter. The heat generated from the milling process was removed by the water

maintained at 13 °C circulated through the jacket of the milling tank. The slurry was dried overnight at 80 °C. The milled nanoparticle sample was called M. The dried milled powder was ion-exchanged twice with 2 M NH_4NO_3 with a ratio of 1:20 by weight at a temperature of 85 °C under reflux and vigorous stirring action for 2h. Afterward, the powder was dried at 110 °C overnight and calcined in static air at 550 °C for 8 h (H-M).

7.3.3 Recrystallization

The milled sample (M) was treated hydrothermally using alkaline silicate solution (18 SiO_2 /12 NaOH /780 H_2O). Fumed silica (Sigma-Aldrich) was dissolved in sodium hydroxide solution. Afterward, 1 g of the milled powder was mixed with the alkaline silicate solution. After mixing for 15 min, the solution was heated at 170 °C for 6 h in an autoclave (Parr). The slurry was centrifuged and washed with deionized (DI) water several times until neutral pH was reached. Solid particles were separated and dried overnight at 110 °C. After ammonium nitrate ion exchange and calcination, as described in section 7.3.3, the sample was labeled as H-R.

7.3.4 Acid Dealumination

The recrystallized sample (H-R) was dealuminated using 1 M hydrochloric acid to partially remove aluminum and other metals. Dealumination was performed under reflux with constant stirring at 350 rpm for 8 and 24 h and maintained at a temperature of 85 °C. The sample were washed several times with deionized water. Next, the samples were dried overnight at 110 °C and calcined for 8 h at 550 °C under static air, labeled as H-R-8 and H-R-24 for dealumination times of 8 and 24 h, respectively.

7.3.5 Catalysts Evaluation

The catalyst powder (0.5 g) was tested in a fixed bed reactor made of Inconel with an inside diameter of 5.16 mm equipped with gas chromatography (GC) online analysis. The temperature was increased from ambient temperature to 500 °C for 30 min and dwelled for 30 min under a flow rate of 20 mL/min nitrogen. The temperature was reduced to 350 °C for 30 min, followed by feeding 2 mL/min of n-butane (99.5%) and 20 mL/min nitrogen and dwelled for 200 min for the n-butane isomerization under atmospheric pressure. The products was observed using GC (Agilent 7890a) with two columns (Agilent HP-INNOWax PEG and Agilent J&W GC-GasPro) and flame ionization detectors.

7.4 Results and Discussion

7.4.1 Characterizations of the Samples

The XRD pattern of the parent sample (H-P) shows that MOR is the major phase with several accessories, i.e., clinoptilolite (HEU) and quartz (Figure 7.2). The crystallinity of all phases was reduced after the high-energy ball milling treatment as the intensity peaks were decreased, as shown by the XRD pattern of H-M sample at 2θ of 9.6°, 22.5°, 25.8°, 27°, and 28°. The hydrothermal recrystallization step has successfully recovered back the MOR crystalline phase. This is indicated by the higher intensity of XRD peaks of MOR on H-R compared to H-M and H-P. Interestingly, some peaks, which belong to HEU in the parent, disappeared after milling and did not recover after recrystallization, such as the peaks at 2θ of 11°, 13°, 17.3°, 26.2°, and 30.5°. The solution composition, temperature, and time applied on the hydrothermal treatment were selective to the growth of MOR crystals. The milling-recrystallization strategy has been also successfully applied in preparing

nanosized ZSM-5, zeolite A, and zeolite X [14, 20, 109]. Acid dealumination over the recrystallized nanoparticles reduced the crystallinity, as showed in the XRD patterns of H-R-8 and H-R-24 as a result of the partial aluminum removal of the MOR framework (Figure 7.2).

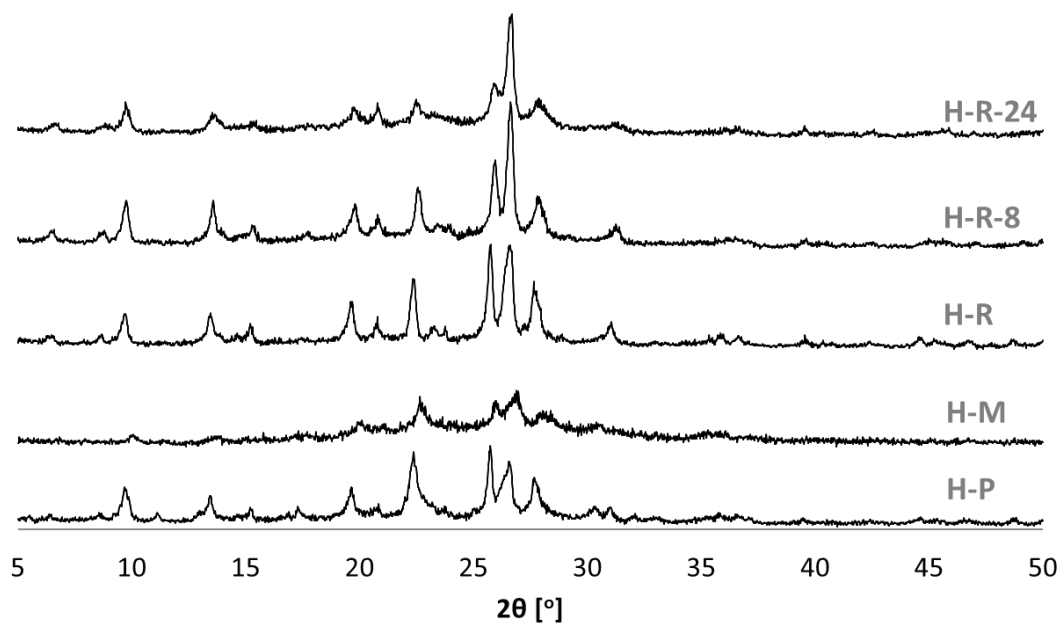


Figure 7.2: XRD patterns of H-MOR parent and modified H-MOR samples.

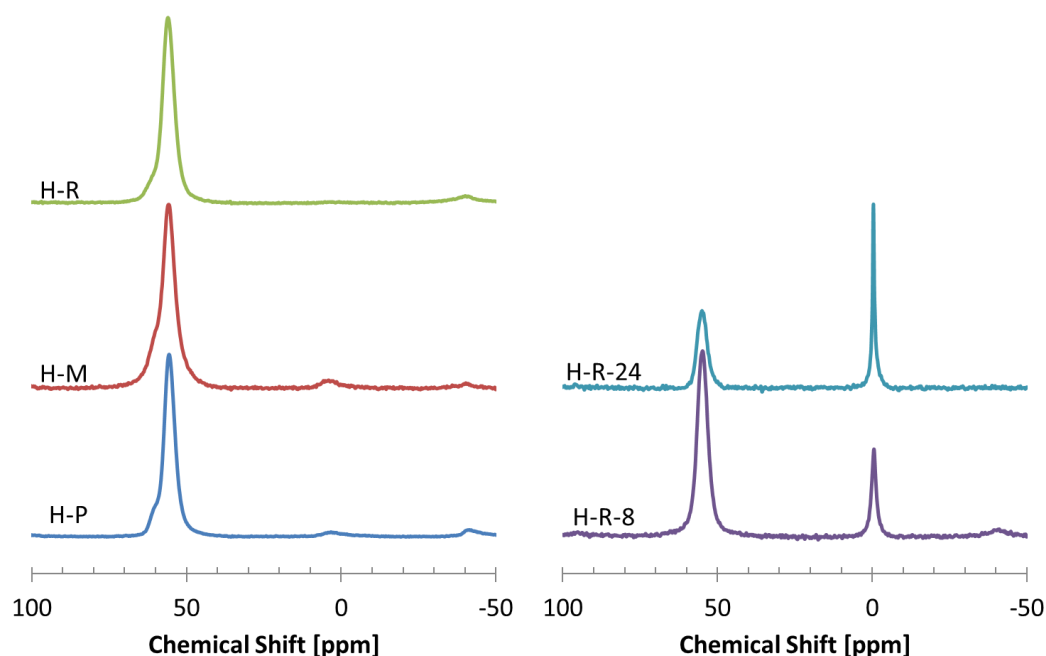


Figure 7.3: ^{27}Al NMR spectra of H-MOR samples

The ^{27}Al NMR spectra of H-MOR samples are presented in Figure 7.3. The parent natural zeolite sample showed a typical zeolite tetrahedral (AlO_4) peak at 55 ppm with a small peak at 0 ppm attributed to the extraframework aluminum (EFAL) of the octahedral (AlO_6). The ball milling led to partial distortion of the AlO_4 structure, as shown by the higher intensity of the shoulder on the main peak at 55 ppm of the H-M curve [178]. A slight increase of the AlO_6 peak at 0 ppm was also observed on the milled sample (H-M), which indicated that the ball milling positively affected the EFAL formation. The recrystallization step removed the AlO_6 peak and reduced the shoulder peak at 55 ppm, which suggested that the tetrahedral AlO_4 structured has been recovered. The peak at 0 ppm in the dealuminated MOR is attributed to the EFAL formation of AlO_6 . The peak

became higher as the time of acid dealumination was applied longer, as shown in H-R-24. The intensity of AlO_4 also decreased after dealumination, as shown on the peak at 55 ppm. Recrystallization of milled nanoparticle has increased the silicon/aluminum ratio from 6 to 9 based on the XRF analysis. Silica was introduced in the recrystallization solution to recover the crystallinity of the milled sample; hence, it was not surprising that the silica content increased in H-R. Despite the high alkalinity, the high silica content in the recrystallization solution avoided desilication of the milled powder. Dealumination with 1 M HCl over the recrystallized nanoparticles partially removed aluminum. The Si/Al ratio increased from 9 to 31, when acid dealumination applied for 8 h. The longer acid treatment time (24 h) led to less aluminum content in the sample, and the silicon/aluminum ratio of H-R-24 increased to 39.

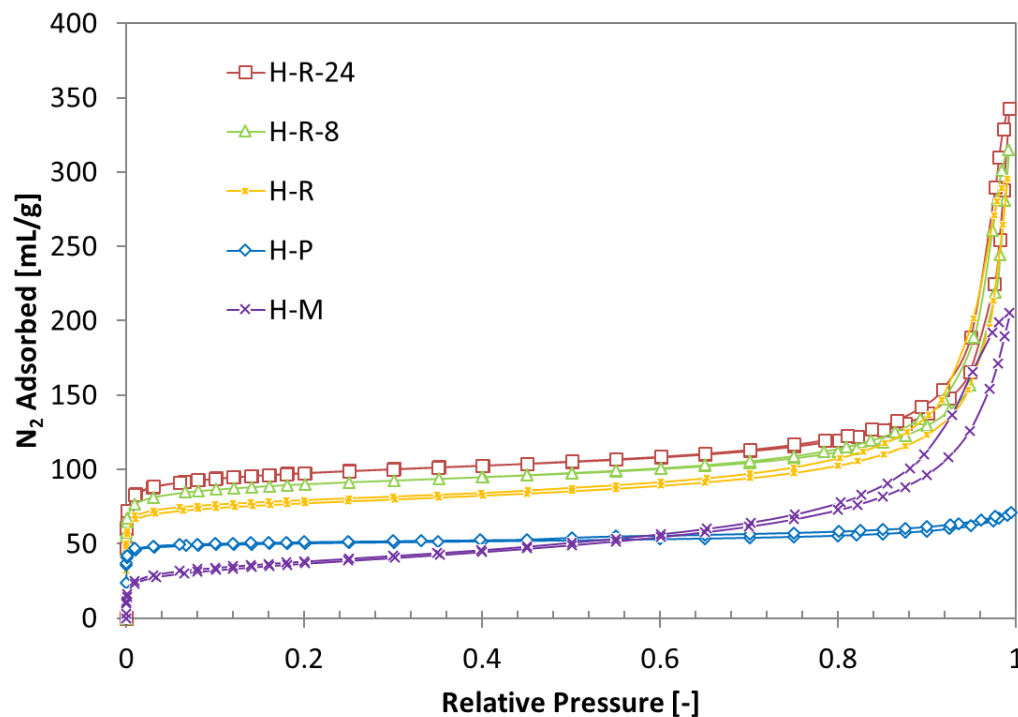


Figure 7.4: Nitrogen isotherms of H-MOR samples.

Table 7.1: Textural properties and silicon/aluminum ratio of the parent and treated samples

Sample	S_{BET} (m^2g^{-1})	S_{t} (m^2g^{-1})	S_{ext} (m^2g^{-1})	V_{total} (cm^3g^{-1})	V_{micro} (cm^3g^{-1})	V_{meso} (cm^3g^{-1})	Si/Al* (-)
H-P	183	160	23	0.100	0.068	0.032	6
H-M	131	31	100	0.238	0.013	0.225	6
H-R	286	215	71	0.303	0.090	0.213	9
H-R-8	333	254	79	0.340	0.105	0.235	31
H-R-24	354	272	83	0.350	0.115	0.235	39

*XRF

Textural properties of the H-MOR samples were analyzed by nitrogen physisorption (Table 7.1). The isotherms of all samples were presented in Figure 7.4. The external surface area increased 4-fold after the milling step from 23 to 100 m^2/g , indicating that the particle size reduced significantly. Unfortunately, the micropore was partially demolished after the milling step, as shown by the decrease of the micropore volume. The micropores recovered and increased after recrystallization compared to the milled and parent samples. Dealumination increased both the micro- and the mesopore volume. It can be seen that, after 8 h dealumination, the micropore volume increased from 0.090 cm^3/g to 0.105 cm^3/g and the mesopore volume increased from 0.213 cm^3/g to 0.235 cm^3/g . Dealumination for 24 h increased the micropore volume from 0.105 cm^3/g to 0.115 cm^3/g , whereas the mesopore remains unchanged. The increase in the micropore over mild acid dealumination was also reported elsewhere as a result of the opening pore of the side pocket 8-MR and creation of the secondary micropore of the MOR channel after aluminum removal from its framework [106].

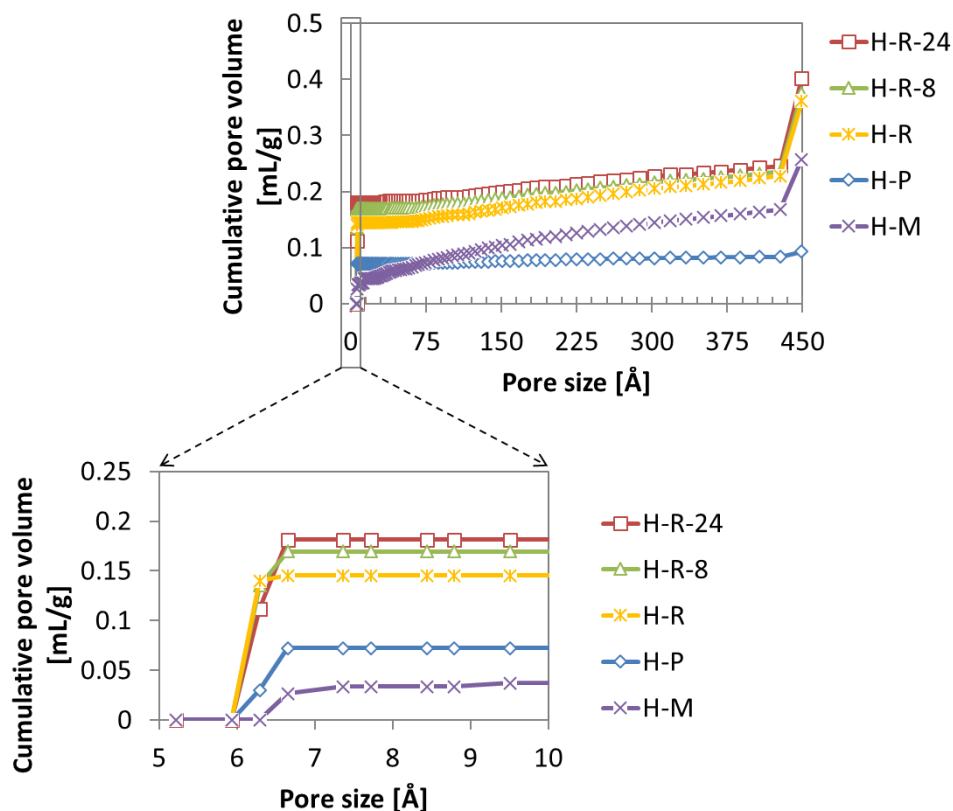


Figure 7.5: Cumulative pore volume versus pore size of the parent and treated samples by the DFT method.

The pore size distribution using the density functional theory (DFT) method is presented in Figure 7.5. The micropore size was within the size range of 5.9 Å–6.7 Å, which is typical of the MOR pore. The mesopores in the milled and recrystallized samples most likely were voids formed as the nanosized particles stacked, which is called the intercrystalline mesopore. It was the milling step that created the hierarchical pore system of zeolite as nanosize was formed during the ball milling. Aluminum was partially removed after dealumination of the recrystallized nanoparticles, creating new micropores and intracrystalline mesopore channels. Acid dealumination increased the micropore volume within the size range from 6.3 to 6.7 Å. The mesopores started from size a 3.5 nm and

increased gradually to 45 nm. The hierarchical pore system consisted of a micropore, intercrystalline mesopore, and intracrystalline mesopore observed in the dealuminated nanosized samples (H-R-8 and H-R-24) .

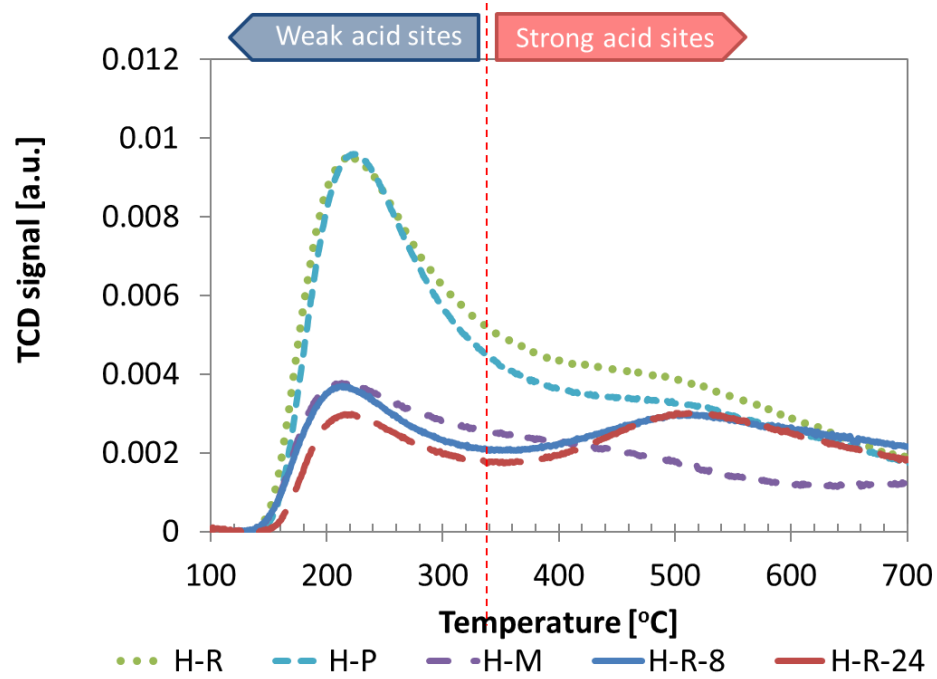


Figure 7.6: Acidity of H-MOR samples by ammonia-TPD.

Table 7.2: Acid sites of the samples by NH_3 -TPD

Sample	Weak acid sites (WAS) [$\mu\text{mol/g}$]	Strong acid sites (SAS) [$\mu\text{mol/g}$]	WAS/SAS [-]	Total acid sites by NH_3 -TPD [$\mu\text{mol/g}$]
H-P	192	134	1.4	326
H-M	80	45	1.8	125
H-R	210	152	1.4	362
H-R-8	74	110	0.7	184
H-R-24	63	107	0.6	170

Ammonia-TPD was conducted to study the acidity of samples (Figure 7.6). The weak acid sites (WAS) are shown from 140 °C to 340 °C, and the strong acid sites (SAS) are shown in the curve from 340 °C to 700 °C. The milling step reduced the total number of acid sites from 326 to 125 μmol of NH_3/g (Table 7.2) as a result of the collapse of the micropore channels, as shown by the nitrogen physisorption study. After recrystallization, the total number of acid sites increased to 362 μmol of NH_3/g , which is higher than the milled and parent samples. This fact is in agreement with the higher micropore volume of the recrystallized sample over the milled and parent samples (Table 7.1). The dealumination step reduced the total acid sites, both the WAS and SAS (Figure 7.6). In fact, decrease of the WAS was observed in a significant amount compared to the SAS. Before dealumination, the ratios of WAS/SAS of the samples (H-P, H-M, and H-R) were more than 1. After dealumination, the ratios of WAS/SAS of the dealuminated samples were less than 1. Niwa et al. [103] reported that the BAS in the 12-MR of MOR were weaker than that in the 8-MR. The data suggested that the partial removal of aluminum greatly affected the WAS in the large-pore channel 12-MR. Dealumination probably opens access to the other SAS in the small 8-MR, which was not accessible before the aluminum removal. As a result, the decrease of SAS was not observed in a large number, as happened in the WAS. To further investigate the dealumination effect on the acidity, we performed FTIR with pyridine as a probe, which is larger than ammonia.

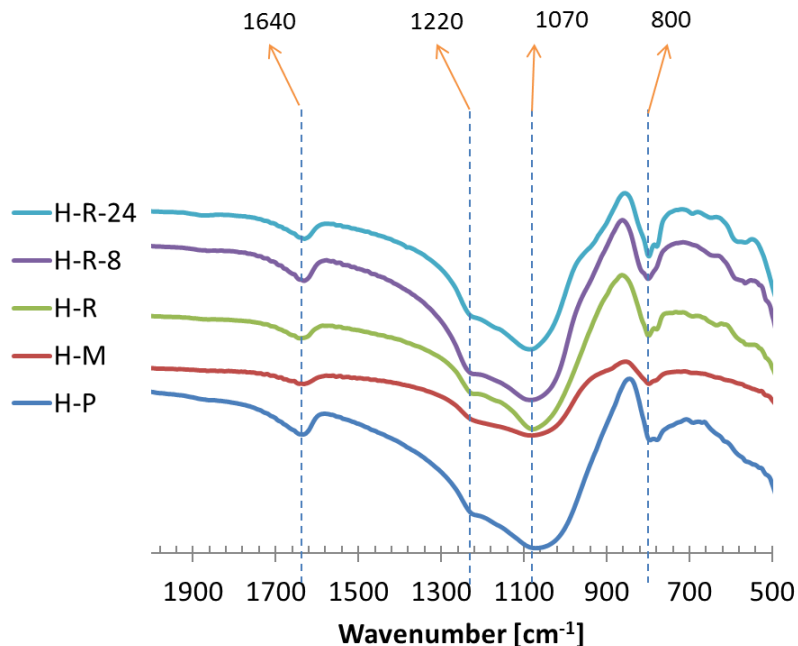


Figure 7.7: FTIR spectra of H-MOR samples.

FTIR study result is presented in Figure 7.7. The absorption band at 1220 cm^{-1} was ascribed as the asymmetric stretching vibration of external linkage and 1070 cm^{-1} assigned to the asymmetric stretching vibration of internal in natural mordenite [179, 180]. The absorption band at 800 cm^{-1} was assigned to symmetric external vibration [180].

Pyridine FTIR was conducted to identify the Brønsted and Lewis acid types (Table 7.2). The Brønsted acid type was found to be dominant in all samples except H-M, which showed the higher amount of the Lewis acid sites (LAS) as the extraframework of aluminum formed after the sequential process of ball milling-ion exchange-calcination. The EFAL in the milled sample was confirmed by the ^{27}Al NMR study (Figure 3). The LAS was also increased significantly after HCl dealumination for 8 h. It was due to that the LAS created as the aluminum partially removed from the framework and formed the

extraframework aluminum which was shown in the ^{27}Al NMR analysis. The LAS over the dealuminated sample for 24 h were higher than the 8 h acid treatment as the removal of the aluminum from the framework became intense. Surprisingly, the Brønsted acid sites (BAS) over the dealuminated H-R-8 and H-R-24 were higher than the non-dealuminated MOR (H-R). The dealumination of recrystallized MOR which derived from the small-pore natural mordenite will open the accessibility to the acid sites in the side pockets 8-MR channel for large probe molecules such as pyridine ca. 5.7 Å due to the partial removal of aluminum of the side pockets [162]. In contrast, the small probe ammonia (ca. 3 Å) was able to penetrate into the small 8-MR channel of the non-dealuminated MOR [181]. As the result, the acid sites concentration of the recrystallized MOR (H-R) was higher on the ammonia-TPD analysis as compared with the dealuminated MOR. We can conclude that the acid dealumination on MOR was important to open the access to the acid sites on the side pockets 8-MR channel of MOR, particularly for large molecules such as pyridine.

Table 7.3: Brønsted and Lewis acidity of the samples

Sample	Brønsted acid sites ($\mu\text{mol/g}$)			Lewis acid sites ($\mu\text{mol/g}$)		
	150 °C	250 °C	400 °C	150 °C	250 °C	400 °C
H-P	67	48	27	23	17	17
H-M	34	23	2	38	31	26
H-R	107	89	50	25	17	17
H-R-8	125	105	58	51	46	44
H-R-24	111	97	57	57	51	47

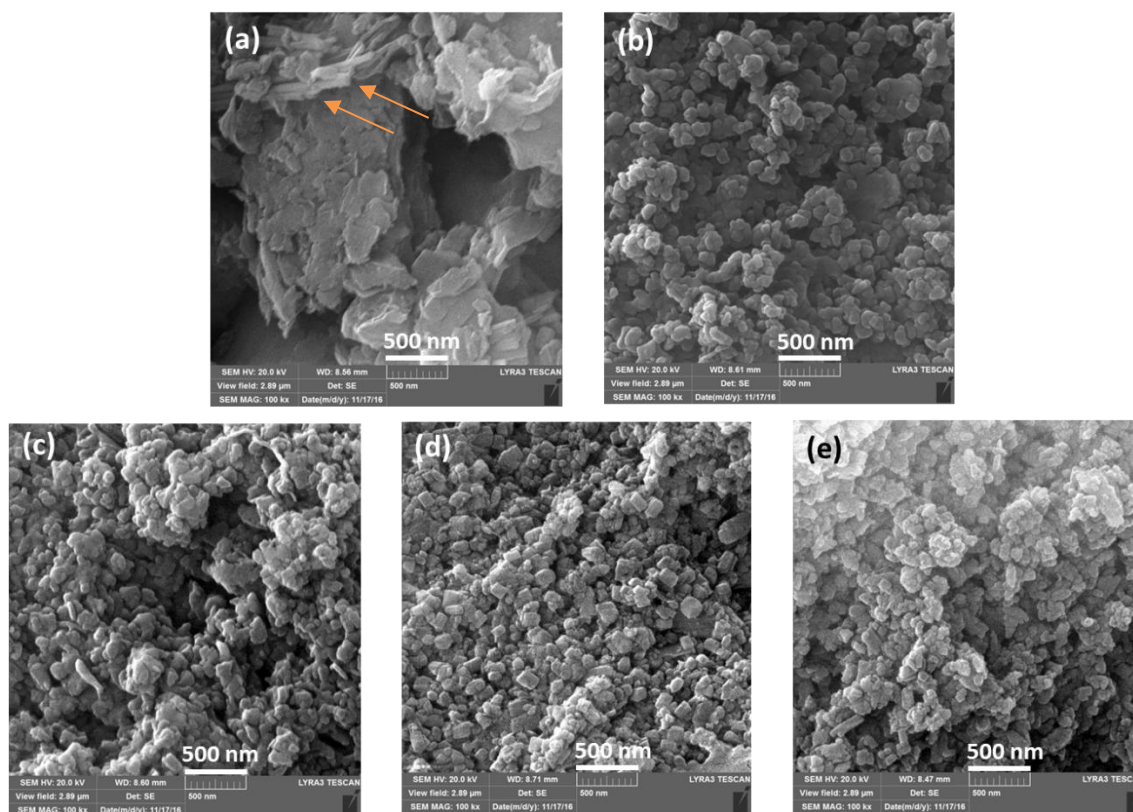


Figure 7.8: SEM images of (a) H-P, (b)H-M, (c) H-R, (d) H-R-8, and (e) H-R-24.

The scanning electron microscopy (SEM) images were studied to measure morphology and the particle size of the samples (Figure 7.8). The parent crystal shape (H-P) was in irregular form; however, a few of them represented the needle shape (indicated by arrows in Figure 7.8a). After the milling step, the particle shape became more regular with the spherical dominant shape. The particle size distribution based on the SEM images is presented as histograms in Figure 7.9. The parent H-P consisting of large a particle size was within the range of 1 to 10 μm . High-energy ball milling was effectively reduced the particle size into nanosize with the size of 20-160 nm, with 80% of the particle size less than 100 nm (Figure 7.9b). The recrystallization process slightly increased the particle sizes as a result of the

growth of crystalline MOR in the hydrothermal step, as confirmed by XRF with the increasing of silica content on the sample of H-R (Figure 7.9c). The particle size distribution of dealuminated-recrystallized 8 h (H-R-8) and 24 h (H-R-24) showed a similar size with recrystallized MOR (Figure 7.9d and 7.9e). The average particle size of H-R, H-R-8 and H-R-24 was about 90 nm.

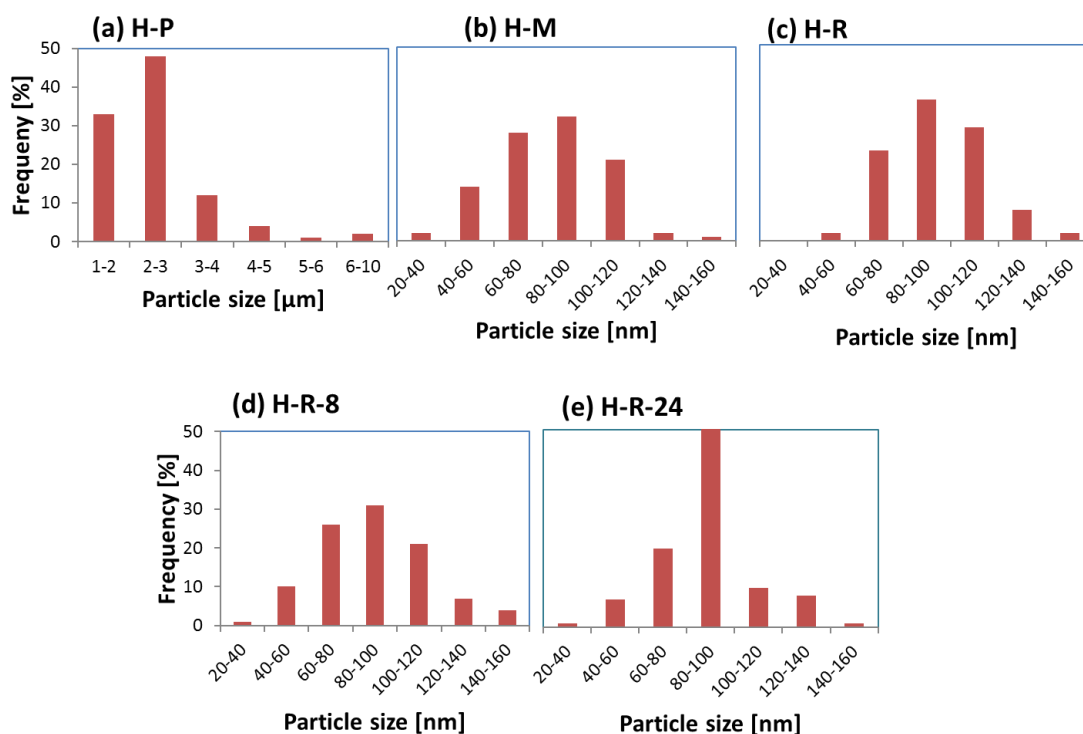


Figure 7.9: Particle size distribution of H-MOR samples.

7.4.2 Particle size effect on n-butane isomerization

Initially, n-butane conversion over the nanosize recrystallized (H-R) sample was slightly higher, ca. 14%, compared to the micro-sized parent (H-P), ca. 13%, at a time on stream (TOS) of 10 min (Figure 7.10). It was due to the H-R sample containing slightly higher total acid sites indicated by ammonia TPD as compared to H-P. After 50 min of reaction,

n-butane conversion over H-P was significantly decreased to only 0.1%. In contrast, the catalyst deactivation over H-R was slower, with n-butane conversion remaining high, ca. 8% at TOS of 50 min. The unidimensional pore of MOR is prone to coke formation, which blockage of the pore; hence, the molecules are unable to reach the acid sites. We observed a more darkening color of the spent parent catalyst compared to the spent recrystallized sample and the spent milled sample, indicating severe coke deposition in the parent catalyst. Wulfers and Jentoft[182] studied the coke deposition on MOR in n-butane isomerization. They found that coke mainly consisted of methyl-substituted naphthalenes, anthracenes, tetracene and polycyclic aromatic species. The H-R nanoparticles have a large external surface area and shorter diffusional pathway; as a consequence, the molecules easily react on the surface and diffuse out, hence retarding the coke deposition.

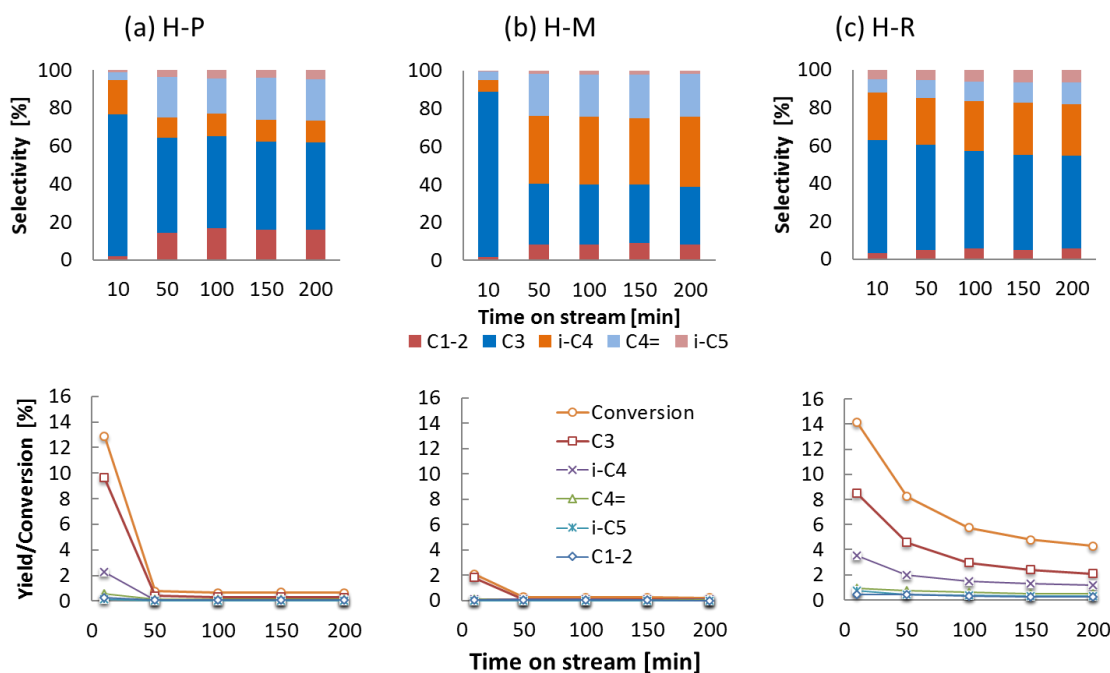


Figure 7.10: Isomerization of n-butane over (a) H-P, (b) H-M, and (c) H-R at $T = 350\text{ }^{\circ}\text{C}$, $\text{C}_4\text{H}_{10} = 2\text{ mL/min}$, $\text{N}_2 = 20\text{ mL/min}$.

The particle size of H-MOR has also affected the product distribution of n-butane conversion (Figure 7.10). The n-butane transformation over nanosized H-R exhibited a higher isobutane product with 28% as compared to the micro-sized H-P of only 11% at TOS 200 min. It was the particle size that governed the higher isobutane selectivity of H-R nanoparticles. The bimolecular mechanism was most likely the main route because it required a high external surface area which provided in nanosized H-R. This finding is supported by the literature discussed elsewhere [174]. The side products of the bimolecular mechanism are propane and pentane via disproportionation. In fact, pentane and butane will undergo a secondary reaction to produce more propane, e.g., $C_4 + C_5 \leftrightarrow 3C_3$ [172]. The nanoparticle size inhibited the secondary reaction, with the pore length shorter than that of micro-sized MOR. It can be seen from Figure 10 that propane selectivity at TOS of 10 min was 60% over H-R, lower than H-P of 75% at relatively similar conversion. These facts suggested that the nanoparticle size increased the isobutane formation and decreased the propane selectivity.

Table 7.4: Conversion of n-butane transformation and products distribution over the mordenite catalysts at TOS = 10 min and 200 min (in the bracket).

Sample	Conversion (%)	Selectivity (%)							
		C1	C2	C2=	C3	C3=	i-C4	C4=	i-C5
H-P	13	1	1	0	72	3	18	4	1
	(1)	(4)	(3)	(9)	(42)	(4)	(11)	(22)	(5)
H-M	2	0	0	2	85	2	6	5	0
	(0)	(0)	(0)	(0)	(0)	(0)	(0)	(0)	(0)
H-R	14	0	0	2	58	2	25	7	5
	(4)	(1)	(1)	(4)	(47)	(2)	(27)	(11)	(7)
H-R-8	15	0	1	2	37	1	49	7	3
	(6)	(0)	(0)	(2)	(27)	(1)	(58)	(9)	(4)
H-R-24	17	0	1	2	31	1	54	7	3
	(11)	(0)	(0)	(1)	(27)	(1)	(58)	(9)	(4)

The propane selectivity was the most decreased product selectivity over TOS in the recrystallized sample (H-R). It decreased from 58% (TOS=10 min) to 47% (TOS=200 min) (Figure 7.10c and Table 7.4). In contrast, the isobutane selectivity slightly increased over TOS from 25% to 27%. It can be explained that the bimolecular pathway occurred on both the mesopores/external surfaces and micropores in the fresh catalyst. The reaction in micropores with high acid density led to high propane and low isobutane selectivities. Over the time, the microporous channel became no longer accessible as a result of the coke blockage on the pore, which indicated by the sharp decrease of activity at TOS = 50 min. Practically, the butane transformation mainly occurred on the mesopores and external surface area, which reduced the propane formation of the secondary reaction.

H-M exhibited the lowest activity since the beginning of the reaction, although the particle size was within the nanosized range (Figure 7.10b). It was due to the total acid site in the H-M sample being the lowest among others, as indicated by NH_3 -TPD. It was also confirmed by pyridine FTIR that the BAS of H-M were the lowest among other samples. The isomerization reaction of n-butane to isobutane was greatly affected by the BAS as reported elsewhere [183]. At 10 min of reaction, the selectivity to propane reached the highest at 87%, while the selectivity to isobutane was only 6%. This is probably due to the acid sites on the external surface area being mostly damaged in the milling step; hence, isomerization through a bimolecular reaction, which is mainly favored on the external surface area, was reduced significantly. Only the small part of acid sites retained in the one-dimensional (1D) micropore channel was active in the transformation of n-butane. The catalytic activity in 1D MOR led to a high propane selectivity through the bimolecular pathway, followed by the secondary reaction in the micropore [172]. Although the external

surface area contributed to the reaction products, the numbers were not significant as compared to the catalytic activity on the acid sites of the micropore. This was confirmed through the product distribution after blockage of the micropore by coke led to catalyst deactivation, which occurred at 50 min (Figure 7.10b). The product distribution shifted with high selectivity to isobutane, ca. 36%, and with low selectivity to propane, ca. 32%. This occurred most likely as a result of the decrease of the propane formation in the micropore being much higher instead of the decrease of the isobutane product.

n-Butane transformation over H-MOR was proposed through the bimolecular mechanism by Asuquo et al. [115] as follows: (i) formation of a butyl carbenium ion (via protonation, hydride abstraction, and thermal cracking) (ii) formation of a C₈ carbenium ion via dimerization (iii) formation of *n*-butane and isobutane via isomerization, and (iv) formation of propane and pentane via disproportionation. The intermediate large molecule C₈ carbenium ion has to be formed in the bimolecular mechanism; hence, the plausible way of the bimolecular mechanism to take place is on the external surface area and mesopore [184]. The product distribution is greatly affected by the mesopore presence on dealuminated MOR which favored the selectivity to isobutane because it prevents the secondary transformations of the reaction products during their diffusion throughout the 1D pore of MOR [172, 176]. We found that the high-density acid sites (Si/Al = 9) with a large external surface area and high intercrystalline mesopore volume on recrystallized MOR (H-R) increased the selectivity to isobutane compared to the parent.

A report suggested another explanation that the product distribution was also driven by the butene concentration on the catalyst bed [177]. The low concentration of butene (<20 ppm) favors the monomolecular mechanism, while the high concentration of butene (>120 ppm)

favors the bimolecular mechanism. The Figure 7.10 shows that the butene concentration was remarkably high, which led to the conclusion that the bimolecular pathway occurred significantly with products of isobutane, propane, and pentane. The investigation of transformation propane over MOR with a Si/Al ratio of 10 showed that the propane conversion was very low [185], indicating the high stability of propane. For low Si/Al ratio MOR, the bimolecular pathway most likely occurred with secondary reactions of isobutane with pentane in the micropore channel leading to high propane. These explain why propane selectivity was very high over the micro-sized particle H-P. In fact, propane selectivity over H-R was almost double isobutane selectivity.

7.4.3 Dealumination of Nanoparticles Recrystallized MOR

The as-received natural zeolites were rich in aluminum ($\text{Si/Al} = 6$). The high aluminum content, particularly when the Si/Al ratio less than 6.1, disfavored the isobutane selectivity [172, 176]. For low a Si/Al ratio, it is necessary to have a high mesopore and a high external surface area to obtain a high selectivity to isobutane. Dealumination with a mild acid concentration increased the activity of MOR to convert *n*-butane and favored selectivity to isobutane. The silicon/aluminum ratio was increased to 31 after 8 h of acid dealumination. The smaller particle size gives benefit in the dealumination process as the removal of aluminum from the pore becomes faster [18]. The ammonia TPD study suggested that the acid sites reduced after acid dealumination (Figure 7.6). The monomolecular reaction, which is more selective to isobutane, occurred on the high Si/Al ratio along with the bimolecular pathway. The monomolecular pathway demands high-strength acid sites, which provided as aluminum become more isolated (less acid site density) based on the next nearest neighbor (NNN) theory. The dealumination also opened

the side pocket 8-MR of the micropore as reported elsewhere [113]. The pyridine FTIR study suggested that the accessibility of the probe molecules to the BAS in the side-pocket 8-MR was increased after the dealumination. The BAS in the 8-MR were reported stronger than that in the 12-MR [105]. The ammonia TPD study also revealed that the ratio of SAS/WAS increased significantly after dealumination. In addition, the micro- and mesopore volumes of the dealuminated samples were higher than those of the recrystallized sample. The increase in the accessibility to the high-strength acid sites in dealuminated MOR favored the isomerization reaction through the monomolecular pathway. Furthermore, the bimolecular pathway most likely prefers the isomerization reaction instead of disproportionation at a low acid site concentration, as reported elsewhere [115]. As a result, the selectivity to isobutane significantly increased to 58% and the selectivity to propane dropped to 27% at TOS of 200 min in both of the dealuminated nanoparticles, H-R-8 and H-R-24 (Table 7.4).

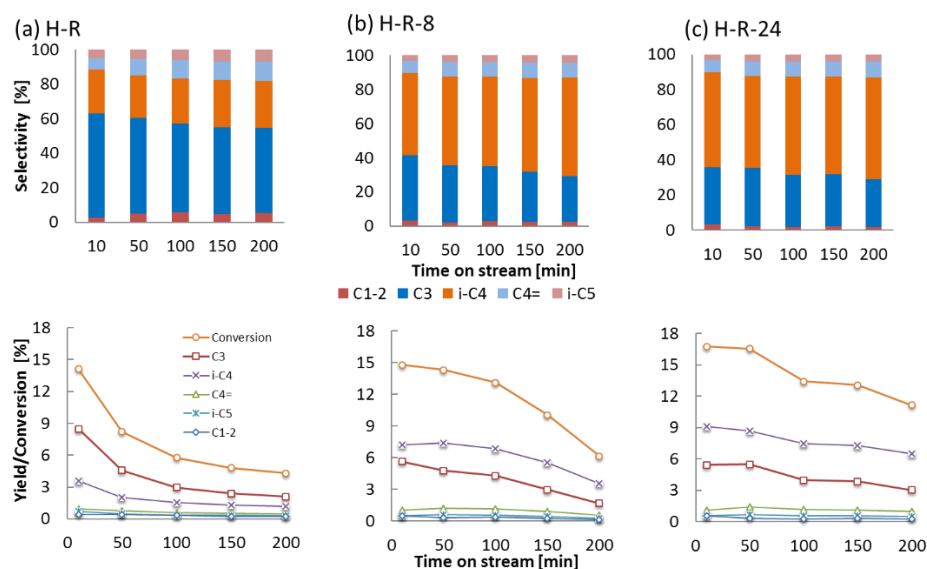


Figure 7.11: Isomerization n-butane over (a) H-R, Brønsted and Lewis acidity of the samples (b) H-R-8 and (c) H-R-24, at T = 350 °C, C₄H₁₀ = 2 ml/min, N₂ = 20 ml/min.

We found that the time of acid dealumination affected the activity and stability of the catalyst. More aluminum was removed from the framework as dealumination applied in a longer time of 24 h, which led to a higher silicon/aluminum ratio of 39. The nitrogen physisorption study showed that the micropore volume increased along with the time of dealumination. The activity of H-R-24 was higher compared to that of H-R-8 (panels b and c of Figure 7.11). It is probably due to the increasing access to the strong BAS in the side-pocket 8-MR of the micropore, as suggested by nitrogen physisorption, ammonia TPD and pyridine FTIR studies (Table 7.1). In addition, the H-R-24 stability was higher compared to that of H-R-8 because less acid concentration reduced the coke formation rate. In fact, the H-R-24 sample showed the brightest color, which indicated that the coke deposition is the lowest among other samples (Figure 7.12). It is worth mentioning that there was no increase in the mesopore volume from 8 to 24 h of acid dealumination treatment. Hence, we can conclude that the high stability of H-R-24 was most likely due to not only the nanosized but also less acid site density, which inhibited the coke formation.

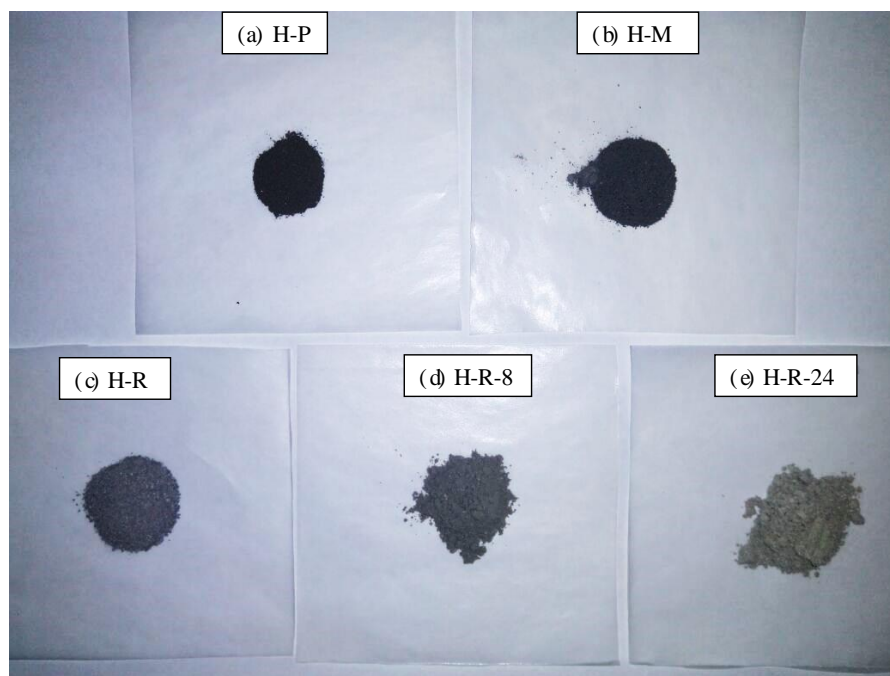


Figure 7.12: The spent catalysts of (a) the micro-sized parent and nanoparticles of (b) the milled, (c) recrystallized, (d) recrystallized-dealuminated 8 h, and (e) recrystallized-dealuminated 24 h.

The extraframework aluminum (EFAL) in the milled sample (H-M) and the dealuminated samples was high as indicated by the ^{27}Al NMR study. The EFAL acts as LAS, which might play a significant role in a catalytic reaction. However, the LAS in the milled sample had no positive effect on the n-butane isomerization as shown by the low activity over the H-M sample. This is in agreement with a study by Babůrek and Nováková [183], which revealed that the presence of LAS in zeolites decreased the n-butane conversion and selectivity to isobutane. The results of n-butane isomerization over H-M support the conclusion that the high conversion of n-butane and selectivity to isobutane over the dealuminated samples were due to the high access to strong BAS in the side pocket.

We also investigated the performance of the dealuminated parent (H-P-8) and dealuminated nanoparticles (H-R-8) under a temperature of 420 °C to further confirm that the particle size was important in the n-butane isomerization. The conversion of dealuminated nanoparticles was higher compared to that of the dealuminated parent, as shown in Figure 7.13. It is suggested that the high external surface area of H-R-8 led the molecules to easily reach the acid sites. The selectivity to isobutane over H-R-8 was also higher than that over the H-P-8. This confirmed that the particle size of the sample before dealumination was important because the performance of the n-butane isomerization reaction was better on dealuminated nanosized MOR.

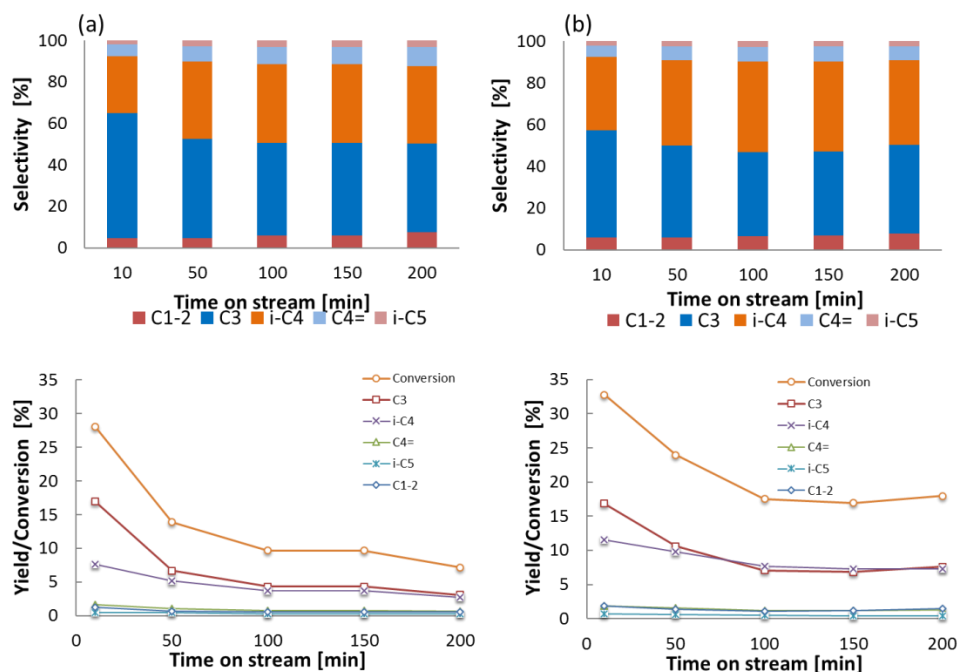


Figure 7.13: Comparison between acid dealuminated 8 h of (a) the parent and (b) nano-MOR in n-butane isomerization at T= 420 °C.

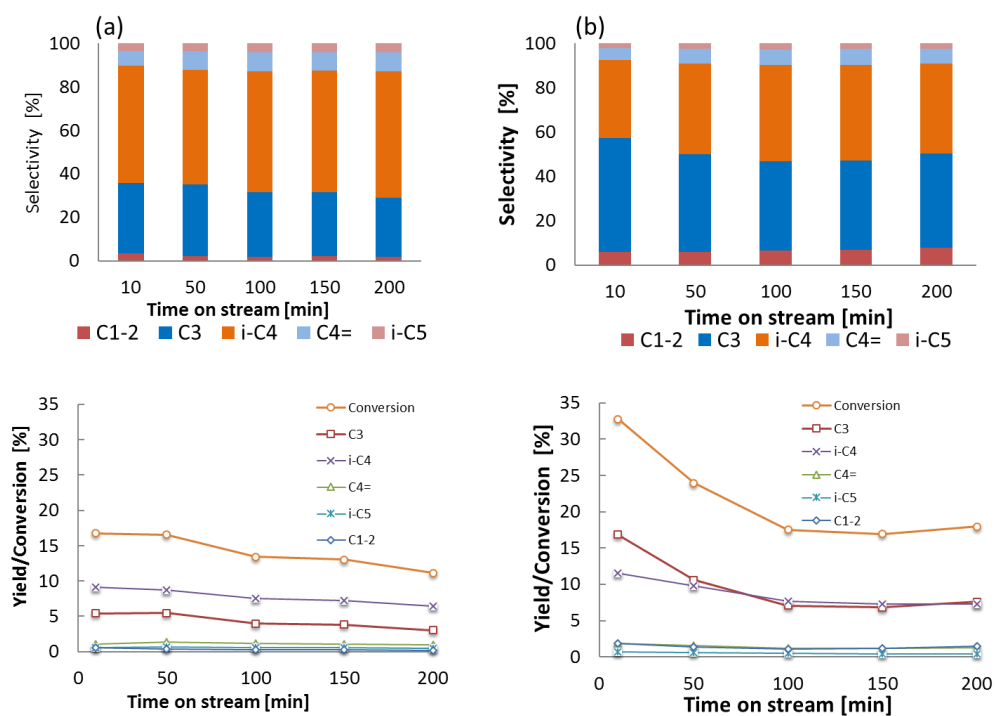


Figure 7.14: Catalytic performance over nano-MOR (H-R-24) for n-butane isomerization at different temperature (a) T= 350 °C and (b) T= 420 °C.

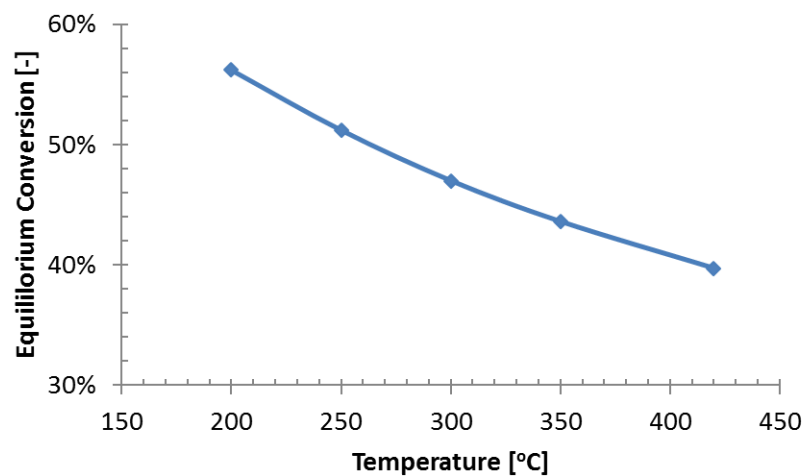


Figure 7.15: Thermodynamic conversion of n-butane isomerization between 200 to 420 °C.

The high temperature has increased the conversion of n-butane over the dealuminated nanoparticle (H-R-8). However, selectivity to isobutane was reduced at a high temperature (Figure 7.14). The yield of isobutane at 420 °C was slightly higher compared to that at temperature of 350 °C. At a high temperature, the reaction rate increased; hence, the conversion of n-butane was also higher. However, from the thermodynamic point of view, the equilibrium conversion of n-butane isomerization to the product of isobutane decreased along with the increase of the temperature, which indicated that n-butane isomerization is an exothermic reaction (Figure 7.15). Another thing is that the high temperature promoted the disproportionation pathway which produced propane and pentane [115]. Those are the reasons why the selectivity to isobutane was decreased as the temperature increased, which is in an agreement with the literature [115, 186].

7.5 Concluding Remarks

The MOR nanoparticles have been manufactured through ball milling from natural MOR, followed by hydrothermal recrystallization to recover the crystallinity. The MOR nanoparticles exhibited higher selectivity and stability in n-butane isomerization compared to micro-sized MOR. The large surface area and high intercrystalline mesopore volume of the MOR nanoparticles favored the isomerization through the bimolecular reaction mechanism. Dealumination of the MOR nanoparticles further increased the selectivity to isobutane. The monomolecular pathway favored the selectivity to isobutane over the dealuminated samples as a result of the higher access to the strong acid sites in the 8-MR. The short diffusion pathway of the nanoparticles and the low acid site density remarkably diminished the rate of coke deposition.

CHAPTER 8

CONCLUSIONS AND RECOMMENDATIONS

8.1 General Conclusions

Natural zeolites are well-known as a low-cost material, which has important application in water purification and waste treatment, agriculture, building materials, and gas purification. However, there was only one commercial application of natural zeolite in the catalytic reaction, which was natural erionite in selectoforming process. The impurities, inconsistency composition of natural zeolites and a limited number of industrial favorable natural zeolite frameworks are among the main factors of rare application of natural zeolites as catalysts. The work presented in this thesis has led to new techniques for upgrading the quality of natural zeolites.

The low crystalline natural mordenite with impurities clinoptilolite and quartz were effectively improved by hydrothermal recrystallization technique using basic silicate solution. The recrystallized mordenite samples were exhibited high crystallinity, superior textural properties, and a high number of acid sites as compared with the parent natural mordenite. The amorphous and clinoptilolite impurity phases were dissolved and recrystallized with assistance from mordenite parent as a template to growth new mordenite crystals. The n-butane isomerization over recrystallized mordenite exhibited a comparable yield with the synthetic mordenite and far higher result as compared to the parent natural mordenite. The facile recrystallization technique is potentially applied to improve textural properties, crystallinity, and total acid sites of low-rank natural mordenite.

Nanoparticles zeolites offer benefits in catalysis i.e. high catalyst activity, improve product selectivity and extend the catalyst lifetime [32, 123]. Nanosized mordenite has been successfully fabricated through high-energy ball milling attritor from natural mordenite with water as a dispersant. The mean particle size studied by DLS was 123 ± 47 nm. The Taguchi analysis showed that the ball to powder ratio was more pronounce on minimizing particle sizes and loss of crystallinity and maximizing external surface, mesopore volume, instead of the water to powder ratio. The high-energy ball milling increased remarkably the external surface area more than 6-fold and mesopore volume 11-fold. However, the micropore volume of the natural zeolites decreased significantly.

The high crystallinity and purity of nanosized mordenite were recovered after recrystallized the milled nano-zeolite in basic sodium silicate solution. In addition, the hierarchical pores system was also formed on the milled and recrystallized mordenite. The textural properties of recrystallized nano-mordenite were improved with enhancements in the external surface area, intercrystalline mesopore, and micropore volume. The fast recrystallization time (2 to 6 h) favored the mordenite phase. The silica and OH^- concentration determined significantly the framework of the recrystallized sample. The high ratio of sample mass to basic silicate solution reduced the crystallinity of recrystallized MOR. We have successfully developed a method to produce hierarchical mordenite nanoparticles from low-rank natural mordenite through high-energy ball milling followed by recrystallization strategy without using the harmful and expensive organic structure directing agents (OSDA).

High conversion of dimethyl ether (DME) and selectivity to olefins was obtained over the milled mordenite. The low acidity after milling step favored high selectivity to olefins. The

nanosized crystals combined with the intercrystalline mesopores generated on the milling step effectively enhance the catalyst activity and selectivity to olefins. An improvement in catalyst lifetime has been achieved over the milled mordenite and the recrystallized mordenite. The recrystallized zeolite gave the highest conversion of DME and the most stable sample in this selected process. Both milling and milling-recrystallization routes are potential to synthesize cost-effective catalyst from natural zeolites. The catalysts were also tested for n-butane isomerization. The recrystallized mordenite nanoparticles exhibited higher selectivity and stability in n-butane isomerization as compared to the micro-sized parent. The large surface area and high intercrystalline mesopore volume of the mordenite nanoparticles favored the isomerization through the bimolecular reaction mechanism.

Finally, the acid dealumination was applied to the recrystallized nanoparticle mordenite. The pyridine-FTIR study suggested that the accessibility of the probe molecules to the Brønsted acid sites (BAS) in the side pocket 8-membered ring (MR) were increased after the dealumination. The BAS in the 8-MR were reported stronger than the one in the main channels 12-MR [105]. The monomolecular pathway which more selective to isobutane was more pronounced due to the higher access to the strong acid sites in the 8-MR. The short diffusion pathway of the nanoparticles and the low acid sites density remarkably diminished the rate of coke deposition over dealuminated nanoparticles MOR.

8.2 Recommendations

Hydrothermal recrystallization and sequential ball milling-recrystallization strategy for other natural zeolite frameworks such as clinoptilolite and chabazite should be investigated to complete the information on various natural zeolites framework. The effect of initial zeolites phase composition should also be investigated as the composition of natural zeolites depend on the deposit location. Hence, the generalize strategy of hydrothermal recrystallization and sequential ball milling-recrystallization could be developed in order to obtain high-quality natural zeolites.

The application of nanoparticles derived from natural zeolites in other catalytic reactions, biomass pyrolysis and cracking of non-conventional oil, is interesting to be investigated. High oxygen content and long polymeric biomass molecules could be restricted for the conventional zeolites. However, the nanoparticles mordenite with high surface area offers the external surface reaction, which could improve the biomass pyrolysis. Heavy oils and oilsands cracking over cost-effective catalysts are interesting for the future research. The cost-effective catalysts can be fabricated from natural zeolites through simple recrystallization and sequential ball milling-recrystallization method. In addition, the catalytic cracking in upgrading the “dirty” non-conventional oils will benefit the process and environment instead of the non-catalytic thermal process.

Interconversion framework of natural zeolites into another zeolite phase is also interesting to be explored. For examples, interconversion mordenite into faujasite and interconversion of clinoptilolite into the ZSM-5. The successful interconversion method will open a wider industrial application of natural zeolites.

REFERENCES

- [1] C. Colella, Applications of Natural Zeolites, Handbook of Porous Solids, Wiley-VCH Verlag GmbH 2008, pp. 1156-1189.
- [2] J.C. Groen, T. Sano, J.A. Moulijn, J. Pérez-Ramírez, Alkaline-mediated mesoporous mordenite zeolites for acid-catalyzed conversions, *J. Catal.* 251 (2007) 21-27.
- [3] D. Verboekend, T.C. Keller, M. Milina, R. Hauert, J. Pérez-Ramírez, Hierarchy Brings Function: Mesoporous Clinoptilolite and L Zeolite Catalysts Synthesized by Tandem Acid-Base Treatments, *Chemistry of Materials* 25 (2013) 1947-1959.
- [4] F.A. Mumpton, La roca magica: Uses of natural zeolites in agriculture and industry, *Proceedings of the National Academy of Sciences* 96 (1999) 3463-3470.
- [5] C. Colella, Natural zeolites, in: J. Čejka, H.v. Bakkum (Eds.) *Studies in Surface Science and Catalysis*, Elsevier 2005, pp. 13-40.
- [6] M.M.J. Treacy, J.B. Higgins, J.B. Higgins, SAPO-56, in: M.M.J. Treacy, J.B. Higgins, J.B. Higgins (Eds.) *Collection of Simulated XRD Powder Patterns for Zeolites*, Elsevier Science B.V., Amsterdam, 2001, pp. 44-45.
- [7] S.-J. Kang, K. Egashira, Modification of different grades of Korean natural zeolites for increasing cation exchange capacity, *Appl. Clay Sci.* 12 (1997) 131-144.
- [8] S.-J. Kang, K. Egashira, A. Yoshida, Transformation of a low-grade Korean natural zeolite to high cation exchanger by hydrothermal reaction with or without fusion with sodium hydroxide, *Appl. Clay Sci.* 13 (1998) 117-135.
- [9] Y. Wang, F. Lin, Synthesis of high capacity cation exchangers from a low-grade Chinese natural zeolite, *J. Hazard. Mater.* 166 (2009) 1014-1019.
- [10] Y. Watanabe, H. Yamada, J. Tanaka, Y. Moriyoshi, Hydrothermal modification of natural zeolites to improve uptake of ammonium ions, *J. Chem. Technol. Biotechnol.* 80 (2005) 376-380.
- [11] A. Charkhi, H. Kazemian, M. Kazemeini, Optimized experimental design for natural clinoptilolite zeolite ball milling to produce nano powders, *Powder Technol.* 203 (2010) 389-396.
- [12] K. Akçay, A. Sirkecioğlu, M. Tatlıer, Ö.T. Savaşçı, A. Erdem-Şenatalar, Wet ball milling of zeolite HY, *Powder Technol.* 142 (2004) 121-128.
- [13] T. Wakihara, Ihara, Inagaki, Tatami, Sato, Komeya, Meguro, Kubota, Nakahira, Top-Down Tuning of Nanosized ZSM-5 Zeolite Catalyst by Bead Milling and Recrystallization, *Crystal Growth & Design* 11 (2011) 5153-5158.
- [14] T. Wakihara, K. Sato, K. Sato, J. Tatami, S. Kohara, K. Komeya, T. Meguro, Preparation of nano-zeolite X by bead-milling and post-milling recrystallization, *Journal of the Ceramic Society of Japan* 120 (2012) 341-343.
- [15] M. Yang, P. Tian, C. Wang, Y. Yuan, Y. Yang, S. Xu, Y. He, Z. Liu, A top-down approach to prepare silicoaluminophosphate molecular sieve nanocrystals with improved catalytic activity, *Chem. Commun.* 50 (2014) 1845-1847.
- [16] S.M. Kuznicki, W.C. McCaffrey, J. Bian, E. Wangen, A. Koenig, C.C.H. Lin, Natural zeolite bitumen cracking and upgrading, *Microporous and Mesoporous Materials* 105 (2007) 268-272.

- [17] K.A. Thrush, S.M. Kuznicki, Characterization of chabazite and chabazite-like zeolites of unusual composition, *Journal of the Chemical Society, Faraday Transactions* 87 (1991) 1031-1035.
- [18] S. Moreno, G. Poncelet, Dealumination of small- and large-port mordenites: A comparative study, *Microporous Materials* 12 (1997) 197-222.
- [19] T. Wakihara, A. Ihara, S. Inagaki, J. Tatami, K. Sato, K. Komeya, T. Meguro, Y. Kubota, A. Nakahira, Top-Down Tuning of Nanosized ZSM-5 Zeolite Catalyst by Bead Milling and Recrystallization, *Cryst. Growth Des.* 11 (2011) 5153–5158.
- [20] T. Wakihara, R. Ichikawa, J. Tatami, A. Endo, K. Yoshida, Y. Sasaki, K. Komeya, T. Meguro, Bead-Milling and Postmilling Recrystallization: An Organic Template-free Methodology for the Production of Nano-zeolites, *Cryst. Growth Des.* 11 (2011) 955-958.
- [21] G.A. Nasser, T. Kurniawan, T. Tago, I.A. Bakare, T. Taniguchi, Y. Nakasaka, T. Masuda, O. Muraza, Cracking of n-hexane over hierarchical MOR zeolites derived from natural minerals, *Journal of the Taiwan Institute of Chemical Engineers* 61 (2016) 20-25.
- [22] G. Nasser, T. Kurniawan, K. Miyake, A. Galadima, Y. Hirota, N. Nishiyama, O. Muraza, Dimethyl ether to olefins over dealuminated mordenite (MOR) zeolites derived from natural minerals, *J. Nat. Gas Sci. Eng.* 28 (2016) 566-571.
- [23] D.S. Coombs, A. Alberti, T. Armbruster, G. Artioli, C. Colella, E. Galli, J.D. Grice, F. Liebau, J.A. Mandarino, H. Minato, E.H. Nickel, E. Passaglia, D.R. Peacor, S. Quartieri, R. Rinaldi, M. Ross, R.A. Sheppard, E. Tillmanns, G. Vezzalini, Recommended nomenclature for zeolite minerals: report of the subcommittee on zeolites of the International Mineralogical Association, Commission on new Minerals and Mineral names, *Canadian Mineralogist* 35 (1997) 1571-1606.
- [24] M.W. Ackley, S.U. Rege, H. Saxena, Application of natural zeolites in the purification and separation of gases, *Microporous and Mesoporous Materials* 61 (2003) 25-42.
- [25] J. Wang, S. Xu, J. Li, Y. Zhi, M. Zhang, Y. He, Y. Wei, X. Guo, Z. Liu, An approach to prepare nanosized HZSM-22 with enhanced lifetime in the methanol to hydrocarbon (MTH) reaction, *RSC Adv.* 5 (2015) 88928-88935.
- [26] M.M.J. Treacy, J.B. Higgins, Preface, in: M.M.J. Treacy, J.B. Higgins, J.B. Higgins (Eds.) *Collection of Simulated XRD Powder Patterns for Zeolites*, Elsevier Science B.V., Amsterdam, 2001, pp. 1.
- [27] C. Colella, Natural zeolites in environmentally friendly processes and applications, *Studies in Surface Science and Catalysis* 125 (1999) 641-655.
- [28] N.Y. Chen, W.E. Garwood, R.H. Heck, M-forming process, *Industrial & Engineering Chemistry Research* 26 (1987) 706-711.
- [29] IZA, <http://www.iza-online.org/natural/>, 2016.
- [30] C. Colella, W.S. Wise, The IZA Handbook of Natural Zeolites: A tool of knowledge on the most important family of porous minerals, *Microporous and Mesoporous Materials* 189 (2014) 4-10.
- [31] I. Marantos, G.E. Christidis, M. Ulmanu, Zeolite Formation and Deposits, in: V.J. Inglezakis, A.A. Zorpas (Eds.) *Handbook of Natural Zeolites* 2012.
- [32] M. Ulmanu, I. Anger, Physical and Chemical Properties, in: V.J. Inglezakis, Z.A. A. (Eds.) *Handbook of Natural Zeolites*, Bentham Science Publishers, SAIF Zone, Sharjah, UAE, 2012.

- [33] F.A. Mumpton, La roca magica: Uses of natural zeolites in agriculture and industry, *Proc. Natl. Acad. Sci. U. S. A.* 96 (1999) 3463-3470.
- [34] S. Wang, Y. Peng, Natural zeolites as effective adsorbents in water and wastewater treatment, *Chemical Engineering Journal* 156 (2010) 11-24.
- [35] F. Schüth, K.S.W. Sing, J. Weitkamp, *Handbook of Porous Solids*, Wiley 2002.
- [36] H. Michikazu, N. Kiyotaka, K. Keigo, Recent progress in the development of solid catalysts for biomass conversion into high value-added chemicals, *Science and Technology of Advanced Materials* 16 (2015) 034903.
- [37] N. Widiastuti, H. Wu, M. Ang, D.-k. Zhang, The potential application of natural zeolite for greywater treatment, *Desalination* 218 (2008) 271-280.
- [38] Butterfield, Borgerding, Tahoe-Truckee Sanitation Agency Internal Report, (1981).
- [39] G. GA, AWT plants makes wastewater potable., *Water Wastes Engin* 16 (1979) 36-44.
- [40] F.A. Mumpton, Using zeolites in agriculture, *Innovative Biological Technologies for Lesser Developed Countries*, Washington, DC: US Congress, Office of Technology Assessment, OTA-13P-F-29, 1985.
- [41]
[https://en.wikipedia.org/wiki/Castel_dell%27Ovo#/media/File:Castel_dell%27Ovo_\(1\)_\(15397707910\).jpg](https://en.wikipedia.org/wiki/Castel_dell%27Ovo#/media/File:Castel_dell%27Ovo_(1)_(15397707910).jpg).
- [42] M. Reháková, S. Čuvánová, M. Dzivák, J. Rimár, Z. Gaval'ová, Agricultural and agrochemical uses of natural zeolite of the clinoptilolite type, *Current Opinion in Solid State and Materials Science* 8 (2004) 397-404.
- [43] W. Parham, Natural zeolites, *Natural Resources Forum* 13 (1989) 107-115.
- [44] L.B. Sand, *Natural Zeolites : Occurrence, Properties, Use*, Pergamon Press, Oxford, 1978.
- [45] N.Y. Chen, S.J. Lucki, E.B. Mower, Cage effect on product distribution from cracking over crystalline aluminosilicate zeolites, *Journal of Catalysis* 13 (1969) 329-332.
- [46] J.E. Kogel, *Industrial minerals & rocks : commodities, markets, and uses*, Society for Mining, Metallurgy, and Exploration, Littleton, Colo., 2006.
- [47] P. Ballirano, A. Pacella, C. Cremisini, E. Nardi, M. Fantauzzi, D. Atzei, A. Rossi, G. Cametti, Fe (II) segregation at a specific crystallographic site of fibrous erionite: A first step toward the understanding of the mechanisms inducing its carcinogenicity, *Microporous and Mesoporous Materials* 211 (2015) 49-63.
- [48] Y. Goto, L.B. Sand, Crystallization of ZSM-5 from natural Japanese mordenite and clinoptilolite, in: D. Kallo, H.S. Sherry (Eds.) *Occurrence, Properties and Utilization of Natural Zeolites*, Akademiai Kiado, Budapest., 1988.
- [49] A. Ates, A. Reitzmann, C. Hardacre, H. Yalcin, Abatement of nitrous oxide over natural and iron modified natural zeolites, *Applied Catalysis A: General* 407 (2011) 67-75.
- [50] J. Barras, J. Klinowski, D.W. McComb, ²⁷Al and ²⁹Si solid-state NMR studies of dealuminated mordenite, *Journal of the Chemical Society, Faraday Transactions* 90 (1994) 3719-3723.
- [51] J.A. Ripmeester, A. Majid, R.E. Hawkins, Magic angle spinning ²⁹Si and ²⁷Al NMR study of mordenite dealumination, *Journal of Inclusion Phenomena* 1 (1983) 193-198.
- [52] T.S. Yusupov, L.G. Shumskaya, Y.A. Kirillova, State and perspectives of natural zeolite beneficiation, *Journal of Mining Science* 36 (2000) 299-304.

- [53] Y. Watanabe, H. Yamada, S. Yokoyama, J. Minato, Y.-J. Kim, S.B. Cho, K. Tamura, G.W. Stevens, Y. Komatsu, Air Classification of Korean Natural Zeolite to Improve Adsorption of Ammonium Ion, *Journal of Ion Exchange* 18 (2007) 530-535.
- [54] <interconversion zeolite sano 2013.pdf>.
- [55] H.G. Karge, P. Anderson, J. Weitkamp, H.K. Beyer, P. Gallezot, R. Harjula, H.G. Karge, U. Ryma, G. Schulz-Ekloff, R.P. Townsend, *Post-Synthesis Modification I*, Springer Berlin Heidelberg 2014.
- [56] O.E. Kartal, I. Onal, SYNTHESIS OF ZSM-5 FROM MODIFIED CLINOPTILOLITE AND ITS CATALYTIC ACTIVITY IN ALKYLATION OF BENZENE TO ETHYLBENZENE, *Chemical Engineering Communications* 195 (2008) 1043-1057.
- [57] D. Kalló, H.S. Sherry, Occurrence, properties and utilization of natural zeolites, *Akadémiai Kiadó* 1988.
- [58] J.T. Miller, P.D. Hopkins, B.L. Meyers, G.J. Ray, R.T. Roginski, G.W. Zajac, N.H. Rosenbaum, The effect of nonframework aluminum on acidity in dealuminated mordenite, *Journal of Catalysis* 138 (1992) 115-128.
- [59] H. Robson, Promotion of crystalline zeolite synthesis, Google Patents, 1973.
- [60] C. de las Pozas, D. Díaz Quintanilla, J. Pérez-Pariente, R. Roque-Malherbe, M. Magi, Hydrothermal transformation of natural clinoptilolite to zeolites Y and P1: Influence of the Na, K content, *Zeolites* 9 (1989) 33-39.
- [61] A. Dziedzicka, B. Sulikowski, M. Ruggiero-Mikołajczyk, Catalytic and physicochemical properties of modified natural clinoptilolite, *Catal. Today* 259, Part 1 (2016) 50-58.
- [62] D. Habibi, M. Nasrollahzadeh, H. Sahebkhari, Green synthesis of formamides using the Natrolite zeolite as a natural, efficient and recyclable catalyst, *J. Mol. Catal. A: Chem.* 378 (2013) 148-155.
- [63] L.I. Gurevich Messina, P.R. Bonelli, A.L. Cukierman, In-situ catalytic pyrolysis of peanut shells using modified natural zeolite, *Fuel Processing Technology* 159 (2017) 160-167.
- [64] A.S.M. Junaid, M. Rahman, H. Yin, W.C. McCaffrey, S.M. Kuznicki, Natural zeolites for oilsands bitumen cracking: Structure and acidity, *Microporous and Mesoporous Materials* 144 (2011) 148-157.
- [65] C. Baerlocher, L.B. McCusker, D.H. Olson, MOR - Cmc, in: C. Baerlocher, L.B.M.H. Olson (Eds.) *Atlas of Zeolite Framework Types* (Sixth Edition), Elsevier Science B.V., Amsterdam, 2007, pp. 218-219.
- [66] R. Moreno-Tost, J. Santamaría-González, E. Rodríguez-Castellón, A. Jiménez-López, M.A. Autié, E. González, M.C. Glacial, C.D.I. Pozas, Selective catalytic reduction of nitric oxide by ammonia over Cu-exchanged Cuban natural zeolites, *Applied Catalysis B: Environmental* 50 (2004) 279-288.
- [67] M.L.M.d. Oliveira, C.M. Silva, R. Moreno-Tost, T.L. Farias, A. Jiménez-López, E. Rodríguez-Castellón, A study of copper-exchanged mordenite natural and ZSM-5 zeolites as SCR-NO_x catalysts for diesel road vehicles: Simulation by neural networks approach, *Applied Catalysis B: Environmental* 88 (2009) 420-429.
- [68] H. Mishima, K. Hashimoto, T. Ono, M. Anpo, Selective catalytic reduction of NO with NH₃ over natural zeolites and its application to stationary diesel engine exhaust, *Applied Catalysis B: Environmental* 19 (1998) 119-126.

- [69] G. Nasser, T. Kurniawan, K. Miyake, A. Galadima, Y. Hirota, N. Nishiyama, O. Muraza, Dimethyl ether to olefins over dealuminated mordenite (MOR) zeolites derived from natural minerals, *Journal of Natural Gas Science and Engineering* 28 (2016) 566-571.
- [70] K.I. Patrylak, F.M. Bobonych, Y.G. Voloshyna, M.M. Levchuk, V.G. Il'in, O.M. Yakovenko, I.A. Manza, I.M. Tsupryk, Ukrainian mordenite–clinoptilolite rocks as a base for linear hexane isomerization catalyst, *Applied Catalysis A: General* 174 (1998) 187-198.
- [71] K.I. Patrylak, F.M. Bobonych, Y.G. Voloshyna, M.M. Levchuk, V.M. Solomakha, L.K. Patrylak, I.A. Manza, O.M. Taranookha, Linear hexane isomerization over the natural zeolite based catalysts depending on the zeolite phase composition, *Catalysis Today* 65 (2001) 129-135.
- [72] E. Agustina, P. Theresia, The Effect of Acid Dealumination of Indonesian Zeolite on its Physical, Chemical and Catalytic Properties, *Studies in Surface Science and Catalysis* 84 (1994) 1021-1026.
- [73] É. Miklósy, J. Papp, D. Kalló, Xylene isomerization on H-mordenites and H-clinoptilolites, *Zeolites* 3 (1983) 139-148.
- [74] R.I. Kusuma, J.P. Hadinoto, A. Ayucitra, F.E. Soetaredjo, S. Ismadji, Natural zeolite from Pacitan Indonesia, as catalyst support for transesterification of palm oil, *Applied Clay Science* 74 (2013) 121-126.
- [75] R. Hartono, B. Mulia, M. Sahlan, T.S. Utami, A. Wijanarko, H. Hermansyah, The modification of ion exchange heterogeneous catalysts for biodiesel synthesis, *AIP Conference Proceedings* 1826 (2017) 020020.
- [76] M.M.J. Treacy, J.B. Higgins, J.B. Higgins, Decamethonium DAF-1, in: M.M.J. Treacy, J.B. Higgins, J.B. Higgins (Eds.) *Collection of Simulated XRD Powder Patterns for Zeolites*, Elsevier Science B.V., Amsterdam, 2001, pp. 118-119.
- [77] D.W. Park, E.Y. Hwang, J.R. Kim, J.K. Choi, Y.A. Kim, H.C. Woo, Catalytic degradation of polyethylene over solid acid catalysts, *Polymer Degradation and Stability* 65 (1999) 193-198.
- [78] P. Djinović, T. Tomše, J. Grdadolnik, Š. Božič, B. Erjavec, M. Zabilskiy, A. Pintar, Natural aluminosilicates for catalytic depolymerization of polyethylene to produce liquid fuel-grade hydrocarbons and low olefins, *Catalysis Today* 258 (2015) 648-659.
- [79] S.-Y. Lee, J.-H. Yoon, J.-R. Kim, D.-W. Park, Degradation of polystyrene using clinoptilolite catalysts, *Journal of Analytical and Applied Pyrolysis* 64 (2002) 71-83.
- [80] M. Rehan, R. Miandad, M.A. Barakat, I.M.I. Ismail, T. Almeelbi, J. Gardy, A. Hassanpour, M.Z. Khan, A. Demirbas, A.S. Nizami, Effect of zeolite catalysts on pyrolysis liquid oil, *International Biodeterioration & Biodegradation* 119 (2017) 162-175.
- [81] H.C. Woo, K.H. Lee, J.S. Lee, Catalytic skeletal isomerization of n-butenes to isobutene over natural clinoptilolite zeolite, *Applied Catalysis A: General* 134 (1996) 147-158.
- [82] H.C. Lee, H.C. Woo, R. Ryoo, K.H. Lee, J.S. Lee, Skeletal isomerization of n-butenes to isobutene over acid-treated natural clinoptilolite zeolites, *Applied Catalysis A: General* 196 (2000) 135-142.
- [83] H.C. Lee, H.C. Woo, S.H. Chung, H.J. Kim, K.H. Lee, J.S. Lee, Effects of Metal Cation on the Skeletal Isomerization of 1-Butene over Clinoptilolite, *Journal of Catalysis* 211 (2002) 216-225.

- [84] T.K. Katranas, A.G. Vlessidis, V.A. Tsiatouras, K.S. Triantafyllidis, N.P. Evmiridis, Dehydrogenation of propane over natural clinoptilolite zeolites, *Microporous and Mesoporous Materials* 61 (2003) 189-198.
- [85] E. Saputra, M.A. Budihardjo, S. Bahri, J.A. Pinem, Cobalt-exchanged natural zeolite catalysts for catalytic oxidation of phenolic contaminants in aqueous solutions, *Journal of Water Process Engineering* 12 (2016) 47-51.
- [86] M.M.J. Treacy, J.B. Higgins, J.B. Higgins, MAPO-39, in: M.M.J. Treacy, J.B. Higgins, J.B. Higgins (Eds.) *Collection of Simulated XRD Powder Patterns for Zeolites*, Elsevier Science B.V., Amsterdam, 2001, pp. 64-65.
- [87] E. Pütün, B.B. Uzun, A.E. Pütün, Rapid Pyrolysis of Olive Residue. 2. Effect of Catalytic Upgrading of Pyrolysis Vapors in a Two-Stage Fixed-Bed Reactor, *Energy & Fuels* 23 (2009) 2248-2258.
- [88] H.W. Lee, Y.-M. Kim, J. Jae, B.H. Sung, S.-C. Jung, S.C. Kim, J.-K. Jeon, Y.-K. Park, Catalytic pyrolysis of lignin using a two-stage fixed bed reactor comprised of in-situ natural zeolite and ex-situ HZSM-5, *Journal of Analytical and Applied Pyrolysis* 122 (2016) 282-288.
- [89] A. Dziedzicka, B. Sulikowski, M. Ruggiero-Mikołajczyk, Catalytic and physicochemical properties of modified natural clinoptilolite, *Catalysis Today* 259 (2016) 50-58.
- [90] E. Ünveren, G. Gündüz, F. Cakicioğlu-Özkan, Isomerization of Alpha-pinene Over Acid Treated Natural Zeolite, *Chemical Engineering Communications* 192 (2005) 386-404.
- [91] B. Atalay, G. Gündüz, Isomerization of α -pinene over H3PW12O40 catalysts supported on natural zeolite, *Chemical Engineering Journal* 168 (2011) 1311-1318.
- [92] M. Syamsiro, H. Saptoadi, T. Norsujianto, P. Noviasri, S. Cheng, Z. Alimuddin, K. Yoshikawa, Fuel Oil Production from Municipal Plastic Wastes in Sequential Pyrolysis and Catalytic Reforming Reactors, *Energy Procedia* 47 (2014) 180-188.
- [93] S.-G. Lee, H.-S. Kim, Y.-H. Kim, E.-J. Kang, D.-H. Lee, C.-S. Park, Dimethyl ether conversion to light olefins over the SAPO-34/ZrO₂ composite catalysts with high lifetime, *Journal of Industrial and Engineering Chemistry* 20 (2014) 61-67.
- [94] A.S.M. Junaid, H. Yin, A. Koenig, P. Swenson, J. Chowdhury, G. Burland, W.C. McCaffrey, S.M. Kuznicki, Natural zeolite catalyzed cracking-assisted light hydrocarbon extraction of bitumen from Athabasca oilsands, *Applied Catalysis A: General* 354 (2009) 44-49.
- [95] A.S.M. Junaid, C. Street, W. Wang, M.M. Rahman, W. An, W.C. McCaffrey, S.M. Kuznicki, Integrated extraction and low severity upgrading of oilsands bitumen by activated natural zeolite catalysts, *Fuel* 94 (2012) 457-464.
- [96] G. Rocha Aguilera, V.G. Gupta, S. Yang, S.M. Kuznicki, W.C. McCaffrey, Pyrrolic Ring Opening and Nitrogen Removal from Solution without Hydrogenation: Natural Chabazite as a Cracking Catalyst, *Energy & Fuels* 28 (2014) 6570-6578.
- [97] G. Rocha Aguilera, S. Yang, A.S.M. Junaid, S.M. Kuznicki, W.C. McCaffrey, Ni and V removal from oil and model compounds without hydrogenation: Natural chabazite as solid acid, *The Canadian Journal of Chemical Engineering* 94 (2016) 938-946.
- [98] S. Goel, S.I. Zones, E. Iglesia, Synthesis of Zeolites via Interzeolite Transformations without Organic Structure-Directing Agents, *Chemistry of Materials* 27 (2015) 2056-2066.

- [99] M. Sawa, M. Niwa, Y. Murakami, Relationship between acid amount and framework aluminum content in mordenite, *Zeolites* 10 (1990) 532-538.
- [100] A.N.C. van laak, R.W. Gosselink, S.L. Sagala, J.D. Meeldijk, P.E. de Jongh, K.P. de Jong, Alkaline treatment on commercially available aluminum rich mordenite, *Applied Catalysis A: General* 382 (2010) 65-72.
- [101] P.A. Zielinski, A. Van Neste, D.B. Akolekar, S. Kaliaguine, Effect of high-energy ball milling on the structural stability, surface and catalytic properties of small-, medium- and large-pore zeolites, *Microporous Mater.* 5 (1995) 123-133.
- [102] J. Xie, S. Kaliaguine, Zeolite ball milling as a means of enhancing the selectivity for base catalyzed reactions, *Appl. Catal., A* 148 (1997) 415-423.
- [103] C. Kosanović, J. Bronić, B. Subotić, I. Smit, M. Stubičar, A. Tonejc, T. Yamamoto, Mechanochemistry of zeolites: Part 1. Amorphization of zeolites A and X and synthetic mordenite by ball milling, *Zeolites* 13 (1993) 261-268.
- [104] C. Colella, A.F. Gualtieri, Cronstedt's zeolite, *Microporous and Mesoporous Materials* 105 (2007) 213-221.
- [105] M.H.M. Ahmed, O. Muraza, A.M. Al-Amer, K. Miyake, N. Nishiyama, Development of hierarchical EU-1 zeolite by sequential alkaline and acid treatments for selective dimethyl ether to propylene (DTP), *Appl. Catal., A* 497 (2015) 127-134.
- [106] N. Viswanadham, L. Dixit, J.K. Gupta, M.O. Garg, Effect of acidity and porosity changes of dealuminated mordenites on n-hexane isomerization, *Journal of Molecular Catalysis A: Chemical* 258 (2006) 15-21.
- [107] C. Colella, Natural zeolites, *Studies in Surface Science and Catalysis* 157 (2005) 13-40.
- [108] G.A. Nasser, T. Kurniawan, T. Tago, I.A. Bakare, T. Taniguchi, Y. Nakasaka, T. Masuda, O. Muraza, Cracking of n-hexane over hierarchical MOR zeolites derived from natural minerals, *Journal of the Taiwan Institute of Chemical Engineers* (2015).
- [109] T. Wakihara, A. Ihara, S. Inagaki, J. Tatami, K. Sato, K. Komeya, T. Meguro, Y. Kubota, A. Nakahira, Top-Down Tuning of Nanosized ZSM-5 Zeolite Catalyst by Bead Milling and Recrystallization, *Cryst. Growth Des.* 11 (2011) 5153-5158.
- [110] E. Ye, D. Lippe, Alkylation provides option to monetize butane surplus, *Oil & Gas Journal*, PennWell Corporation, Tulsa, 2013, pp. 74-76,78.
- [111] W.W. Kaeding, C. Chu, L.B. Young, B. Weinstein, S.A. Butter, Selective alkylation of toluene with methanol to produce para-Xylene, *Journal of Catalysis* 67 (1981) 159-174.
- [112] C.A. Emeis, Determination of Integrated Molar Extinction Coefficients for Infrared Absorption Bands of Pyridine Adsorbed on Solid Acid Catalysts, *Journal of Catalysis* 141 (1993) 347-354.
- [113] N. Viswanadham, M. Kumar, Effect of dealumination severity on the pore size distribution of mordenite, *Microporous and Mesoporous Materials* 92 (2006) 31-37.
- [114] J.C. Groen, T. Sano, J.A. Moulijn, J. Pérez-Ramírez, Alkaline-mediated mesoporous mordenite zeolites for acid-catalyzed conversions, *Journal of Catalysis* 251 (2007) 21-27.
- [115] R.A. Asuquo, G. Edermirth, J.A. Lercher, n-Butane Isomerization over Acidic Mordenite, *Journal of Catalysis* 155 (1995) 376-382.

- [116] M.M.J. Treacy, J.B. Higgins, J.B. Higgins, EMC-2, Calcined, in: M.M.J. Treacy, J.B. Higgins, J.B. Higgins (Eds.) Collection of Simulated XRD Powder Patterns for Zeolites, Elsevier Science B.V., Amsterdam, 2001, pp. 132-133.
- [117] M.M.J. Treacy, J.B. Higgins, J.B. Higgins, (Na, Tetramethylammonium)-E, in: M.M.J. Treacy, J.B. Higgins, J.B. Higgins (Eds.) Collection of Simulated XRD Powder Patterns for Zeolites, Elsevier Science B.V., Amsterdam, 2001, pp. 128-129.
- [118] L. Liu, L. Zhao, H. Sun, Simulation of NH₃ Temperature-Programmed Desorption Curves Using an ab Initio Force Field, *The Journal of Physical Chemistry C* 113 (2009) 16051-16057.
- [119] E. Babůrek, J. Nováková, Isomerization of n-butane over acid zeolites, *Applied Catalysis A: General* 185 (1999) 123-130.
- [120] N. Chaouati, A. Soualah, M. Chater, M. Tarighi, L. Pinard, Mechanisms of coke growth on mordenite zeolite, *Journal of Catalysis* 344 (2016) 354-364.
- [121] J.I. Villegas, N. Kumar, T. Heikkilä, A. Smiešková, P. Hudec, T. Salmi, D.Y. Murzin, A highly stable and selective Pt-modified mordenite catalyst for the skeletal isomerization of n-butane, *Appl. Catal., A* 284 (2005) 223-230.
- [122] V.L. Struzhko, S.N. Orlik, M.G. Martsenyuk-Kukharuk, V.P. Stasevich, V.A. Ostapyuk, T.V. Mironyuk, The effect of the modification conditions of natural mordenite on their catalytic characteristics in the selective reduction of NO_x, *Theor. Exp. Chem.* 35 (1999) 120-124.
- [123] Handbook of Natural Zeolites, Bentham Science Publishers, SAIF Zone, Sharjah, UAE, 2012.
- [124] E. Koohsaryan, M. Anbia, Nanosized and hierarchical zeolites: A short review, *Chinese Journal of Catalysis* 37 (2016) 447-467.
- [125] S. Gopalakrishnan, S. Yada, J. Muench, T. Selvam, W. Schwieger, M. Sommer, W. Peukert, Wet milling of H-ZSM-5 zeolite and its effects on direct oxidation of benzene to phenol, *Applied Catalysis A: General* 327 (2007) 132-138.
- [126] A. Ozkan, M. Yekeler, M. Calkaya, Kinetics of fine wet grinding of zeolite in a steel ball mill in comparison to dry grinding, *International Journal of Mineral Processing* 90 (2009) 67-73.
- [127] C. Kong, T. Tsuru, Zeolite nanocrystals prepared from zeolite microparticles by a centrifugation-assisted grinding method, *Chemical Engineering and Processing: Process Intensification* 49 (2010) 809-814.
- [128] P.A. Zielinski, A. Van Neste, D.B. Akolekar, S. Kaliaguine, Effect of high-energy ball milling on the structural stability, surface and catalytic properties of small-, medium- and large-pore zeolites, *Microporous Materials* 5 (1995) 123-133.
- [129] C.C. Koch, Y.S. Cho, Nanocrystals by high energy ball milling, *Nanostructured Materials* 1 (1992) 207-212.
- [130] R.K. Gupta, D. Fabijanic, T. Dorin, Y. Qiu, J.T. Wang, N. Birbilis, Simultaneous improvement in the strength and corrosion resistance of Al via high-energy ball milling and Cr alloying, *Materials & Design* 84 (2015) 270-276.
- [131] W.D. Harkins, G. Jura, An Adsorption Method for the Determination of the Area of a Solid without the Assumption of a Molecular Area, and the Area Occupied by Nitrogen Molecules on the Surfaces of Solids, *The Journal of Chemical Physics* 11 (1943) 431-432.

- [132] P. Tarazona, Free-energy density functional for hard spheres, *Physical Review A* 31 (1985) 2672-2679.
- [133] I.A. Bakare, O. Muraza, A.M. Al-Amer, Z.H. Yamani, The effect of non-ionic surfactant in the microwave-assisted synthesis of MTT zeolite optimized by Taguchi method, *Journal of the Taiwan Institute of Chemical Engineers* 50 (2015) 314-321.
- [134] J.E. Becker, Attrition Mill Grinding of Refractories, A Collection of Papers Presented at the 96th Annual Meeting and the 1994 Fall Meetings of the Materials & Equipment/Whitewares/Refractory Ceramics/Basic Science: Ceramic Engineering and Science Proceedings, John Wiley & Sons, Inc.2008, pp. 115-126.
- [135] R.E. Schilling, M. Yang, Attritors and ball mills how they work, Union Process Inc. (2000).
- [136] E. Kasai, H. Mimura, K. Sugiyama, F. Saito, K. Akiba, Y. Waseda, Mechano-chemical changes in natural and synthetic zeolites by dry grinding using a planetary ball mill, *Advanced Powder Technology* 5 (1994) 189-203.
- [137] A.L. Patterson, The Scherrer Formula for X-Ray Particle Size Determination, *Physical Review* 56 (1939) 978-982.
- [138] J. Perez-Ramirez, C.H. Christensen, K. Egeblad, C.H. Christensen, J.C. Groen, Hierarchical zeolites: enhanced utilisation of microporous crystals in catalysis by advances in materials design, *Chemical Society Reviews* 37 (2008) 2530-2542.
- [139] J. Perez-Ramirez, C.H. Christensen, K. Egeblad, C.H. Christensen, J.C. Groen, Hierarchical zeolites: enhanced utilisation of microporous crystals in catalysis by advances in materials design, *Chem. Soc. Rev.* 37 (2008) 2530-2542.
- [140] T. Wakihara, K. Sato, K. Sato, J. Tatami, S. Kohara, K. Komeya, T. Meguro, Preparation of nano-zeolite X by bead-milling and post-milling recrystallization, *J. Ceram. Soc. Jpn.* 120 (2012) 341-343.
- [141] G.A. Nasser, T. Kurniawan, T. Tago, I.A. Bakare, T. Taniguchi, Y. Nakasaka, T. Masuda, O. Muraza, Cracking of n-hexane over hierarchical MOR zeolites derived from natural minerals, *J. Taiwan Inst. Chem. Eng.* (2015).
- [142] R.I. Kusuma, J.P. Hadinoto, A. Ayucitra, F.E. Soetaredjo, S. Ismadji, Natural zeolite from Pacitan Indonesia, as catalyst support for transesterification of palm oil, *Appl. Clay Sci.* 74 (2013) 121-126.
- [143] K. Sato, T. Wakihara, S. Kohara, K. Ohara, J. Tatami, A. Endo, S. Inagaki, I. Kawamura, A. Naito, Y. Kubota, Characterization of Amorphized Zeolite A by Combining High-Energy X-ray Diffraction and High-Resolution Transmission Electron Microscopy, *J. Phys. Chem. C* 116 (2012) 25293-25299.
- [144] B.O. Hincapie, L.J. Garces, Q. Zhang, A. Sacco, S.L. Suib, Synthesis of mordenite nanocrystals, *Microporous Mesoporous Mater.* 67 (2004) 19-26.
- [145] W. Chu, X. Li, X. Zhu, S. Xie, C. Guo, S. Liu, F. Chen, L. Xu, Size-controlled synthesis of hierarchical ferrierite zeolite and its catalytic application in 1-butene skeletal isomerization, *Microporous Mesoporous Mater.* 240 (2017) 189-196.
- [146] T. Kurniawan, O. Muraza, K. Miyake, A.S. Hakeem, Y. Hirota, A.M. Al-Amer, N. Nishiyama, Conversion of Dimethyl Ether to Olefins over Nanosized Mordenite Fabricated by a Combined High-Energy Ball Milling with Recrystallization, *Ind. Eng. Chem. Res.* (2017).

- [147] C. Cobzaru, Modified Zeolites: Modification of Natural Zeolites for Catalytic Applications, in: V.J. Inglezakis, A.A. Zorpas (Eds.) Handbook of Natural Zeolites, Bentham Science Publishers, SAIF Zone, Sharjah, UAE, 2012.
- [148] L.B. Sand, Synthesis of large-port and small-port mordenites, Molecular sieves, Society of Chemical Industry London, 1968, pp. 71-77.
- [149] F. Raatz, C. Marcilly, E. Freund, Comparison between small port and large port mordenites, Zeolites 5 (1985) 329-333.
- [150] P.C. Van Geem, K.F.M.G.J. Scholle, G.P.M. Van der Velden, W.S. Veeman, Study of the transformation of small-port into large-port mordenite by magic-angle spinning NMR and infrared spectroscopy, J. Phys. Chem. 92 (1988) 1585-1589.
- [151] M.H.M. Ahmed, O. Muraza, A.M. Al Amer, Y. Sugiura, N. Nishiyama, Development of desilicated EU-1 zeolite and its application in conversion of dimethyl ether to olefins, Microporous Mesoporous Mater. 207 (2015) 9-16.
- [152] M.H.M. Ahmed, O. Muraza, A.M. Al-Amer, K. Miyake, N. Nishiyama, Development of hierarchical EU-1 zeolite by sequential alkaline and acid treatments for selective dimethyl ether to propylene (DTP), Applied Catalysis A: General 497 (2015) 127-134.
- [153] S. Stefanidis, K. Kalogiannis, E.F. Iliopoulou, A.A. Lappas, J.M. Triguero, M.T. Navarro, A. Chica, F. Rey, Mesopore-modified mordenites as catalysts for catalytic pyrolysis of biomass and cracking of vacuum gasoil processes, Green Chem. 15 (2013) 1647-1658.
- [154] S. Inagaki, K. Sato, S. Hayashi, J. Tatami, Y. Kubota, T. Wakihara, Mechanochemical Approach for Selective Deactivation of External Surface Acidity of ZSM-5 Zeolite Catalyst, ACS Appl. Mater. Interfaces 7 (2015) 4488-4493.
- [155] M.M.J. Treacy, J.B. Higgins, J.B. Higgins, Mordenite, in: M.M.J. Treacy, J.B. Higgins, J.B. Higgins (Eds.) Collection of Simulated XRD Powder Patterns for Zeolites, Elsevier Science B.V., Amsterdam, 2001, pp. 242-243.
- [156] G. Kühn, Modification of Zeolites, in: J. Weitkamp, L. Puppe (Eds.) Catalysis and Zeolites, Springer Berlin Heidelberg 1999, pp. 81-197.
- [157] P. Simoncic, T. Armbruster, Peculiarity and defect structure of the natural and synthetic zeolite mordenite: A single-crystal X-ray study, Am. Mineral. 89 (2004) 10.
- [158] G. Gottardi, E. Galli, Zeolites of the Mordenite Group, Natural Zeolites, Springer Berlin Heidelberg 1985, pp. 223-255.
- [159] H. Valdés, V.A. Solar, E.H. Cabrera, A.F. Veloso, C.A. Zaror, Control of released volatile organic compounds from industrial facilities using natural and acid-treated mordenites: The role of acidic surface sites on the adsorption mechanism, Chem. Eng. J. 244 (2014) 117-127.
- [160] J.B. Lad, Y.T. Makkawi, Adsorption of dimethyl ether (DME) on zeolite molecular sieves, Chem. Eng. J. 256 (2014) 335-346.
- [161] J.-L. Guth, H. Kessler, Synthesis of Aluminosilicate Zeolites and Related Silica-Based Materials, in: J. Weitkamp, L. Puppe (Eds.) Catalysis and Zeolites, Springer Berlin Heidelberg 1999, pp. 1-52.
- [162] A.S. Al-Dughaiter, H. de Lasa, Neat dimethyl ether conversion to olefins (DTO) over HZSM-5: Effect of SiO₂/Al₂O₃ on porosity, surface chemistry, and reactivity, Fuel 138 (2014) 52-64.

- [163] F.X. Cormerais, G. Perot, M. Guisnet, Selectivity of the dimethylether to hydrocarbons conversion on various zeolites, *Zeolites* 1 (1981) 141-144.
- [164] S. Gopalakrishnan, S. Yada, J. Muench, T. Selvam, W. Schwieger, M. Sommer, W. Peukert, Wet milling of H-ZSM-5 zeolite and its effects on direct oxidation of benzene to phenol, *Appl. Catal., A* 327 (2007) 132-138.
- [165] M. Shemfe, S. Gu, B. Fidalgo, Techno-economic analysis of biofuel production via bio-oil zeolite upgrading: An evaluation of two catalyst regeneration systems, *Biomass Bioenergy* 98 (2017) 182-193.
- [166] <https://us.vwr.com/store/product/9881375/zeolite-mordenite-sodium>.
- [167] <https://www.alfa.com/en/catalog/045877/>.
- [168] F. Raatz, E. Freund, C. Marcilly, Study of small-port and large-port mordenite modifications. Part 1.-Preparation of the HM forms, *Journal of the Chemical Society, Faraday Transactions 1: Physical Chemistry in Condensed Phases* 79 (1983) 2299-2309.
- [169] W. Vermeiren, J.P. Gilson, Impact of Zeolites on the Petroleum and Petrochemical Industry, *Topics in Catalysis* 52 (2009) 1131-1161.
- [170] V. Adeeva, W.M.H. Sachtler, Mechanism of butane isomerization over industrial isomerization catalysts, *Appl. Catal., A* 163 (1997) 237-243.
- [171] Y. Yuan, L. Wang, H. Liu, P. Tian, M. Yang, S. Xu, Z. Liu, Facile preparation of nanocrystal-assembled hierarchical mordenite zeolites with remarkable catalytic performance, *Chinese Journal of Catalysis* 36 (2015) 1910-1919.
- [172] M.T. Tran, N.S. Gnep, G. Szabo, M. Guisnet, Isomerization of n-Butane over H-Mordenites under Nitrogen and Hydrogen: Influence of the Acid Site Density, *Journal of Catalysis* 174 (1998) 185-190.
- [173] J.C. Yori, M.A. D'Amato, G. Costa, J.M. Parera, Influence of platinum and hydrogen on n-butane isomerization on H-Mordenite, *Reaction Kinetics and Catalysis Letters* 56 (1995) 129-135.
- [174] P. Cañizares, A. de Lucas, F. Dorado, n-Butane isomerization over H-mordenite: role of the monomolecular mechanism, *Appl. Catal., A* 196 (2000) 225-231.
- [175] R.A. Asuquo, G. Eder-Mirth, K. Seshan, J.A.Z. Pieterse, J.A. Lercher, Improving the Stability of H-Mordenite for n-Butane Isomerization, *Journal of Catalysis* 168 (1997) 292-300.
- [176] M.T. Tran, N.S. Gnep, G. Szabo, M. Guisnet, Comparative study of the transformation of n-butane, n-hexane and n-heptane over H-MOR zeolites with various Si/Al ratios, *Appl. Catal., A* 170 (1998) 49-58.
- [177] M.J. Wulfers, F.C. Jentoft, Mechanism of n-butane skeletal isomerization on H-mordenite and Pt/H-mordenite, *Journal of Catalysis* 330 (2015) 507-519.
- [178] H. Zhou, Y. Wang, F. Wei, D. Wang, Z. Wang, In situ synthesis of SAPO-34 crystals grown onto α -Al₂O₃ sphere supports as the catalyst for the fluidized bed conversion of dimethyl ether to olefins, *Appl. Catal., A* 341 (2008) 112-118.
- [179] J. Hlavay, I. Vassányi, J. Inczédy, Quantitative determination of the mordenite content of natural zeolite rocks by infrared spectroscopy, *Spectrochimica Acta Part A: Molecular Spectroscopy* 41 (1985) 1457-1458.
- [180] C. Li, Z. Wu, *Microporous Materials Characterized by Vibrational Spectroscopies, Handbook of Zeolite Science and Technology*, CRC Press 2003.

- [181] K. Segawa, T. Shimura, Effect of dealumination of mordenite by acid leaching for selective synthesis of ethylenediamine from ethanolamine, *Appl. Catal., A* 194–195 (2000) 309-317.
- [182] M.J. Wulfers, F.C. Jentoft, Identification of carbonaceous deposits formed on H-mordenite during alkane isomerization, *Journal of Catalysis* 307 (2013) 204-213.
- [183] E. Babůrek, J. Nováková, Isomerization of n-butane over acid zeolites: Role of Brønsted and Lewis acid sites, *Appl. Catal., A* 185 (1999) 123-130.
- [184] P. Cañizares, A. de Lucas, F. Dorado, A. Durán, I. Asencio, Characterization of Ni and Pd supported on H-mordenite catalysts: Influence of the metal loading method, *Appl. Catal., A* 169 (1998) 137-150.
- [185] M. Guisnet, P. Bichon, N.S. Gnep, N. Essayem, Transformation of propane, n-butane and n-hexane over H₃PW₁₂O₄₀ and cesium salts. Comparison to sulfated zirconia and mordenite catalysts, *Topics in Catalysis* 11 (2000) 247-254.
- [186] G.A. Urzhuntsev, E.V. Ovchinnikova, V.A. Chumachenko, S.A. Yashnik, V.I. Zaikovskiy, G.V. Echevsky, Isomerization of n-butane over Pd–SO₄/ZrO₂ catalyst: Prospects for commercial application, *Chemical Engineering Journal* 238 (2014) 148-156.

VITAE

Name : Teguh Kurniawan

Nationality : Indonesian

Date of Birth : May 6, 1983

Email : teguh@kfupm.edu.sa; teguh@untirta.ac.id

Address : 1. Al Nafees Street 30a, Ar Rakah Janubiyah, Al Khobar,
Saudi Arabia
2. Jurusan Teknik Kimia, Universitas Sultan Ageng
Tirtayasa, Jl. Jenderal Sudirman, Km.03, Cilegon,
Banten, Indonesia

Academic Background : Bachelor Degree in Chemical Engineering from
Institut Teknologi Bandung, 2005
Master Degree in Chemical Engineering from
Institut Teknologi Bandung, 2011

LIST OF PUBLICATIONS

Publications Based on the Dissertation

1. T. Kurniawan, O. Muraza, A.M. Al-Amer. Potential natural zeolites as cost-effective catalysts for renewables and clean technology: A review. Manuscript in preparation. **(CHAPTER 2)**
2. T. Kurniawan, O. Muraza, I.A. Bakare, Mohammed A. Sanhoob, A.M. Al-Amer. Isomerization of n-butane over cost-effective mordenite catalysts fabricated via recrystallization of natural zeolites. Manuscript submitted to *Industrial & Engineering Chemistry Research*. Under review **(CHAPTER 3)**
3. T. Kurniawan, O. Muraza, A.S. Hakeem, I.A. Bakare, M. Qamaruddin, A.M. Al-Amer. High-energy ball milling attritor and hydrothermal recrystallization to prepare mordenite nanoparticles: the effects of the relative weights of the balls and water. Manuscript submitted to *Powder Technology*. Under review **(CHAPTER 4)**
4. T. Kurniawan, O. Muraza, A.S. Hakeem, A.M. Al-Amer, Mechanochemical Route and Recrystallization Strategy to Fabricate Mordenite Nanoparticles from Natural Zeolites, *Crystal Growth & Design*, 17 (2017) 3313-3320. **(CHAPTER 5)**
5. T. Kurniawan, O. Muraza, K. Miyake, A.S. Hakeem, Y. Hirota, A.M. Al-Amer, N. Nishiyama, Conversion of Dimethyl Ether to Olefins over Nanosized Mordenite Fabricated by a Combined High-Energy Ball Milling with Recrystallization, *Industrial & Engineering Chemistry Research*, 56 (2017) 4258-4266. **(CHAPTER 6)**
6. T. Kurniawan, O. Muraza, A.S. Hakeem, I.A. Bakare, T. Nishitoba, T. Yokoi, Z.H. Yamani, A.M. Al-Amer. Selective isomerization of n-butane over mordenite nanoparticles fabricated by sequential ball milling-recrystallization-dealumination route, *Energy & Fuels*, 31 (2017) 12691-12700. **(CHAPTER 7)**

Publications Related to the Natural Zeolites

1. G. Nasser, T. Kurniawan, K. Miyake, A. Galadima, Y. Hirota, N. Nishiyama, O. Muraza, Conversion of dimethyl ether to olefins over dealuminated mordenite (MOR) zeolites derived from natural minerals, *Journal Natural Gas Science and Engineering*, 28(2016) 566-571.
2. G. Nasser, T. Kurniawan, T. Tago, I.A. Bakare, T. Taniguchi, Y. Nakasaka, T. Masuda, O. Muraza, Cracking of n-hexane over hierarchical MOR zeolites derived from natural minerals, *Journal of the Taiwan Institute of Chemical Engineers*, 61 (2016) 20-25.

Publications Related to the Synthetic Zeolites

1. I.A. Bakare, O. Muraza, T. Kurniawan, Z.H. Yamani, E.N. Shafei, A.K. Punetha, K.-H. Choi, T. Yokoi, Hydrothermal stability of MTT zeolite in hot water: The role of La and Ce, *Microporous and Mesoporous Materials*, 233 (2016) 93-101.